Design and assessment of experimental and numerical characterization of a three-blade horizontal axis hydrokinetic water turbine (HAHWT) in a low-velocity channel

Roberta Ferraiuolo

Ph.D. Coordinator
Prof. Eng. Andrea Papola

Tutors
Prof. Eng. Maurizio Giugni
Prof. Eng. Giuseppe Del Giudice
Prof. Eng. Eduardo Álvarez Álvarez
Eng. Gianluca Sorgenti degli Uberti

OCTOBER 2023

UNIVERSITY OF NAPLES FEDERICO II

Department of Civil, Architectural and Environmental Engineering

Ph.D. Course in
Civil Systems Engineering
Thirty-fifth Cycle

Ph.D. Candidate
Ferraiuolo Roberta
MR: DR993796

Thesis's Title

Design and assessment of experimental and numerical characterization of a three-blade horizontal axis hydrokinetic water turbine (HAHWT) in a low-velocity channel

Dissertation for the Doctor of Philosophy in Civil Systems Engineering degree with a European Label

Ph.D. Coordinator	**Tutors**
Prof. Eng. Andrea Papola	Prof. Eng. Maurizio Giugni
	Prof. Eng. Giuseppe Del Giudice
	Prof. Eng. Eduardo Álvarez Álvare
	PhD Eng. Gianluca Sorgenti degli Uberti

OCTOBER 2023

Affiliation and scholarship information

Ph.D. Candidate	Ferraiuolo Roberta
Tutors	Prof. Eng. Maurizio Giugni, Prof. Eng. Giuseppe Del Giudice, Prof. Eng. Eduardo Álvarez Álvarez, PhD Eng. Gianluca Sorgenti degli Uberti
Ph.D. Coordinator	Prof. Eng. Andrea Papola
Ph.D. Course	Civil Systems Engineering
Cycle	Thirty-fifth
Year	Third
Scholarship code	DOT1318449-Borsa 2
CUP	E65F19001220007
Title of Research	Design and assessment of experimental and numerical characterization of a three-blade horizontal axis hydrokinetic water turbine (HAHWT) in a low-velocity channel

The additional scholarship of National Operative Program (PON) Research and Innovation (PON) 2014-2020 (CCI 2014IT16M2oP005) finances this work by European Social Fund Asse I "Capitale Umano," Action I.1 **"Innovative Ph.D. with industrial characterization."**

To Cinzia, Lucio and,

Floriano.

Ringraziamenti

Fermarmi ed osservare questi anni di Dottorato trascorsi, mi fa pensare che questa sia stata, senza dubbio, un'esperienza enorme, che ha consentito di espandere sicuramente la mia crescita professionale e personale.

Se sono riuscita a sviluppare questo lavoro di ricerca, è grazie all'aiuto e alla guida costante di molte persone che ho avuto la fortuna di incontrare lungo il mio percorso di questi anni.

Prima di tutto, voglio ringraziare il Professore Maurizio Giugni, per la sua incredibile disponibilità ed abilità ad accogliere ogni mia necessità. Le sono grata per aver creduto in me, rendendomi parte del suo gruppo di ricerca.

Ringrazio il Professore Giuseppe Del Giudice, per le sue osservazioni sempre costruttive e pertinenti. La ringrazio per avermi dimostrato continuo supporto ed umanità. Attraverso la sua esperienza, ho imparato anche cosa vuol dire fare didattica e diventare un insegnante.

Uno speciale ringraziamento va al mio collega Professore Francesco Pugliese, per la sua capacità di esserci sempre. Durante questi anni hai contribuito in maniera incisiva alla mia formazione, dandomi spunti pratici e risolutivi nel produrre questo lavoro di ricerca.

Ti ringrazio per l'affetto per la comprensione e la pazienza, e per aver condiviso con me un po' della tua esperienza con totale disinteresse.

Sono convinta inoltre, che questi anni non li ricorderei con la stessa intensità se non avessi passato i sei mesi in Spagna ad Oviedo, cittadina splendida nel nord della Spagna; che mi ha donato tanto e dove ho sviluppato la parte saliente della mia ricerca.

A questo proposito, un ringraziamento non può che andare al Professore Eduardo, che non solo ha dato un decisivo contributo alla mia ricerca, ma ha anche saputo fornirmi una calorosa accoglienza durante i mesi trascorsi lì.

Ricorderò per sempre la collaborazione dell'intero gruppo di ricerca spagnolo del Dipartimento di Energia, specialmente il Professore Joaquín Fernández, per la sua enorme gentilezza e capacità di risolvere qualunque problema tecnico anche a distanza.

La mia gratitudine va anche ad Ahmed Ghirab Sayed Yorsy, per la sua capacità nell'avermi insegnato a maneggiare una stampante 3D, condividendo con me le sue conoscenze, e continuando a supportarmi con grande pazienza, anche quando sono tornata in Italia.

Estendo i miei ringraziamenti anche al Prof. Eduardo Marigorta e agli altri colleghi Aitor, Victor e Rodolfo.

Ringrazio Aitor, per il supporto dimostratomi nel costruire il set-up sperimentale su cui ho lavorato, nel Laboratorio di Idraulica di Mieres. Indimenticabile anche l'aiuto del Tecnico di Laboratorio di Gijón Fran.

Ringrazio i miei revisori, la Professoressa Portoghese Helena Ramos e il Professore Spagnolo Joaquín Fernández, per essere stati di grande aiuto a rendere migliore questo lavoro di ricerca.

Un sentito ringraziamento va anche al Professore Andrea Papola, Coordinatore del Ciclo di Dottorato, per la sua precisione, velocità nel darci informazioni utili, e infinita pazienza.

Posso dire che tutto questo non sarebbe stato possibile senza la presenza dei miei molti colleghi del DICEA e del mio Ciclo e non, che nel corso di questi anni ho avuto modo di conoscere. Ogniuno con il proprio carattere, ha reso ogni mio giorno trascorso all'interno del Dipartimento, più leggero, divertente e stimolante.

Ringrazio: Francesco, Dina, Guadalupe, Maria Cristina, Andrea D'Aniello, Sara, Mimmo, Andrea Del Gaudio, Valeria, per la loro presenza in questi anni di alti e bassi. Tutti i miei colleghi che, vengono da altre parti del Mondo, Diego, Khim, Ruodan, Fathima, Luiz, grazie per avermi aperto lo sguardo sulle realtà dalle quali provenite.

Ringrazio profondamente la mia famiglia, per il costante sostegno, per esserci sempre nelle difficoltà e nei momenti di gioia.

A Cinzia, Lucio, Emma, Francesco, i pilastri della mia vita.

Dedico questo lavoro a membri della mia famiglia che sfortunatamente sono passati a miglior vita quest'anno, a Zia Teresa e Zio Lino che mi proteggono dall'alto e con i quali avrei voluto condividere questo momento.

Ai miei amici di sempre, che ci sono stati e spero, sempre saranno miei riferimenti nei momenti importanti della vita. Senza di voi non sarebbe lo stesso. Le mie amiche Ingegnere con cui ho condiviso gli anni più belli della vita.

In fine non per ordine d'importanza, la mia gratitudine va al mio compagno di vita Floriano, per il suo amore sconfinato, la sua tenerezza, il suo supporto e la sua pazienza,

Dimostri ogni giorno di essere una persona speciale.

Questo lavoro per me è anche un po' tuo.

Acknowledgments

These four years of Ph.D. allowed me to expand my professional and personal growth. If I could develop this work, it was mainly thanks to the help and guidance of many people I was lucky to meet during these years.

First, I would like to thank my Tutor, Professor Maurizio Giugni, for his incredible willingness and ability to accommodate my every need. I am also grateful to him for believing in me and making me part of his research group.

Thanks to my second Tutor, Professor Giuseppe Del Giudice, for his always pertinent and informative observations. I thank him for his humankind and demonstrated support. Through his experience, I have learned how to interact with students and how to become a teacher.

A special acknowledgment is reserved to my colleague Prof. Francesco Pugliese, for his tireless ability to always be by my side over the years and for always providing me with valuable practical advice. I thank him with affection for sharing his experience with me disinterestedly, despite not being one of my official Tutors.

Undoubtedly, one of the most formative steps of this experience was the time I spent in Oviedo in the north of Spain, where I developed the core of the entire research work. To this end, a special thank goes to my Spanish Tutor, Professor Eduardo Álvarez Álvarez, who was not only able to provide a huge practical contribution to my research work but also for allowing me to integrate well in a new town during my period abroad.

I appreciated the collaboration of the entire Spanish research group at the Energy Department of Oviedo University, especially Professor Joaquín Fernández, for his incredible kindness and valuable capacity to solve problems even from a distance.

My gratitude goes to the researcher Ahmed Gharib Sayed Yosry for his great ability to teach me how to manage the 3D printing prototype, sharing his knowledge about the CFD Model implementation, and continuing to do so, even when I came back to Italy.

I extend my special thanks to all the members of the research teams, including Prof. Eduardo Blanco Marigorta and the other colleagues Aitor, Victor, and Rodolfo.

A special thanks goes to Aitor, who helped me build the laboratory set-up at the Hydraulic Laboratory of the Polytechnical Engineering School of Mieres. I cannot forget the valuable assistance and practical support of the laboratory technician Fran, whom I thank.

I especially thank the reviewers of this thesis: Professor Helena Ramos and Professor Fernández, who will certainly provide points of observation aimed at improving this work.

I thank Professor Andrea Papola for his constant support and remarkable patience as a Ph.D. Program Coordinator over these years.

This experience wouldn't have been the same without the incredible support of my colleagues from the DICEA Department. Especially to my dear colleagues Francesco Pugliese, Dina Pirone, Guadalupe Torre Gómez, Maria Cristina Morani, Andrea D'Aniello, Sara Tuozzo, Mimmo Migliano, Andre Del Gaudio, Valeria Guadagno. You have made these years fun and stimulating at the same time.

I thank the new colleagues that have come along these years and months from several countries, which have opened my mind to the cultures from they come from, giving me more than I expected and making these years unforgettable.

I would also like to deeply thank my whole family to always supporting me, in moment of joy or sadness. To Cinzia, Lucio, Emma, and Francesco, the pillar of my life, for their tireless words of encouragement.

I dedicate this work and my sacrifice, to members of my family who passed away this year, the uncles I grew up with. You will always remain an example of life for me. I would have liked to share this achievement with you.

To my lifelong friends who have always been there by my side and, who I hope will remain at a certain point in my life.

Without them everything would have been more boring and more complex.

Last but not least, my lovely thanks to my sweetheart Floriano, for his immensurable love, care, support, and patience in every aspect of my life, this work is also dedicated to you.

Every day you prove to be a special person.

Table of Contents

Abstract (Italiano)

Il cambiamento climatico influenza ogni anno di più la nostra vita quotidiana e la nostra società. Inoltre, i terribili incrementi di periodi siccitosi, piogge brevi, di alta intensità, inondazioni e frane conseguenti ai livelli sempre più elevati di temperature medie registrate; hanno conseguenze più o meno gravi a seconda della vulnerabilità dell'area geografica considerata. Questa situazione rappresenta senz'altro, un'opportunità da cui partire per fornire soluzioni energeticamente più sostenibili, specialmente per i paesi in via di sviluppo che soffrono maggiormente degli effetti dei cambiamenti climatici.

A tale scopo, il presente lavoro di ricerca tratta del recupero energetico mediante l'utilizzo di una turbina idrocinetica ad asse orizzontale, costituita da tre pale. Negli ultimi anni, infatti, tale tipologia di turbine idrocinetiche risulta attrarre investimenti sempre crescenti, grazie al loro semplice design, ai contenuti costi ad esse associati, e alla necessità di non realizzare aggiuntive infrastrutture, come nel caso del classico idroelettrico. Tale tipologia di turbina, dunque, risulta essere adeguata alla generazione di energia nell'ambito del cosiddetto "pico-hydro" specialmente all'interno delle comunità rurali dislocate e non connesse alla rete elettrica nazionale.

Nello specifico, la caratterizzazione del modello di turbina studiato è stata analizzata sia dal punto di vista sperimentale che numerico. Per questo specifico caso studio, il profilo idrodinamico impiegato per la progettazione della pala del rotore è del tipo Eppler818. Tale profilo è stato preliminarmente studiato mediante il software Q-Balde, in accordo con il campo di velocità ipotizzato e, dunque, compatibile con le limitazioni di velocità riproducibili in laboratorio. Successivamente, è stato possibile analizzare tramite il medesimo software le principali forze idrodinamiche agenti sul profilo, consentendo la geometrizzazione ottima della pala. Parallelamente, è stato creato un modello preliminare Computazionale Fluidodinamico (CFD) bidimensionale, tramite l'ausilio del software specializzato ANSYS ® Fluent ™ per l'applicazione della Teoria del Disco Attuatore, in condizioni di stato stazionario e per un dominio

confinato sia superiormente che inferiormente. Tale modello numerico ha permesso di comprendere, in via teorica e preliminare alla sperimentazione in laboratorio, come le dimensioni del dominio esterno e l'effetto di bloccaggio ad esso associato, influiscano sulle prestazioni della stessa. I punti di massima potenza calcolati in via analitica, mediante una trattazione proposta in letteratura da Guy Tinmouth Houlsby allegata nell' Appendice 1, sono stati poi confrontati con quelli calcolati da tale modello.

Successivamente, ci si è occupati della progettazione del prototipo, mediante un software di CAD specializzato: SolidWorks® 2019, che ha consentito di disegnare ciascun pezzo costituente il prototipo per poi procedere alla stampa 3D dello stesso, ed infine al suo inserimento all'interno di un canale idrico di ricircolo. Le sperimentazioni sono state condotte presso il Laboratorio di Idraulica della Scuola Politecnica di Mieres, afferente all'Università di Oviedo (Spagna).

Tale prototipo è stato dunque testato analizzando un campo crescente di Portate Q e 5 punti di velocità per ciascuna delle portate considerate. A tale scopo, è stata definita una metodologia sperimentale al fine di tracciare le curve caratteristiche del prototipo in termini di Velocità Angolare [rpm] su Potenza Meccanica [W], e delle grandezze derivate ad esse connesse, adimensionali, comunemente utilizzate per la caratterizzazione delle turbomacchine, ovvero "Tip Speed Ratio" su "Cp" Coefficiente di Potenza.

I test sperimentali hanno confermato come l'effetto del Bloccaggio influisca positivamente sull'estrazione di potenza Meccanica, con una conseguente riduzione dell'altezza idrica di monte [m] e della velocità d'ingresso fino ad un determinato punto limite, oltre il quale al contrario, le prestazioni della macchina risultano essere ridotte. Si è visto inoltre che il Bloccaggio è strettamente correlato alle condizioni idrodinamiche della corrente che si instaurano nel canale; quindi, al passaggio per la Condizioni di Stato Critico, misurate mediante il Numero di Froude sperimentale.

Per tale ragione, in prima istanza, i risultati numerici sono stati utilizzati come dati di input per risolvere una seconda soluzione analitica proposta dallo stesso Houlsby, e allegata nell'Appendice 2, al fine di confrontare il valore del

fattore di induzione assiale *a*, in grado di massimizzare la potenza estratta, con quello calcolato analiticamente e sperimentalmente.

In seconda istanza, è stato implementato un modello 3D CFD multifasico del tipo Volume of Fluid (VOF), calibrato attraverso le risultanze sperimentali, allo scopo di confrontare le curve caratteristiche estratte sperimentalmente con quelle calcolate numericamente, in specifiche condizioni della corrente.

Inoltre, il modello numerico così calibrato è stato poi validato attraverso il confronto tra i tiranti idrici misurati a monte e valle della turbina, con quelli restituiti dal modello numerico.

Lo scopo di realizzare tale confronto risiede nella volontà di fornire uno strumento predittivo ed integrativo alla sperimentazione in laboratorio di eventuali altri prototipi, con geometrie e profili di pala differenti, inserite in canali con caratteristiche altrettanto variate, per agevolare la progettazione di tali macchine.

Si è inoltre andato ad indagare su come tale modello così realizzato, e validato, sia in grado di fornire una previsione dell'andamento dell'interfaccia tra acqua ed aria, e su come essa influenzi l'estrazione di potenza generata.

Infine, si è dimostrato come tale strumento sia in grado di fornire soddisfacenti risultati con specifico riferimento a condizioni operative con velocità inferiori a 0.50 m/s.

In conclusione, si è provato ad indagare su come l'esperienza sperimentale possa essere estesa anche ad un caso differente, definendo mediante l'analogia di Reynolds e di Froude i parametri di scala, utili alla caratterizzazione di un prototipo di turbina di dimensioni maggiori.

Parole Chiave: Recupero Energetico da Canali a Pelo Libero, Turbina Idrocinetica ad Asse Orizzontale, Pico-Hydro Generazione, Modelli Fluidodinamici (CFD), Stampa 3D, Progetto Prototipo

Abstract

Climate change is impacting, even more, our daily life and our society. Moreover, this terrible increment in droughts, flash floods, land floods, and temperatures has a different impact according to the vulnerability of the considered geographic area. Therefore, this situation represents an opportunity to provide more sustainable energy solutions, especially for undeveloped countries with more climate change consequences. To this end, the present research deals with water energy recovery using a three-blade horizontal axis hydro-kinetic water turbine (HAHWT). Expressly, the turbine model characterization has been provided experimentally, and then these results were used to calibrate a 3D Multi-phase CFD Model. The hydrokinetic turbines have attracted significant interest in the last decades, due to their simple design and low initial investment costs. As a result, it is becoming suitable for pico-hydro generation in rural communities non-connected to electricity services, not requiring additional infrastructures to be built. Hence, for this specific case study, the employed blade profile is an Eppler818, preliminarily studied through Q-Blade software according to the velocity range presumed in the experiments, considering the limitations of the future laboratory set-up in which the prototype would have been tested. The Q-Blade software has allowed a preliminary understanding of the main hydrodynamic forces acting on the hydrofoil. Furthermore, the same software has helped design the prototype blade's geometry.

As the first step, a simplified 2D Computational Fluid Dynamics (CFD) Model has been implemented, starting from the basic bidimensional aerodynamic model: the Linear Momentum Actuator Disk Theory (LMADT). This model has been released due to the auxiliary of the commercial ANSYS ® Fluent ™ code in a Steady State condition. This CFD model has allowed to simulate several external domains to investigate preliminary, the Blockage ratio effect, which means the ratio between the turbine and channel areas, owing to assessing the numerical results with an analytical solution proposed by Guy Tinmouth Houlsby (Appendix 1). Afterwards, each prototype piece was successfully designed in and printed through a 3D printer in Polylactic Acid (PLA), to be experimentally tested inside a recirculating water channel, located at the Polytechnic Engineering School of Mieres (the University of Oviedo) in a low-velocity scenario (v inlet < 1 m/s).

By changing the height of the gate downstream of the flume, the designed prototype has been tested under three increasing values of flow rate [m^3/s], by assessing five velocity points for each considered flow rate.

Therefore, in this work, the methodology adopted to extract the experimental characteristics curves based on measured and indirectly computed parameters, such as P Mechanical Power [W], ω Angular velocity [rpm], Power Coefficient and TSR λ respectively, which maximize the theoretical turbine efficiency, are defined, and discussed.

Moreover, it has been proved that the Blockage effect determines an increment of the maximum measured Power Coefficient with a consequent reduction in the water depth and growth in flow velocity inlet. Nevertheless, Blockage is not the unique effect that strongly affects turbine performance. Still, there is a strict correlation with the transition from a subcritical to a supercritical flow. So, the turbine's behavior is also linked to the Froude Number variation that has also been evaluated and considered in the results analysis.

With this end, the experimental data was firstly used as an input parameter to solve a computational sequence proposed by Houlsby for an Actuator Disk in an open channel flow, which calculation is attached in (Appendix 2). With the aim of comparing the experimental and analytical axial induction factor a, maximizing the power extraction.

Secondly, a multi-phase three-dimensional CFD simulation has been calibrated with the same experimental data to compare, on the other hand, the characteristic curves experimentally and numerically obtained in specific hydraulic fluid conditions.

Thirdly, it has been applied another validation strategy of the CFD model, by investigating on the free-surface variation measured and numerically computed, in specific sections located upstream and downstream of the turbine.

Therefore, the Volume of Fluid (VOF) model implemented gives information and capture the water-air interface resulting in a useful integrative tool to study other kind of prototypes, although the experimental assessment undoubtedly remains an essential part of this kind of studies.

In conclusion, to investigate how the experimental experience could also be extended to a different case, by defining the scale parameters, useful to characterize a larger turbine prototype, the Reynolds and the Froude analogy have been introduced.

Keywords: Channel Energy Recovery, Horizontal Axis Hydrokinetic Water Turbine (HAHWT), Pico-Hydro Generation, CFD Model, Experimental Performance Curves, 3D printed, Prototype Design.

Lists of Figures

List of Tables

List of Symbols

P	Mechanical Power	[W]
ρ	Water Density	[kg/m^3]
g	Acceleration of Gravity	[m/s^2]
Q	Flow Rate	[m^3/s]
η	Turbine Efficiency	[-]
C_p	Power Coefficient	[-]
C_T	Thrust Coefficient	[-]
α	Angle of Attack	[°]
θ	Pitch Angle	[°]
δ	Angle of Construction	[°]
ϕ	Inflow Angle	[°]
c	Blade Chord Length	[m]
λ	Tip Speed Ratio	[-]
ω	Angular Velocity	[rpm]
R	Turbine Radius	[m]
D	Turbine Diameter	[m]
V	Water Velocity	[m/s]
σ	Solidity	[-]
N	Number of Blades	[-]
C_L	Lift Coefficient	[m]
C_D	Drag Coefficient	[-]
C_M	Moment Coefficient	[-]
C_T	Thrust Coefficient	[-]

$\frac{C_L}{C_D}$	Profile Efficiency	[-]
L	Lift Force	[N]
D	Drag Force	[N]
T	Thrust Force	[N]
M	Moment of Force	[Nm]
$\frac{\partial p}{\partial r}$	Pressure Gradient	[Pa/m]
r	Curvature of Streamlines	[1/R]
Re	Reynolds Number	[-]
Fr	Froude Number	[-]
ν	Kinematic Viscosity	[m^2/s]
Q	Dynamic Pressure	[Pa]
C_{pr}	Pressure Coefficient	[-]
P_0	Local Static Pressure	[Pa]
P_∞	Free Stream Static Pressure	[Pa]
P_{atm}	Atmospheric Pressure	[Pa]
P_V	Vapor Pressure	[Pa]
σ_c	Amount of Cavitation	[-]
U	Fluid Particle's Velocity	[m/s]
U_{rel}	Relative Velocity	[m/s]
$U_{cavitate}$	Cavitation Velocity	[m/s]
$C_{pr,min}$	Minimum Pressure Coefficient	[-]
B_r	Blockage Ratio	[-]
$\dot{m}$	Mass Flow Rate	[Kg/s]
a	Axial Induction Factor	[-]

a'	Angular Induction Factor	[-]
r	Radial Distance	[m]
u	Axial velocity component	[m/s]
v	Radial velocity component	[m/s]
p_u	Inflow Pressure	[Pa]
p'	Outflow Pressure	[Pa]
p_w	Wake Pressure	[Pa]
ω_w	Wake Angular Velocity	[m/s]
u_w	Wake axial velocity component	[m/s]
v_W	Wake Radial velocity component	[m/s]
b_{wk}	Wake Axial Induction Factor	[-]
dM	Elemental Torque	[Nm]
dT	Infinitesimal Thrust	[N]
dP	Power Gen. to Each Radial Element	[W]
dC_p	Elemental Power Coefficient	[-]
dF_L	Infinitesimal Lift Force	[N]
dF_D	Infinitesimal Drag Force	[N]
dF_L	Infinitesimal Lift Force	[N]
V_a	Axial Velocity	[m/s]
V_{rot}	Rotational Velocity	[m/s]
H	Total Pressure	[m]
Δt	Time Step	[s]
ΔP	Pressure Drop	[Pa]
ΔH	Free-Surface Drop	[m]
Ω	Angular Velocity of the wake	[m]

A	Swept Area	[m²]
A_1	Upstream Cross-Section	[m²]
A_2	Downstream Cross-Section	[m²]
s	Precision Index	[-]
X_i	Made Measurement	[-]
$\bar{X}$	Averaged Measurement	[-]
U	Uncertainties	[%]
B	Bias Limit	[-]
t_{95}	Student's t Distribution	[-]
f	Pumps Frequency	[Hz]
μ	Mean Value	[-]
Γ_a	Surface Tension Term	[N/m]
β	By-pass Coefficient	[-]
r	Refinment factor	[-]

List of Abbreviations

CFD	Computational Fluid Dynamic
GSE	Gestore dei Servizi Energetici
EDO	European Drought Observatory
SPI	Standard Precipitation Index
GDO	Global Drought Observatory
ERCC	Emergency Response Coordination
GHD	Global Hydropower Database
IEA	International Energy Agency
GEMSTAR	Generatore Elettrico Marino, Sustainable Tethered Advanced Rotors
CFT	Crossflow Turbines
WDN	Water Distribution Network
PAT	Pumps As Turbines
BMP	Best Management Practices
PRV	Pressure Reducing Valves
WCT	Water Current Turbines
HAHWT	Horizontal Axis Hydrokinetic Water Turbines
VAHWT	Vertical Axis Hydrokinetic Water Turbines
BEMT	Blade Element Momentum Theory
TSR	Tip Speed Ratio
ADM	Actuator Disk Model
ADT	Actuator Disk Theory
LMADT	Linear Momentum Actuator Disk Theory

VOF	Volume of Fluid
RANS	Reynolds-Averaged Navier-Stokes
MRF	Moving Reference Frame
LLT	Lifting Line Theory
CAD	Computer-Aided Design
SIMPLE	Semi-Implicit Method for Pressure-Linked Equations
PRESTO	Staggering Pressuring Option
FVM	Finite Volume Method
GCI	Grid Convergence Index
MPP	Maximum Power Point
PLA- HD	Hight-Density Polylactic Acid
FDM	Fused Deposition Modelling
PIV	Particle Image Velocimetry
PTV	Particle Tracking Velocimetry
LDV	Laser Doppler Velocimetry
CFL	Courant-Friedrichs-Lewy
SST	Shear Stress Transport

Aims and Objective

This thesis is structured in VI Chapters and two Appendices.

Chapter I

Introduces an overview of the application of renewable energies and their distribution all around the Word and illustrates a brief review of the classic hydropower extraction. Furthermore, the classification of hydrokinetic turbine, with particular attention on horizontal axis one, is provided by mentioning some real examples.

Chapter II

Presents the main hydrodynamic and performance parameters considered in the process to design the horizontal axis hydrokinetic turbine prototype. Moreover, an excursus on the crucial Theoretical Analytical and Numerical Models adopted to assess the blade geometry has been described.

Chapter III

Shows the methodology adopted to optimize the blade's implemented design process of the prototype. Therefore, the described hydrofoil and its features are explained in detail. Then, a preliminary 2D CFD Model is introduced, and the results obtained are assessed concerning the analytical solution attached in Appendix 1.

Chapter IV

Provides the 3D printing process to go through the experimental set-up description where the turbine was tested in. The methodology adopted to measure the main performance parameters, such as the Mechanical Power [W], the Angular velocity ω [rpm], is explained. Then, the errors associated to the experimental measurements are computed.

Chapter V

Describes the implementation of the 3D CFD Model and its calibration based on the experimental results. An assessment between the experimental and analytical results obtained by the calculation sequences attached in Appendix 2, is described, and discussed.

Chapter VI

Deals with the experimental and numerical results discussion. The characteristics curves extracted experimentally are explained in detail, through different viewpoints. The validation of the CFD Model is also discussed by comparing the experimental and numerical performance curves. Moreover, an assessment between the water depths measured and the numerical ones is discussed and used as further validation strategy. In conclusion, are described the most common similitude laws useful to assess the scale consideration of turbines. This approach is crucial to expand the performance study of the HAHWTs working in different environmental conditions, in terms of geometrical, hydraulic and velocity conditions.

Chapter I

Renewable Energy and Hydropower Classification

In this section, the general background of existing renewable energy sources is illustrated, and their distribution around the World is described and discussed. It also explains the main drawbacks of classical hydropower sources and which countries are the major hydro-power producer and investor. A brief excursus on the classical hydropower sources is also given, to highlight the most common widespread turbines, and their typical classification.

The energy transition is identified as a critical solution to reduce the fossil fuel dependency and mitigate climate change's impact energy demand. In this regard, an overview on primary challenging renewable energy sources, paying a specific attention on hydrokinetic technologies and their main application and differences are described in detail. In this regard, through this first chapter, we intend to lay the foundations for defining the background in which this thesis work fits.

1.1. Background

Traditional hydroelectric plans are hugely applied worldwide to provide electricity to the most populated areas. In 2021, global net hydropower additions reached 26 GW (+40% from 2019), reversing the five-year trend of growth decline. As shown in **Figure 1** from the Renewables Status Report 2021 [1], the top 10 countries for installed capacity accounted for more than two-thirds of the global total are (in descending order): China, Brazil, Canada, the United States, Russia Federation, India, Norway, Turkey, Japan, and France. China led in commissioning new hydropower capacity in 2021, followed by

Canada, India, Nepal, the Lao People's Democratic Republic (PDR), Turkey, Indonesia, Norway, Zambia, and Kazakhstan.

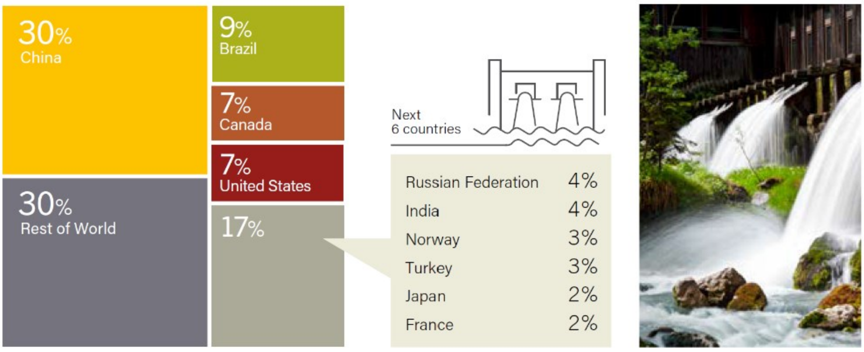

***Figure 1** Hydropower Global Capacity, Share of Top 10 Countries and rest of Restored 2021 [1]*

From what concerns Italy, it is the oldest country harnessing power from hydropower sources. Its history was in the late 1800s when the Italian peninsula was the world leader in developing water systems capable of generating clean energy. Although solar and wind power are likely the two leading candidates driving Italy's green future, hydropower still accounts for over a third of the country's renewable energy scene. According to data gathered by the GSE (Gestore dei Servizi Energetici) [2], at the end of 2020, Italy had a total hydropower installed capacity of 19.106 MW, around 34% of the national power derived from green sources. The 2020 statistical report on Italian renewables released by the GSE [2] shows that the number of active hydropower plants in Italy equals 4503, mostly related to small hydropower plants with a total installed power of fewer than 1 MW.

On the other hand, more than 81% of 19.106 MW of hydropower plants installed in Italy at the end of 2020 is concentrated in power plants with power capacity bigger than 10 MW. The increase of small hydropower plants characterizes the time frame from 2006 to 2020; the installed power in Italy grows with an average annual rate of +0.7%, as shown in **Figure 2** and **Figure 3**. As a direct consequence of this phenomenon, it witnessed the progressive contraction of the average size of hydropower plants, which decreased from 8.3 MW in 2006 to 4.2 MW in 2020.

Figure 2 *Total power installed and several of hydropower plants in Italy GSE Terna data [2]*

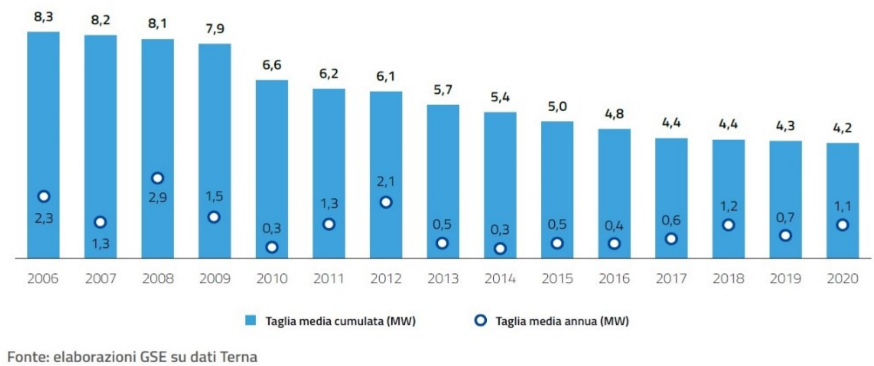

Figure 3 *Contraction of the average size of hydropower plants in Italy GSE Terna data [2]*

Even though hydropower plants are traditionally considered sources of renewable energy, it is undeniable that they have a strong environmental impact, and the development of these power plants should be carefully analysed [3]. For instance, one of the most critical problems affecting the vast hydropower plants is the climate change, evident through the frequency increment in drought [4] and heatwaves, loss of glacial icecaps, and the consequent evaporation of water reservoirs detected by dams. So, the greenhouse effect, with the resultant temperature increment and rainfall reduction, on the one hand, strictly affects the global hydrological cycle; on the other hand, produces direct drought consequences, for instance, the growth in pollutants concentration in the water, groundwater, and soil. This provokes even more wastage of energy to make drinkable water, even beyond severe damage to agriculture and all connected ecosystems. In addition, of course, this has a tremendous socio-economic impact with a different magnitude according to the geographic vulnerability of the parts of the World most exposed to the problem. In this regard, meteorological and drought conditions are continuously updated and monitored in European Drought Observatory (EDO) through various indicators, ranging from the Standardized Precipitation Index (SPI) computed over multiple aggregation periods to modelled soil moisture and remotely sensed vegetation anomalies [5]. More recently, a parallel global-scale monitoring system has been implemented, namely the Global Drought Observatory (GDO, *http://edo.jrc.ec.europa.eu/gdo/),* with a greater focus on supporting the Emergency Response Coordination Centre (ERCC) of the European Commission. Although additional indicators explicitly focusing on dynamic drought risk assessment are implemented in GDO, the base indicators used to monitor the propagation of drought hazards within the hydrological cycle are analogous to those available in EDO.

Furthermore, it has also been studied how the impact of streamflow drought negatively affects hydroelectricity production at a global scale through the generation of a hydroelectricity production (HP) model based on a new Global Hydropower Database (GHD) containing 8,716 geo-localized plant records and a hydrological model specifically implemented [6].

Moreover, the International Energy Agency (IEA) confirms that hydropower generation decreased in 2021 by 15 TWh (down 0.4%) to 4327 TWh, despite relatively high-capacity growth due to persistent droughts.

For this reason, the most evident drop in a generation was caused in hydropower-rich countries, such as Brazil, the United States, Turkey, China, India, and Canada, leading towards lower-than-usual hydro capacity utilisation. On the other hand, it is worth noting that when hydropower plants are 45-60 years old, as nowadays usual in Italy, major modernization and refurbishment are required to sustain or improve the performance of old hydro-power plants and increase their flexibility. In addition to renewing major equipment such as turbines and generators, modernization and digitalization can significantly increase the plant flexibility, make the plant safer, and solve environmental and social issues, such as an inadequate drought management and flood control, depending on the country's regulations. All these aspects are part of a more complex issue highlighting the importance of involving more than one feasible strategy and profoundly analyzing its disadvantages and advantages. Furthermore, the impacts of the COVID-19 outbreak, and the current energy crises trigged by the conflict between Russia and Ukraine have demonstrated even more the resilience of renewable sources and their fundamental role in the future of ecological transition, as in **Figure 4**. In such a context, the global electricity demand is expected to grow by close to 5% in 2021 and 4% in 2022, driven by the likely global economic recovery [7]. For these reasons, seeking more sustainable ways to harness the energy and attempting to obtain power, usually considered insufficient to be remunerative, could be the right direction to optimize the available energy sources.

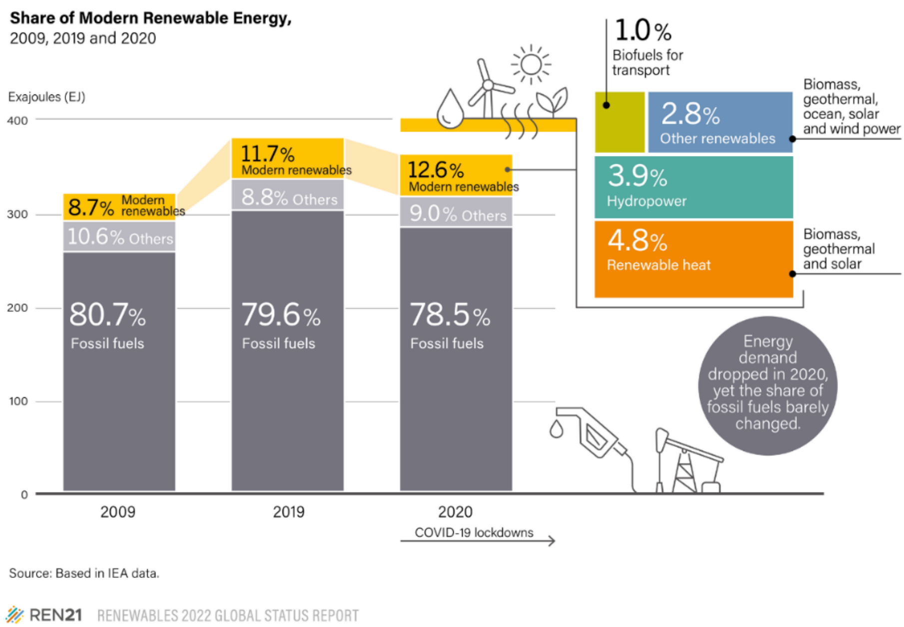

Figure 4 Global renewable energy trend [7]

In this scenario, the development of self-consumption energy systems through micro and pico hydrokinetic turbines represents a valid alternative to reduce the global energy demand, considering modernizing irrigation and water distribution systems significantly impacts the total energy saving [8][9].

Therefore, energy recovery in the irrigation or water distribution systems through hydro-kinetic turbines may represent a valid alternative to improve the overall system's efficiency. In such a context, the present thesis focuses on mini-hydropower facilities by designing and assessing the performances of a prototype experimentally and numerically, aimed at providing an alternative and cheap energy device suitable for the poorest countries where electricity grid is missing.

1.2. Type of Hydropower

According to the considered power plant, hydropower is the energy extracted from falling or fast-running water. Namely, the central hydropower plants are classified as reservoir-based, run-of-river, pumped storage, and offshore. It is widespread to classify the hydropower plant according to the power generated; however, a global agreement about the hydropower plant classification is limited, varying from country to country. Generally, they are classified in terms of power produced or available water head:

- Large-scale system with a capacity bigger than 1 MW
- Small-scale system with a capacity between 100 KW and 1 MW
- Micro/Pico-scale system with a capacity below 100 KW

The basic principle of hydropower generation is the impulse momentum. Water potential is converted into mechanical energy by rotating the turbine, and mechanical energy is converted into electrical energy using a generator.

The block diagram of converting energy is shown in **Figure 5**, and the mechanical energy produced by the turbine shaft is given as in equation (1):

$$P = \eta \rho g Q H \tag{1}$$

where:

P is the mechanical power produced at the turbine shaft	[W]
ρ is the water density998,2	[Kg/m^3]
g is the acceleration due to the gravity 9,81	[m/s^2]
Q is the flow rate passing through the turbine	[m^3/s]
H is the available hydraulic head	[m]
η is the total efficiency	[-]

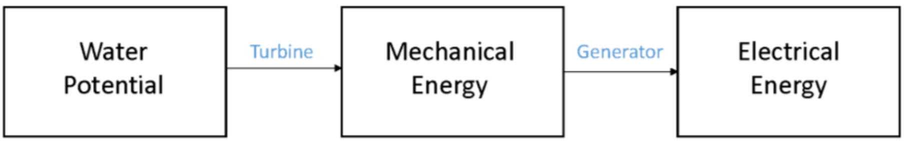

Figure 5 *Block diagram of hydropower generation*

Traditional hydropower plants are site-specific; the hydrological and orographic characteristics strongly affect the facilities that can be built. As mentioned above, conventional hydropower plans can be categorized into four main typologies:

Figure 6 Spèccheri (TN) domed dam Italian storage hydropower plant [10]

- **Storage Hydropower**: this system always has a dam to impound the river water and create water storage (Figure 6), which covers the baseload and peak-load electricity demand according to the daily electricity pattern variation. This happens through its capacity to be shouted down or started up quickly. Moreover, according to the river capacity and dam size, the water storage could supply the electricity demand for many weeks, months, or even years.
- **Run-of-river hydropower:** this plant is the most widespread solution. It consists of realizing a beam (fixed or movable; **Figure 7**) with a small storage capacity upstream and a channel or a penstock that drives the turbines. So, the plant operation is strictly related to the hydrological river condition, producing an endless amount of electricity, and providing the **base load** of the electricity demand pattern. In addition, these facilities include some flexibility of operation for daily/weekly fluctuations in demand through water flow that the facility regulates.

Figure 7 *Run-of-river hydropower [11]*

- **Pumped storage hydropower:** this type of hydropower energy storage is used by electric power systems for loading balancing. In this kind of system, there are always two reservoirs at different elevations, as shown in **Figure 8**; in this way, when the energy demand is low, and the energy prices are the lowest, the pumps take the water from the lowest to the highest-level reservoir, storing water in the form of gravitational potential energy. On the contrary, when the electricity demand is the highest of the day, the water moves from the most elevated reservoir to the lowest, passing through the turbines and producing more electricity. This system provides **peak-load supply** when the energy surplus is used in intense demand. The same pump could be used in both modes by changing the rotational direction and speed. However, the operation point in pumping usually differs from the operational point in turbine mode.

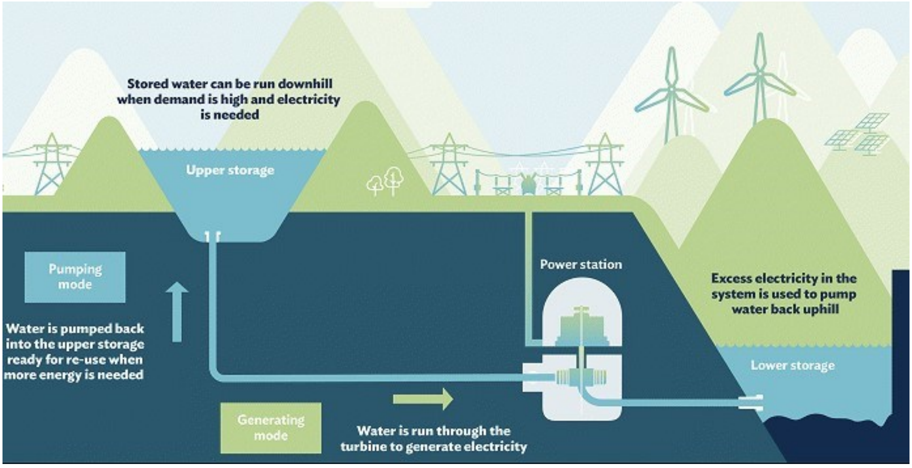

Figure 8 *Pumped storage hydropower scheme [12]*

- **Off-shore marine and other new technologies:** tides and ocean currents worldwide generate significant kinetic energy. However, there still low exploitation depends on the high complexity and costs of technologies required to operate underwater, as demonstrated by C.M. Johnstone et al. [13] [14] and on political decisions.

Meanwhile, the high predictability of the current's direction and speed and their abundance in some coastal regions make this technology vital in the world's electrical energy supply system. A practical and original example of this kind of turbine is appreciable through the project realized by SeaPower scrl called GEMSTAR System [15]. This tidal current system comprises two hydrokinetic turbines supported by a floating submerged structure capable to adjust its alignment to the flow direction variation. The floating system is linked to a flexible mooring cable lean to the seabed, as shown in **Figure 9**.

Figure 9 GEMSTAR System [15]

- **Hydrokinetic turbines:** in this scenario, several studies are based on the development of experimental and numerical assessment of micro hydrokinetic turbines able to use water-flowing currents under free conditions, not requiring the installation of additional infrastructures [16] [17]. Most of the time, these technologies can recover energy at a specific point where it is usually wasted, resulting in interest even though the energy potential is not high. The primary and minor energy returns are closely related to the area swept by their blades, the rate of water current, its density, and the conversion efficiency of the equipment. However, due to the complexity of implementing experimental tests on this kind of turbine, the Computational Fluid Dynamics (CFD) method is commonly used as an auxiliary tool to predict the hydrodynamic performance, given its high accuracy and relatively low costs, especially in a context where experimental tests are no easy to implement.

Before describing the theory and mathematical modelling that are the bases of the present thesis work, it is worth doing a brief overview of the traditional classification of classic turbines. This helps understand the main differences between the typical turbomachinery used for hydropower generation and the context wherein the topic is inserted. Generally, the turbines are classified in impulse and reaction turbines.

1.3. Impulse Turbines

Impulse turbines are devices in which high-velocity water sprays impinge on the turbine blades, turning the turbine and generating electrical power. An impulse turbine is so-called because operates on the stimulation power generated by a special dagger on the water jet. Therefore, this type of turbine generally uses the water velocity to move the runner and discharge to atmospheric pressure. The resulting impulse spins the turbine and leaves the fluid flow with diminished kinetic energy, and all the pressure drop takes place in the stationary blades, namely in the nozzles. Therefore, an impulse turbine is generally suitable for high head and low flow rates, applied when the piece of water is low. In addition, the pressure is heightened because of the high position of the water column.

The main types of impulse turbines are Pelton, Turgo, and Crossflow turbines.

1. **Pelton** turbine is the most well-known type of impulse turbine. Each bucket used has double cups with splitters between the cups. An example of this kind of turbine is shown in **Figure 10**. It is suitable for large-head and low-flow sites [18]. Recently, turbines have been applied for small and micro-hydro power configurations using a single jet. Generally, a Pelton turbine has a high-efficiency rate of up to 95%, and its performance is dynamic because of the unsteady flow in the rotating buckets in time and space.

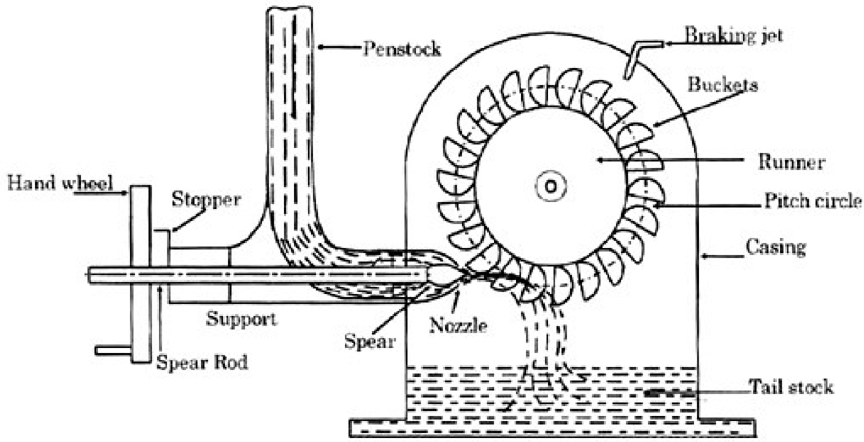

Figure 10 *Pelton Turbine* https://www.rgpvonline.com/answer/basic-mechanical-engineering/15.html

2. **Turgo** turbine is best suited for medium head operations, achieving 87-90% efficiency. The operating principle and design of the Turgo turbine are like the Pelton one, as in **Figure 11** below. However, the water jet strikes the center of the buckets on the runner at an acute angle instead of a right one. Generally, the Turgo turbine can also handle lower heads and higher flow rates than the Pelton turbine, whereas it can work at a head range greater than Francis and Pelton models. Even though many large Turgo installations exist, they are also famous for small hydro, where low investment cost is a preeminent factor. Williamson et al. [19] [3] optimised the Turgo turbine model micro-and pico-projects, modifying the location of low heads from 3.5 m down to 1 m to improve the turbine performance. Generally, the efficiency of the Turgo turbine depends on many factors, such as a nozzle or jet inclination, cup design, and speed ratio. The Turgo turbine efficiency for micro-hydro is very sensitive to jet position and inclined jet angle [20] [21]. References [19] [21] defined that the optimum jet inclination angle to achieve the peak efficiency of a Turgo turbine for the low head is approximately equal to 20°.

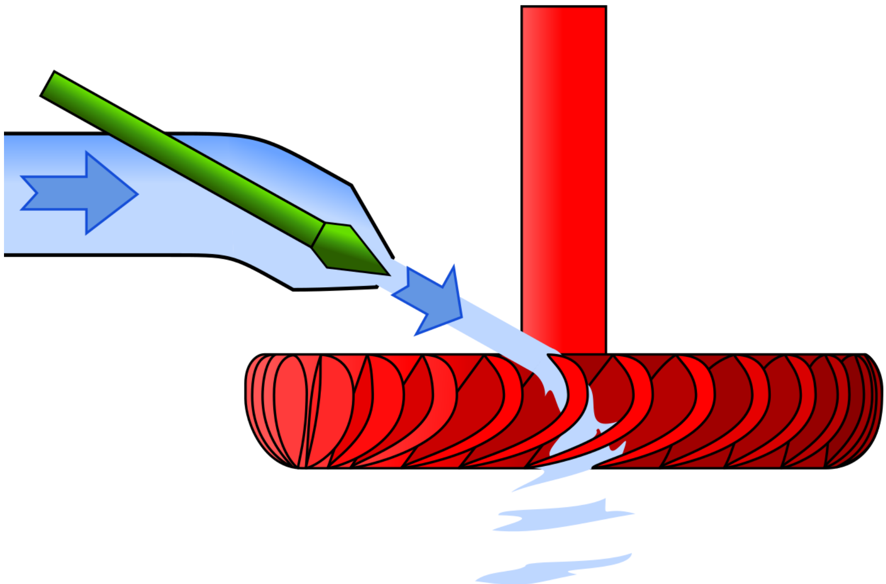

Figure 11 *Turgo Turbine* wiki/File:Turgo_Turbine_Sketch.svg

3. **Crossflow Turbine** (CFT) is another powerful impulse turbine mainly used in small hydropower plants. The crossflow turbine was developed in 1903 by Anthony Michel, Donne Banki, and Friz Osberg. It is commonly applied in horizontal and vertical configurations. This type of turbine usually works at a higher flow rate and lower head than the Pelton and Turgo turbines [22]. The water jet enters from the top of the runner, passing twice through the gutter-shaped blades. This blade's configuration allows the water to transfer momentum on each passage before falling away with little residual energy [23] as in **Figure 12**. The average efficiency of CFT turbines is usually 80% for small and micro-power outputs; however, it can reach up to 86% at medium and large units [24]. The operational effectiveness of CFT depends on geometrical parameters, such as the number of blades, the runner diameter, the nozzle entry arc, and the angle of attack. An exciting work concerns a modified CFT, designed by Tucciarelli et al. [25] [26] has been patented and released to couple the pressure

regulation and the hydropower generation within the Water Distribution Network WDN of Palermo (Italy) Municipality, as in **Figure 13**.

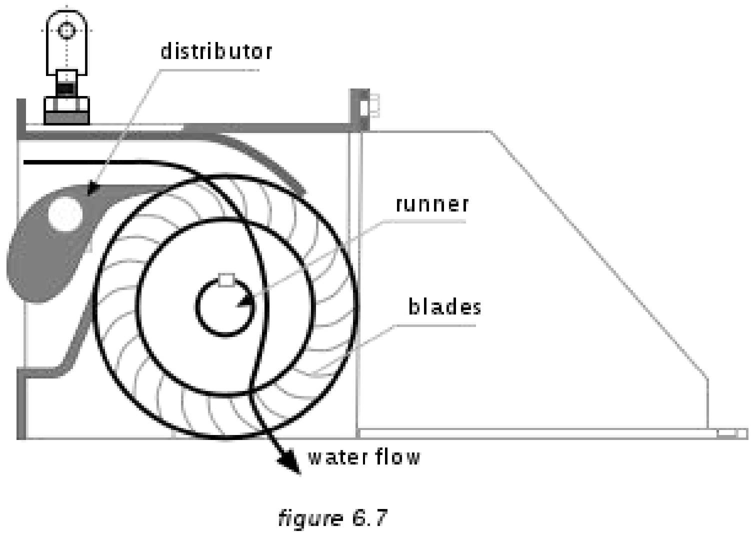

Figure 12 *Crossflow Turbine or Banki Ossberger turbine [25]*

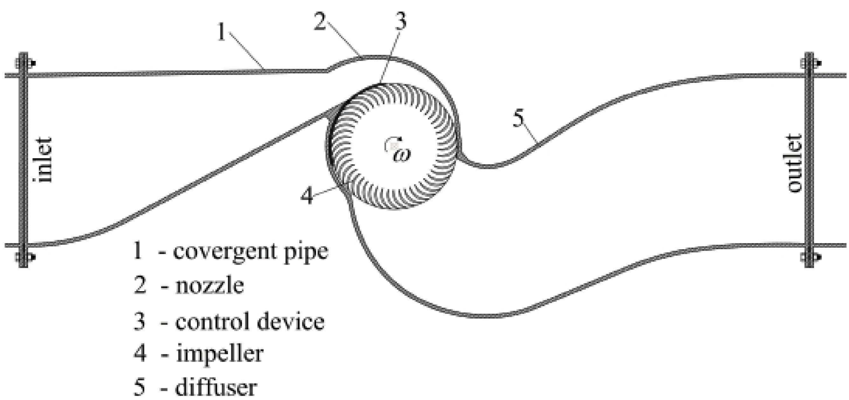

Figure 13 *Tucciarelli et al. Crossflow Turbine implemented in the Palermo WDN [28]*

The main component of whichever impulse turbine can be summarized in the following features:

- Penstock: a channel or pipe to deliver water to the turbine. This penstock brings the water to the turbine at the high head. The penstock is commonly associated with a water reservoir, typically several meters high.
- Nozzle: they increase the kinetic significance of water and stream water on turbine blades. This nozzle constitutes a high-speed jet. Due to the nozzle, water discharge is pushed in a specific direction to the blade. An impulse turbine can use one or more nozzles.
- Runners: it is a circular disk mounted on a rotating shaft. This rotating shaft is comprehended as a rotor. On the runner, there are also cup-shaped blades that are evenly rounded. A cup-shaped cutter is called a bucket.
- Bucket: they are cup or spoon-shaped blades of a turbine. The bucket is positioned around the perimeter, so the pressurized liquid hits the bucket, accelerating it.
- Casing: it is helpful to prevent water splashing and contain water flow so that it does not overflow. This cover is also used to preserve components from the external environment.

1.4. Reaction Turbines

A reaction turbine develops power from pressure and moving water combined. The runner is placed directly in the water stream flowing over the blades rather than striking each individually. Reaction turbines are generally used for sites with low-head and higher flow rates than compared with the impulse turbine. Conventional reaction turbines include Kaplan, Francis, Bulb, and Pumps-as-Turbines (PATs). Francis and PATs can generally exploit higher heads than Kaplan or Bulb turbines. However, the design flow rate usually constrains the flow of these turbines, so when such turbines go under low flow conditions, turn a decrement in efficiency [29].

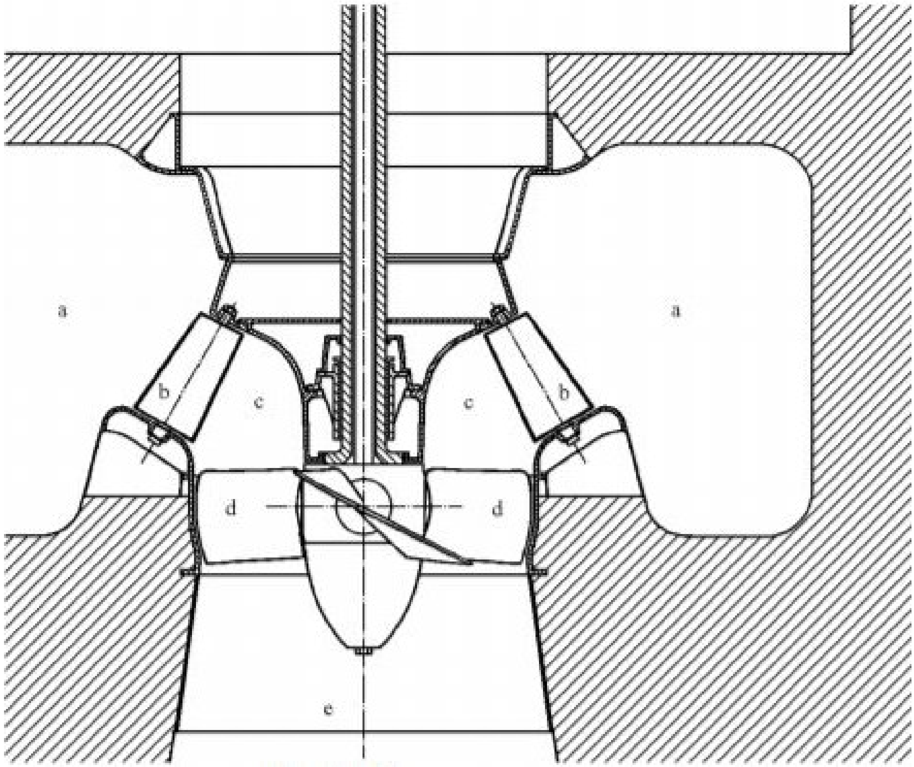

__Figure 14__ Kaplan Turbine cross-section [30]

1. **Kaplan** turbines utilize water to flow through the inlet guide vanes that act upon the propeller-like blades to create shaft power, as in **Figure 14**. The runner vanes of the Kaplan turbine are adjustable, making it one of the most adaptive turbines in the market.
2. **Francis** turbines are introduced by radial water at the runner's entrance and turn 90° within the runner to discharge axially at the outlet, as in **Figure 15.** Unlike the Kaplan turbine, the runner vanes are not adjustable. Moreover, Francis turbines are typically installed at higher-head sites such as gravity-fed pipelines and irrigation canals.

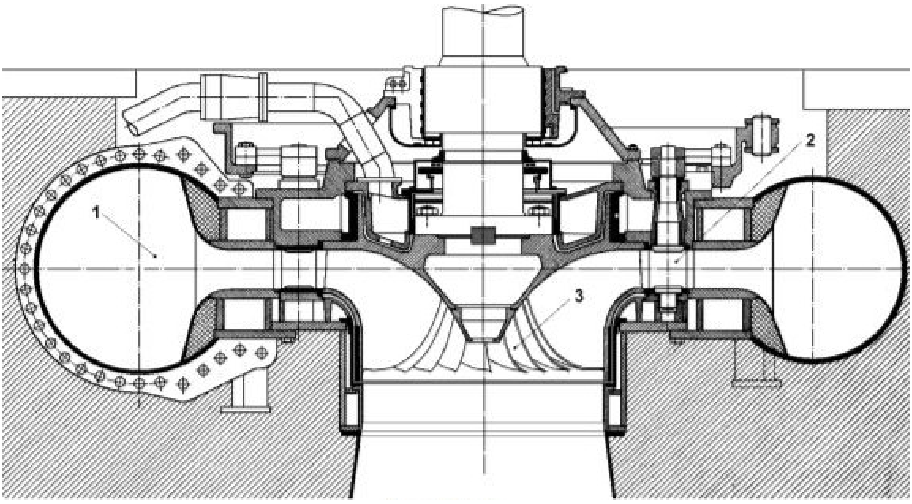

Figure 15 *Francis Turbine cross-section*
https://lnx.itimarconinocera.org/mi/energia_pulita/energia.php?pag=contenuti/idroelettrica/tecnologia/descriz_turbine

The **Bulb** turbine, see **Figure 16** below, is a Kaplan turbine variation. However, unlike Kaplan turbines, the generator and the runner are housed in a large bulb. This compact design allows more powerhouse construction flexibility compared to Kaplan turbines. Nevertheless, there are two significant disadvantages of the bulb turbine:

a) Generator maintenance could be improved by the limited space and access available within the bulb.
b) the low inertia of the rotating parts means that in some generating networks, provoking issues, such as synchronizing speed and frequency fluctuations.

This is why engineers designed the tube turbine, putting the generator outside the water path as the turbine drives it through an extended shaft.

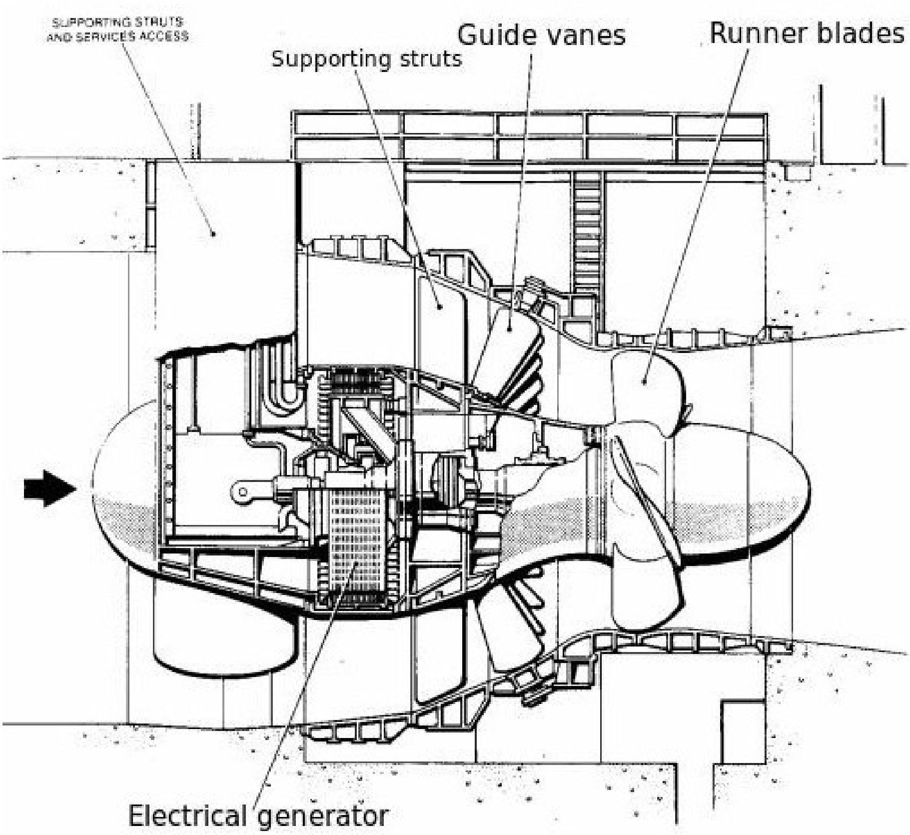

Figure 16 *Bulb Turbine* https://sciencenaturalphenomena.com/2022/02/bulb-turbine/

As in **Figure 17**, a Pump as Turbine (PAT) is a centrifugal pump working in reverse mode, physically and hydraulically operating as a Francis turbine. Due to PAT's compact design and the availability of a comprehensive set of models suitable for working in reverse mode, they are low-cost and energy-efficient solutions. The use of PAT represents a relevant topic in the field of innovative Best Management Practices (BMPs) of WDNs because addressed to both the pressure regulation and the hydropower generation. Thus, it could represent an alternative approach to the use of Pressure Reducing Valves (PRVs), harnessing the energy surplus to produce sustainable energy, otherwise dispersed. A basic PAT's issue is the knowledge limitation about their performances, because of information shortage about their performance curves, hardly ever provided by manufacturers.

Nevertheless, since the wide water flow variability in a WDN hydraulic and electrical regulation is needed by installing a bypass link and a frequency regulator [31] [32] [33].

In this regard, the PAT hydraulic regulation consists in combine a production line where the machine is installed, and a by-pass branch operating in parallel configuration.

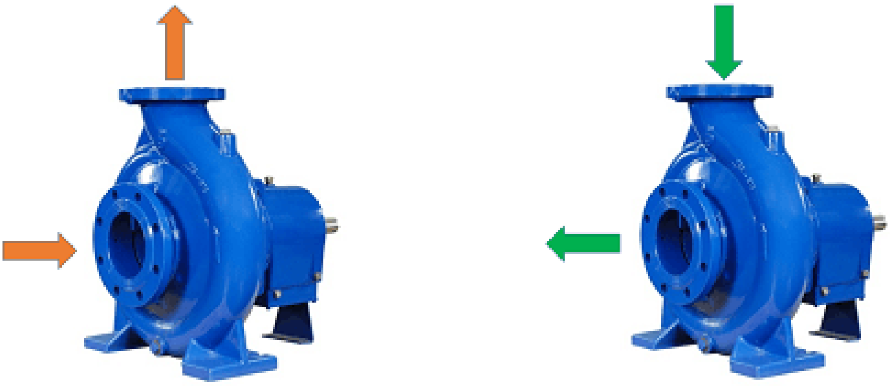

Figure 17 *Pumps as Turbines PAT: Pump mode on the left side, Turbine mode on the right side [32]*

On both lines, two regulation Pressure Reducing Valves (PRVs) are installed to regulate the flow thrugh the PAT, ad to perform a pressure regulation able to guarantee the required pressure at each delivery point.

1.5. Hydrokinetic turbines

The hydrokinetic turbines are powered by kinetic instead of potential energy. This turbine category is often defined like "zero-head," "ultra-low," "in-stream," and current water turbines (WCTs).

The systems can operate in rivers, artificial channels, tidal waters, or ocean currents. Kinetic systems do not require significant civil work. However, they can use existing bridges, tailraces, and canals. This kind of energy source has been used throughout the century, starting from the first models of watermills to drive mechanical processes such as grinding and rolling hammering. Tidal currents and channel streams are the main areas where hydrokinetic turbine devices could be installed to extract energy.

Moreover, due to their low investment and maintenance costs, this technology is more cost-effective and environmentally friendly than other technologies [34]. For instance, the water passing through the generator is directly traced back to the stream with a shallow impact on the ecology and, more generally, on the surrounding ecosystems.

The power harnessed from the water is directly proportional to the cross-sectional area swept by the turbine, the cubed velocity inlet, and the considered fluid's density. It is evident how the energy production chain between water and wind turbine is similar. Namely, a wind turbine transforms the kinetic energy in the wind into mechanical energy in the shaft and finally into electrical power in the generator. However, the main difference is related to the water/wind density since the first one has a density value of three orders of magnitude greater than that of air. This implies that the required swept area to harness the same power could be more contained. Furthermore, the velocity range may be smaller than wind turbines because the energy produced is strictly related to cubed velocity.

As in **Figure 18,** based on the mutual turbine position between the rotor axis and fluid flow direction, we can distinguish the hydrokinetic turbines into two main categories:

- Vertical Axis Hydrokinetic Turbines VAWHTs or crossflow turbines.
- Horizontal Axis Hydrokinetic Turbine HAWHTs or axial turbines.

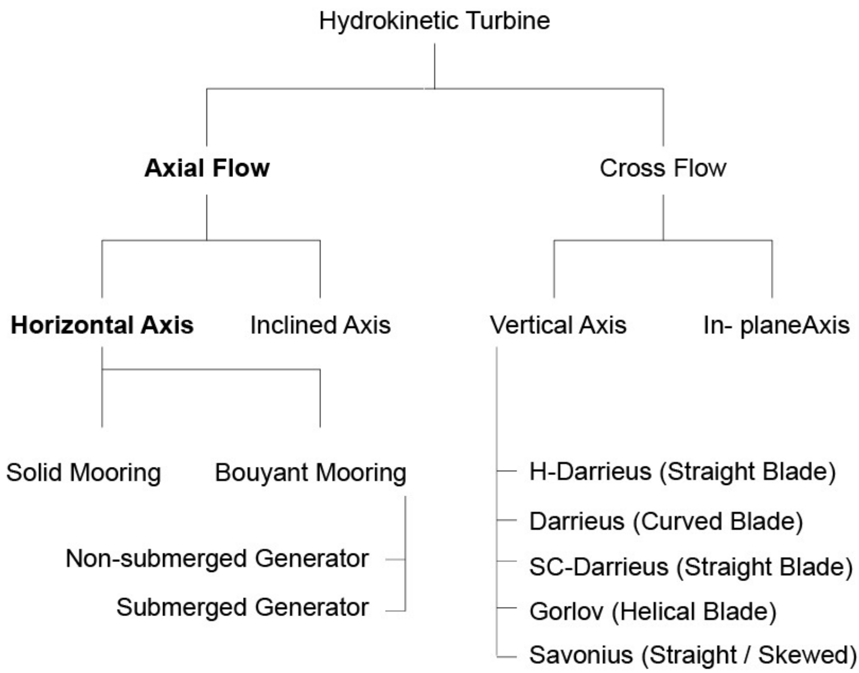

Figure 18 *Hydrokinetic Turbines Classification*

Namely, the VAHWTs have an axis perpendicular to the flow direction; meanwhile, the HAHWTs have an axis parallel to the water flow direction, similar to the classic wind turbine [35][36].

Axial turbines have a design like horizontal wind turbines, fully submerged, and more efficient in energy conversion than crossflow turbines. However, a significant task with axial turbines is their arrangement in the water since the electrical generator is often submerged, implying the need to use a watertight chamber to avoid contact with water. As a result, this increases the cost of this equipment and makes maintenance difficult.

In this regard, **Figure 19** shows several feasible arrangements of electrical generators that exist according to the most appropriate solution and site selection choice.

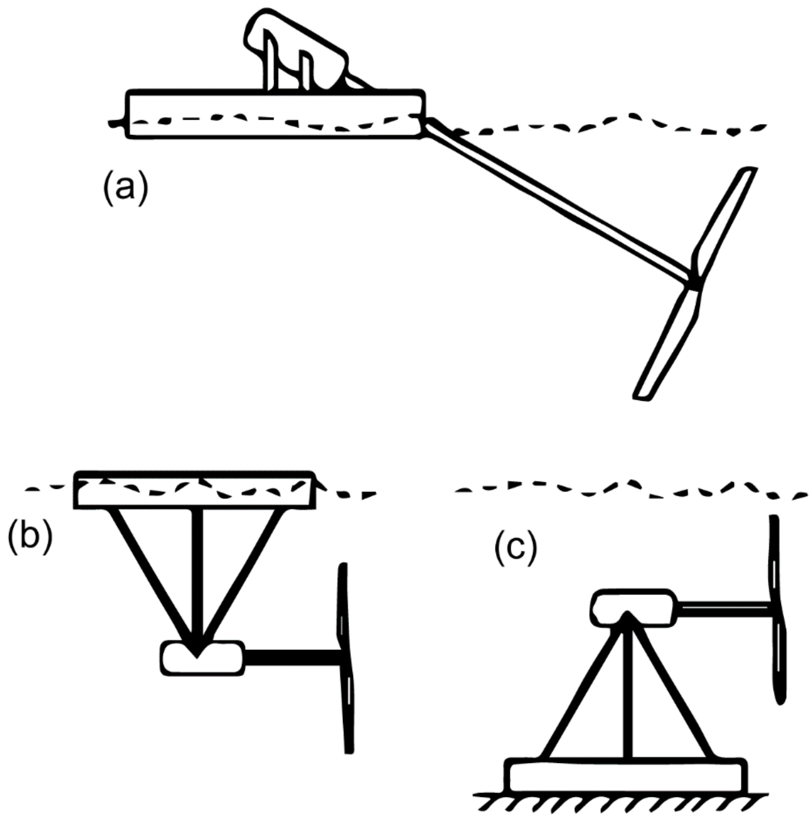

Figure 19 *Axial flow water turbine: (a) inclined axis, (b) float mooring, and (c) rigid mooring [29]*

The Vertical Axis Hydrokinetic Turbines (VAHWTs) can be divided into two main categories according to the type of forces predominant in their blades for torque generation: Drag or Lift turbines, mainly due to the blade shape are defined drag or lift devices.

The most crucial advantage of Drag turbines is related to their easy start-up rotation while, on the other hand, Lift turbines achieve higher efficiency.

Examples of commercial designs include the Savonius rotor or Banki-Michell as Drag turbines and the Darrieus and Gorlov rotor as Lift turbines. A key aspect of Lift turbines is the blade design, as discussed in Chapter III, according to the process followed for the blade design of the studied prototype.

Crossflow turbines are based on the already known rotors of the wind industry as vertical shaft turbines, for example, type as shown in **Figure 20** below:

- Savonius,
- Darrieus,
- Gorlov.

The main advantage of using cross-flow turbines is related to the fact that these devices can work regardless of the flow direction, which makes them significantly attractive in water current applications, especially in marine environments where the flow changes frequently [37]. On the other hand, although less efficient than axial turbines, the simplicity of the mechanical rotor-generator coupling system reduces the construction cost [38].

In addition, if it were considered a turbine farm installation, it would allow greater use of the current's cross-sectional area, obtaining power at a slow speed [39] and even a lower condition on the environment since their dimensions hardly ever exceed 2 m in diameter [40].

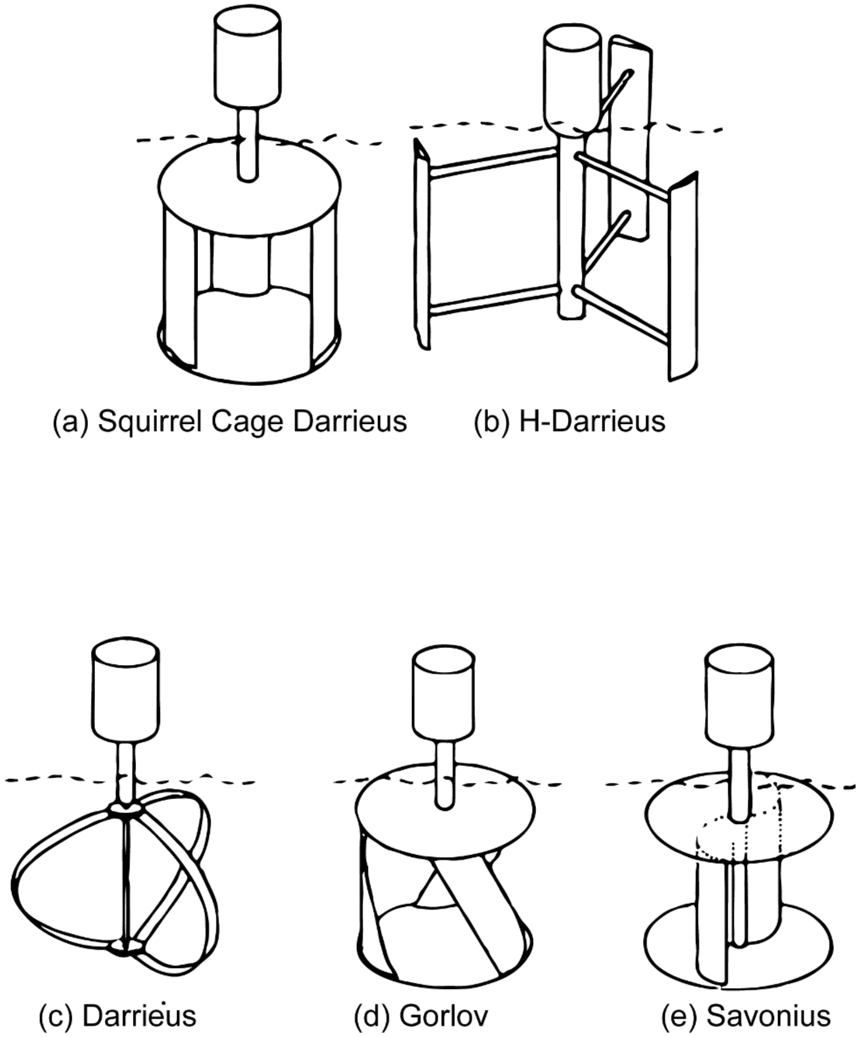

Figure 20 *Vertical Axis Tidal Current Turbines [41]*

Chapter II

Turbine Theory and Literature Review

Chapter II provides a detailed examination of the most crucial hydrodynamic design parameters of a HAHWTs. These parameters are essential to understand because they have a direct effect on the turbine performance.

Many aspects such as Number of Blades, Blade Profile, Solidity, Swept Area, Tip Speed Ratio, are explained in detail to figure out the parameters to consider in designing a turbine ad how these aspects affect the Power output production.

A simple and satisfactory numerical model, such as Blade Element Momentum Theory BEM will be introduced, along with the base theoretical model helpful to design the turbine.

2.1. Hydrodynamic Design parameter of HAHWTs

It is widely assumed that the hydrokinetic turbine behavior is like wind turbines. This is because the current water turbines extract the kinetic energy of a moving fluid, with a comparable mechanism to wind turbines [1]. The HAHWTs usually produce a low power coefficient if they are not optimized, which is also the main barrier to their commercialization. The optimisation of these HAHWTs is a challenging task that necessitates the analysis of several interconnected design parameters, such as:

- Pitch angle
- Angle of Attack
- Tip Speed Ratio
- Solidity and number of blades
- Reynolds Number
- Blade Profile

- Cavitation Problems
- Blockage Effects

In the following sections, these parameters are presented and described.

2.1.1. Power Coefficient

Its power or power coefficient characterizes the efficiency of a hydrokinetic conversion device. The generated power [P] is calculated by the product of rotor Momentum [N*m] and the rotor angular velocity [rad/s]. Therefore, the Power Coefficient (C_P) is a dimensionless parameter that measures the turbine's performance; therefore, it is calculated as the ratio of the harnessed power on the kinetic energy crossing perpendicular to the rotating rotor and so through the turbine's swept area. In other words, the swept area is the area described by the rotor, so strictly dependent on the Turbine Radius. The C_P is calculated as in the following formula:

$$C_P = \frac{P}{\frac{1}{2}\rho A V^3} \tag{2}$$

where:

- P is the mechanical power produced at the turbine shaft [W]
- ρ is the water density 998,2 [Kg/m^3]
- A the swept area [m^2]
- V is the inlet velocity [m/s]

2.1.2. Thrust Coefficient

The thrust coefficient C_T is also an essential dimensionless factor in turbine design. It is calculated by dividing the Thrust Force exerted on the rotor (T) by the dynamic pressure force acting perpendicularly on the rotor's plane of rotation.

$$C_T = \frac{T}{\frac{1}{2}\rho A V^2} \tag{3}$$

2.1.3. Pitch Angle and Angle of Attack

Pitch local angle (θ) is a geometric characteristic measured as the angle between the hydrofoil chord and the rotational plane of the rotor, as in **Figure 21**. Alteration of (θ) allows for the control of rotational speed and power output. On the other hand, the angle of attack (α) is the angle between the incoming relative flow and the hydrofoil chord. In other words, as shown in the **Figure 21** and **22**, the chord is the imaginary line that connects the so-called Leading Edge, i.e., the "front of the hydrofoil", the portion that meets the water first. Conversely, the Trailing Edge is the back of the hydrofoil, as illustrated in **Figure 22**. Therefore, it is a crucial design parameter for the turbine blade. Whereas, what is normally defined by the Greek letter β, is the twist angle of the blade which represents the angle between the rotational plane and the chord measured at the tip of the blade. The sum of these two angles is the so-called **Angle of Construction δ = (α+β)**.

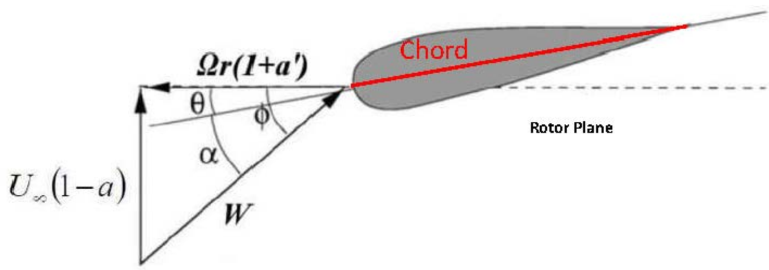

α: Angle of attack

θ: Local pitch angle

ϕ: Angle between the relative flow and the rotor plane

$\theta = \theta_P + \beta$

θ_P: Global Pitch angle

β:Twist angle

$\alpha = \phi - \theta = \phi - (\theta_P + \beta)$

$\tan(\phi) = \frac{(1-a)U_\infty}{(1-a')\Omega_r}$

Figure **21** Petch and Angle of Attack [43]

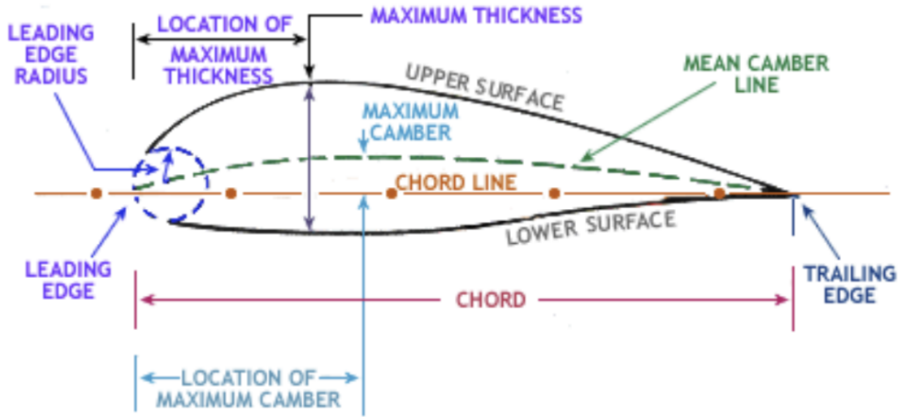

***Figure* 22** *Hydrofoil scheme [44]*

As illustrated in **Figure 22,** the camber of the hydrofoil is different from the chord. Therefore, it measures the asymmetry between the upper and lower surface of the hydrofoil. As a result, a hydrofoil/airfoil not cambered is a symmetric hydrofoil.

2.1.4. Tip Speed Ratio (TSR)

The Tip Speed Ratio (TSR) is a dimensionless parameter used to control the power output. It is a measure of the ratio between the velocity at the Tip of the Blade and the upstream flow velocity, thus it is the ratio between the tangential speed of the blade tip and the upstream rate. The operational range of the TSR is the range in which the turbine operates at high efficiency.

$$TSR = \frac{\omega * R}{V} \tag{4}$$

where:

- ω is the Angular Velocity [rad/s]
- R is the Rotor Radius [m]
- V is the Water Speed [m/s]

2.1.5. Solidity and Number of Blades

The solidity (σ) significantly affects the turbine performance and measures the ratio between empty and entire area. In other words, solidity measures the working surface of turbine blades. Increasing the solidity can increase the turbine's moment to a limit where the flow impedance through the rotor becomes high, and the moment starts to decline again. Therefore, a turbine should be designed concerning an optimal solidity value to improve efficiency. Solidity is defined as the ratio of the sum of the chord length of all the blades, namely the so-called representative chord, usually equal to c/4, traditionally located at c/4 from the Leading Edge to the circumference of the rotor.

$$\sigma = \frac{cN}{2\pi R} \tag{5}$$

where:

- c is the chord length [m]
- N is the number of Blades [-]
- R is the Rotor Radius [m]

Several experimental and numerical studies have been conducted to investigate the effect of solidity and the blade number on wind/water turbine performance [45] [46] [47] [48]. Increasing the solidity and the number of blades has a favorable effect on the aero/hydrodynamic gains. For example, Subhra et al. [49] developed a CFD simulation and demonstrated that a 3-blades HAHWT with untwisted blades generates more power than two and 4-blade with similar solidities. It was observed that the power peak shifted to lower TSR as the solidity increased. The solidity variation significantly influences the optimum TSR but is slightly affected by the change in blade number. Madrigal et al. [45] studied the solidity effect on the performance of an axial water turbine in a low-velocity scenario, changing the number of blades. The results confirm that the power range against different TSRs shrink as edges are added. Therefore, it is essential to consider a trade-off between performance, efficiency, stability, and cost when selecting the number of blades for HAHWTs.

2.1.6. Blade profile

The blade profile and its thickness are strongly related to the flow nature over the blade surface and consequentially to the performance exposed by the turbine. A well-designed hydrofoil or airfoil profile can maximize the lift and minimize the drags forces even at large angle of attack, producing the global maximization of the profile efficiency, which is the lift-to-drag ratio. In the profile design analysis, it is necessary to define the geometrical parameters to lead an efficient energy conversation and allow higher power output. The features of symmetrical and non-symmetrical profiles regarding their chord line, which is the imaginary straight line drown through the airfoil from the leading edge to the trailing edge, are several and have been widely investigated [50]. As in **Figure 23**, another critical airfoil or hydrofoil parameter is the camber, the curve from its upper or lower surface, respectively. This curve is measured according to how much it departs from the chord. Some hydro/airfoils have alighted camber, i.e., the airfoil seems flat, while others have a higher degree of camber, so the airfoil has a more prominent curve.

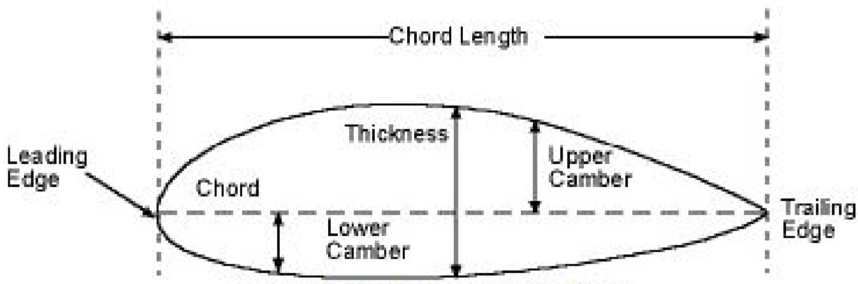

Figure 23 *Element of an airfoil* https://commons.wikimedia.org/wiki/File:Aerodynamic_camber.jpg

Moreover, the camber of an airfoil affects its lift. However, it has been demonstrated that increasing the blade thickness broadens the range of tip speed ratios, in which the turbine operates efficiently, extracting more energy [51]. Nevertheless, if the viscosity increases excessively, the drag also increases, producing a significant drop in power coefficient values. That means that is recommended an intermediate profile which combines both advantages. The most used airfoil profile is the NACA 4-digit series demonstrating a good performance in air and water, both for vertical and horizontal hydrokinetic turbines. Additionally, numerical, and experimental analyses for the horizontal axis hydrokinetic turbine using the Eppler 420 hydrofoil profile have also been performed [52]. It has been deducted by an optimization study that the multi-element Eppler 420 hydrofoil with a flap-arrangement significantly increases the turbine performance compared to the traditional Eppler 420 hydrofoil.

2.1.7. Lift Drag Coefficient and Reynolds Number

Pressure difference and viscous stress caused by water flowing over blades generate hydrodynamic forces that cause turbine rotation. In addition, the pressure difference between the upper and lower hydrofoil surfaces generates forces normal to the blade's surface. Meanwhile, viscous stress induces normal and tangential forces on the blade surfaces. These forces can be decomposed into either parallel (Drag Force) or normal (Lift Force) components to the relative flow. Because of rotation, each section of the turbine blade "could see" a velocity which is the vectorial composition between the axial velocity, directly proportional to the upstream velocity V_∞, and the tangential component, proportional to the product of angular velocity to its level arm concerning the blade root (the geometrical transition between the cylindrical blade roots and the hydrodynamic blade profile).

When a hydrofoil stalls, the Drag Forces increase faster than the lift ones, due to the increased pressure forces in the streamwise direction [53] [54]. The Lift Coefficient (C_L) and Drag Coefficient (C_D) are non-dimensional parameters defined as:

$$C_L = \frac{L}{1/2 \rho V^2 c} \tag{6}$$

$$C_D = \frac{D}{1/2 \rho V^2 c} \tag{7}$$

where:

- ρ is the water density 998,2 [kg/m³]
- C chord length [m]
- L and D it is the Lift and Drag forces, respectively [N/m]
- V Upstream Velocity [m/s]

To describe the forces completely, it is necessary to introduce the moment M of a specific point in the hydrofoil. This point is often located at c/4 from the Leading edge (see **Figure 22**). The standard convention is to consider the positive moment when it turns the hydrofoil clockwise. In this regard, the Moment Coefficient is defined as:

$$C_M = \frac{M}{1/2\rho V_\infty^2 c^2} \tag{8}$$

The physical explanation of the lift is that, due to the shape of the hydrofoil, the streamlines tend to bend around the hydrofoil geometry as in **Figure 24**. The pressure gradient, as defined in Eq. [8], can curve the streamlines:

$$\frac{\partial p}{\partial r} = \frac{\rho V^2}{r} \tag{9}$$

where:

- r is the Curvature of Streamlines
- V is Upstream Velocity

Moreover, the pressure gradient acts as a centrifugal force. Therefore, the pressure on the upper side of the hydrofoil must be lower than the atmospheric one, which is the pressure far from the hydrofoil. On the contrary, the pressure must be higher on the lower side than the atmospheric one. Therefore, this pressure difference generates a lift force on the hydrofoil, as shown in **Figure 24**. When the hydrofoil is almost aligned with the flow, the boundary layer stays attached, and the associated Drag is caused by the friction with the fluid considered, water or air.

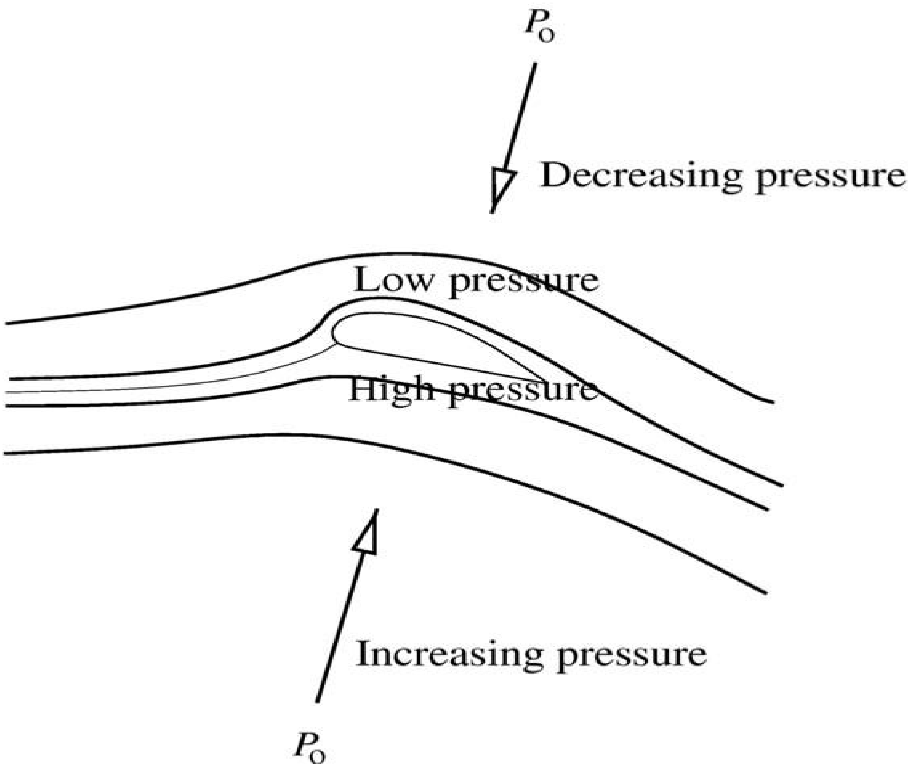

Figure 24 *Generation of lift [54]*

The coefficients C_L C_D and C_M are a function of α Angle of attack and Re Reynolds Number.

The Reynolds number in fluid mechanics is a dimensionless quantity that helps to predict fluid flow patterns in different situations by measuring the ratio between the inertial and viscous forces. For example, in the case of hydrofoil, it is defined as in the following expression:

$$Re = \frac{cV}{\nu} \tag{10}$$

Where:

- c the chord the characteristic hydrofoil length [m]

- V is the upstream velocity [m/s]
- ν is the kinematic viscosity for water at 20 °C is equal to 1.00E-0.6 [m^2/s]

Since the ratio between inertia and viscous forces within a fluid is subjected to a relative internal movement due to the different flow velocities, the region in which this behaviour changes are known as a boundary layer.

At a low Reynolds number, flows tend to be dominated by laminar flow, while at a high Reynolds number, flows tend to be turbulent. This means that, in laminar flow conditions, the flow is dominated by viscous forces and is characterized by smooth and constant fluid motion. While in turbulent flow, the dominant forces are the inertial ones which tend to produce chaotic eddies, vortices, and other flow instabilities.

Therefore, this quantity is beneficial to predict the transition from laminar to turbulent flow.

In this regard, the pre-design of a hydrofoil consists in understanding how the hydrodynamic parameters C_L C_D and C_M change according to the Angle of Attack and Reynolds Number variations and, consequently, to the characteristic environment where the hydrofoil is inserted in.

This analysis can be computed by plotting these quantities on the so-called polars of a hydrofoil, according to the selected hydrofoil.

Generalizing, the Lift Coefficient trend increases linearly with α until a particular value of α, where a maximum value of C_L is reached. Hereafter, the hydrofoil is said to stall, and C_L decreases in a truly geometrical way. On the other hand, the Drag Coefficient C_D is almost constant for small Angles of Attack but increases rapidly after stall. In **Figures 25** and **26**, an example of polars for an airfoil FX67-k-170 is plotted from Martin Hansen's book [54], showing that the Reynolds dependency affects more C_L than C_D; in fact afterwards the Reynolds number reaches a specific value, the dependency becomes small.

Since the stall occurs on a specific point of the hydrofoil, in which the boundary layers go from laminar to turbulent flow, it is evident how the stall condition is highly dependent on geometry.

Moreover, it has been demonstrated that a hydrofoil with a very sharp nose, in other words, with a high curvature around the Leading Edge (see **Figure 22**), stalls more abruptly than a thick one.

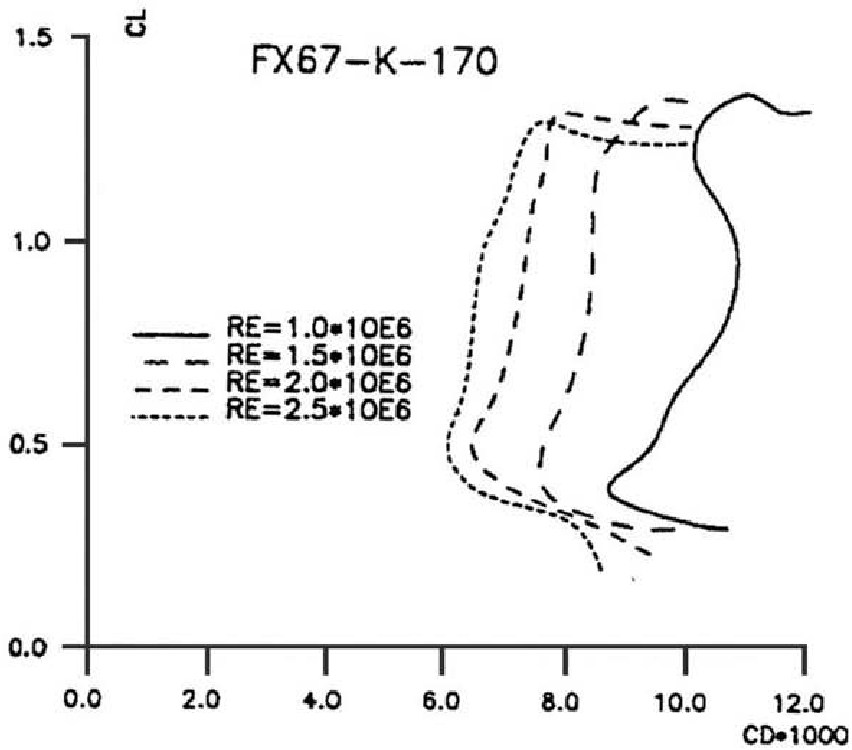

Figure 25 *C_L on C_D according to the Reynolds Number Variation [54]*

To compute the power output from a wind/water turbine, it is necessary to have C_L (α, Re) and C_D (α, Re) data for the airfoils applied along the blades. These data can be measured or computed using advanced numerical tools. However, since the flow becomes unsteady and three-dimensional after the stall, obtaining realizable data for high Angles of Attack is a challenging task.

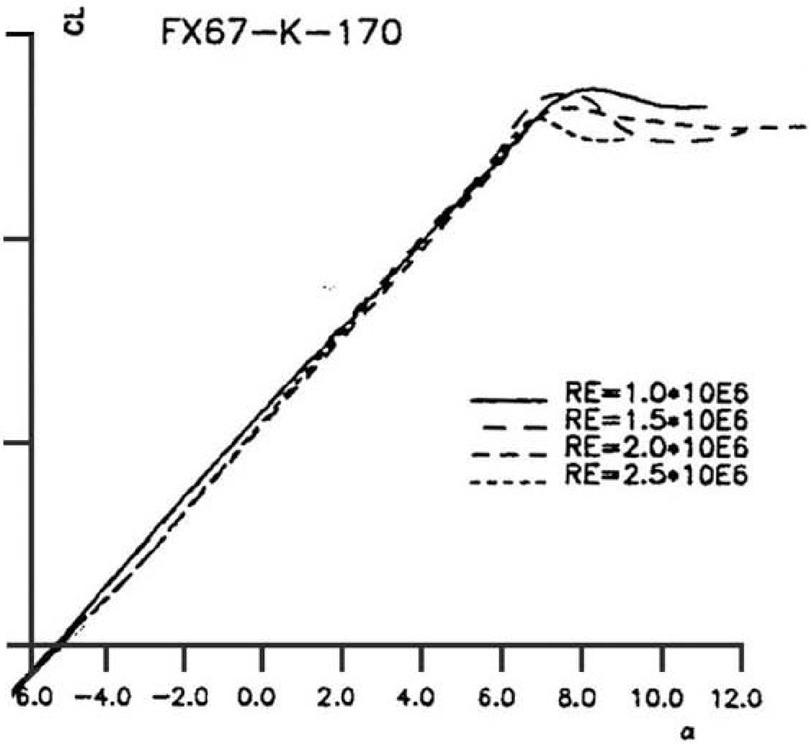

Figure 26 *C_L on alfa [54]*

2.1.8. Cavitation Problems

Cavitation problems on turbines mainly depends on the pressure coefficient on the blade's sections. Pressure Coefficient (C_{pr}) is a dimensionless parameter which measures the relative pressure on the hydrofoil surface. The typical pressure distribution on the upper and lower side of the hydrofoil is given in **Figure 27**.

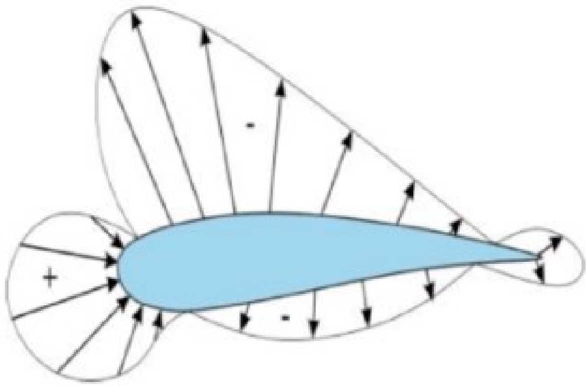

Figure 27 *Positive and negative pressure distribution along the hydrofoil surfaces [55]*

The Pressure Coefficient is defined as follows:

$$C_{pr} = \frac{P_0 - P_\infty}{\frac{1}{2}\rho U_{rel}^2} \tag{11}$$

However, for the sake of simplicity, the Pressure Coefficient can be written as a function of velocity:

$$C_{pr} = 1 - \left(\frac{U}{U_\infty}\right) \tag{12}$$

where:

P_0 is the local static pressure.

P_∞ is the free stream static pressure.

U is the fluid particle's velocity.

The cavitation problems occur when the water's pressure is below the liquid vapor pressure, producing local bubbles. Under this condition, the bubbles grow and make shock waves, noise, and other dynamic effects. Cavitation significantly damages the blades, pranking decrement in performance and causes failures. Most subject to this kind of problems are the elements of the blade rotating at very high value, such as the blade tips. This implies that the cavitation is one of the biggest constraints when modelling a turbine and should be covered in the design process. The equation required to calculate the amount of cavitation in any section of a turbine blade is given by:

$$\sigma_c = \frac{P_0}{P_v} \tag{13}$$

$$P_0 = P_{atm} + \rho g h + \frac{1}{2}\rho U_\infty^2 a(2-a) - \frac{1}{2}\rho(\Omega b)^2 \tag{14}$$

$$q = \frac{1}{2}\rho U_{rel}^2 \tag{15}$$

$$U_{rel} = \sqrt{U_\infty^2(1-a)^2 + (\Omega r)^2(1+b)^2} \tag{16}$$

Where:

σ_c is the amount of cavitation

P_0 is the local pressure.

P_v is the is the Vapor Pressure

P_{atm} Atmospheric pressure

q is the Dynamic pressure

a is the axial induction.

b Interference factor

Ω Angular velocity of the wake

If the absolute value of Pressure Coefficient assumes a value greater than the cavitation number ($|C_{pr}| > \sigma_c$) the blade is more susceptible to cavitation problems. However, the blade is not exposed to cavitation until cavitation velocity (U) exceeds ($U_{cavitate}$) the relative velocity (U_{rel}) [55].

$$U_{cavitate} = \sqrt{\frac{P_{atm} + \rho g h + \frac{1}{2}\rho U_\infty^2 a(2-a) - \frac{1}{2}\rho(\Omega b)^2}{-\frac{1}{2}\rho(C_{pr,min})^2}} \tag{17}$$

where $C_{pr,min}$ is the minimum pressure coefficient. At high Reynolds Numbers, the boundary layers tend to be turbulent more quickly along the airfoil surface, so delay the boundary layer separation means seat back the stellation problems at higher Angle of Attack.

2.1.9. Blockage Effects

The Blockage (Br) is the ratio between the Turbine Area (πR^2) and the Channel area (bh).

$$Br = \frac{At}{Ac} \tag{18}$$

The flow characteristics around and behind a turbine operating in a confined environment differ from that of open environment operations, wind turbines and the so-called Betz Theory [56]. So that, the wind-based counterparts are fundamentally different in several key aspects. Most importantly, hydrokinetic turbines operate in presence of free surface with impact of flow blockage. Conversely, wind turbines operate within the atmospheric boundary layer, whereas the hydrokinetic turbines are subjected to the wall boundary layer effects. This implication directly impacts the operation of these two types of turbines. This Blockage accelerates the flow speed at the rotor plane and enhances the system efficiency [37] [57], even though shown an insignificant effect when the Blockage values are lower than 10%. So that, the Blockage is a fundamental aspect affecting the hydrokinetic turbines' operationally for narrowed channels. Moreover, the surrounding effects control the wake structure behind constrained rotors, including walls, channel beds, or possibly other wakes developed by neighboring turbines [58].

Therefore, the flow in a confined channel experiences changes in three primary parameters: the fluid velocity around the rotor, the pressure changes in the wake and, the longitudinal pressure gradients associated with boundary layer of the channel. This increases the dynamic pressure at the rotor plane, which generates a higher passing flow and, thus, a higher harnessed power when compared to a turbine operating in an unconfined flow. Therefore, the blockage effects are essential and should be considered when designing a hydrokinetic turbine. When creating and analyzing wind/water/hydrokinetic turbines that operate in arrays or channels, it is critical to account for the impacts of Blockage. Blockage correction models are usually applied for their simplicity to account for blockage effects. The widely used technique is commonly developed based on the Actuator Disk Model (ADM). It applies the principles of continuity and equilibrium of momentum of streamlined volume that passes through and around the disk. Blockage correction models based on the actuator disk concept have been addressed in various studies ([59] [60]). The Blockage correction ADM takes the Blockage Ratio and thrust coefficient as an input to adjust the power and the thrust coefficient in a confined rotor.

2.2. Analytical and Numerical Approaches

The basic equations in some wind mathematical models can be applied to fluid, such as water, because these models are based on the Bernoulli equation [61]. General aerodynamic concepts are then introduced. Next, the details of momentum theory and Blade-Element Theory are developed. The combination of two approaches, blade-element momentum theory (BEM), is then studied to outline the governing equations for the aerodynamic design and power prediction of a turbine rotor. To improve and optimize the HAHWTs, efficient analytical and numerical approaches are essential. Several theoretical approaches have been developed to define the Actuator Disk Theory, considering the Froude Number, the free surface-drop behind the turbine [62], and the mixing zone downstream [59]. Moreover, some models explain how these effects affect the power output from a power array [63]. On the numerical level, several are the investigations on both single-phase models, to study the flow field around the HAHWT and, VOF models (Volume of Fluid), to trace the water surface variation in presence of a turbine [64]. Typically, these studies are focused on solving the classical Navier-Stokes equations in a fixed free surface, with sliding mesh technique, and Reynolds-Averaged Navier-Stokes (RANS) turbulent models, to simulate the turbine rotation. The sliding mesh technique is demonstrated to produce better results than Moving Reference Frame (MRF).

2.2.1. Actuator Disk Theory (ADT)

A simple model, generally attributed to Betz (1926), can be used to determine the power from an ideal turbine rotor, the trust of the wind/water on the ideal rotor and the effect of the rotor operation on the local wind/water field. The simplest aerodynamic model is known as the "actuator disk model", in which the turbine is represented by a uniform actuator disk, creating a discontinuity of pressure in the stream tube of air flowing through it. Actuator Disk Theory is based on linear momentum theory developed over 100 years ago to predict the performance of slip propellers.

This analysis uses the following assumptions:

- Homogeneous, incompressible, steady-state fluid flow
- No friction drags.
- An infinite number of blades
- Uniform thrust over the disk or rotor area.

The static pressure far upstream and downstream of the rotor equals the undisturbed ambient static pressure.

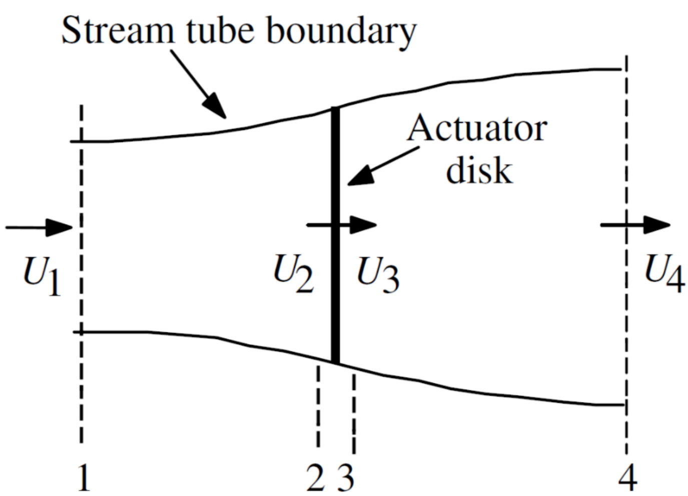

Figure 28 *Actuator disk model of a wind turbine, U mean air velocity; 1, 2, 3, and 4 indicate locations [65]*

Applying the conservation of linear momentum to the control volume enclosing the whole system (See **Figure 28**) allows finding the net force on the contents of the control volume. The point is equal and opposite to the thrust, T, which is the force of the wind/water on the turbine. From the conservation of linear momentum for one-dimensional, incompressible, time-invariant flow, the thrust is equal and opposite to the change in rate of air /water stream.

$$T = U_1(\rho A)_1 - U_4(\rho A)_4 \tag{19}$$

where ϱ is the air/water density, A is the cross sectional area, U is the air/water velocity and the subsripts indicate values at numbered cross section as in **Figure 28**. For steady state flow, $(\rho A)_1 = (\rho A)_4 = \dot{m}$, where $\dot{m}$ is the mass flow rate. Therefore:

$$T = \dot{m}(U_1 - U_4) \tag{20}$$

The thrust is positive so the velocity behind the rotor U_4 is lower than the free stream velocity, U_1. No work is done on either side of the turbine rotor. Thus the Bernoulli function can be used

in the two control volumes on either side of the actuator disk: in the stream tube upstream of the disk:

$$p_1 + \frac{1}{2}\rho U_1^2 = p_2 + \frac{1}{2}\rho U_2^2 \tag{21}$$

and in the stream tube downstream of the disk:

$$p_3 + \frac{1}{2}\rho U_3^2 = p_4 + \frac{1}{2}\rho U_4^2 \tag{22}$$

where

it is assumed that the far upstream and the far downstream pressures are equal ($p_1 = p_4$) and that velocity across the disk stays the same ($U_2 = U_3$). The thrust can also be expressed as the net sum of the forces on each side of the actuator disk:

$$T = A_2(p_2 - p_3) \tag{23}$$

If one solves for (p_2-p_3) using Equations (21) and (22) and substitutes that into the Equation (23), one obtains:

$$T = \frac{1}{2}\rho A_2(U_1^2 - U_4^2) \tag{24}$$

Equating the thrust values from (20) and (24) and recognising that the mass flow rate is the product between U_2 and A_2, we have:

$$U_2 = \frac{U+U}{2} \tag{25}$$

Thus, using this simple model, the wind/water velocity at the rotor plane is the average of the upstream and downstream wind/water speeds. If one defines that the axial induction factor a as the fractional decrease in wind/water velocity between the free stream and rotor plane, then:

$$a = \frac{U_1 - U_2}{U_1} \tag{26}$$

$$U_2 = (U_1 - a) \tag{27}$$

$$U_4 = (U_1 - 2a) \tag{28}$$

The entity, U_1a, is often referred to as the induced velocity at the rotor, in which case the velocity of the wind/water at the rotor is a combination of the free stream velocity and the induced wind/water velocity. As the axial induction factor increases from 0, the wind/water speed behind the rotor slows more and more. If a = 1/2, the wind/water slowed to zero velocity behind the rotor, and the simple theory is no longer applicable. The power output, P, is equal to the thrust multiplied by the velocity at the disk:

$$P = \frac{1}{2}\rho A_2\,(U_1^2 - U_4^2)U_2 = \frac{1}{2}\rho A_2\,(U_1 - U_4)(U_1 - U_4 \tag{29}$$

Substituing U_2 and U_4 from Eq. (27) and (28), we can define the Power as a function of the axial induction factor a:

$$P = \frac{1}{2}\rho A U^3 4a(1-a)^2 \qquad (30)$$

where the control volume area at the rotor, A_2 is replaced with A, the rotor area, and the free stream velocity U_1, with U. From Eq. (30), the Power Coefficient C_P can be expressed as:

$$C_P = \frac{P}{\frac{1}{2}\rho U^3 A} = 4a(1-a)^2 \qquad (31)$$

The maximum C_p is determined by taking the derivative of the Power Ccoefficient (31) and setting it equal to zero, yielding a = 1/3. Thus:

$$C_{pmax} = \frac{16}{27} = 0.5926 \qquad (32)$$

when a = 1/3. For this case, the flow through the disk corresponds to a stream tube with an upstream cross-sectional area of 2/3 the disk area that expands to twice the disk area downstream. This result indicates that if an ideal rotor was designed and operated such that the wind/water speed at the rotor was 2/3 of the free stream wind/water speed, it would operate at the point of maximum power production. Furthermore, this is the maximum power possible given these fundamental physics laws. From Eq. (24),(25) and (26), the axial thrust on the disk is:

$$T = \frac{1}{2}\rho A {U_1}^2[4a(1-a)] \qquad (33)$$

Similarly to the power, the thrust on a ideal wind/water turbine can be characterized by a dimensionaless thrust coefficient, using Eq. (33):

$$C_T = \frac{T}{\frac{1}{2}\rho U^2 A} = 4a(1-a) \qquad (34)$$

This Thrust Coefficient has a maximum of 1.0 when a = 0.5 and the downstream velocity is zero. At maximum power output (a = 1/3), C_t is 0.88. A graph of the power and thrust coefficients for an ideal Betz turbine and non-dimensionalized downstream wind/water speed is illustrated in **Figure 29.**

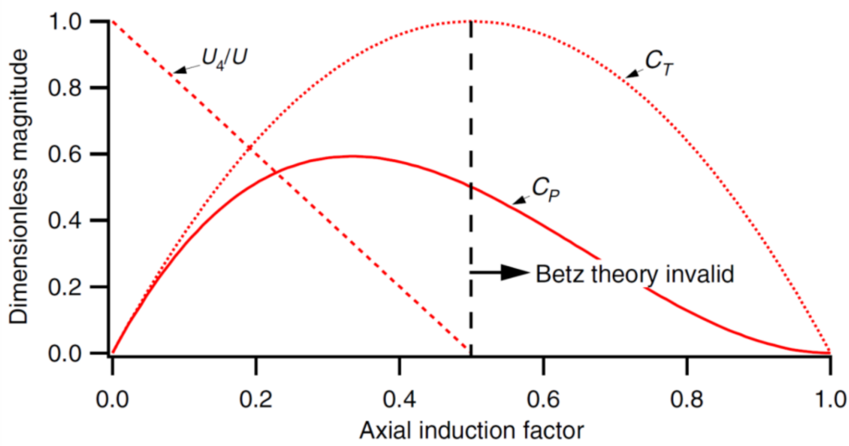

Figure 29 *Operating parameters for Betz turbine, U, the velocity of undisturbed air/water; u4 air/water velocity behind the rotor, C_p Power Coefficient C_t, thrust coefficient [54]*

As already said, this idealised model is invalid for axial induction factors greater than 0.5. In fact, as the axial induction factor approaches and exceeds 0.5, complicated flow patterns not represented in this simple model result in thrust coefficients that can go as high as 2.0.

2.2.2. General Momentum and Rotor Disk Model

The axial momentum theory of the previous section has been developed considering no rotational motion in the slipstream and replacing the turbine with an actuator disk which produces in the fluid a sudden decrease in pressure without any change in velocity.

Generalizing, the streamlines will have a rotational motion due to the torque of the blade, producing further energy losses. Intending to extend and include the effect of the rotational motion in theory, it is necessary to modify the quantities of the actuator disk by assuming that it can also provide a rotational component to the fluid velocity. Meanwhile, the axial and radial components remain constant. Therefore, starting from a stream tube analysis, is possible to derive equations expressing the relation between the wake velocities (both axial and rotational) and the corresponding wind/water velocities at the rotor disk. **Figure 30** below shows the annular stream tube model to visualize the wake rotation, while **Figure 31** shows the geometry of the stream tube.

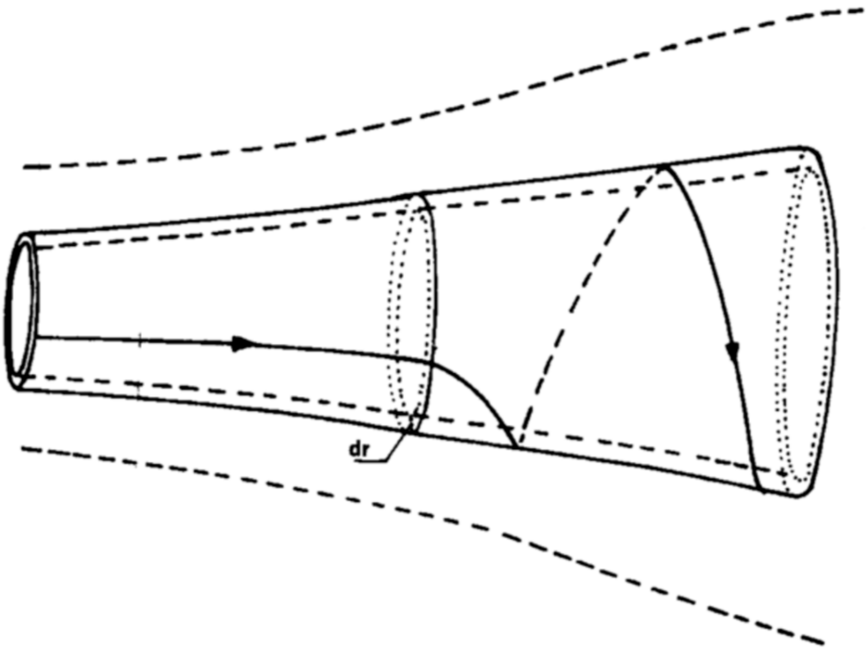

Figure 30 *Stream tube model including wake rotation [66]*

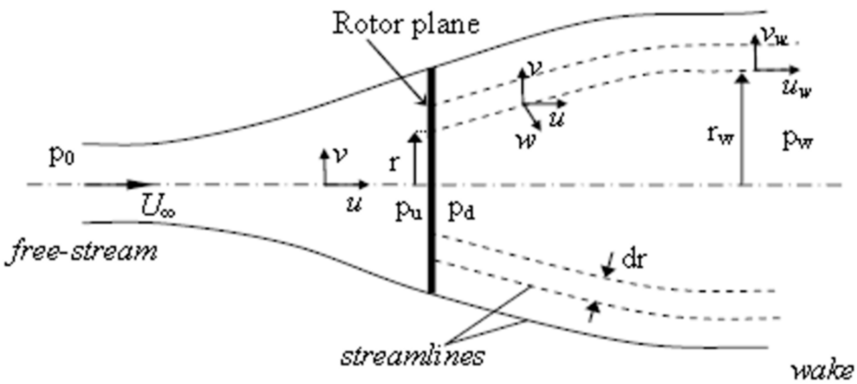

Figure 31 *Geometry of stream tube model [54]*

In **Figure 31**, the r is the radial distance of any annular element of the rotor plane, u and v the inflow (the flow immediately in the front of the rotor plane) axial and radial components of the fluid velocity, respectively. On the other hand, p_u is the inflow pressure, and p' is the outflow pressure decrease associated with an angular velocity w. In the final wake, p_w is the pressure, u_w is the axial velocity, and w_w is the angular velocity at a radial distance r_w from the axis of the slipstream. By applying both the flow continuity equation and the constancy of angular momentum, it is going to obtain:

$$u_w r_w dr_w = urdr \tag{35}$$

$$w_w {r_w}^2 = wr^2 \tag{36}$$

Since the element of torque of radial blade element is equal to the angular momentum extracted in unit time to the corrisponding annular element of the slipstream

$$dM = \rho w r^2 dA \tag{37}$$

where $dA = 2\pi dr$

To make the energy equation, Bernoulli equation can be used from both the free flow condition to the inflow and the outflow to wake condition:

$$H_0 = p_0 + \frac{1}{2}\rho U_\infty^2 = p_u + \frac{1}{2}\rho(u^2 + v^2) \tag{38}$$

$$H_1 = p_d + \frac{1}{2}\rho(u^2 + v^2 + w^2 r^2) = p_w + \frac{1}{2}\rho({u^2}_w + {w^2}_w + {r^2}_w) \tag{39}$$

Hence,

$$H_0 - H_1 = p' - \frac{1}{2}\rho(w^2 r^2) \tag{40}$$

Equation (40) shows that the total pressure head decrease passing through the blade element is below the thrust per unit area p' by a term rappresenting the kinetic energy of the rotational motion providing to the flow by the torque of the blade. The expression for the total pressure head gives:

$$p_0 - p_w = \frac{1}{2}\rho({u^2}_w - U_\infty^2) + \frac{1}{2}\rho {w^2}_w {r^2}_w + H_0 - H_1$$

$$= \frac{1}{2}\rho({u^2}_w - U_\infty^2) + \frac{1}{2}\rho({w^2}_w {r^2}_w - w^2 r^2) + p' \tag{41}$$

To find the pressure drop p', the Bernoulli equation can be applied between the inflow and the outflow relative to the blade, rotating with angular velocity Ω. It is worth noting that behind the rotor, the flow rotates in the opposite direction to the rotor, in reaction to the torque extracted by the flow on the rotor. Hence, the angular velocity of the air/water relative to the blade increases from Ω to (Ω+w), whereas the axial component of the velocity remains constant. The result is:

$$p' = \frac{1}{2}\rho[(\Omega + w)^2 - \Omega^2]r^2 = \rho\left(\Omega + \frac{w}{2}\right)wr^2 \quad (42)$$

Combining Eqs. (42), (41) and (36), the pressure drop in the wake becomes:

$$p_0 - p_w = \frac{1}{2}\rho({u^2}_w - U_\infty^2) + \rho\left(\Omega + \frac{w}{2}\right){w^2}_w{r^2}_w \quad (43)$$

The pressure gradient in the wake is governed by the following equation:

$$\frac{dp_w}{dr_w} = \rho {w^2}_w r_w \quad (44)$$

Therefore, by differentiating the Eq. (43) on r_w and setting it equal to (44), a differential equation which connects the axial and rotational velocities in the wake is obtained:

$$\frac{1}{2}\frac{d}{dr_w}[U_\infty^2 - {u^2}_w] = (w_w + \Omega)\frac{d}{dr_w}(w_w {r_w}^2) \quad (45)$$

The equation of axial momentum for the blade element can be extracted from the previous section:

$$T = \int \rho u_v(U_\infty - u_w)dA_w + \int(p_0 - p_w)dA_w \quad (46)$$

and in a differential form:

$$dT = \rho u_v(U_\infty - u_w)dA_w + (p_0 - p_w)dA_w \quad (47)$$

From the pressure decrease at the rotor plane, dT can also be written as:

$$dT = p'dA \quad (48)$$

By substituing Eq. (40) into its place in Eq. (48), one obtains:

$$dT = \rho\left(\Omega + \frac{w}{2}\right)wr^2 dA \quad (49)$$

Finally, combining Eqs. (35), (41), (47) and (49):

$$\frac{1}{2}[U_\infty - u_w]^2 = \left[\frac{\Omega+\frac{w_w}{2}}{u_w} - \frac{\Omega+\frac{w}{2}}{U_\infty}\right] u_w w_w {r_w}^2 \tag{50}$$

It should be noted that the axial momentum equation is based on the assumption that the axial force due to the pressure on the lateral boundary of the streamline is equal to the pressure force (p_0A_0-p_wA_w) over its end. This implies that the interface between several annular elements has been neglected, but the actual deviations from Eq. (49) are considered extremely small. The second assumption is that the rotor was treated as having a vast number of very narrow blades (infinite), by neglecting somewhat an axial component of the flow velocity, and the air/water is incompressible and inviscid, i.e., fluid drag is zero.

The Eqs. (35), (36), (45) and (50), even if their complex form, are enough to determine the relationship between the blade's thrust and torque and the flow in the slipstream. At the same time, by combining Eq. (50) with (35) and (36), the axial and rotational speeds in the rotor plane can be calculated. The rotor thrust and torque are obtained from Eqs. (49) and (37).

By defining the axial velocities u and u_w as:

$$u = U_\infty(1-a) \tag{51}$$

$$u_w = U_\infty(1-b_{wk}) \tag{52}$$

where b_{wk} is the axial induction factor far the wake.

After some algebraical manipulations, from Eq. (50), it can be obtained:

$$a = \frac{a}{2}\left[1 - \frac{(1-b_{wk})a^2}{4\lambda^2(a-b_{wk})}\right] \tag{53}$$

Examination of Eq. (53) shows that the axial velocity reduction of the rotor disk is always approximately one-half the reduction in the far-wake for the tip-speed ratio above 2, which is the same result reached in the previous **Section (2.2.1**) when the wake rotation was neglected.

For the approximate solution, the following assumption is made. The angular velocity w provided to the wake is tiny compared with angular velocity Ω relative to the blade and therefore, can be simplified the general equations by neglecting specific terms involving w^2. On this basis of approximation, the pressure p_w of the air/water and the decrease of pressure p' across the rotor disk equal the reduction of the total pressure head *(H_0-H_1)*. Therefore, the relationship connecting the thrust and the axial velocity u are the same as in the simple momentum theory, the axial velocity u at the rotor disk is the arithmetic mean of the axial velocity U_∞ and the wake velocity u_w, and the element of thrust is:

$$dT = 2\rho u(u - U_\infty)dA = 4\pi\rho U_\infty^2 a(1-a)rdr \tag{54}$$

Alternatively, from Eq. (40):

$$dT = p'dA = 2\pi\rho\left(\Omega + \frac{w}{2}\right)wr^3dr \tag{55}$$

and defining the angular induction factor a' = w/2Ω:

$$dT = 4\pi\rho\Omega^2 a'(1+a')r^3dr \tag{56}$$

Equating the two expressions for the thrust given in Eq. (54) and (56), a relationship is obtained between the axial induction factor, a and angular induction factor a'.

$$\frac{a(1-a)}{a\prime(1-a')} = \frac{\Omega^2 r^2}{U_\infty^2} \tag{57}$$

The element of torque is obtained from Eq. (37) as following:

$$dM = \rho wr^2 dA = 4\pi\rho U_\infty \Omega a'(1+a)r^3dr \tag{58}$$

The Power generated to each radial element dP is given by the following equation:

$$dP = \Omega dM \tag{59}$$

By substituiting dM from Eq. (58) into Eq. (59) and using the definition of local tip speed ratio λ, the expression for the power generated at each radial element becomes:

$$dP = \frac{1}{2}\rho A U_\infty^3\left[\frac{8}{\lambda^2}a'(1-a)\lambda^3 d\lambda_r\right] \tag{60}$$

The incremental contribution to the power coefficient from each annualr ring is given by:

$$dC_P = \frac{dP}{\frac{1}{2}\rho A U_\infty^3} \tag{61}$$

By plotting Eq. (60) into Eq. (61) and integrating the elementar power coefficient from the local tip speed ratio, *Cp* is obtained as:

$$C_P = \frac{8}{\lambda^2}\int a'(1-a)\lambda^3 d\lambda_r \tag{62}$$

To integrate Eq. (62), it is necessary to relate the variables a, a′ and λ_r. By solving Eq. (57), *a′* in terms of *a*:

$$a' = -\frac{1}{2} + \frac{1}{2}\sqrt{1 + \frac{4}{\lambda_r^2}a(1-a)} \tag{63}$$

The aerodynamic condition for the maximum possible power production occurs when the term a′(1-a) in Eq. (62) is at its maximum value. Substituting the value for a′ from Eq. (63) into the term a′(1-a) and setting derivative concerning a and setting the equation equal to zero yields:

$$\lambda_r^2 = \frac{(1-a)(4a-1)^2}{(1-3a)} \tag{64}$$

Moreover, using Eqs. (64) and (57), it is found that for maximum power in each annular ring:

$$a' = \frac{(1-3a)}{(4a-1)} \tag{65}$$

If the Eq. (64) is differentiated with respect to a, a relationship between λ_r and *da* at these conditions is obtained:

$$2\lambda_r d\lambda_r = \left[\frac{6(4a-1)(1-2a)^2}{(1-3a)^2}\right] \tag{66}$$

Now, substituting the Eq. (64), (65) and (66) into the Eq. (62) gives:

$$C_{p,max} = \frac{24}{\lambda^2}\int_{a1}^{a2}\left[\frac{(1-a)(1-2a)(1-4a)}{(1-3a)}\right]^2 da \tag{67}$$

a_1 corrisponding axial induction factor for $\lambda_r = \lambda_h$

a_2 corrisponding axial induction factor for $\lambda_r = \lambda$

Also from Eq. (61):

$$\lambda^2 = \frac{(1-a_2)(1-4a_2)}{1-3a_2} \tag{68}$$

Eq. (68) can be solved for a value corresponding to operations at tip speed ratios of interest. Note also from Eq. (68) that $a_2 = 1/3$ is the upper limit of the axial induction factor giving an infinitely large tip speed ratio.

2.2.3 Blade Element Theory

The momentum theories explained in the previous section are based on the mean axial and rotational velocity hypotheses in the slipstream to determine the thrust and torque employed on the blades from the decreased rate of fluid momentum. These theories determine an upper limit to the power coefficient extracted, neglecting the effect of rotor geometry (i.e. blade hydrofoil section, chord and twist).

On the contrary, the Blade Element Theory is an alternative method for analysing the blade behaviour in their motion through the fluid.

In this theory, the blade consists of several hydro-dynamically isolated sections that do not interact. Therefore, the force of the whole blade can be derived by adding the contribution of all the ements. **Figure 32** shows the schematic annular control volume used for this analysis.

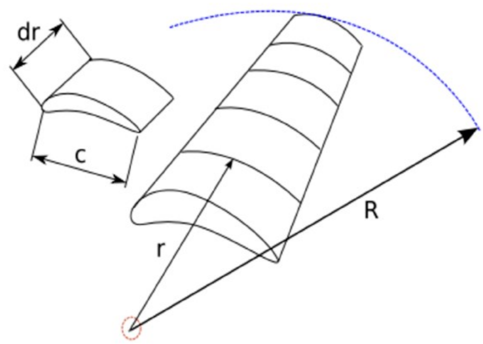

Figure 32 *Schematization of Blade Element [67]*

The relative water velocity U_{rel} is the vectorial sum of water velocity at the rotor plane U_∞ *(1-a)* (i.e. the vector sum of the free-stream water velocity U_∞ and the induced axial velocity *-a* U_∞) and the water velocity due to the rotation of the blade. Therefore, this rotational component is the vectorial sum of the blade section velocity *Ωr* and the induced angular velocity a′Ωr. Hence, the relative water velocity will be as in the **Figure 33**. The minus sign in term U_∞ *(1-a)* is due to the flow's deley while the water approaches, conversely plus sign term *Ωr(1+a′)* as shown in figure below.

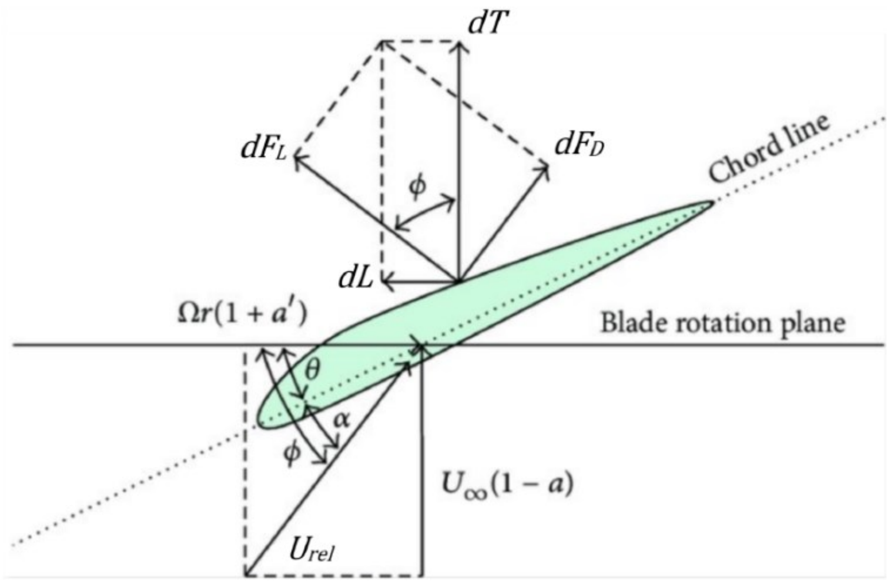

Figure 33 *Forces and velocity triangles for an airfoil section of a rotating wind/water turbine blade [68]*

From **Figure 33** the following relationship can be deducted:

$$U_{rel} = \frac{U_\infty(1-a)}{\sin(\varphi)} \tag{69}$$

$$\tan(\varphi) = \frac{U_\infty(1-a)}{\Omega r(1+a')} = \frac{(1-a)}{(1+a')\lambda_r} \tag{70}$$

$$dF_D = C_D \frac{1}{2}\rho U_{rel}^2 c dr \tag{71}$$

$$dF_L = C_L \frac{1}{2}\rho U_{rel}^2 c dr \tag{72}$$

$$dN = dF_L \cos(\varphi) - dF_D\, sin(\varphi) \tag{73}$$

$$dL = dF_L\, sin(\varphi) - dF_D\, cos(\varphi) \tag{74}$$

If the rotor's number of Blade is equal to *N*, by rearrannging Eqs. (74) and (73) with the use of Eqs. (69), (71) and (72), the total normal and tangential forces on the element at a distance *r* are:

$$dN = N\frac{1}{2}\rho U_{rel}^2(C_L \cos(\varphi) + C_D \sin(\varphi)\, cdr) \tag{75}$$

$$dL = N\frac{1}{2}\rho U_{rel}^2(C_L \sin(\varphi) + C_D \cos(\varphi)) \tag{76}$$

The element torque due to tangential forces dL, operating at distance r from the center is given by:

$$dM = rdL \tag{77}$$

Hence, the element torque by putting Eq. (76) into (77):

$$dM = N\frac{1}{2}\rho U_{rel}^2(C_L\, sin(\varphi) + C_D\, cos(\varphi))crdr \tag{78}$$

By defining solidity ratio σ, as following:

$$\sigma = \frac{Nc}{2\pi r} \tag{79}$$

and inserting Eqs. (62) and (72) into Eqs. (66) and (71), the general form of the element thrust and the torque equations become:

$$dT = \sigma\pi\rho\frac{U_\infty^2(1-a)^2}{\sin(\varphi)}(C_L\, cos(\varphi) - C_D\, sin(\varphi))rdr \tag{80}$$

$$dM = \sigma\pi\rho\frac{U_\infty^2(1-a)^2}{sin(\varphi)}(C_L\, sin(\varphi) - C_D\, cos(\varphi))r^2dr \tag{81}$$

Therefore, two Eqs. (80) and (81) have been calculated from the blade element. They define the normal force (thrust) and the tangential force (torque) on an annular rotor section as a function of the angles at the blades and hydrofoil characteristics.

It is possible to deduct the following assumptions based on the Blade Element Theory:

1. The behaviour of an element is independent of the adjacent elements of the same blade;
2. the hydrofoil features for the blade elements.

The independence of blades elements assumed in the blade element theory and all later developments theories is equal to the assumption adopted in the general momentum theory (**section 2.2.2**), that the thrust on an elementary rotor's annulus may be expressed as $dT = 2\rho u(u\text{-}U_\infty)dA$. In the discussion of general momentum theory, it was highlighted that this equation may not be established rigorously. Similarly, in the blade element theory, it is impossible to give a rigorous proof of the blade element's independence, and the validity of evidence an appeal of relevantly experimental results must be a relevant assumption. If this hypothesis is valid, the thrust on the blade element at radial distance r with the blade angle θ should be independent regardless of the variation of the blade angle and the blade span. An assumption's check can therefore be obtained by taking two propellers of different pitch with blades linked to the same plan form and section, by rotating the blades of one rotor so that the blade angles of both rotors have the same value of chosen radial distance. The thrust distribution along the blades should then show the same element of thrust on the blade elements under examination. This means that a series of experiments has been established the indipendence of the blade elements over the principal part of the blades.

Concerning the second assumption, it is possible to assume that two-dimensional hydrofoil characteristics can be used for the blade elements. Hydrofoil two-dimensional characteristics are commonly determined from tests on a rectangular hydrofoil of different aspect ratios. Hence, the lift and drag characteristics are dependent on the aspect ratio. However, in the fully-attached regime, hydrofoil section characteristics are not generally affected by aspect ratio. In conclusion, when two-dimensional data are used, a tip-loss factor must be added as described in the next section.

2.2.4. Blade Element Momentum Theory (BEMT)

Several authors have derived methods for predicting the steady-state performance of wind/water turbine rotors. The wind turbine classical analysis was originally developed by Betz and Glauert [69]. Then, the theory was extended and adapted for digital computer's solutions [70]. In all these methods, momentum theory and blade element theory are combined into a blade element momentum theory that calculates the performance characteristics of an annular rotor's section. The force on the whole blade can be derived by integrating, or summig up, the values for each annular section. This appraoch is described in the next section for the mathematical modelling of HAHWTs.

2.2.5. BEMT for HAHWTs

The general momentum theory highlighted the fluid's motion and how it affects acting on the blades. However, the drawback of the general momentum theory is that it doesn't give indication on the shape. The blade element theory's principle was to consider the forces on the rotor's blade in their motion through the air, and this theory is strictly related to the geometrical shape. To overcome the gap between these two theories, the general momentum and the blade element, the blade element momentum theory (BEM), has been developed. The major discovery of this theory is the finite blade number's effect. The BEM's assumptions are the combiation of those which were made for general momentum and blade element theory. The most critical assumption of BEM theory is that individual stream tubes (i.e. stream tube section between the stream tube and streamream tube by the blades) can be analysed regardless of the rest of the flow as assumed before in the blade element theory. The second important assumption of BEM theory is that spanwise flow is negligible, so the airfoil profile data, as previously in the blade element theory, is acceptable. The third assumption is that the flow condition doesn't vary the circumferential discretisation, i.e. asymmetric flow.

In conclusion, since BEM theory allows to determine the wind turbine performance by equating the element thrust force defined in the Eq. (54) from general momentum theory and the Eq. (80) from element theory, the following expressions are obtained:

$$\frac{a}{(1-a)} = (\sigma C_L)\frac{\cos(\varphi)}{4sin^2(\varphi)}\left[1+\left(\frac{C_D}{C_L}\right)\tan(\varphi)\right] \tag{82}$$

Moreover, matching the elementary torque derived in both general momentum Eqs. (57) and blade element theory (81)

$$\frac{a\prime}{(1-a)} = \frac{\sigma C_L}{4\lambda_r \sin(\varphi)}\left[1-\left(\frac{C_D}{C_L}\right)cot(\varphi)\right] \tag{83}$$

where λr is the local tip speed ratio. Eq. (83) can be rearranged by using Eq. (69), which relates a, a′, ϕ and λr based on geometric considerations:

$$\frac{a\prime}{(1-a)} = \frac{\sigma C_L}{4cos(\varphi)}\left[1-\left(\frac{C_D}{C_L}\right)cot(\varphi)\right] \tag{84}$$

It is a common practice to consider C_D equal to zero to calculate the axial and rotational induction factor, a and a′, regardless of the geometric airfoil characteristics. It is evident that for airfoil/hydrofoil with a low drag coefficient, this simplification introduces minor error; otherwise, the Eqs. (82), (83), and (84) can be rewritten considering the drag coefficient equal to zero.

$$\frac{a}{(1-a)} = (\sigma C_L)\frac{\cos(\varphi)}{4sin^2(\varphi)} \tag{85}$$

$$\frac{a\prime}{(1-a)} = \frac{(\sigma C_L)}{4\lambda_r sin(\varphi)}$$

$$\frac{a\prime}{(1-a\prime)} = \frac{(\sigma C_L)}{4cos(\varphi)}$$

By using these three equations, the following beneficial relationship results in after some algebric manipulations:

$$C_L = \frac{4\sin(\varphi)(\cos(\varphi)-\lambda_r\sin(\varphi))}{\sigma(\sin(\varphi)+\lambda_r cos(\varphi))} \tag{86}$$

$$a = \frac{1}{\left[1+\frac{4sin^2(\varphi)}{\sigma C_L \cos(\varphi)}\right]}$$

$$a' = \frac{1}{1+\left[\frac{4cos(\varphi)}{\sigma C_L}\right]-1}$$

$\frac{a}{a\prime} = \frac{\lambda_r}{\tan(\varphi)}$

To determine the Power Coefficient of a wind/water turbine, the power contribution from each annular ring along the blade length should be integrated, and the Power Coefficient can be obtained. Therefore, the elemental power from each blade element was defined in Eq. (59) as:

$$dP = \omega dM \tag{87}$$

and the total power from the rotor is:

$$P = \int_{rh}^{R} dP = \int_{rh}^{R} \omega dM \tag{88}$$

Hence, the power coefficient C_p becomes:

$$C_p = \frac{P}{0.5\rho A U_\infty^2} = \frac{\int_{rh}^{R} \omega dM}{0.5\rho A U_\infty^2} \tag{89}$$

where r_h is the rotor radius at the hub of the blade. Using the expression for elemental torque, the power coefficient can be expressed as:

$$C_P = \frac{2}{\lambda^2} \int \sigma C_L \frac{(1-a)^2}{\sin(\varphi)} \left[1 - \left(\frac{C_D}{C_L}\right) \cot(\varphi)\right] \lambda_r^2 d\lambda_r$$
(90)

Finally, by using Eqs. (85), (86) and (87) the general form of power coefficient can be obtained:

$$C_P = \frac{8}{\lambda^2} \int_{\lambda_r}^{\lambda} \lambda_r^3 a'(1-a) \left[1 - \left(\frac{C_D}{C_L}\right) cot(\varphi)\right] d\lambda_r \tag{91}$$

It is worth noting that when C_D is equal to zero the above equation for C_P is the same as the one derived from the general momentum theory.

2.3. Free-surface Effects

Most of the time, the single-phase models could be more realistic in describing the performance and hydrokinetic turbine flow pattern. This inadequacy lies in not incorporating the free surface variation analysis in the results. In this regard, [71] have found that the single-phase simulation over-predicts the turbine output for horizontal-axis turbines compared to the multiphase ones.

Concerning horizontal turbines, it also has been studied the closeness effect of the channel walls, and the free surface on the turbine's performance [58], the wake recovery and drop of free surface behind the rotor, or the influence to the proximity of critical Froude Number [72].

Chapter III

Turbine Blade Design

Chapter III illustrates the followed methodology to design the blade implemented for the experimental tests. Considering the theoretical bases explained in the Chapter II, the Q-Blade software is introduced. This software indeed is widely used to design both vertical and horizontal wind/water turbines to simulate the hydrodynamic behaviour of wind/water turbine blade.

3.1. Blade design parameters

The initial step, when designing a hydrokinetic turbine blade, is the characterization of parameters that primarily depend on the available energy source and the features of deployment-site. With this end, to create the studied turbine blade, the geometrical and hydraulic characteristics of channel in which the turbine will be inserted and tested are first evaluated. The recirculating water channel will be meticulously described in Chapter IV section 4.2.

The deployment-site characteristics are crucial because they affect the definition of the turbine diameter and the water velocity field according to the laboratory set-up limitations.

With this aim, since the channel is 0.30 m in width, it is fixed that the turbine doesn't exceed a 0.24 m in diameter. Usually, to characterize the operating condition of an energy system, the rated flow speed is defined as a current speed at which theoretically the generator reached the rated power. Whereas the cut-out speed is the maximum water current at which normal power production is possible. Moreover, to reduce the moveable parts, and to simplify the design of the studied turbine, fixed pitch blades was chosen for the present case study.

Hence, it has been imposed that the variation of TSR ranging from 2 to 8 to analyze the possible angular velocity correlated to the current velocity speed, which has a minimum value (rated current speed) of 0.43 m/s and a cut-out speed of 0.68 m/s.

Since, the rotor characteristics, and the operating conditions were chosen as in **Table 1,** the blade geometry was optimized with a single optimum design goal. Therefore, knowing the rated and cut-out speed realizable in experimental recirculation water channel, it possible to understand the corresponding angular velocity as in **Table 2**. The rated TSR equals four for the predictable rotational speed, namely the mean value of the analysed possible TSRs. This means that a chord linear distribution along the blade span is imposed, starting from the reference chord, corresponding to a quarter of the radius length 0.118 m/4 = 0.03 m until a chord length at the tip equal to 0.018 m. Moreover, a fixed solidity value of 0.10 corresponds to a chord length of 0.024 m, this chord value is reached at 75% of blade span. This assumption is commonly used to select a representative chord, and this comes from the explanation of Chapter II (**section 2.1.7**), namely it is applied at R/4, the vectorial resultant of hydrodynamic forces and it is also the point regarding which the momentum is calculated considering the contribution of all the discretized blade section. It is worth noticing that the radius length is deducted by subtracting from the total turbine diameter of 0.24 m both the radius of the hub, equal to 0.025 m in which the blades are fixed, and the height of the linker peace, which connects the transition from Eppler818 hydrofoil to circular shape. Generally, an optimum turbine blade is narrower at the tip and broader near the root. The edge is also thicker at the root, where greater strength is required, and tends to become thinner at the tip, where drag must be minimized [73].

Table 1 Rotor geometry characteristics

Rotor geometry	
Rotor Radius [m]	0.118
hub radius [m]	0.025
number of blades [-]	3

Table 2 Rated and cut-out speed according to TSR variation.

TSR = 2			
Parameter	Value	Parameter	Value
Number of rotors	1	Number of blades (Nb)	3
Rated Power [W]	6.92	Rotor radius [m]	0.12
Rated current speed [m/s]	0.43	Rated cut-out speed [m/s]	0.68
Rated rotational seed [rpm]	69.87	Cut-out rotational speed [rpm]	110.26
TSR = 3			
Rated rotational seed [rpm]	104.8	Cut-out rotational speed [rpm]	165.3
TSR = 4			
Rated rotational seed [rpm]	139.7	Cut-out rotational speed [rpm]	220.5
TSR = 5			
Rated rotational seed [rpm]	174.6	Cut-out rotational speed [rpm]	275.6
TSR = 6			
Rated rotational seed [rpm]	209.6	Cut-out rotational speed [rpm]	330.7
TSR = 7			
Rated rotational seed [rpm]	244.5	Cut-out rotational speed [rpm]	385.9
TSR = 8			
Rated rotational seed [rpm]	279.4	Cut-out rotational speed [rpm]	441.0

3.2. Single optimum design goal and Q-Blade software

The performance of the rotor implemented was calculated using a classical Blade Element Momentum Theory (BEMT) numerical solver (see **section 2.2.4** and **2.2.5** Chapter II). BEMT provides for the relationship between the global thrust and torque generated by the rotor and the sectional forces extracted by the flow on the blades [54][51]. BEMT is considered sufficient for preliminary analysis in a wide range of operating conditions and successfully used in designing both wind and water turbines. One of the most restrictive approximations of the BEMT is that, by dividing the rotor in uniform flow discrete annular regions with no interactions between them, assumes that all the spanwise sections work in a 2D flow. This approximation is valid when the effects of 3D phenomena such as radial flow generated by centrifugal forces are minor, with a very modest even the thrust and torque generation. However, experimental, and numerical studies have demonstrated that around the blades there is a reflex flow field, therefore this method is helpful in the preliminary design step, and to geometrize the edge. The Q-Blade is a public source simulation software developed at Hermann Föttinger Institute of TU Berlin for wind turbine blade design and aerodynamic simulation. An updated stable version (v0.96) was released in August 2015, including a new aerodynamic module which replaced the BEM of QBlade with a new advanced Lifting Line Theory (LLM). In this software, choosing the hydro/airfoil allows discretizing the blade in several sections, changing pitch and twist angle.

Moreover, this software allows users to rapidly design custom airfoil and capture their performance curves, in a range of 360° Angle of Attack, and for several Reynolds number (see **section 2.1.7**). The so-called single optimum design goal aims to find linear chord distribution able to maximize the total efficiency of hydrodynamic forces acting on the blade. To do that, is forced that each blade section "sees" the same α which maximizes the global efficiency of the entire profile.

3.3. Eppler 818

Based on previous research [15], for the present case study an hydrofoil Eppler 818 has been chosen because it showed good performance for hydrokinetics applications. **Figure 34** shows that the hydrofoil has a maximum thickness (see **section 2.1.4 and 2.1.6** Chapter II) of 16.34% and a camber of 3.13%.

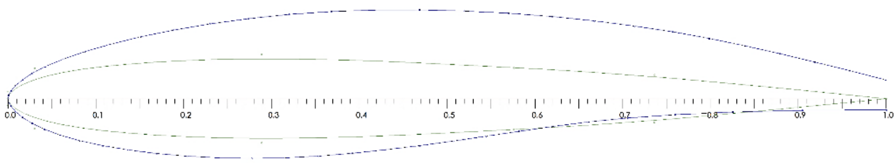

Foil

	Name	Thickness (%)	at (%)	Camber (%)	at (%)	Points	TE Flap (deg)	TE XHinge	TE YHinge	Show	Points	Centerline	Style
1	Spline foil	9.03	31.20	0.00	0.00	60	0.00	0.00	0.00	☑	☐	☐	
2	Circular Foil	100.00	50.00	-0.00	99.90	101	0.00	0.00	0.00	☐	☐	☐	
3	New Foil	16.04	33.05	2.78	67.00	67	0.00	0.00	0.00	☐	☐	☐	
4	Nuovo Profilo	16.34	35.39	3.13	65.38	59	0.00	0.00	0.00	☑	☑	☐	

Figure 34 *Eppler 818 profile characteristics*

This is a modification of the classical Eppler hydrofoil, owing a more considerable thickness and camber in percentage.

So, as first step, it is necessary to divide in an arbitrary number of sections the blade along its radius span. The methodology to attribute a chord length value to each section is based on hydrodynamic consideration. Sure enough, fixing a rated value of TSR equal to 4, and knowing the consequent angular velocity correlated to the velocity range of current flow (0.43 ÷ 0.68 m/s), the value assumed by the Relative Velocity, which is the vectorial composition between the local radial component $\omega(R/r)$ and the axial velocity directly proportional to the current speed, has been analyzed.

Hence, the turbine along its blade span was divided into 11 sections of r in length, choosing an arbitrary step of 0.0084 m, up to the last section, with a total radius blade length of R = 0.084 m. As in **Figure 35**, the local Angle of Attack is given by pitch of the airfoil θ, the axial and rotational velocity at rotor plane, denoted by V_a and V_{rot}, respectively.

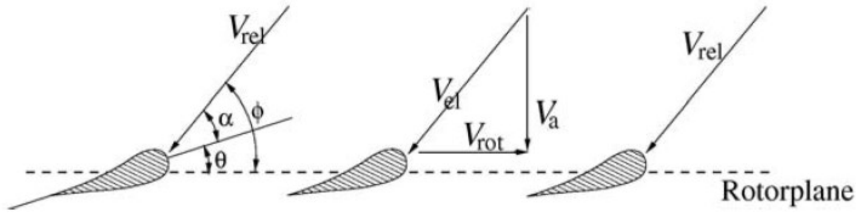

Figure 35 *Radial cut in a wind rotor turbine showing airfoil at r/R [45]*

$$\alpha = \phi - \theta \tag{92}$$

where the flow angle ϕ can be calculated by the following equation:

$$tang\ \phi = \frac{V_a}{V_{rot}} \tag{93}$$

From the analysis of the polar (**see section 2.1.7)** of hydrofoil extracted from the Q-Blade and visible in **Figure 36**, according to a Reynolds Number variation, ranging from 1.0E+04 to 1.5E+05, it is assumed that the global Angle of Attack that maximizes the global profile efficiency C_l/C_d is equal to 6°.

As it can see from the chart, it has been considered a wide range of Reynolds Number, to include the possible current inlet velocity, which directly increases the Lift Coefficient and the global efficiency of the hydrofoil C_l/C_d.

Therefore, forcing the assumption that each blade section sees the same Angle of Attack maximizing the global profile efficiency as in **Figure 11**, it is possible to calculate the local pitch angle by the difference between the flow angle ϕ and the Angle of Attack α.

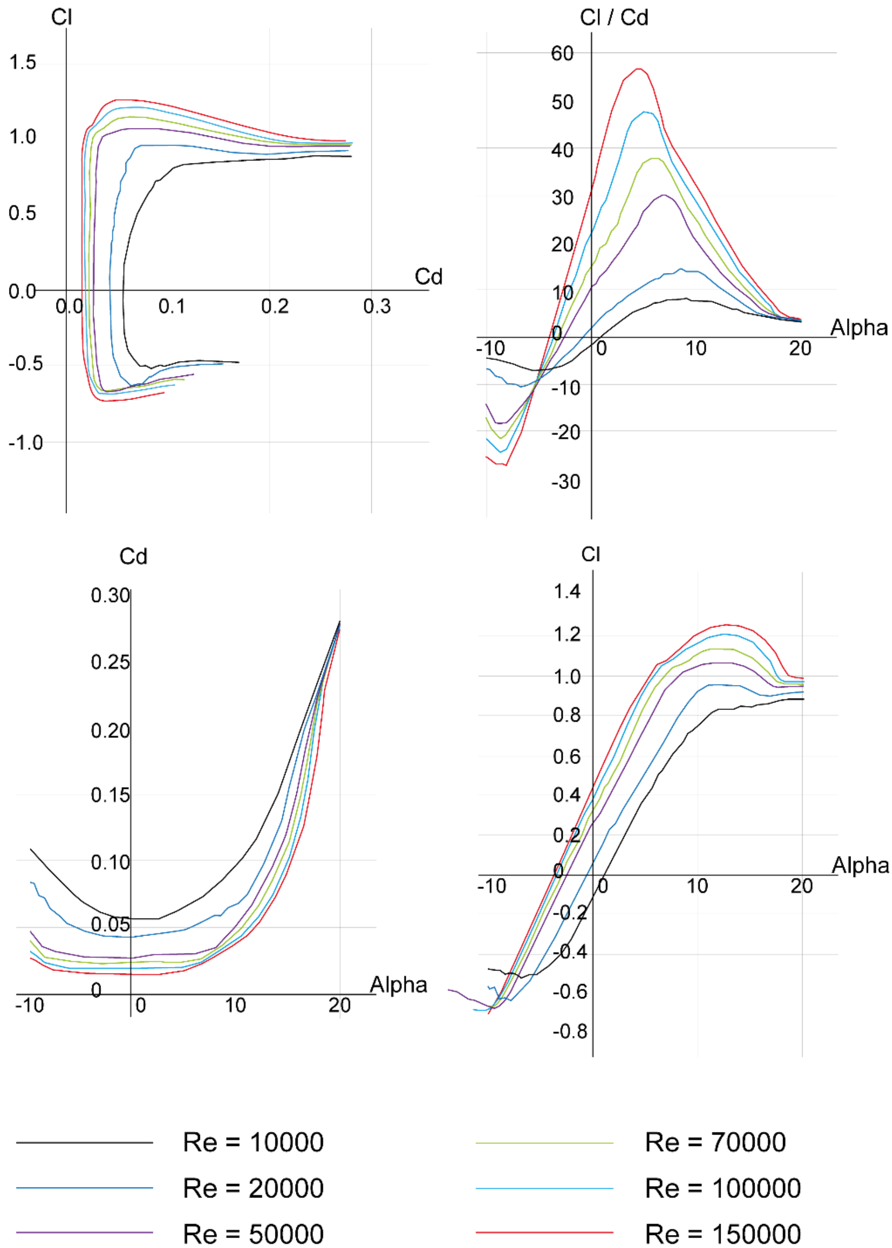

Figure 36 *Polar of the Eppler 818 profile extracted from Q-Blade*

The following table summerizes the chord linear distribution along the blade span:

Table 3 Chord Linear distribution along the blade span

N. sez.	r [m]	local solidity σ=cN/(2Rπ) [-]	chord [m]	r/R [-]	Twist [°]
1	0.000	0.14	0.030	0.000	45.75
2	0.008	0.12	0.029	0.095	41.25
3	0.017	0.12	0.028	0.200	36.22
4	0.025	0.11	0.027	0.300	30.28
5	0.034	0.11	0.026	0.400	23.96
6	0.042	0.11	0.025	0.500	18.60
7	0.050	0.10	0.024	0.600	14.79
8	0.059	0.10	0.022	0.700	11.98
9	0.067	0.09	0.021	0.798	9.00
10	0.076	0.08	0.020	0.899	8.50
11	0.084	0.08	0.018	1.000	8.00

This table is the result of some modifications applied to the first calculation. This is due to the fact that the flow is not bidimensional, so the ϕ is reduced at the initial section along the blade span. Morever, this is a semplification that allows to define a chord distribution easily, as in **Figure 37**.

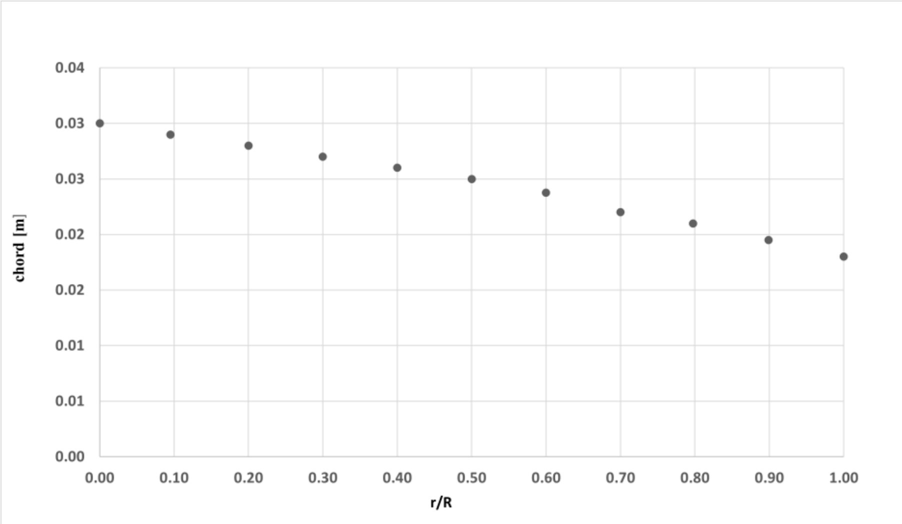

Figure 37 *Linear distribution of chord length along the blade span*

Figure 38 *Profile discretization along the blade span*

The pressure distribution on the Eppler818 chosen, is shown in **Figure 39** according to the Reynolds Number variation.

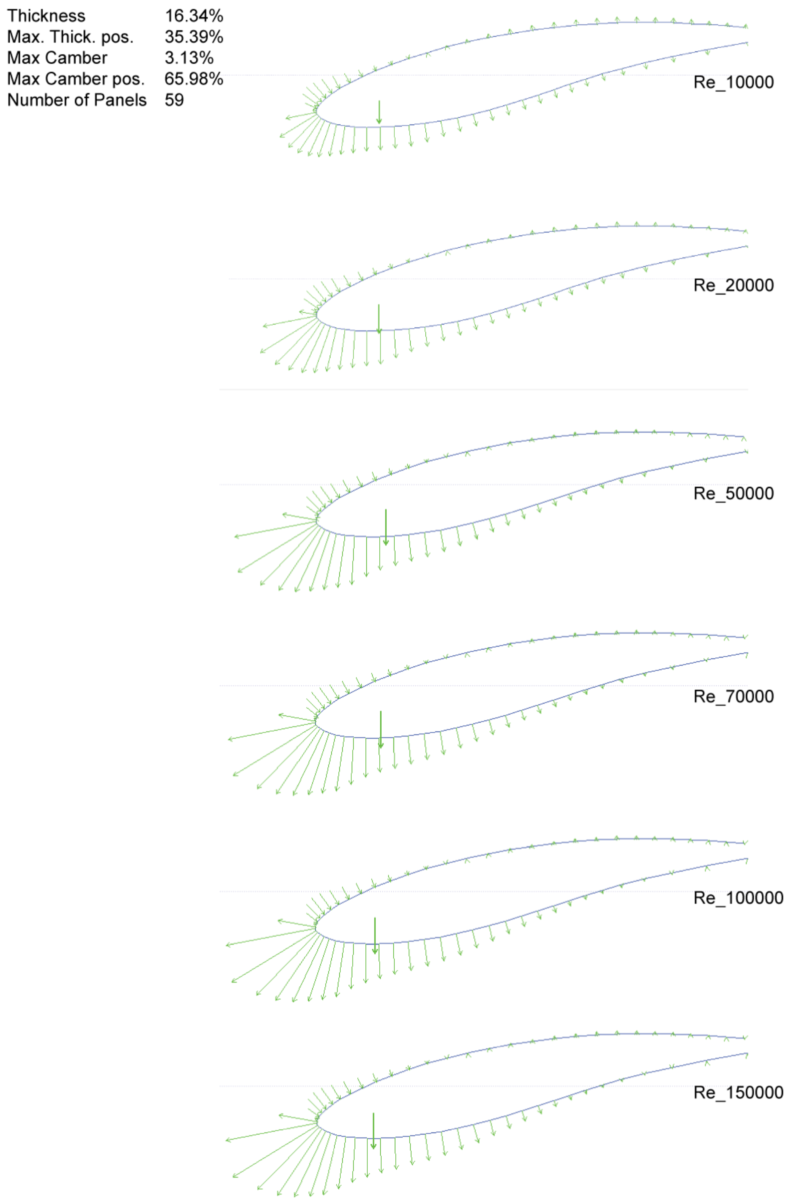

Figure 39 *Pressure distribution according to the Reynolds Number variation extracted from Q-Blade*

Notice that the chord increases from tip towards roots [73], the twist angle is also larger near the roots compared to the tip. At this stage, once the blade is geometrized in all its length, it was necessary to design the linker piece between the Eppler shape and the circular one, as shown in **Figure 40**.

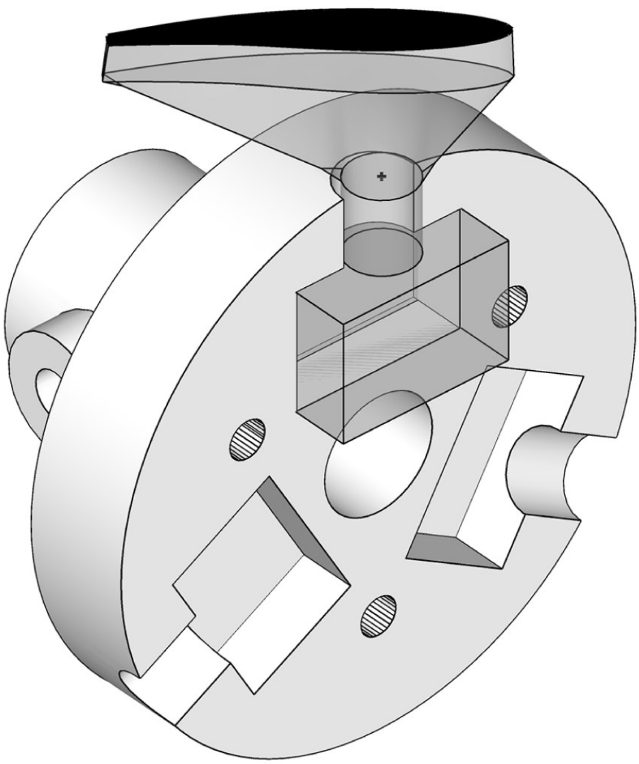

Figure 40 *Detail on Square Locked System inside the Turbine Hub*

This step passes from designing this specific piece, through an auxiliary CAD software, that for the specific case is Solid Works [74]. Finally, to proceed with the printing of the 3D prototype, it was necessary to extract the blade shape through the hydrofoil coordinates extracted from Q-Blade. Then, with a spline function, it was possible to design the entire blade as in **Figure 41**.

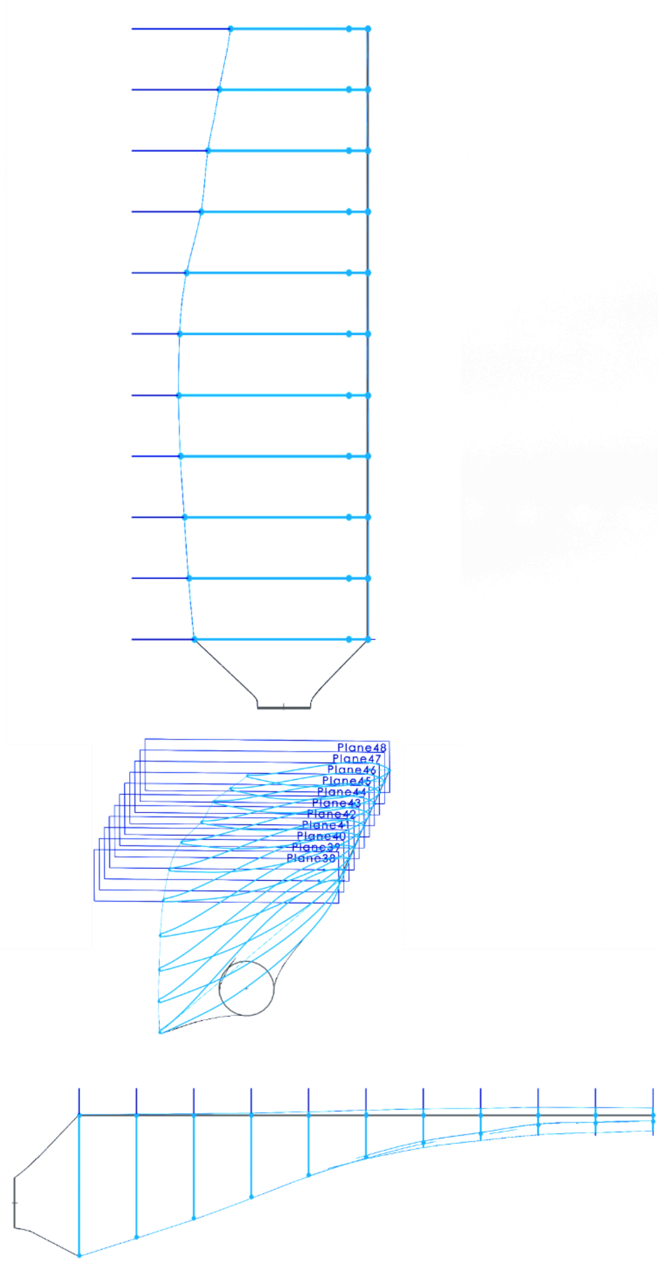

Figure 41 *CAD Project on SolidWorks 2019 blade design*

3.4. Preliminary 2D CFD Model

The first step towards the preliminary implementation of the CFD model, developed in ANSYS FLUENT environment [75], is the implementation of an adequate Fluid Domain, which may correctly interpretate the Actuator Disk Theory (ADT), described in the above section **2.2.1**.

This Actuator Disk Model has the advantage of requiring a reduced mesh density compared to other available numerical models for CFD simulations, which is helpful for preliminary analyses. This is computationally less expensive and is utilized to simulate the Blockage Effects [59].

Namely, numerically is much easier to change the ratio between the area of the rotor and the domain area, in which the turbine is fitted. The first attempt was realizing through a 2D asymmetric domain, extended for 6 Diameters upstream and 15 Diameters downstream of the Disk.

In this study, the equation of LMADT was solved simultaneously with Navier-Stokes Equations by the Semi-Implicit Method for Pressure-Linked Equations (SIMPLE) algorithm, which is a suitable Steady-State solver for incompressible flow modeling.

A standard two-equations k-ε model with turbulent kinetic energy 0.8, turbulent dissipation rate 0.8 and turbulent viscosity equal to 1 is used, to model the turbulent state.

The Finite Volume Method (FVM) using the Upwind Scheme is employed to discretize the equations, and the iterations will stop when the residuals of each equation reach 10E-05 value.

According to the theory, in the CFD Model the Disk represented the turbine and is conceptualized as a circle surface with length equals to the turbine diameter of D = 0.24 m, with a zero thickness, which extracts energy from the flow by applying an increasing pressure drop.

The pressure drops at which the disk reaches the maximum Power Coefficient is strictly related to the Thrust Coefficient. The latter is the product between the Pressure Drop applied on the Disk, and its Area.

In this CFD model it was attempted to find the value of the Axial Induction Factor a at which the maximum Power Coefficient is reached, increasing the pressure drop applied on the disk. According to the Betz theory, the power extraction maximizes when the axial induction factor equals a = 1/3, in an open flow condition.

In the CFD model, it is reproduced a confined domain with walls that get closer and closer to the disk surface as in **Figure 42**, to investigate numerically how the wall presence and velocity inlet condition influence the Power extraction. In this regard, the effect of three kinds of 2D domains with height of 12D, 6D, and 3D, was tested.

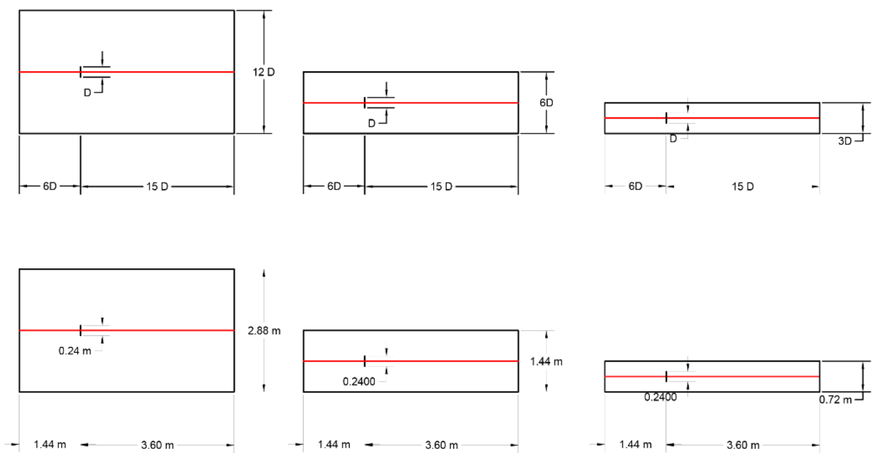

Figure 42 *Domain Considered in the 2D preliminary CFD Model*

Therefore, we considered a Blockage of 1% in the first domain considering the wall sufficiently far from the disk, then of 3% and eventually of 11%, in the third case.

The Blockage is computed as the ratio between the Circular Disk Area and the domain area which decreases according to the external domain diameter considered for the three cases (12D, 6D and 3D):

$$Br = \frac{(\pi D^2)/4}{(\pi(12D)^2)/4} \tag{94}$$

However, since the problem is axial-symmetrical, to limit the computational times, it has been considered only one-half of the entire domain, saving simulation times.

Assuming an inlet velocity range compatible with the experimental constraints of the future experimental set-up in which the prototype will be tested, a boundary condition of constant velocity inlet from 0.43 to 0.68 m/s was set in the model. In more critical details, for the simulation three inlet velocities 0.43, 0.51 and 0.68 m/s included in the range were selected, just to understand the combined effect of both wall approximation and velocity inlet. These will be the same velocity range tested in the experiments, described in the following Chapter IV.

The value of ΔP is computed from the calculation sequence proposed in the Appendix 1. This Pressure Drop value corresponds to the value maximizing the Power Coefficient analytically. In this regard, it was possible to compare the analytical solution with the CFD model implemented.

3.4.1. Boundary conditions

The domain has a length of 6D upstream of the fun, which simulate the Disk, and 15D downstream, enough to contain the effect in the wake downstream, as shown in **Figure 43**.

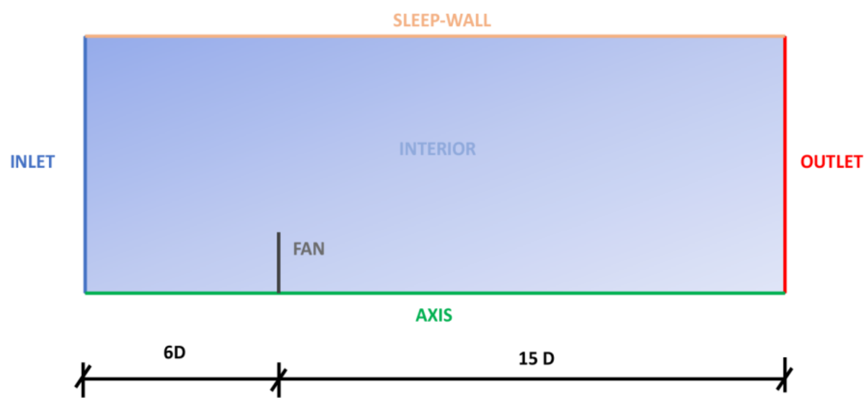

Figure 43 *Boundary Conditions*

The Disk is conceptualized through a fan boundary condition. The fan model is a lumped parameter model that can be used to determine the impact of a fan with known characteristics upon some larger flow fields. The fan boundary type allows you to input an empirical fan curve which governs the relationship between head (pressure rise) and flow rate (velocity) across a fan element. Specifying radial and tangential components of the fan swirl velocity is also possible. The fan model does not accurately describe a detailed flow through the fan blades. Instead, it predicts the amount of flow through the fan. A fan is infinitely thin, and the discontinuous pressure rise across it is specified as a function of the velocity through the fan. The relationship may be a constant, a polynomial, a piecewise-linear, a piecewise-polynomial function, or a user-defined function. In this specific case, a constant value gradually increased was set, whereas a constant gauge pressure of 0 Pa was set at the outlet and sleep-wall with no shear stress rate was set to define the additional boundary wall of the domain concerning the unbounded case. The inner part of domain is defined as an interior boundary condition. And, as mentioned above, the problem is axial-symmetrical, so only half of the domain can be regarded as.

3.4.2. Mesh independency

Two different kinds of mesh were assessed, a structural and therahedral one. However, due to the regular geometry of the computational domain since they gives similar results, it was prefered an exaedral mesh.

Before running the model, a sensitivity analysis on the mesh size is a pivotal step, based on the methodology proposed by [76].

In this case only two levels of mesh were considered, a Medium and Coarse, with 22742 and 7727 number of elements, respectively, as shown in **Figure 44**:

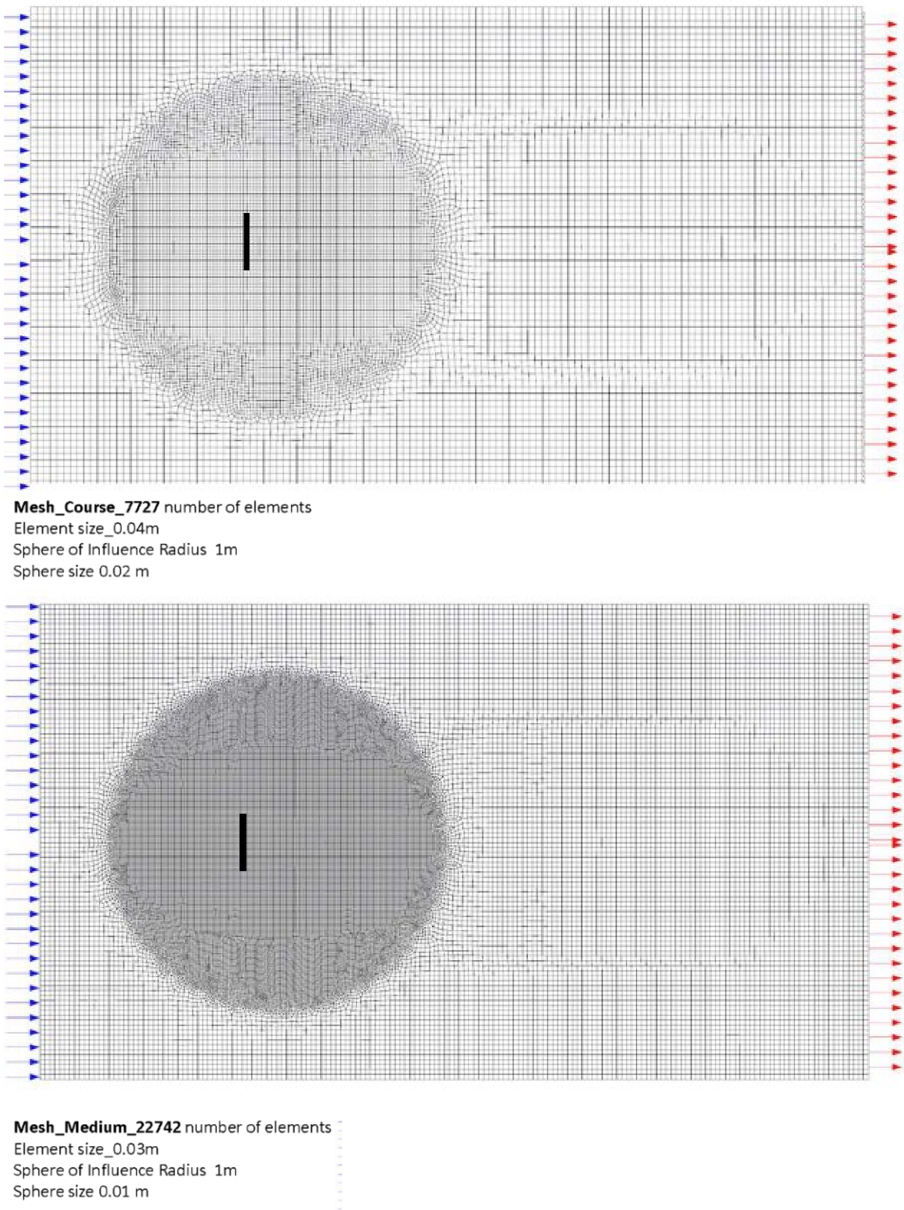

Figure 44 *Comparison between larger and denser mesh*

The mesh resolution tested were selected to accomplish Mesh Convergence. The procedure was based on the calculation of Grid Convergence Index (GCI), which can be defined as:

$$GCI^{21} = \frac{1.25e_a^{21}}{r_{21}-1} \qquad (95)$$

Where e_a^{21} is the approximate relative error [-] and r_{21} is the refinment factor [-], calculated respectively as:

$$e_a^{21} = \left|\frac{\phi_1-\phi_2}{\phi_1}\right| \qquad (96)$$

$$r = h_{coarse}/h_{fine} \qquad (97)$$

where h define the rappresentative grid size [m], and depending on whether the problem is 2D or 3D, calculation can be estimated as:

$$h = \frac{1}{N}\left[\sum_{i=1}^{N}(\Delta A_i)\right]^{1/2} \qquad (98)$$

$$h = \frac{1}{N}\left[\sum_{i=1}^{N}(\Delta V_i)\right]^{1/3} \qquad (99)$$

where ΔA and ΔV are the area and the volume of the *i*th cell [m^2] [m^3], respectively. *N* is the number of cells used for the computations. The mesh sizes selected respected the reccomended value of $r \geq 1/3$. In greater detail, the results obtained from the two levels of meshes analysed were compared by assessing the avarage velocity value ϕ computed on the fan in the operative condition which concide with pressure value that maximize the power extracts. At this reguard, it was chosen a velocity inlet value of 0.43 m/s and a Pressure drop applied on the fan of 84 Pa. The results of this sensitivity analysis are summerized in **Table 4**.

Table 4 2D Model Sensitivity analysis

Fan Velocity with ΔP applied of 84 Pa		
N_1,N_2	22742	7727
r21	1.87	
φ_1	0.2960	
φ_2	0.2895	
φ_{21ext}	0.30	
ea_{21}	2.18%	
φ_{21ext}	2.45%	
GCI $_{fine}$	3.14%	

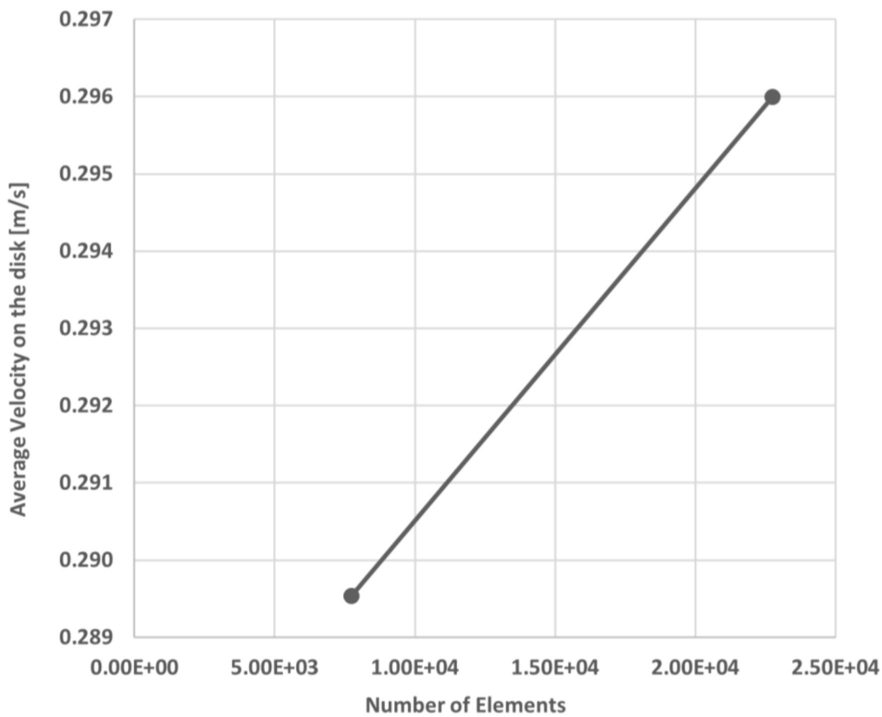

Figure 45 *Sensitivity analysis*

There is a very few difference between the velocity computed on fan section for both meshes considered, for velocity of 0.43 m/s, as shown in **Figure 45.**

A GCI between Mesh 1 and Mesh 2 of 3.14% was assumed as acceptable. Therefore, the Medium Mesh was chosen for simultations.

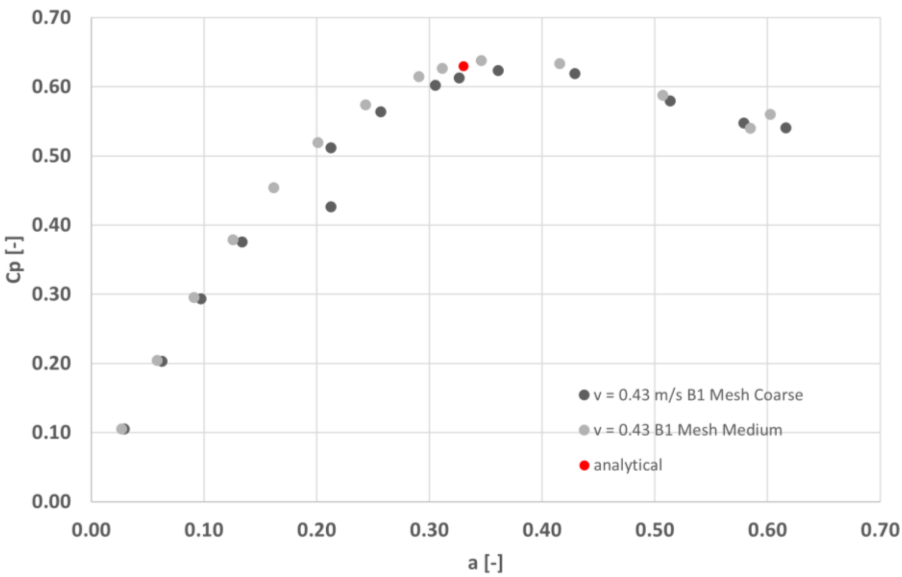

Figure 46 *Cp-a curves extracted from both Mesh considered.*

Figure 46 confirms that the refined mesh returns better results concerning the corresponding C_p value analitically computed. Moreover, the coarse mesh presents an outlier on the extracted performance curve and slightly overestimates the maximum C_p concerning the analytical model.

Then, to analyze the Blockage Effect on Power Production, the mesh was tighten nearby the fan through a Sphere of Influence, which center is located in the global domain of the geometrical reference and has a decreasing radius and size, according to the reduction of the global area generated by the wall approximation to the boundary, as shown in **Figure 47.**

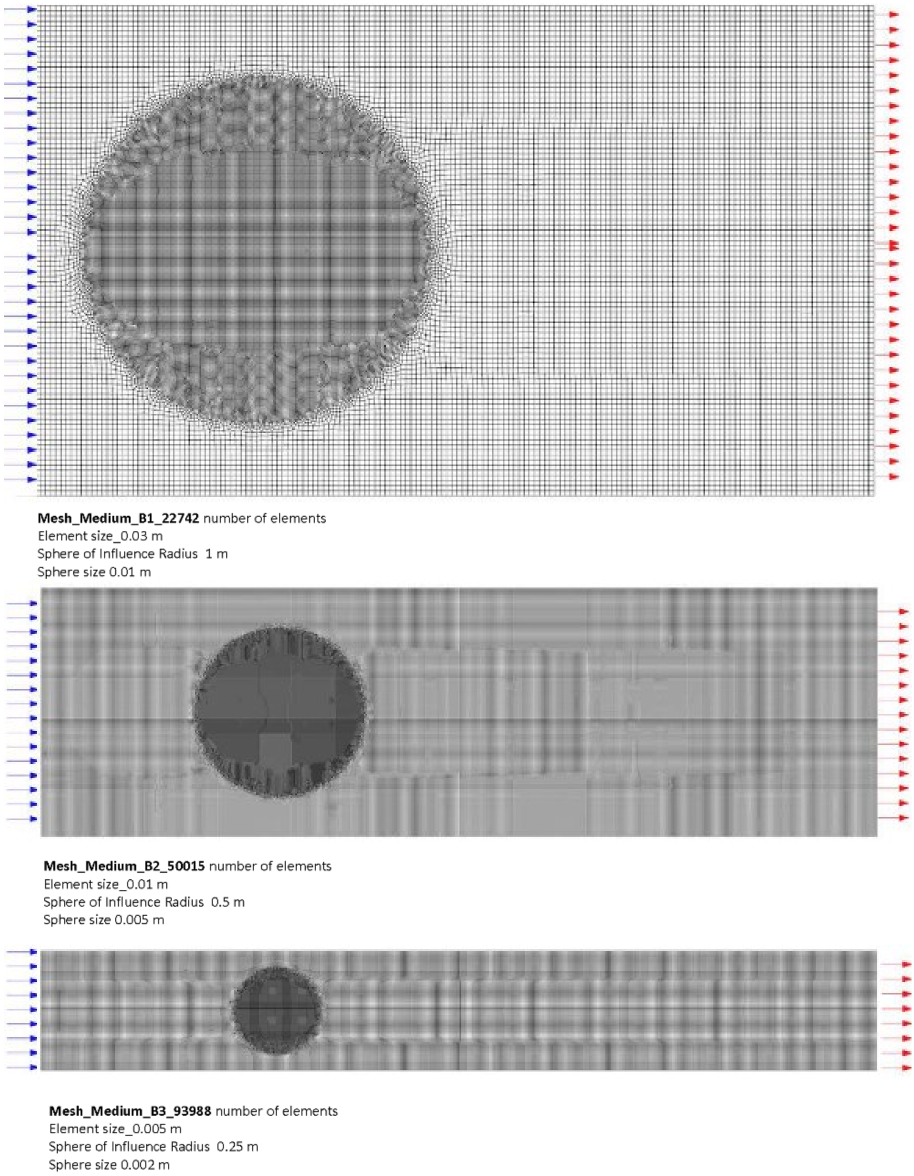

Figure 47 *Number of mesh elements at increasing the Blockage.*

This means that a more detailed mesh should be considered according the the walls approximation, by increasing the total number of elements aimed at assuring a proper comparison.

3.4.3. CFD Preliminary results

In **Figure 48** the curves extracted for the three values of Blockage analysed are plotted, in terms of $C_P(a)$ and $P(\Delta P)$. The axial induction factor measures the decrease in velocity at the fan section due to a rising pressure applied to the fan.

The Maximum Power Point (MPP) predicted by the Analitical Model take as reference, was compared to the Maximum Power Point obtained numerically, through the 2D CFD Model implemented.

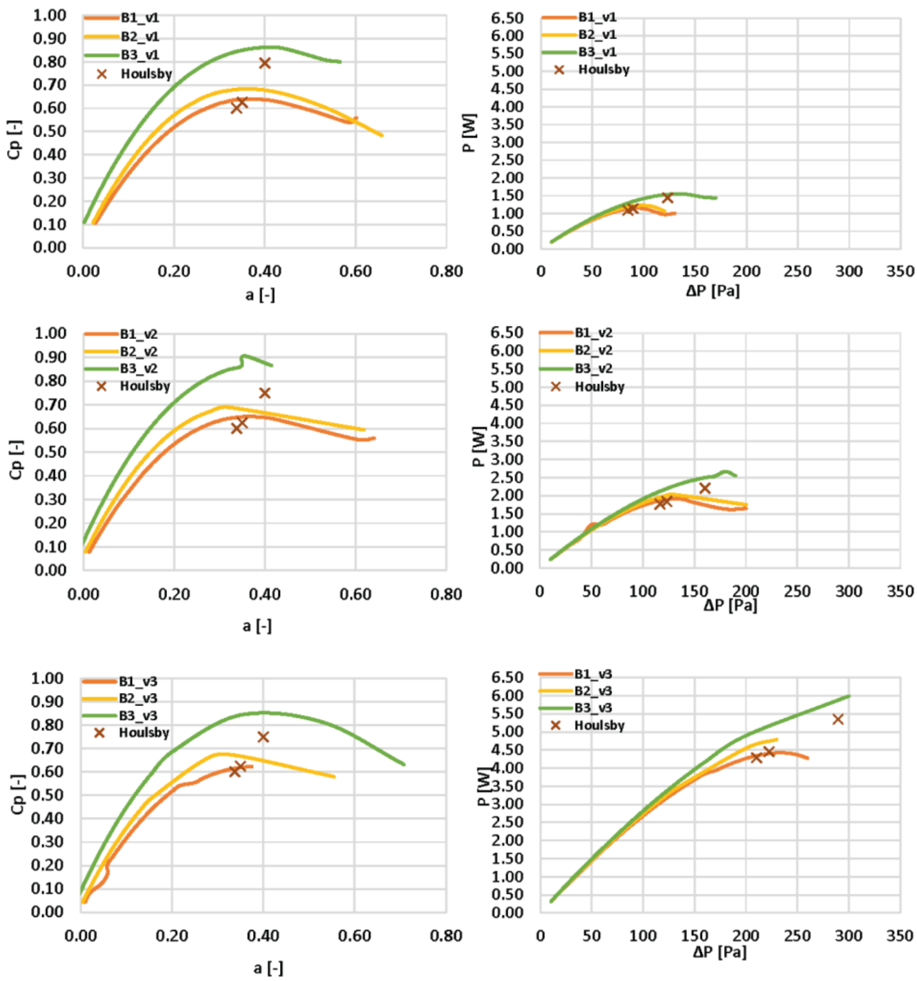

Figure 48 Assessment of Performance Curves extracted numerically, with Pick Power Point predicted analytically from the Calculation Sequence proposed by Houlsby (Appendix A)

We can observe a good agreement between the numerical results obtained and the analytical computed by equation (61), marked with red crosses. This point is reched when the axial induction factor on Disk section ranging from 34% to 40%, which means that the velocity measured on the disk section is approximately 1/3 of the velocity at inlet; so the axial indution factor increases at the Blockage rising.

However, the analitical model slightly underestimates the maximum Power Point and C_p compared to the results of the numerical model.

This is because the analytical calculation understimates the disspation effect due to turbulence against the numerical model that computes it via two separates and indipendently transport equations, according to the k-ε turbolence model choosen for simulations.

Figure 49 summerizes the relative error with respect to the numerical model for all the anlysed cases for P, C_p, T and C_t, respectively:

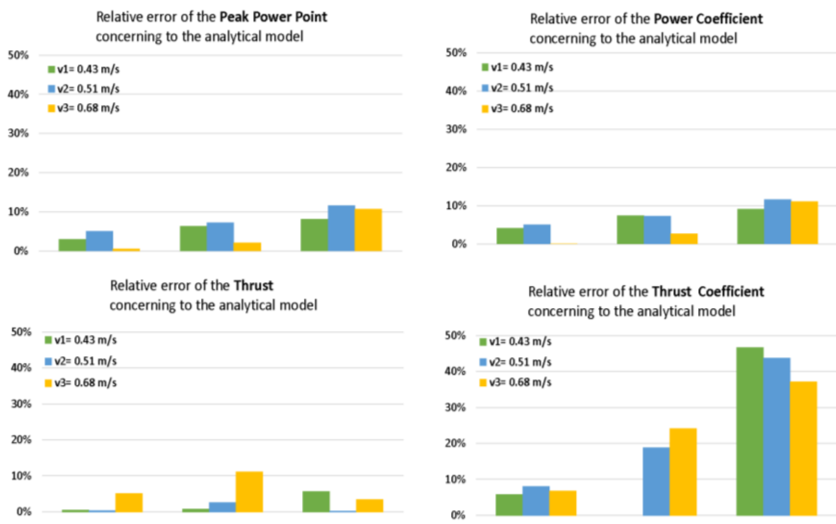

Figure 49 *Relative error concerning the analytical model on P, C_p, T, C_t at increasing the Blockage.*

The relative error on each computed quantity increases in the cases of the highest Blockage and velocity inlet. Even though, in absolute terms, P, C_p, and C_t result smaller in the lowest analysed veocity.

Moreover, it is evident how for the same considered velocity value (see **Figure 48**), the effect of flow compression due to the approximation of wall domain to the disk, and so due to the increment in Blockage, produces a consequent increment in Power extracted from 1.6 to 6 W and this is observed for Peak Power Coefficient, as well.

It is worth noting that the Peak Power Coefficient is shifted up according to the increase in water velocity inlet simulated. However, the Blockage effect predominates on water velocity inlet in obtaining more outstanding C_p as shown in **Figure 50**.

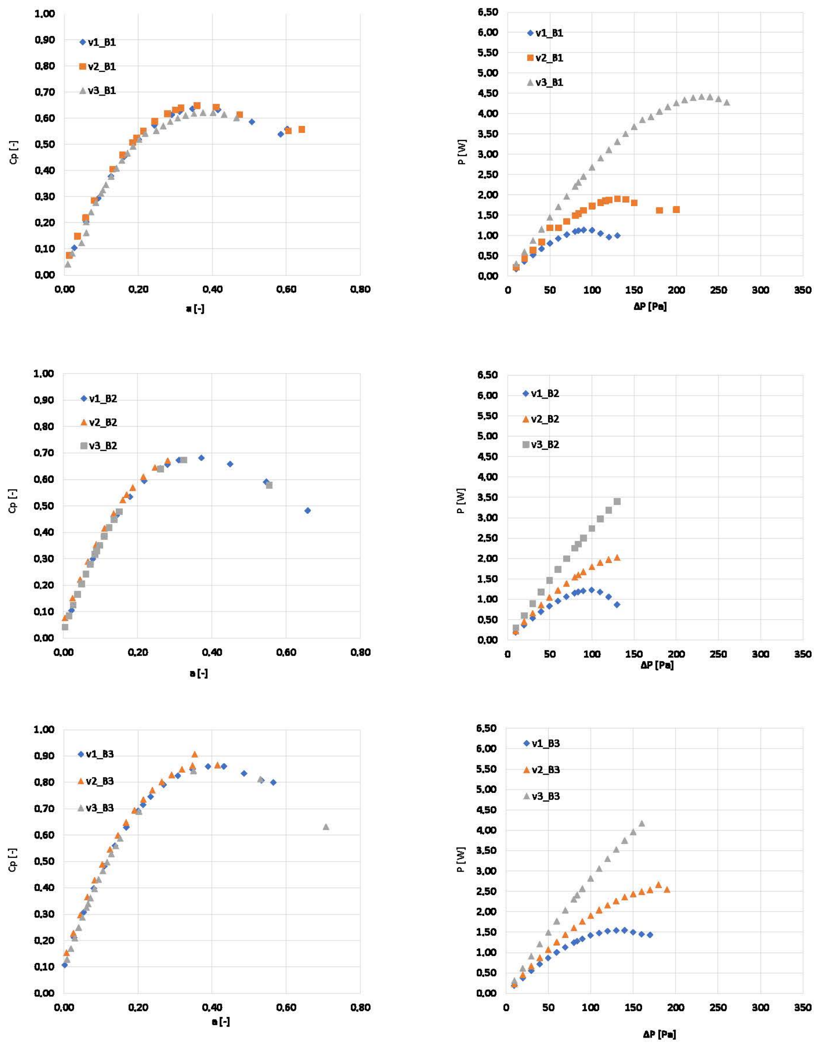

Figure 50 *Comparison of performance curves with the same Blockage at velocity increasing.*

Therefore, a slight variation in C_p is appreciable in **Figure 50** according to the increasing inlet velocity considered in the simulations. Nevertheless, the Power Curve on ΔP applied to the Disk is observed shifted up due to increasing velocity. Therefore, putting toghether all the curves extracted numerically as in **Figure 51**, is clear how the Blockage affects the turbine performance more than velocity.

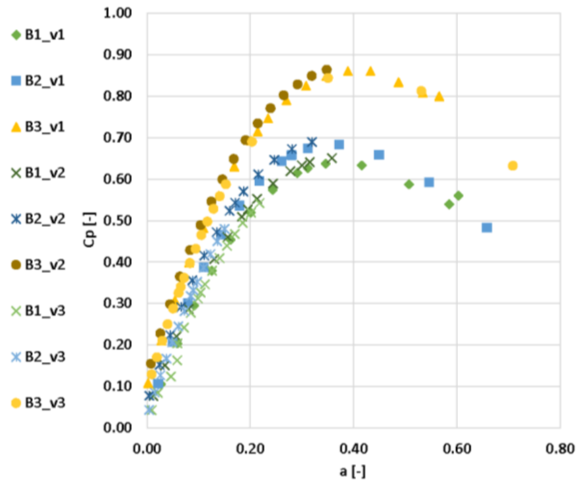

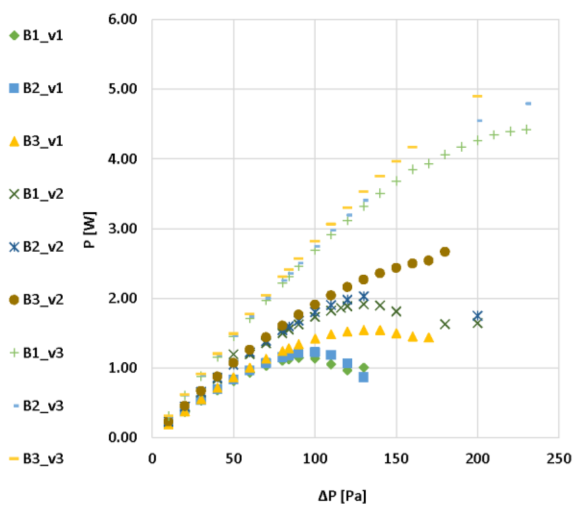

Figure 51 *Predominant effect of Blockage on velocity*

Furthermore, a good agrement is achieved by comparing the analytical and numerical Maximum Power Point (MPP) computed increasing the inlet velocity, as shown in **Figure 52**.

An increasing trend of MPP is visible according to the velocity increase.

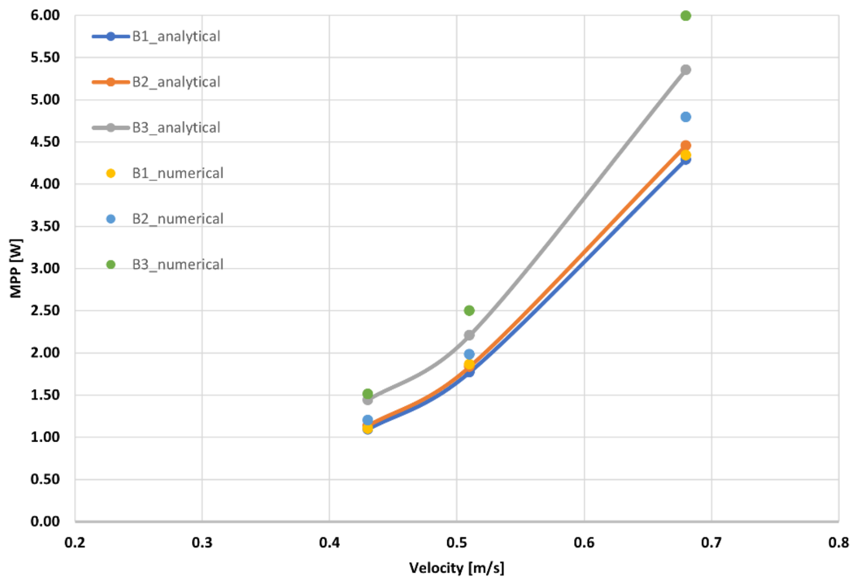

Figure 52 MPP on velocity inlet

Moreover, to better understand the results extracted from the CFD Model, the velocity and the pressure profiles are plotted along the axis boundary condition (see **section 3.4.1.**), which corresponds to the flow axis direction. Similarly, pressure and velocity behaviours along the flux tube axis are given in **Figure 53**.

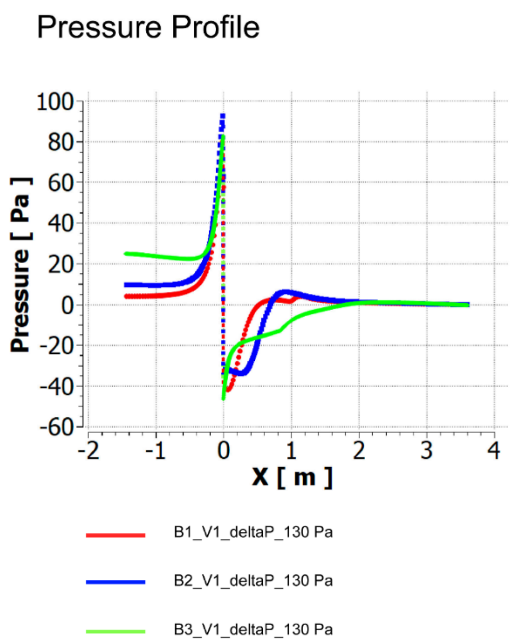

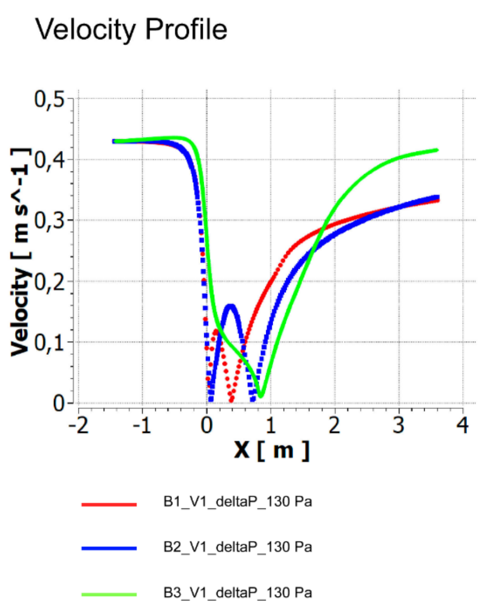

Figure 53 *Velocity and Pressure Profile along the axis of flux tube*

Since we have considered a k-ε turbulance model, with a priori imposed boundary conditions of velocity inlet and pressure outlet, we can observe that the model response to the increment in Blockage is reflected in velocity and pressure increase at outlet and inlet sections, respectively.

More generally, in the Disk section a velocity decrease provoked by the flux extraction of kinetic part of the energy is observed. On the other hand, in the mixed zone downstream of the Disk, the turbulence dissipation due to the produced swirl generates a slowly recovery area, which increases at the Blockage rising.

The velocity is then totally recovered after approximately 4D downstream, and reaches quite the same velocity inlet value at the maximum Blockage investigated. In **Figures 54** and **55** we can observe the velocity and pressure contours, whereas in **Figure 56** the velocity streamlines are plotted for the three investigated Blockage cases.

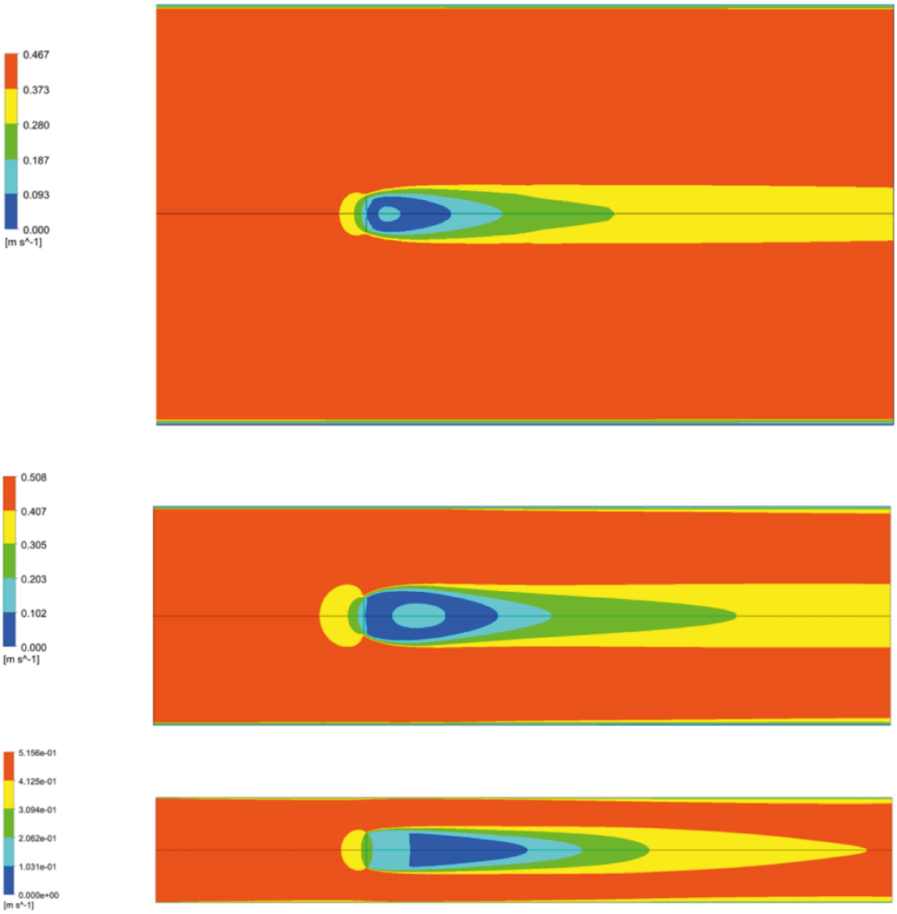

Figure 54 *Velocity contour in the three Blockage cases simulated, case: v_1_0.43 m/s and ΔP_130 Pa.*

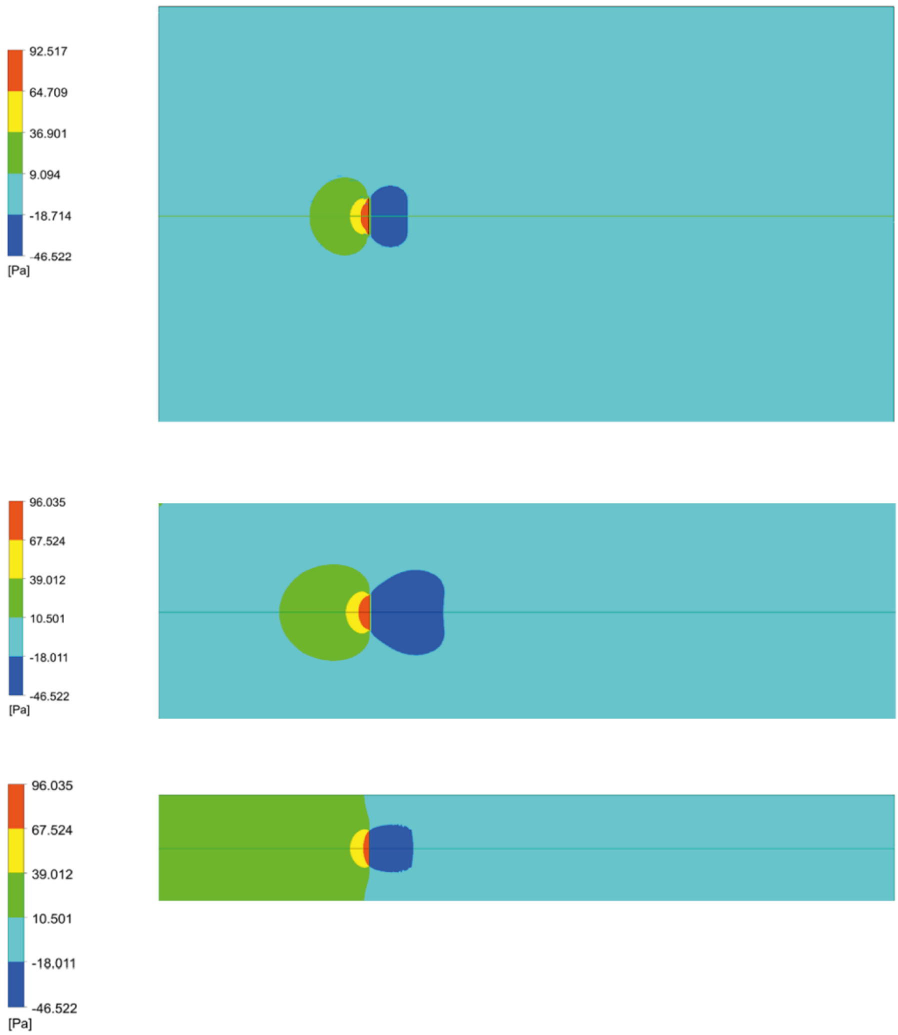

Figure 55 *Pressure contour in the three Blockage cases simulated case: v_1_0.43 m/s and ΔP_130 Pa.*

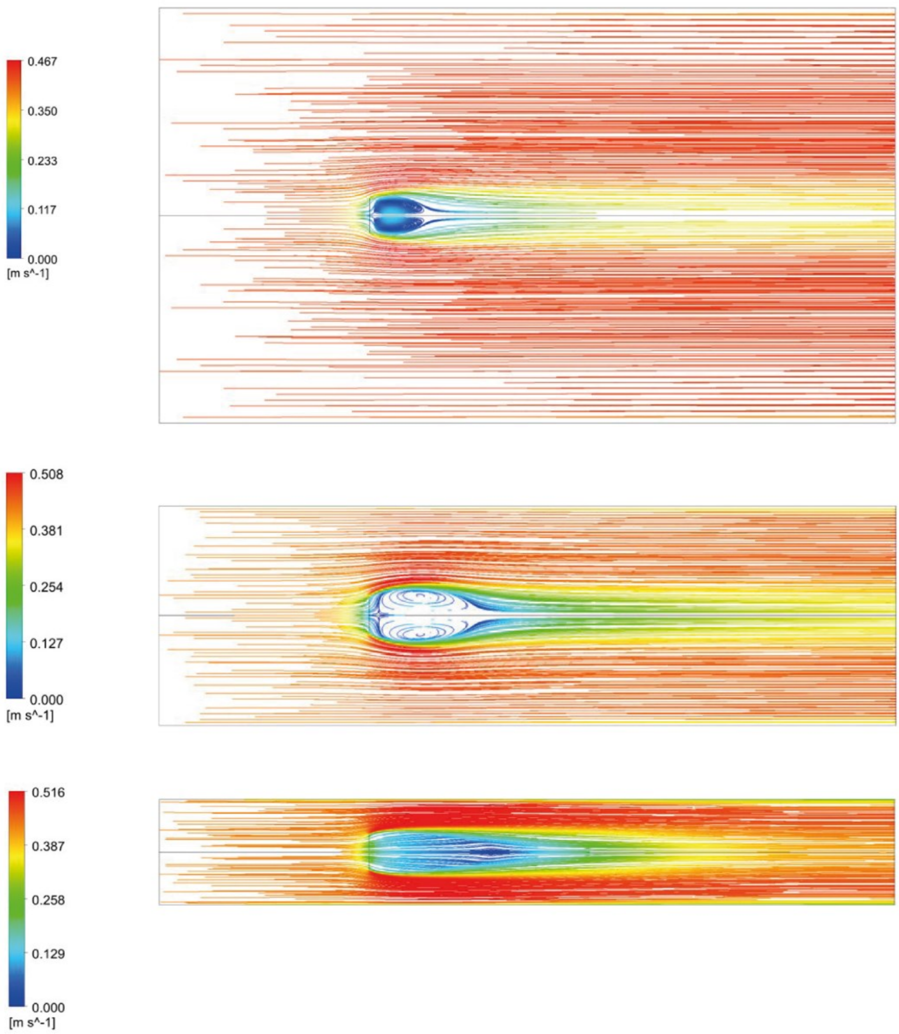

Figure 56 *Velocity Streamlines in the three Blockage cases simulated case: v_1_0.43 m/s and ΔP_130 Pa.*

In conclusion, expecially in **Figure 56**, the mixed zone is marked and the flux tube shape is detectable.

To respect the continuity equation the reduction of the upstream velocity upstream should entail the streamline divergence for the Disk section and, consequently, a more significant swepped area producing the typical flux tube shape.

It is also noticed that the Blockage produces a flow velocity increment in the by-pass zone, namely in the region between the walls and the Disk. This is due to the flow compression and the related velocity increase. On the other hand, there is a divergence from the theoretical Betz Limit in unconfined condition, as much as evident as the walls approximation for the Disk.

Furthermore, the behaviour within the mixing zone, produced by a different configuration of the downstream vortices, affects the velocity recovery that can occur at as many diameters downstream of the Disk as the Blockage is considered more significant.

Chapter IV

Experimental Investigation of HAHWT

4.1. Description of the 3D printing process

The turbine model has been designed using a 3D-CAD software and fabricated through the additive manufacturing technology using Polylactic Acid (PLA). As in **Figure 57** below, to realize the reviewed turbine prototype, a middle-size 3D printer, Prusa I3 model, with a plate of 20 x 20 cm and height of 20 cm, has been used. Furthermore, the employed nozzle has a dimension of 0.4 mm.

Figure 57 *3D printer used model Prusa I3*

The use of 3D printers has been even more overspread in the last decades because they allow quick and economical realizing prototypes in both laboratories and on a 1:1 scale. Moreover, thanks to specialized software, which allows setting all the guidelines' parameters, it is possible to design the accuracy of the printed piece of prototype. These parameters are numerous, such as the nozzle temperature, which is strictly dependent on the employed material and its fusion temperature. Moreover, the layer height, the typology of support necessary to realize no regular pieces, the "travel speed" (the mutual speed between the plate and nozzle), or the infill typology and, its density or distance are all parameters that should be defined according to the typology of the piece to print.

This means that many aspects should be evaluated since they affect the printing accuracy, whatever piece of a prototype is considered. Therefore, it is possible to set up all the printing parameters in advance, according to recommended indications on the type of piece to be printed and based on user experience. However, the more specific the CAD project, the more effective the results.

Specifically, for the analyzed prototype, the main characteristics are:

- Print Speed: 50 mm/s
- Infill Speed: 50 mm/s
- Wall Speed: 25 mm/s
- Travel Speed: 120 mm/s
- Initial layer Print speed: 25 mm/s
- Initial layer Travel speed: 60 mm/s
- Print acceleration: 1750 mm/s^2
- Printing temperature: 200 °C
- Build Plate Temperature: 55 °C
- Support Pattern: Zig Zag

The chosen material is High-Density Polylactic Acid, also known as PLA-HD, with high strength and flexibility. In addition, this material has been selected for its excellent durability in a wet environment. The table below summarizes the main mechanical features and the printer settings that the **WINKLE** manufacturer of employed filament in PLA-HD suggests [77].

Table 5 Mechanical PLA-HD characteristics

MECHANICAL PROPERTIES	AVERAGE VALUES	UNITS	STANDARDS
TENSILE MODULUS	3500	MPa	ISO 527-1
TENSILE STRENGTH	45	MPa	ISO 527-1
STRAIN AT YIELD	5% (max)		ISO 527-1
CHARPY NOTCHED IMPACT 23° C	≤5	KJ/m^2	ISO 179-1eA

PRINTING PROPERTIES	AVERAGE VALUES	UNITS	STANDARDS
NOZZLE TEMPERATURE	190-230	°C	
HOT BED TEMPERATURE	50-70	°C	
COOLING FAN	ON (100)	%	

The base technology of the 3D printer used for the creation of the studied prototype is the so-called Fused Deposition Modelling (FDM), as in **Figure 58**.

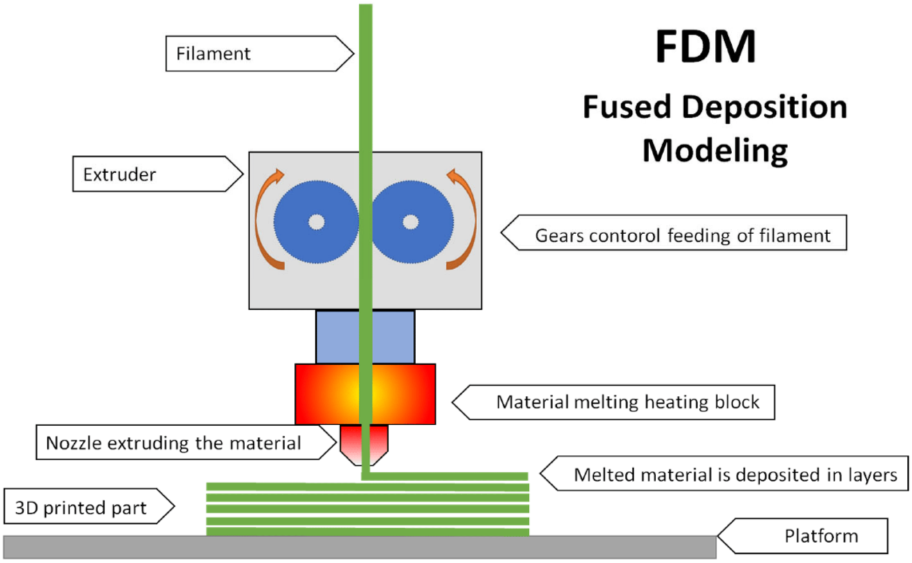

Figure 58 *Technology Fused Deposition Modeling*

The workflow of the productive process of FDM technology is described in the following conceptual scheme of **Figure 59**.

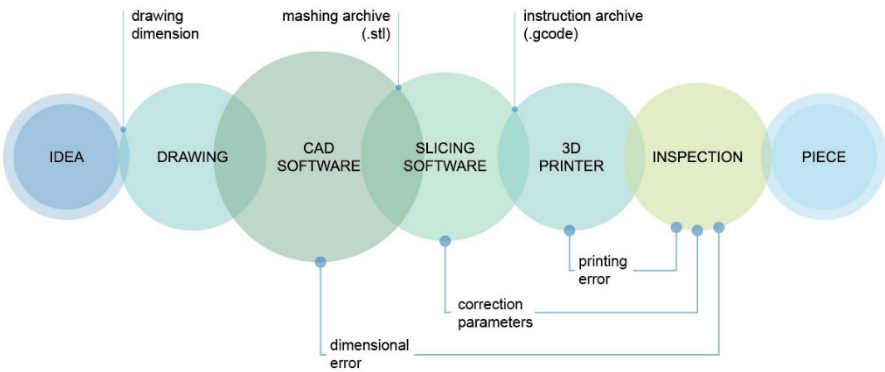

Figure 59 *Flow chart description of 3D printed prototype*

Therefore, the process begins by conceptualizing what you want to realize. Afterwards, it should consider designing the piece with suitable tolerance according to the nozzle dimension of the 3D printer involved. Then, it is necessary to change the archive in a meshing (**.STL)** file, and by specialized slicing software see **Figure 60**, all printing parameters are manageable. Finally, when the piece is printed, all the possible errors committed are helpful to correct the project and go back to print it again. In this specific case, **Ultimaker Cura** is the slicing software for the printing prototype. The prototype has been designed to assess several blade airfoil profiles and materials. This is why the blades could be climbed into the hub through a sort of pilar with a square locked system that perfectly fits between two plates where the edges are mounted, as in **Figure 61.**

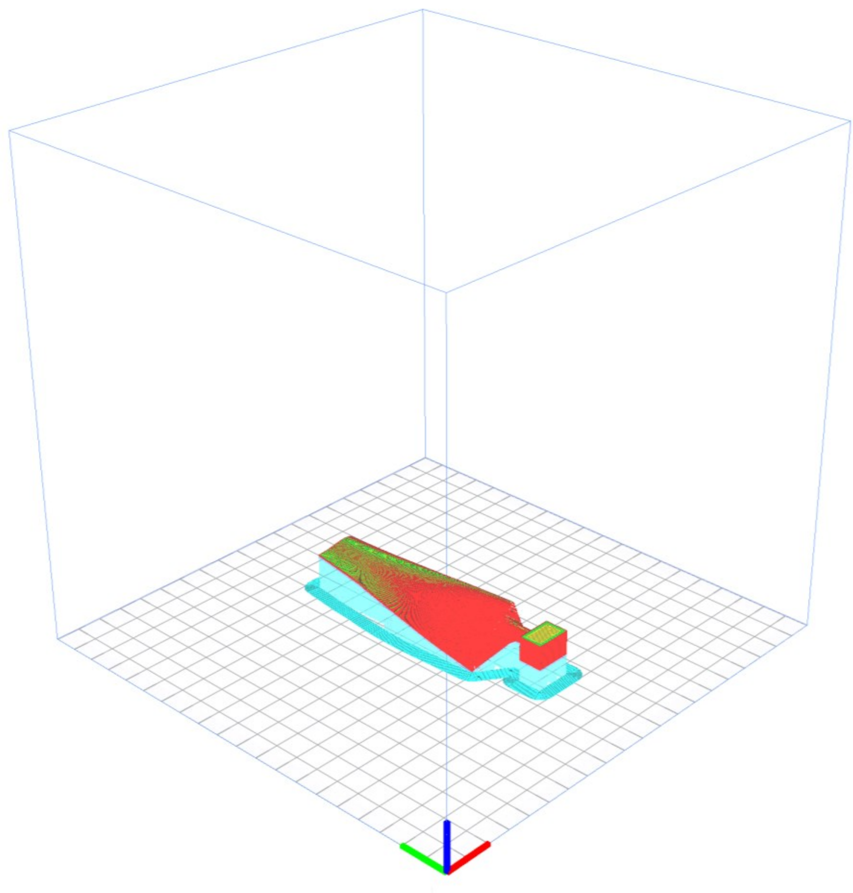

Figure 60 *Slicing software configuration*

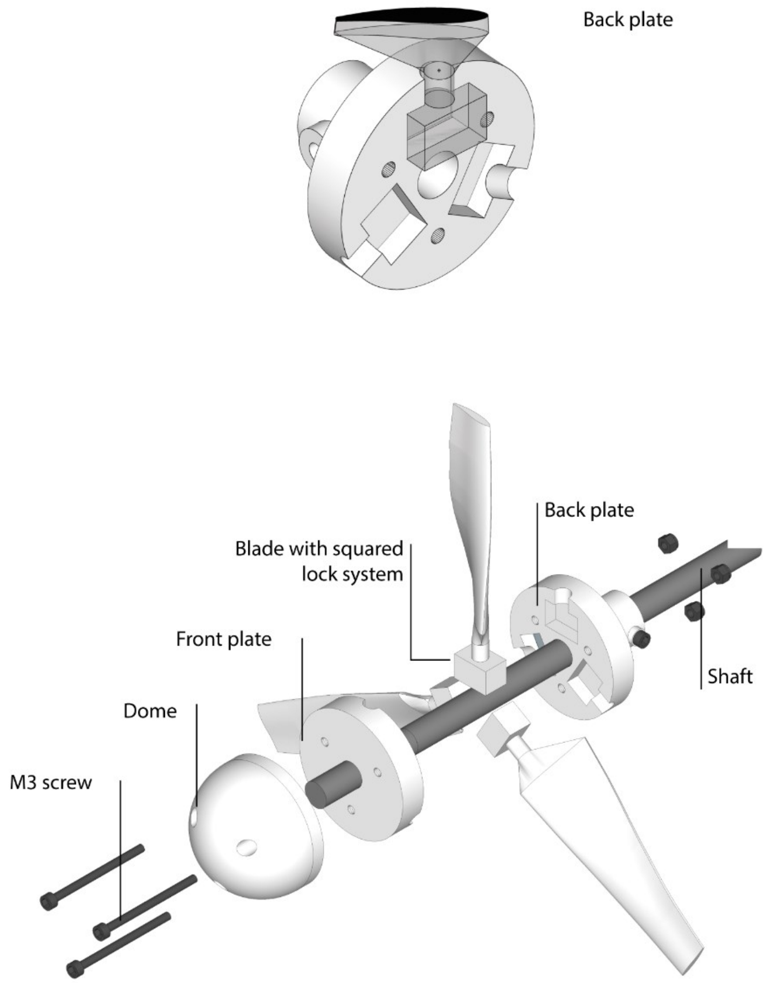

Figure 61 Detail on snap-fit blade

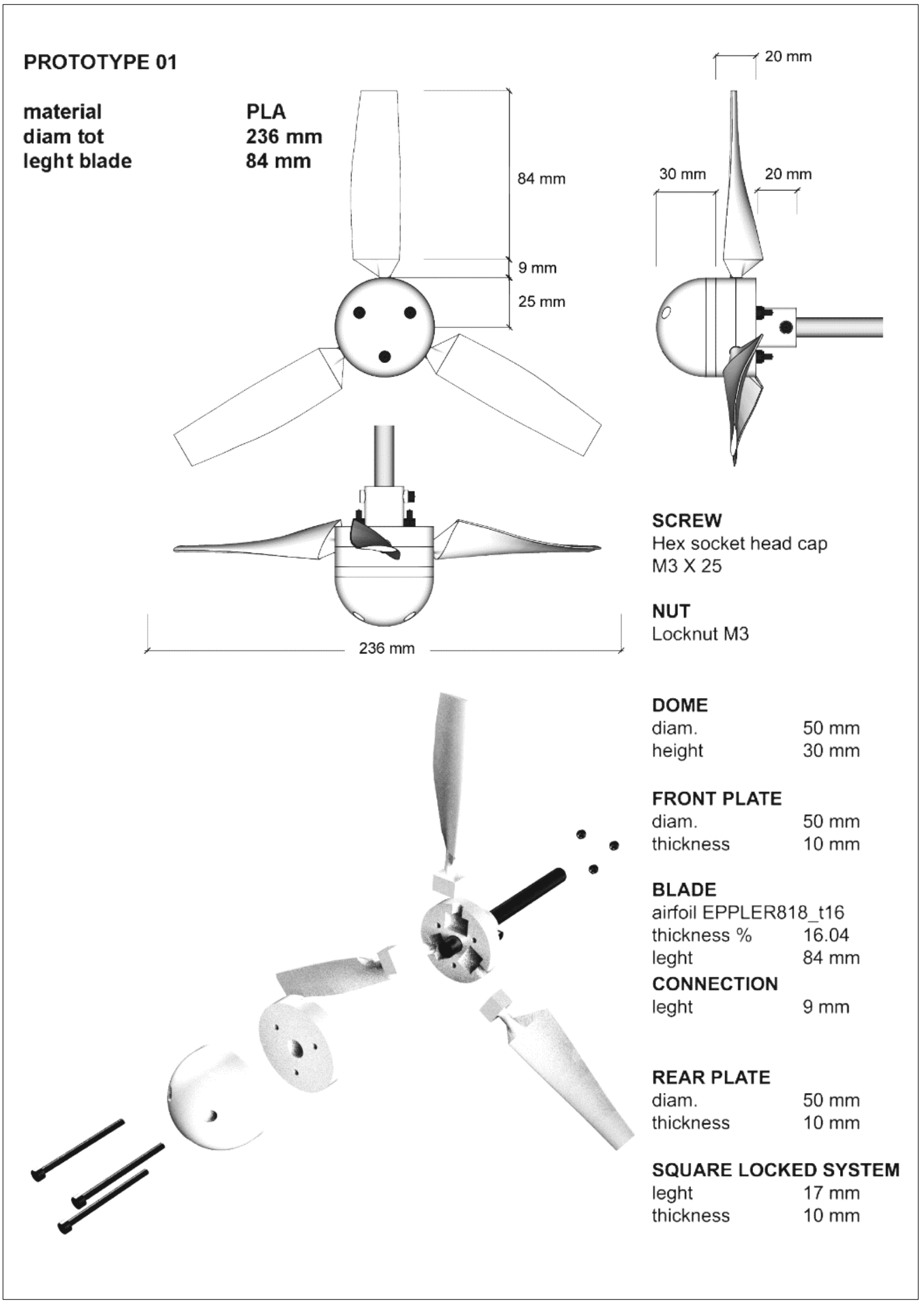

Figure 62 *Turbine Dimensions*

The adaptation draws inspiration from the research of [78]. The turbine rotates around a horizontal shaft of 10 mm diameter, which goes through the hub, the rear, and the front plate. Therefore, the pieces have fixed each other with three M3 screws. The Hydrofoil profile employed is an Eppler 818, which has been previously used in another research for a tidal current system named GEMSTAR [2] (Marin Electrical Generator, Sustainable Tethered Advanced Rotor) implemented by the research group of the Industrial Engineering Department of University of Naples Federico II lead by Prof. Domenico Coiro. The aspect which concerns the blade design has been developed in collaboration with this research group. SolidWorks 2019 is the 3D software used to design each piece separately, and then the CAD model is converted into an STL file to be printed. **Table 6** below summarizes the main geometric characteristics of the studied turbine, which is tested in a low-velocity scenario. At the same time, the **Figures 63**, **64** and **65** are captures of the printed prototype.

Table 6 Turbine features and velocity range tested.

Velocity range [m/s]	Blade Radius [m]	Chord length [m]	Hub radius [m]	Number of blades [m]
0.43 ÷ 0.68	0.084	0.03	0.025	3

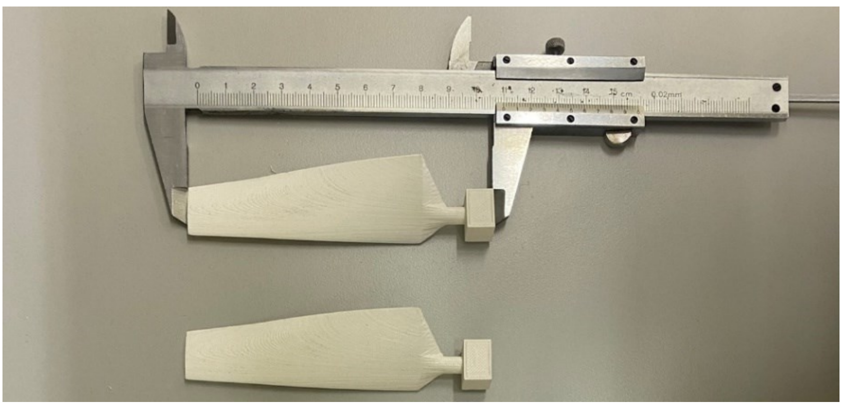

***Figure 63** Blade capture*

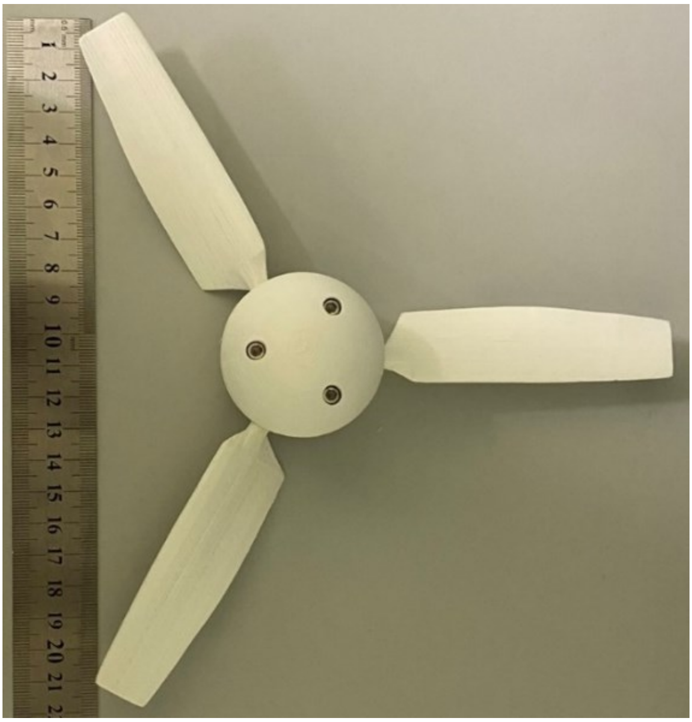

Figure 64 *Assembled prototype*

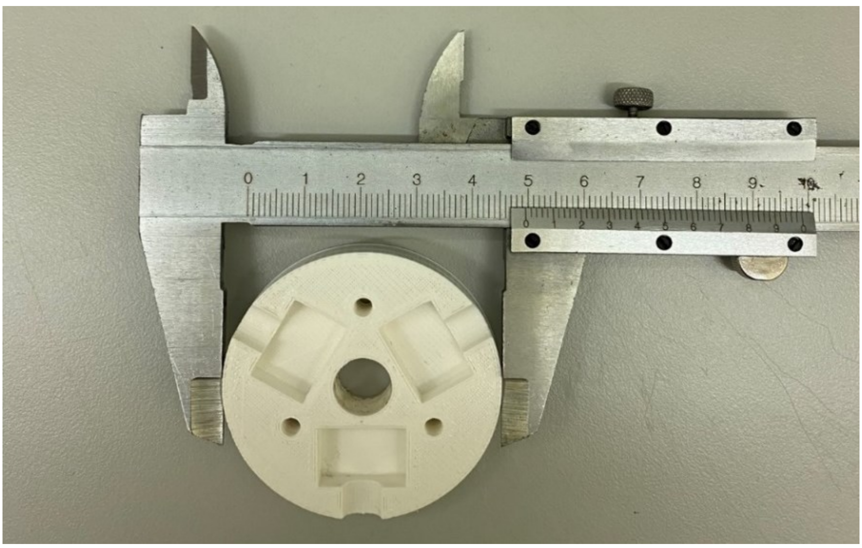

Figure 65 *Detail on hub front plate*

4.2. Laboratory set-up

The turbine prototype is inserted inside a recirculating water flume of 0.30 m in width, 0.55 m in height, and 3.5 m in length. The channel has transparent glass wall and is currently located at Polytechnic Engineering School of Mieres (Oviedo University, Spain) as in **Figure 66**.

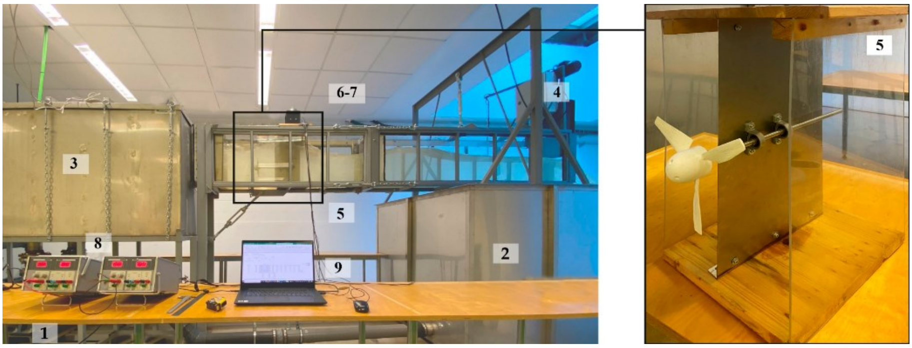

(a) *(b)*

Figure 66 *Laboratory set- up (a) wooden box with transparent walls (b)*

(c) *(d)*

Figure 67 *Zoom on supplied system centrifugal pumps Pedrollo (c) and inverter that governs the pumps (d)*

For the analyzed cases, the slope of the channel is considered equal to zero, resulting in a perfectly horizontal flume. The low slope and its roughness (built-in glass) allow us to assume a constant velocity in the section of uniform flow upstream and downstream of the turbine.

As in **Figure 66**, water recirculation was provided by two centrifugal pumps **(1)**, better visible in the **Figure 67(c)**, belonging to the **F100/160** series produced by Pedrollo of 15 KW and a nominal flow rate of 300 m^3/h each, governed by two **OMRON 3G3Rx** inverter models [79]. By changing the power frequency, these inverters can operate the pumping equipment. Therefore, the Pumps suck water out of a 5 m^3 tank **(2)** and push the fluid higher into a **stilling tank (3)** just before the channel, from which water enters the flume freely and falls back into the suction tank.

The water flows in the recirculating tank downstream **(2),** where a variable height gate **(4)** allows different operating conditions, varying in the **subcritical flow** condition.

The passage from subcritical to supercritical flow can be measured through the Froude Number that is defined as follows:

$$Fr = \frac{v}{\sqrt{gh}} \; [-] \tag{100}$$

This dimensionless number defines the ratio between the inertia and viscous forces. Therefore, the **Froude Number** is pivotal and results directly proportional to the flow velocity inlet v and inversely to the square roots of the water depth h multiplied by the acceleration of gravity g. In the tests carried out, this parameter varies from an estimated value of 0.20 to approximately 0.40. This means that the turbine gets close to the critical condition hydraulically, never reaching it.

However, the evaluation of the Froud Number is allowed through the imposition of a reference fixed section in which the water height upstream of the turbine it can be measured.

As a result, the velocity range under which the performance turbine curves are traced, goes from a minimum approximate velocity of 0.43 m/s to a maximum of 0.68 m/s, computed as average velocity for unit section $v_1=Q/(bh_1)$.

Figure 66 (b) shows that the turbine prototype has been inserted inside a wooden box **(5)** with transparent walls. A longitudinal steel foil in the middle is fixed below and above the box by two brackets. Moreover, to allow the turbine rotation, four horizontal radial bearings with an internal diameter equal to the used shaft are bolted to the steel foil to make the shaft parallel to the flow direction and the turbine orthogonal to the latter. These radial bearings are designed to work submerged, allowing rotation in optimal conditions. Therefore, as shown in **Figure 68,** the process can be transmitted from the horizontal to the vertical shaft where the measurement devices are installed using two **bevel gears**.

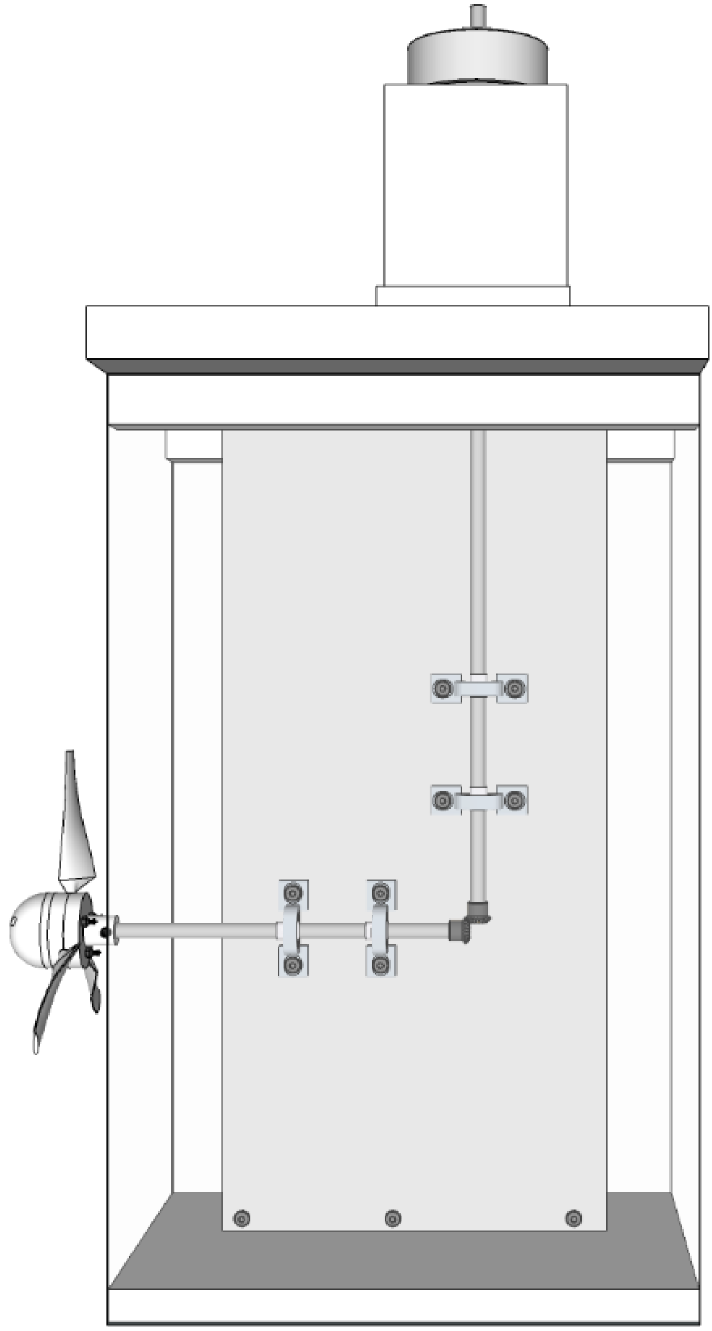

__Figure 68__ Detail of Bevel gears

On the top of the box a **high precision torque** and the **rotational speed meter** **(6) Magtrol TS103** (0.5 Nm of rated torque and one max torque, with an accuracy less than 0.1% and 1.5 rpm max speed, accuracy less than 0.015%) are installed. This system measures resistant torque using a gauge by converting that value into an electrical signal whose electronic value is recorded. In addition, it features a high-frequency tachometer so that the turbine rotation speed and the relative position of the blades are instantly known during each complete revolution. This measurement analyses torque variation based on the blades during rotor rotation. A data-tracking frequency of 80 data per second has been selected to get the measurement spectrum as accurately as possible.

The electrical brake used and installed on the torque meter is a **hysteresis (7), Magtrol HB-140 M-2,** controlled by **DC (8)**. In addition, the manufacturer of the employed measure device provides the **TORQUE V10** specific software that, via USB, connects the high-precision torque meter to the PC **(9)** allowing it to record the following mechanical parameters in their instantaneous value: Torque [N*m], Angular Velocity [rpm], Angle [°], Mechanical Power [W] and Time [s], as plotted in **Figure 69**. The torque and the rotational velocity meter are mechanically fixed to the shaft by a flexible coupling, as shown in **Figure 70**.

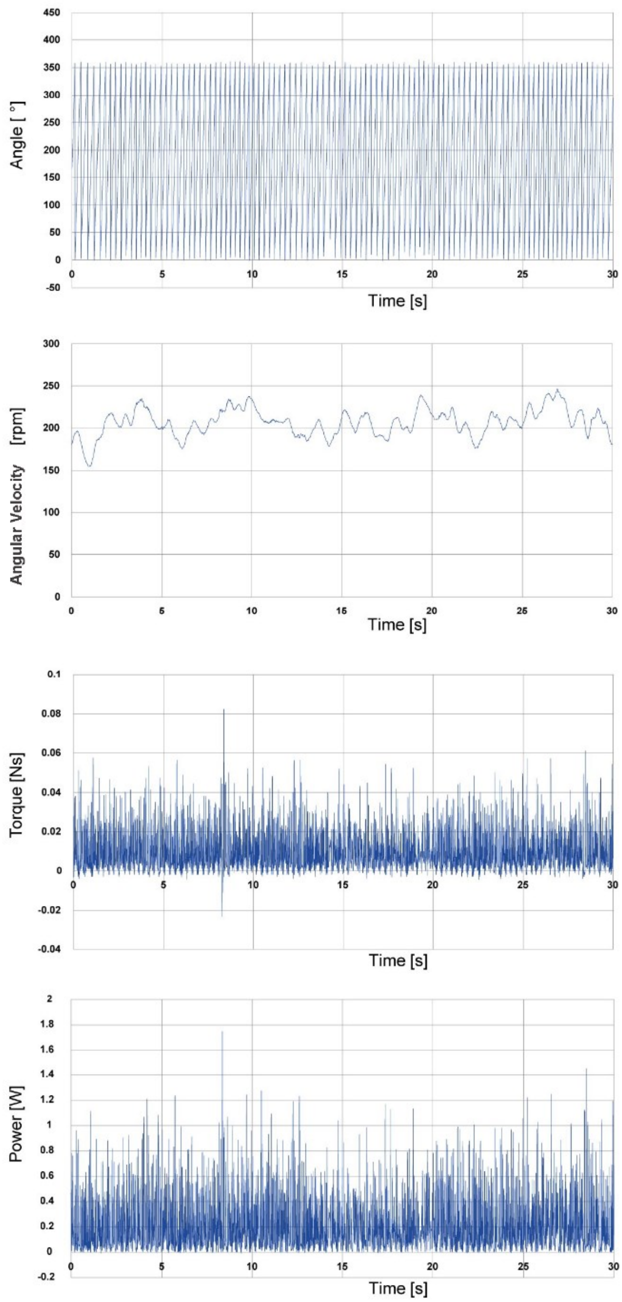

Figure 69 *Instantaneously quantity measured in a timeframe of 30 s by the speed and torque meter Magtrol TS-103*

The duration of the tests and the instantaneous values recorded are observed in 30 s timeframes. The scheme in **Figure 70** shows the whole data acquisition process.

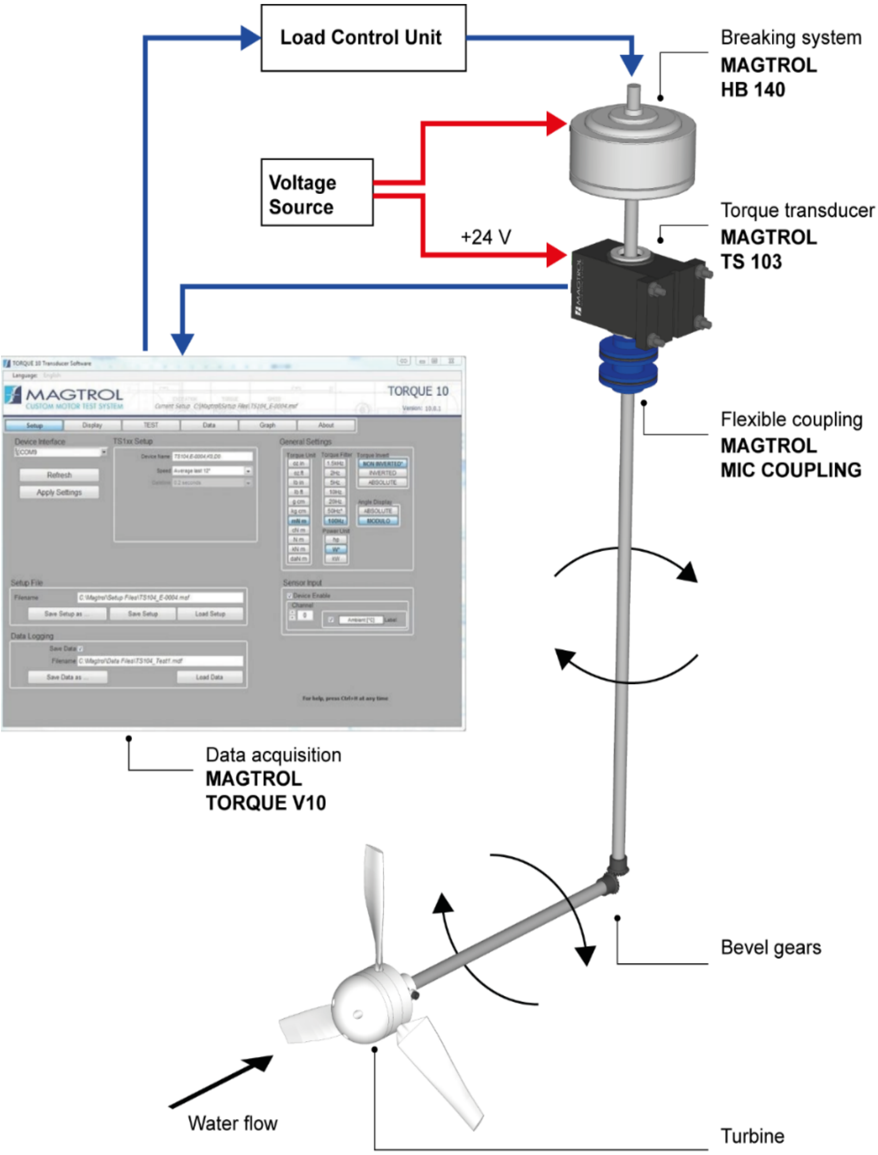

Figure 70 *Scheme of acquisition measurement system*

The tests conducted could be schematized in four steps:

1. Firstly, the turbine is free to rotate, and the Torque produced is just enough to compensate for the mechanical losses (**$T = T_{min}$**), as in **Figure 71(a)**.
2. Secondly, the turbine is gradually loaded with a 0.5 Voltage increment applied on the brake; to obtain the braking torque value able to stop the turbine rotation completely.
   In other words, as is shown in **Figure 71(a) and (b)**, the 0 V corresponds to the maximum angular velocity ($n = n_{max}$) recorded and to the **Minimum Power Production**.
3. Thirdly, as the loaded increases, the rotational speed slows down, and the Torque rises until reaching the **Maximum Power Point** (**MPP)** recorded, corresponding to the curve's maximum in **Figure 71(b),** marked with the black dot.
4. Above that point, if the loaded is increased, the turbine reaches the condition in which it cannot produce enough Torque and it arrests abruptly.

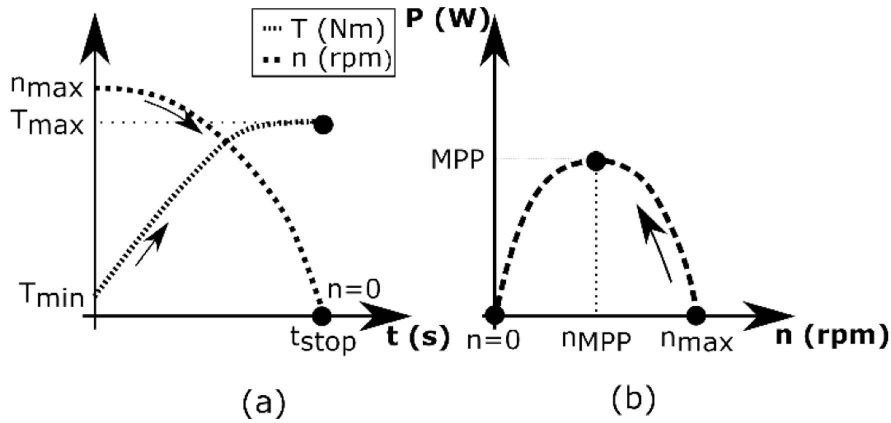

Figure 71 *Test methodology of performance curves extraction*

Furthermore, the experimental tests are organized considering three increasing values of flow rates, knowing the calibration law, obtained from previously study carried out in the Mieres Laboratory. This law, obtained experimentally, correlates the power frequency governing the pump's engine system and the corresponding flow rate.

The analyzed three flow rate values are:

1. **Q_1 = 0.052 m³/s**
2. **Q_2 = 0.059 m³/s**
3. **Q_3 = 0.065 m³/s**

They are calculated through linear interpolation between points obtained from calibration. Moreover, these values, as in **Table 7,** correspond to the frequency of the pump's engines respectively of:

Table 7 Calibration law

f [Hz]	Q [m³/s]
10	0.022
15	0.036
20	0.047
23	**0.052**
25	0.055
27	**0.059**
30	0.064
31	**0.065**
35	0.071
40	0.076
45	0.081
50	0.085

As shown in **Figure 72** the calibration law has a **R-squared** of 0.99.

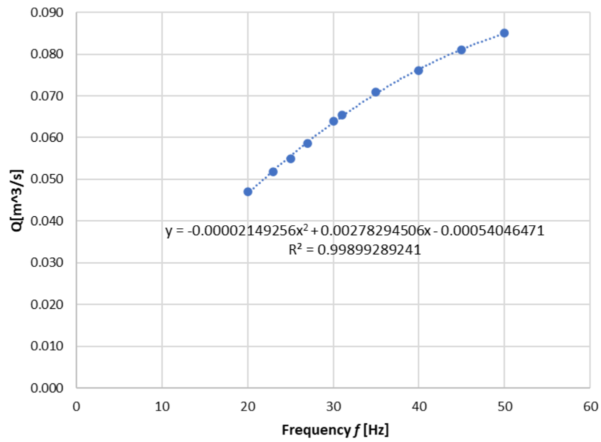

***Figure** 72 Calibration law pumps engine frequency and flow rate*

Five different downstream heights of the gate have been considered for each flow rate, from the nearly closed condition to the almost opened one, as in **Table 8** and in the three **Figures 73**, **74** and **75**.

Table 8 Tested flow rate and velocity current conditions

Q_1 = 0.052 m³/s					
h_1 upstream measured [m]	0.40	0.38	0.37	0.28	0.27
v upstream deducted [m]	0.43	0.45	0.47	0.62	0.64
h gate [m]	0.12	0.13	0.14	0.15	0.16
Br [-]	0.36	0.38	0.39	0.52	0.54
Q_1 = 0.059 m³/s					
h_1 upstream measured [m]	0.45	0.42	0.39	0.31	0.30
v upstream deducted [m]	0.43	0.47	0.50	0.63	0.65
h gate [m]	0.15	0.16	0.17	0.18	0.19
Br [-]	0.32	0.35	0.37	0.47	0.49
Q_1 = 0.065 m³/s					
h_1 upstream measured [m]	0.49	0.44	0.43	0.33	0.32
v upstream deducted [m]	0.44	0.50	0.51	0.66	0.68
h gate [m]	0.16	0.17	0.18	0.19	0.20
Br [-]	0.30	0.33	0.34	0.44	0.46

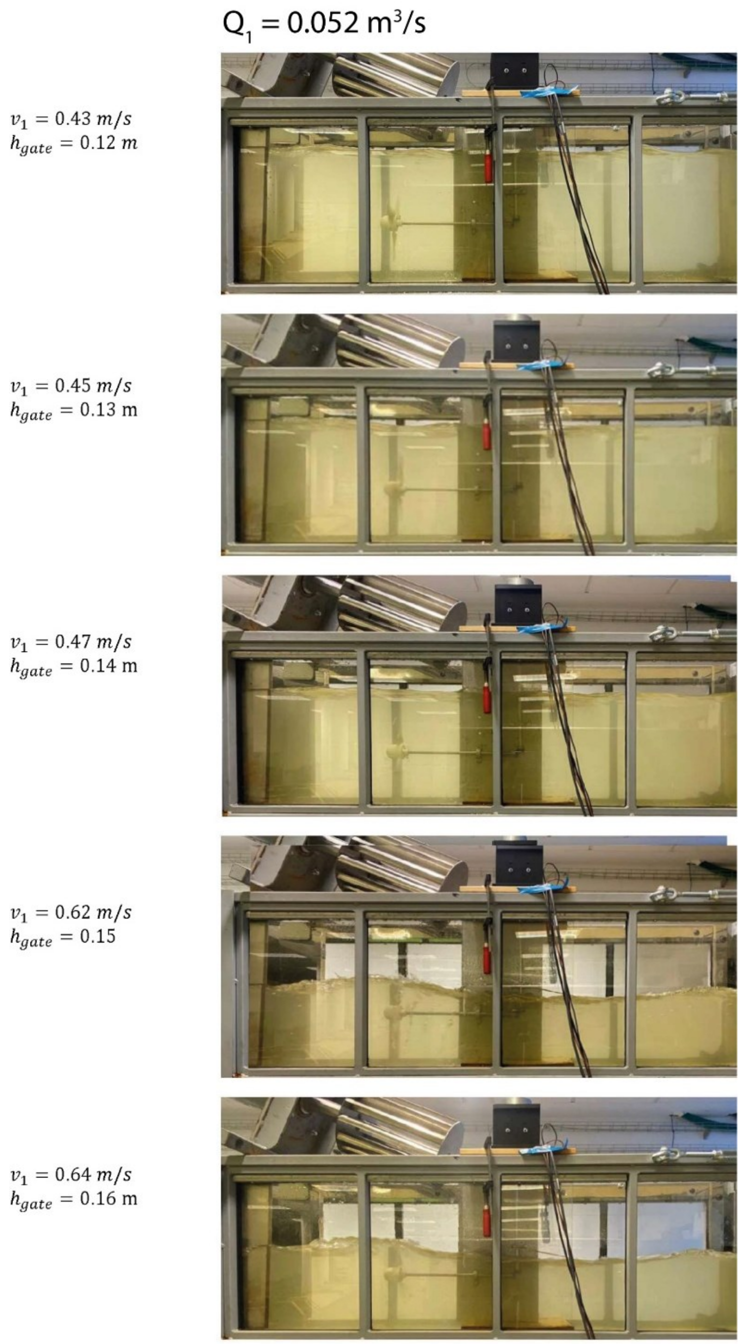

Figure 73 *Minimum flowrate 0.052 m³/s for five heights of the gate from 0.12 to 0.16 m*

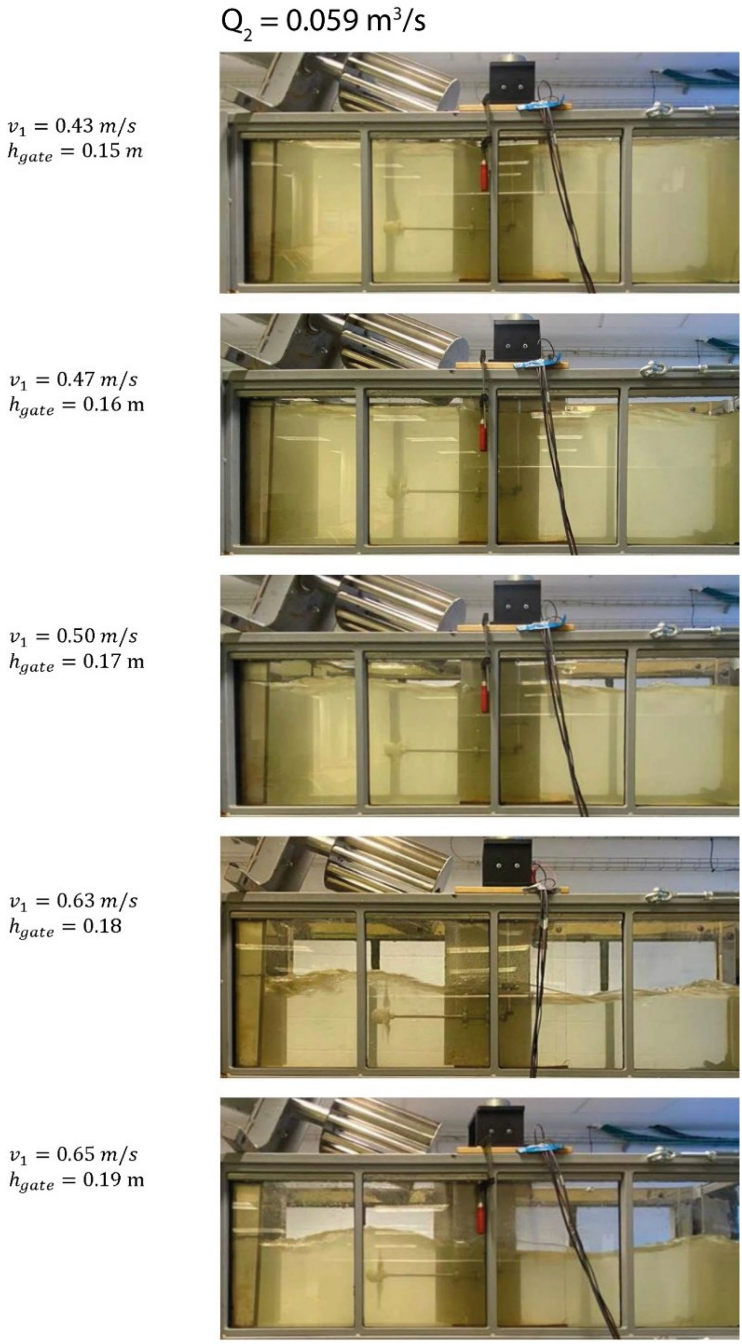

Figure 74 *Medium flowrate 0.059 m^3/s for five heights of the gate from 0.15 to 0.19 m*

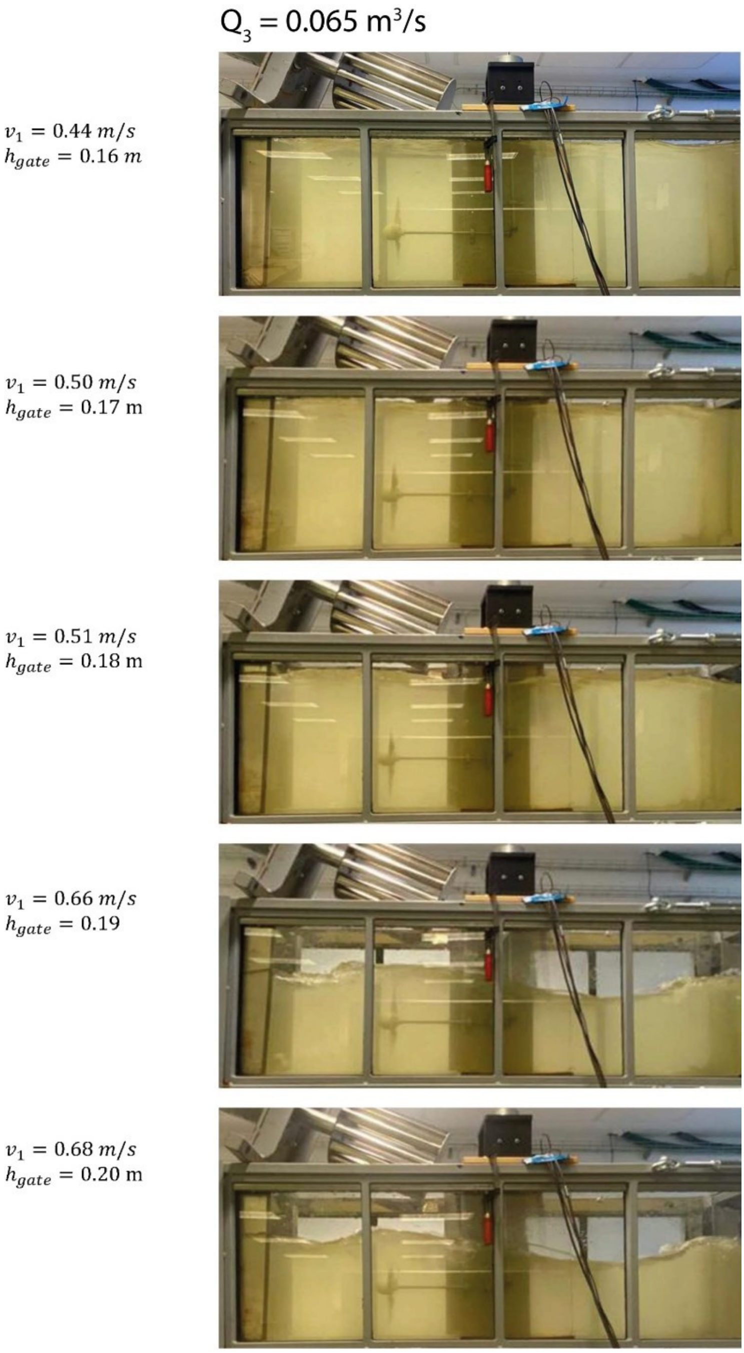

Figure 75 *Maximum flowrate 0.065 m³/s for five heights of the gate from 0.16 to 0.20 m*

The above captions represent the tests summarized in **Table 8**.

To each elevating height gate, an increasing value of velocity inlet for each flow rate is considered.

Due to the water depth fluctuation generated by the turbine rotation, to understand the average value of **water velocity inlet** the water depth has been measured in 13 sections upstream and downstream of the turbine, deployed at 10 cm each other. Moreover, this approach is useful to trace the water height variation along the channel length.

However, the average velocity upstream is referred to h_1 section located at 0.54 m to the inlet section. The average section velocity is obtained by knowing the flow rate and measuring the corresponding water height. Therefore, section h_1 has been used as reference section to calculate the parameters necessary to trace the characteristics curves as shown in **Figure 76,** because repeating the tests several times showed experimentally that the water height changes less in that sections that in all the other considered.

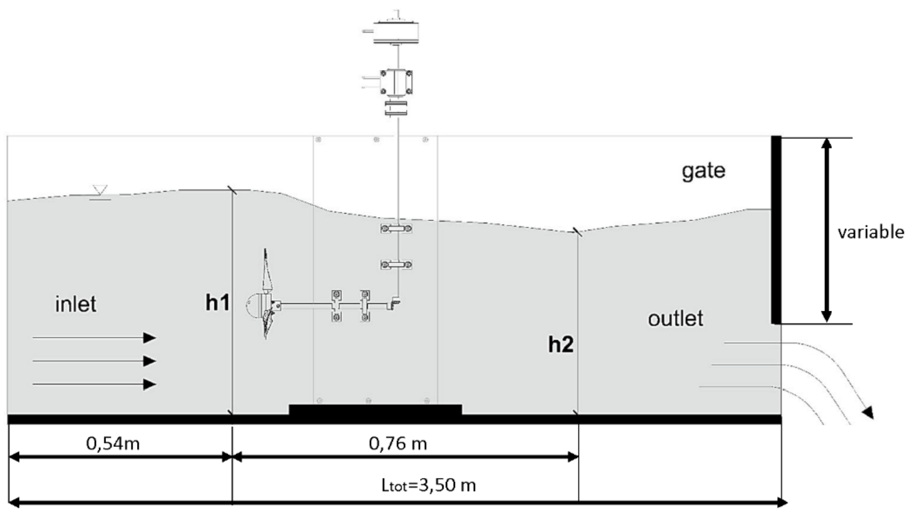

Figure 76 *Scheme of laboratory set-up, channel cross section view sections measured next to the turbine.*

Because of the gate's height rise from the channel bed, it is evident that the water depth also decreases. As stated before, this means experiencing a more considerable velocity in the flume each time.

So, the **Blockage ratio Br**, namely the turbine on the channel cross area, is increased in each experimentally tested point according to the high gate risen as in **Table 8**.

Therefore, on one hand, we want to understand experimentally how the Blockage could affect the power turbine performance; on the other hand, we must assume that up to the **Maximum Power Point (MPP)** measured, we cannot account for the point located on the unstable part of the chart, shows in **Figure 71(b)** forward the black dot.

This is because the increment of turbine load produces a rotational speed decrement, which means a different vectorial distribution between flow direction and a further consequent distribution between lift and drags forces up to a certain point where the drug forces increase more quickly than lift one, producing the so-called **hydrofoil stall condition**.

In other words, the increase of the turbine load causes a decrement in rotational speed and a consequent increase in the Angle of Attack between flow and blades. This higher Angle of Attack produces more lift and, consequently, more torque and power. This means that when the stall condition is reached, the lift force falls, and the drug grows.

As a result, a sudden drop in torque is produced. Furthermore, from that point forward, the turbine power output decreases when decreasing the rotational speed, making this part of the chart unstable.

For practical reasons, an active blade patch control system does not supply the turbine because, differently from wind turbines, turbulent fluctuation for water current is significantly lower than atmospheric wind, reducing the need for a very reactive control system.

This is even more true in the case of the prototype analyzed in this thesis work, which, as specified before, does not have an active control system. For this reason, all the points on the chart’s left side are not measured.

As in the research [3], the turbine's theoretical performance curves could be divided into three different regions of the control system.

First, the rated velocity is the current speed corresponding to the point at which the rated power is reached. In contrast, the **cut-out velocity** is the maximum water current speed at which normal power production is feasible. The rated and cut-out current speed choice depends on the available energy source of the deployment site. Therefore, the more significant the cut-out current velocity, the more exploitable the open energy source.

As **Figure 77** shows, if the turbine was supplied with a control system below the rated current speed in region 2, the control system would work trying to reach the MPP; on the contrary, if the turbine was through region 3, the control system would increase the rotational speed keeping a constant power output.

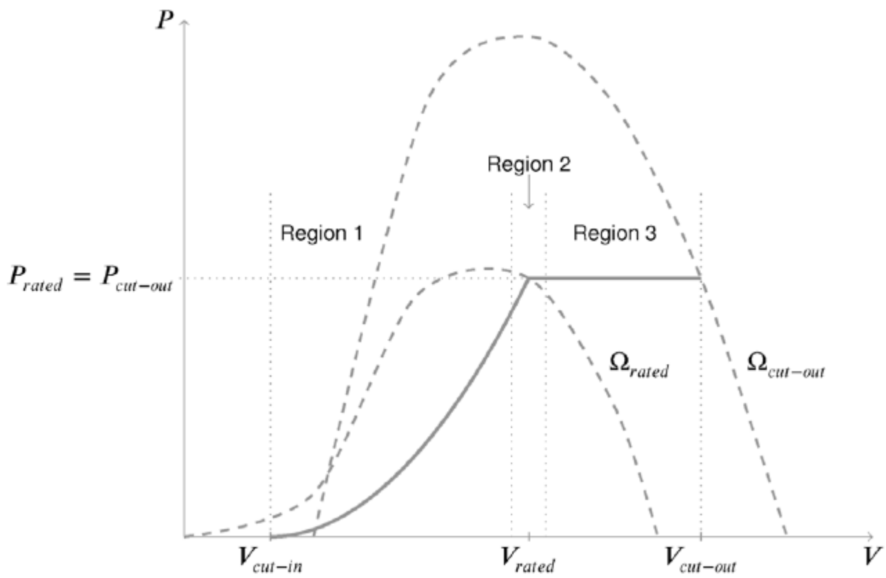

Figure 77 *Turbine's theoretical performance curves divided in three regions.*

Therefore, it is worth noting that, for the present experiments, the velocity has been measured as mean velocity in 12 cross sections upstream and downstream of the turbine, measuring the water depth through a graduated rod glued on the transparent walls of the channel each 10 cm, along 1,3 m between upstream and downstream, knowing the flowrate. This allows us to plot the flow profile for the 15 cases analyzed experimentally.

However, it also true that nowadays more sophisticated techniques exist to trace the velocity in a flume. Unfortunately, the Laboratory of Mieres (Spain), wherein all the experiments were performed, was not supplied at that moment, of this type of equipment. The more common techniques implemented to this aim are: 2D-3D Particle Image Velocimetry **(PIV),** Particle Tracking Velocimetry **(PTV),** or Laser Doppler Velocimetry **(LDV)**.

Furthermore, their implementation implies an appropriate choice of several parameters, i.e., the number and the proper density of particles implemented, performance of the cameras in terms of frame per second, to correctly describe the phenomena. Moreover, good image post-processing is crucial to find out the velocity field, and all these aspects make this technique more challenging to implement and not properly cheap.

The water depths and the angular velocity measured experimentally have been used to calibrate the CFD model, as discussed in Chapter V.

Then, the water depths measured are also used to calculate the upstream Froude Number and the Blockage applied. So, it was possible to solve the calculation sequence proposed by Houlsby for the LMADT in open channel flow, described in (Appendix 2).

Moreover, the calculation sequence allows to define the drop in water depth downstream of the turbine and the pressure drop able to maximize the Power extraction.

Therefore, in Chapter VI, the results obtained by the experimental and analytical comparison will first be described.

Finally, the calibrated CFD Model based on the experimental data will be validated through the testing and numerical results assessment.

4.3. Experimental uncertainties

The uncertainties analyses on the experimental measurement have been done according to the method of Abernethy and Thompson [81]. The uncertainty analysis comes from the difference between what is experimentally measured and what is the actual value.

The instrument's precision, measurement techniques, data acquisition process, and the user's lack of expertise could cause this discrepancy.

The model of mathematical uncertainty **U** considers the error to be composed of two main components:

- The **Precision Error** or Random Error **R**
- The **Bias Error** or Fixed Error **B**

Random errors are seen in repeated measurements; if the measures do not agree exactly, we will not expect them to. They are several minor effects which affect disagreements. The random errors between repeated measurements are called precision errors. One way to estimate the precision error in statistics is through the standard deviation σ; a significant value of standard deviations means much scatter in the measurements; on the contrary, a little one means a relatively tiny one.

To estimate the precision error (**Figure 78**) is used the **precision index** *s* defined as the expression below (101):

$$s = \sqrt{\frac{\sum(X_i - \bar{X})}{N-1}} \tag{101}$$

N is the number of measurements or statistical degree of freedom;

X_i measurement we have made;

$\bar{X}$ the average of measurements.

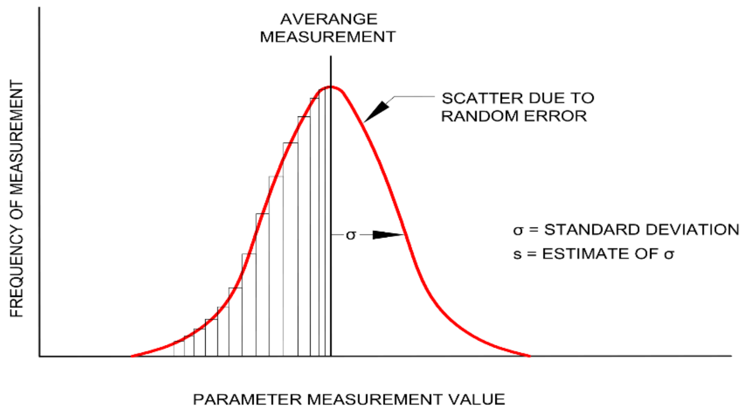

***Figure 78** Precision error*

The second component, bias, is the constant or systematic error, which means the bias stays the same in repeated measurements, as in **Figure 79**.

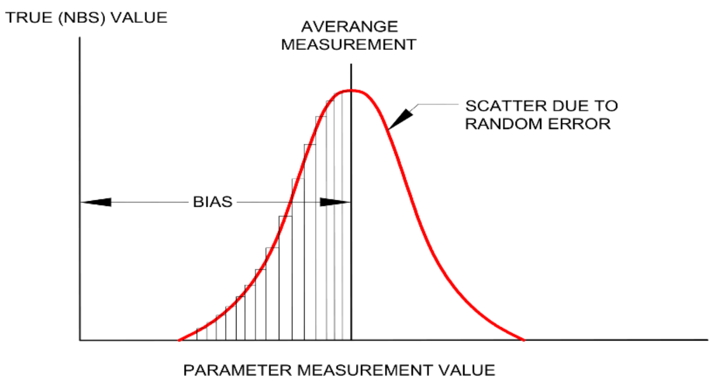

***Figure 79** Bias error*

It is necessary to define the actual value to determine the magnitude of the bias component in a measurement situation. Unfortunately, this absolute value is always unknown. For this reason, the only way to do that is through the engineering assessment of the instruments and measurement engineers to provide a bias upper limit. Generally, we can define five classes of bias error, such as large known biases, small known biases, significant unknown biases, and small unknown biases, that may have an unknown sign (±).

The significant known biases are solvable through the calibration process, which allows a comparison between the instrument and a standard one to obtain a correction. On the other hand, the small biases are correctable or not according to the magnitude of the bias and the difficulty in getting the correction. On the contrary, large, and small biases unknown are not correctible. Moreover, large unknown bias errors come from human errors in processing data, correctly installing instrumentations or unexpected external disturbances.

We must assume that the large unknown does not exist in a controlled measurement process. Moreover, it is impossible to define a rigorous statistic because a bias is an upper limit based on judgments with unknown characteristics. Therefore, any function of these two numbers should be described as a hybrid combination of an unknown entity (bias error) and a statistic one (precision error). So, the importance of estimating errors through a single number is so great that we are forced to adopt an arbitrary standard (**Figure 80**).

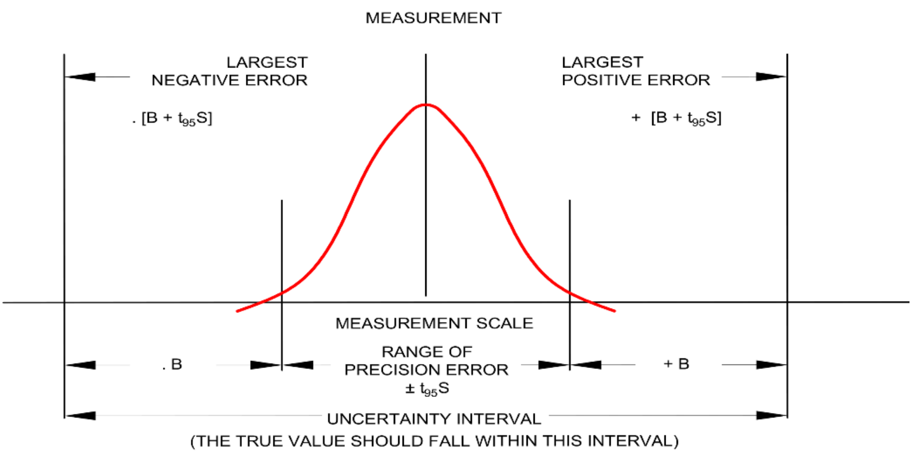

Figure 80 *Measurement uncertainty, symmetrical bias*

One of the most widely used is the Bias limit plus a multiple of the precision error index $\boldsymbol{s}$ as in the expression below (102):

$$U = \pm(B + t_{95}\boldsymbol{s}) \tag{102}$$

- U The uncertainties
- B Bias limit
- $\boldsymbol{s}$ The precision error index
- t_{95} Is the 95-th percentile point for the two-tailed Student's "t" distribution.

Moreover, t_{95} was set equal to 2.00 for the presented experimental analysis, consistently with [82].

Another fair point to highlight is that most of the time in the experimental field, only the base quantities are measured, such as Force, Pressure, Temperature, and Torque. On the contrary, the performance, or the derivative amount, is calculated as a function of the combination of different measurements.

This process causes the Propagation of the Error, which means that the measurement error is reflected in the derivative quantities through the function. The technique to estimate how the mistake of measuring are reflected in the derived quantities is based on Taylor's Series through the expression (103):

$$B = \sqrt{\sum_{j=1}^{M} \left(\frac{\partial f^*(x)}{\partial x_i} \; B(x_j) \right)^2} \tag{103}$$

Where f^* is the function to calculate the required quantity, M is the number of x_j measured entities to calculate $f^*(x)$, and $B\ (x_i)$ is the fixed error of the *j-th* measured parameter x_j.

4.4. Direct and indirect measurements and their related uncertainties

In the experiments carried out, it has been measured by a high precision torque and rotational speed meter, Magtrol TS103 with 0.5 Nm of nominal rated torque, accuracy lower than 0.1% and a max speed of 15000 rpm with a precision less than 0.015%, respectively. The manufacturer suggests those values as reported in the manual attached in [83].

In addition, on the rotational and toque speed meter, the hysteresis electrical brake Magtrol HB-140 M-2 [84] has been installed**;** it is powered on the one hand by DC with a tension of 24 V; on the other hand, through a Tension Variator, it can be handled the value of electrical tension applied on the brake, and so the consequent resistive torque applied to the turbine.

Moreover, as explained in (**section 4.2**), two OMRON 3G3Rx inverters govern the flow rate in the channel type, with a rated frequency of 400 Hz and an accuracy of 0.01%, as reported by the manufacturer [79].

Therefore, knowing the analytical law that links the electrical engine's frequency [Hz] and the flow rate (**see Figure 72**), is possible to understand all the intermediated values inside the values range calibrated.

On the other hand, the water depth fluctuation has been measured using a rod graduated of 0.5 m with mm precision, measuring the water depth in different sections upstream and downstream of the turbine to trace the free-surface water variation.

Therefore, the directly measured quantities are:

- T Torque [N*m] applied to the turbine
- ω Angular Velocity [rpm] with the turbine rotates
- h Water depth [m]
- f Pump*s* Frequency [Hz]

It is worth noticing that Torque and Angular velocities have been measured over and over in time, according to the Tension [V] value applied to the Brake, ranging from 0 to 10 Volts, for each tested downstream control gate position and each value of flowrate used in the experiments.

The maximum tension applied to the brake produces a resistive torque as high as arrests its rotation. However, the tension range is wide according to the velocity point analysis and the flow rate considered.

Then, for each value of brake tension, a measurement with a time frame of 30 s has been recorded, so the points of the curves analyzed in the (ω- P) charts in Chapter VI, are the mean in time of each measured quantity of interest for each deal of tension, in the same observation time.

However, the Power measurement is not a direct measure regardless the instrument returns its value instantaneously; this is because the device produces a Power value calculated as the product of the instantaneous value of Torque and Angular velocity.

The same is verified for the flow rate value as an indirect measurement of the electrical frequency of pumps that supply the channel.

Moreover, along with Power and Flowrate, other two crucial parameters which are strictly related to the total efficiency of the studied turbine are calculated indirectly, and they are: the Power Coefficient *Cp* and the Tip Speed Ratio *TSR* which could be calculated by applying the following equations:

$$C_p = \frac{P}{0.5\rho A v^3} = \frac{2Power\pi^2 R^2}{\rho Q^3} \tag{104}$$

$$TSR = \frac{\omega R}{v} = \frac{\omega \pi R^3}{Q} \tag{105}$$

where:

- $Power$: Mechanical Power measured [W] by the product of Torque and Angular velocity by the speed and torque meter Magtrol TS103
- *Q*: is the flow rate that corresponds to a specific value of the engine's pumps frequency due to the calibration low explained in **Table 7**
- *ω*: The Angular velocity [rpm]
- *R*: The turbine radius [m]
- *ρ:* The water density is 998.2 [Kg/m^3]

So, the **Precision Error R** related to a repeated measurement in time for Torque [N*m], and Angular Velocity [rpm] has been computed. For both, the mean value ***μ*** and the standard deviation value **σ** have been calculated to understand the statistical dispersion of data extracted as in Eq. (106). This index is helpful because it means using a not disturbed index to define the minor or significant data dispersions from the mean value according to its assumed value.

$$S = \sqrt{\frac{\sum_{i=1}^{Nt}(x_{i,t}-\mu)^2}{N-1}} \tag{106}$$

where:

- $N\text{-}1$ = is the statistical degree of freedom
- $x_{i,t}$ = Torque, Angular Velocity, Power measured at *i*-th measurement
- μ = mean value corresponding to 30 s of time observation

Then, the maximum precision index *s* obtained along 240 measurements, and the mean value for Torque and Angular Velocity were computed, and the results are, respectively:

s (Torque) = 0.022 Nm with μ= 0.163 Nm

s (Angular Velocity) = 48.135 rpm with μ = 423.653 rpm

Conversely, for the indirect measurements, the Propagation error has been calculated considering the uncertainty of Torque, Angular velocity, Frequency and, Power as follows:

$$P = \omega * Torque = U(Power) = \left[\frac{\partial Power}{\partial Torque} * U(Torque)\right]^2 + \left[\frac{\partial Power}{\partial \omega} * U(\omega)\right]^2 = [\omega * U(Torque)]^2 + [Torque * U(\omega)]^2 \tag{107}$$

$$Q = U(Q) = \left[\frac{\partial Q}{\partial Frequency} * U(Frequency)\right]^2 \tag{108}$$

$$C_p = \frac{P}{0.5\rho A v^3} = \frac{2Power\pi^2R^2}{\rho Q^3} = U(C_p) = \left[\frac{\partial C_p}{\partial Power} * U(Power)\right]^2 + \left[\frac{\partial C_p}{\partial Q} * U(Q)\right]^2 = \left[\frac{2\pi^2R^2}{\rho Q^3} * U(Power)\right]^2 + \left[-\frac{6Power\pi^2R^2}{\rho Q^4} * U(Q)\right]^2 \tag{109}$$

$$TSR = \frac{\omega R}{v} = \frac{\omega\pi R^3}{Q} = U(TSR) = \left[\frac{\partial TSR}{\partial \omega} * U(\omega)\right]^2 + \left[\frac{\partial TSR}{\partial Q} * U(Q)\right]^2 = = \left[\frac{R^3\pi}{Q} * U(\omega)\right]^2 + \left[-\frac{\omega R^3\pi}{Q^2} * U(Q)\right]^2 \tag{110}$$

The **Bias error** for Torque, Angular velocity, water depth and Frequency and the relative uncertainties are calculated as follows:

1. Torque

According to the manufacturer, the absolute Bias error is:

$$Bias_{(Torque)} = 0.1\% * 0.5 = 0.001\ Nm \tag{111}$$

$$U_{(Torque)} = \pm(B + t_{95}s) = \pm(0.001 + 2 * 0.022) = \pm 0.04\ Nm \tag{112}$$

Comparing the uncertainties to the scale bottom of the instrument we obtain a relative uncertainty:

$$U_{Torque} = \frac{0.04}{0.5} = 8.88\% \tag{113}$$

2. Angular velocity

With same methodology

$$Bias_{(\omega)} = 0.015\% * 15000 = 2.25\ rpm \tag{114}$$

$$U_{(\omega)} = \pm(B + t_{95}s) = \pm(2.25 + 2 * 48.135) = \pm 98.52\ rpm \tag{115}$$

$$U_{\omega} = \frac{98.52}{15000} = 0.66\% \tag{116}$$

3. Water depth

$$Bias_{(h)} = 0.10\% * 1 = 0.001\ m \tag{117}$$

$$U_{(h)} = \pm(B + t_{95}s) = \pm(0.001 + 2 * 0) = \pm 0.01m \tag{118}$$

$$U_{\omega} = \frac{0.001}{1} = 0.01\% \tag{119}$$

4. Frequency

$$Bias_{(f)} = 0.01\% * 400 = 0.04\ Hz \tag{120}$$

$$U_{(f)} = \pm(B + t_{95}s) = \pm(0.04 + 2 * 0) = \pm 0.04Hz \tag{121}$$

Comparing the uncertainties to the scale bottom of the instrument and so with the maximum frequency measured:

$$U_{f} = \frac{0.04}{50} = 0.08\% \tag{122}$$

From what concerns the Propagation of error of indirect measurements, namely Power, Flowrate, C_P and TSR, the results of the partial differential equation allow us to calculate the following percentage of uncertainties compared to their scale bottom:

$$U_P = 0.85\% \tag{123}$$

$$U_Q = 0.035\% \tag{124}$$

$$U_{Cp} = 0.88\% \tag{125}$$

$$U_{TSR} = 0.69\% \tag{126}$$

In conclusion, the only value affected by high uncertainty percentage is the Torque, and it is explicable from its high variation in time concerning its mean value (see **Figure 69**).

Chapter V

Computational Fluid Dynamics (CFD) Model validation

The CFD modelling, as already mentioned in the literature review of Chapter II, is a potent tool used in compliance with experimental modelling to understand the hydraulic behavior of a specific studied case. Therefore, Chapter V introduces the procedure to implement a CFD model of the studied horizontal axis hydrokinetic turbine.

In greater detail, the herein-presented analysis focused on validating the numerical model with experimental results obtained in the laboratory. As a result, the numerical model reproduces the hydraulic recirculation channel's geometrical features.

In this regard, a three-dimensional multiphase analysis considering the water-free surface has been performed using the ANSYS FLUENT software.

The primary geometric parameters of the channel and the HAHWT are summarized in **Table 9**:

Table 9 *Geometric channel characteristics of the tested model*

Channel length	[m]	3.50
Channel width	[m]	0.30
Channel height	[m]	0.50
Turbine Diameter	[m]	0.24

In other words, the CFD model is developed asymmetrically concerning the turbine position as in the laboratory set-up. More precisely, the turbine is in the geometric reference of the entire model and has the same diameter of actual prototype, as shown in **Figure 81**. The inlet section is located at 0.540 m, reference section for the average velocity measurement, from the center of the rotational domain including the turbine.

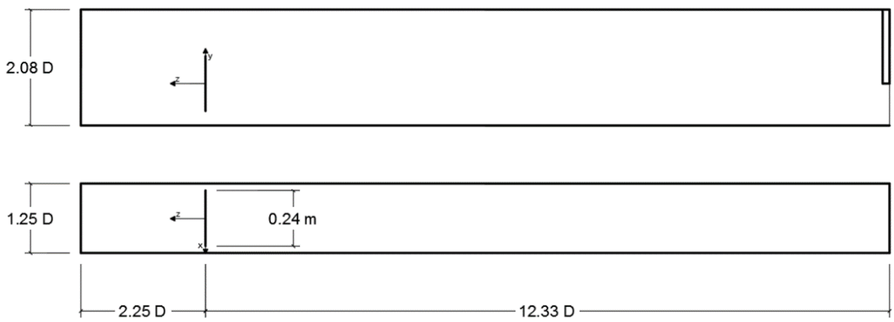

Figure 81 *CFD Model scheme side view (up) top view (down)*

Therefore, the first step concerns realizing the geometric turbine domain and the channel one separately in the specific Design Modeler session provided by the software. In this regard, the computational domain is divided into two central regions: the inner domain, which involves the turbine model and corresponds to the rotating region, and an outer domain for the surroundings channel, corresponding to the stationary region. Then, exploiting the sliding-mesh model of the solver, the simulation domain was divided into two subdomains to allow the turbine's rotation, as proposed by [85]. Finally, in the second step, the mesh generation was developed separately to be assembled in a unique mesh, as in the Design Modeler section. Therefore, a mesh sensitivity analysis was carried out, aiming to define the most suitable resolution as a good trade-off between accuracy and computational costs.

Moreover, a steady-state simulation was first implemented to initiate the model and fill up the flume, using the same parameters corresponding to the experimental test case (velocity inlet and control height gate) to achieve a better convergence solution. After the steady-state simulation, a comparison of the Mass-Flow rate has been made concerning the experiments to understand if the continuity equation was respected. Successively, after the steady simulation stabilizes and converges, a transient simulation was run to assess the turbine interaction in its rotation with the water flowing in the channel.

In this regard, knowing one of the experimental angular velocities measured corresponded to a specific value of brake tension, it was possible to understand the corresponding value in revolution per second (rps).

Moreover, the time to fulfil a complete revolution was computed by the inverse of the angular velocity in revolution per second. This implies that a sensitivity analysis was also required to understand which time step it should select to simulate a reasonable number of revolutions in the time consumed for each simulation.

However, the choice of the time step size is strictly related to the value that the Courant Number assumes, and the dimension of characteristic cells length of the mesh considered, which tends to reduce, according to the mesh tighten, from the coarsest to the finest mesh.

The following steps were directed to the simulation setting by adequately choosing the most appropriate turbulence model and the boundary conditions.

From the experimental results, 15 different cases have been analyzed for the numerical simulations. Specifically, five height gates have been tested for each considered flow rate. Therefore, 15 operations from the lowest to the maximum velocity has been numerically tested.

Therefore, for each numerical simulation, the control gate height has changed from the slightly closed condition, i.e., to the nearly open condition, passing through all the intermediate control gate positions. This means that the comparison between the experimental and numerical curves has been applied in a specific point for each velocity inlet value. As a result, the numerical simulations allow to compare the experimental performance curves in one specific point, which corresponds to the same braking tension value applied to the prototype, thus, related to the measured angular velocity.

This procedure has been implemented to validate the numerical model, aiming to compare, on one hand, how far the numerical model forecasts the water depth and free surface against the experimental observations. And how, on the other hand, the characteristics points extracted numerically approach those calculated experimentally.

5.1. 3D Model

The geometric model of HAHWT was developed in SolidWorks® 2019 considering only the external surface of the turbine and then was implemented in ANSYS ® Design Modeler ™ tool, (**Figure 82**).

Firstly, the HAHWT was involved in a circular domain of 60 cm in thickness, symmetrical to the geometrical center of the turbine, to create interfaces between the rotational (turbine) and the stationary (channel) domain.

Then the turbine structure was removed from the circular fluid domain and was inserted in a rectangular stationary model represented by the channel. The channel model is simplified, because the stilling tank (**Figure 66**) is not drowned; however, the channel has the same geometrical features as the experimental set-up in terms of height and width.

This procedure aimed to analyze the fluid interaction between rotational and stationary domains.

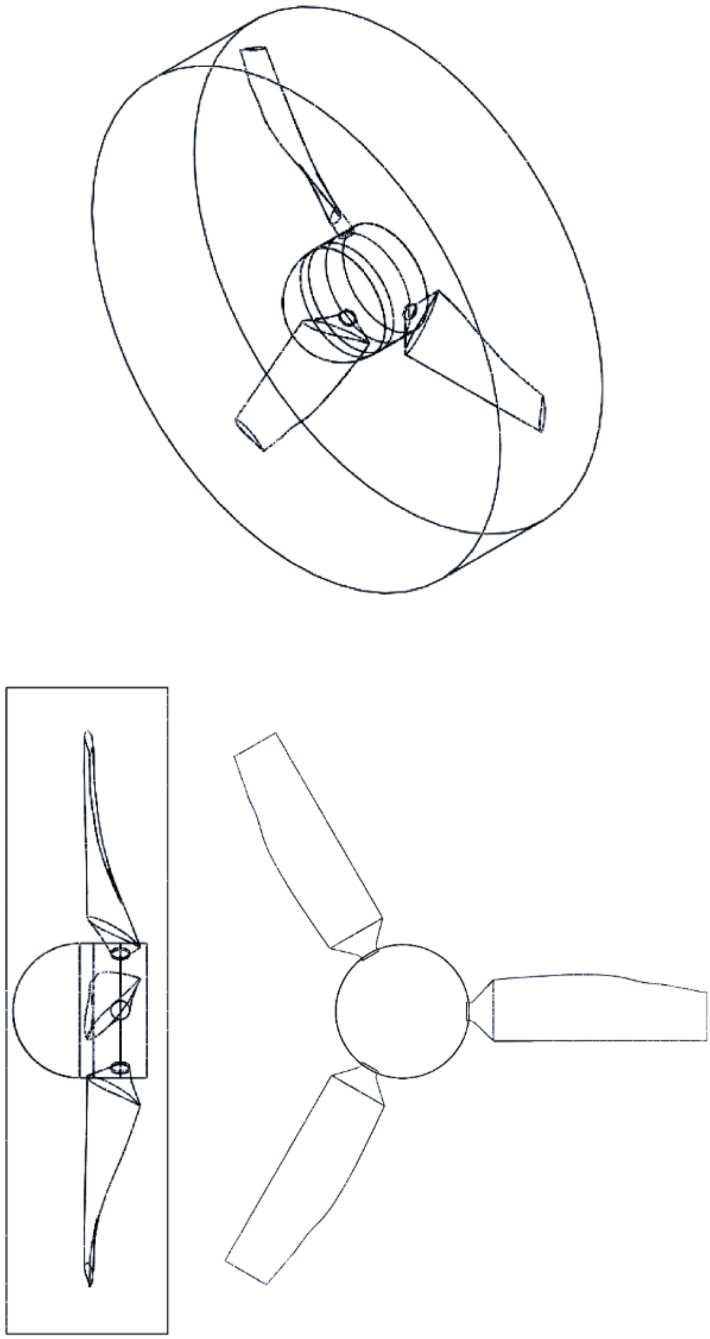

Figure 82 *Isometric, side, and frontal view of HAHT*

5.2. Mesh Generation, mesh size time step sensitivity analysis

The mesh used for this problem is an unstructured mesh with tetrahedral cells.

Spectral convergence was verified for the presented computational domain using the Richardson extrapolation-based Grid Convergence Index (GCI) method [76]. This method provides and estimates the error in compliance with specific solution quantities due to the discretisation error. In more critical detail, analysing from the finest to the coarsest mesh considered in the simulations, three different mesh sizes were studied by increasing the growth ratio from 1.05 to 1.15 and the global element size, as shown in **Figures 84** and **85**.

Specifically, the growth ratio represents the increase in element edge length with each successive layer of elements from the edge or face. For example, a growth rate of 1.15 results in a 15% increase in element edge length with each successive layer of elements.

Therefore, three successively refined meshes were considered; these have N_1 = 8.07E+06, N_2 = 2.74E+06 and N_3 = 1.11E+06 number of elements, respectively. All simulation conditions were held constant for each mesh; a summary of this study is given in **Table 10**.

Table 10 3D CFD Model sensitivity analysis

	φ Torque [Nm]	
N_1, N_2, N_3	8069742; 2744482; 1106203	8069742; 2744482; 1106204
r_{21}	1.582	1.582
r_{32}	1.414	1.414
φ_1	0.096	
φ_2	0.093	
φ_3	0.092	
$\varphi_{ext21/32}$	**9%**	**10%**
$\varphi_{a21/32}$	**1%**	**3%**
$\varphi_{ext21/32}$	**2%**	**5%**
$GCI_{21\ fine21/32}$	**2%**	**6%**

The refinement ratio between the characteristic length of the coarse and the fine mesh is defined as r_{21} and $r_{32} = h_{course}/h_{fine,}$ being verified because it is more significant than 1.3.

The solution quantity selected as a reference value is the Torque [Nm] employed on the blades represented by φ_1, φ_2 and φ_3 for each representative mesh.

Therefore, knowing the rate of convergence, the extrapolated value for the solution quantities (φ_{ext21}), the relative error (φ_{a21}), and the extrapolated relative error (ext_{21}), the Gird Convergence Indexes $(GCI_{fine})_{21}$ and $(GCI_{fine})_{32}$ were calculated.

The $(GCI_{fine})_{21}$ results = 2% whereas $(GCI_{fine})_{32}$ = 6%, this corresponds to a change in Torque of 4%.

From the results, an error band of 6% on torque and thrust was accepted due to discretization rather than 2%. This 6% corresponds to a change in Torque of 4% when the mesh is refined from the medium to fine mesh, indicating that further refinement of the baseline mesh has a minor influence on output results, allowing shorter computational time.

As a result, the medium mesh N_2 presents a good trade-off between results accuracy and related computational costs, and it was thus selected for simulations. Moreover, it has been observed numerically that as reported in **Figure 83** for each tested mesh, the Power Coefficient at the beginning of the solution gives results affected by a remarkable instability along the computational time, until 6 s of the simulated time, followed by transient phase from 6 to 10 s. Afterwards, only above 10 s of simulation the behavior of detected coefficients, approximates to more stable condition, reaching a periodical behavior. This means that each simulation was conducted for at least 10 s.

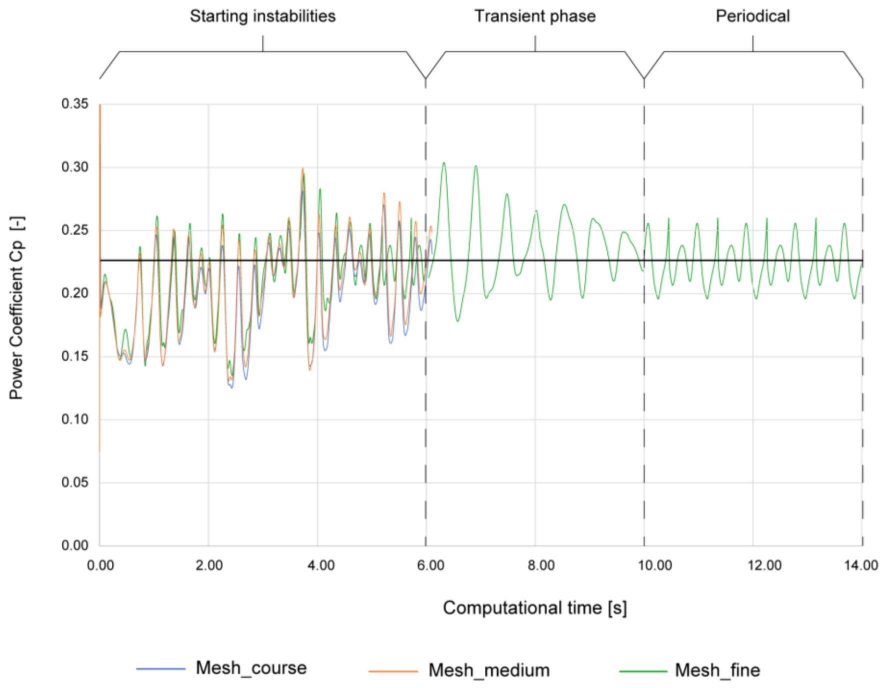

Figure 83 Numerical calculation of Power Coefficient over 14 s of simulation

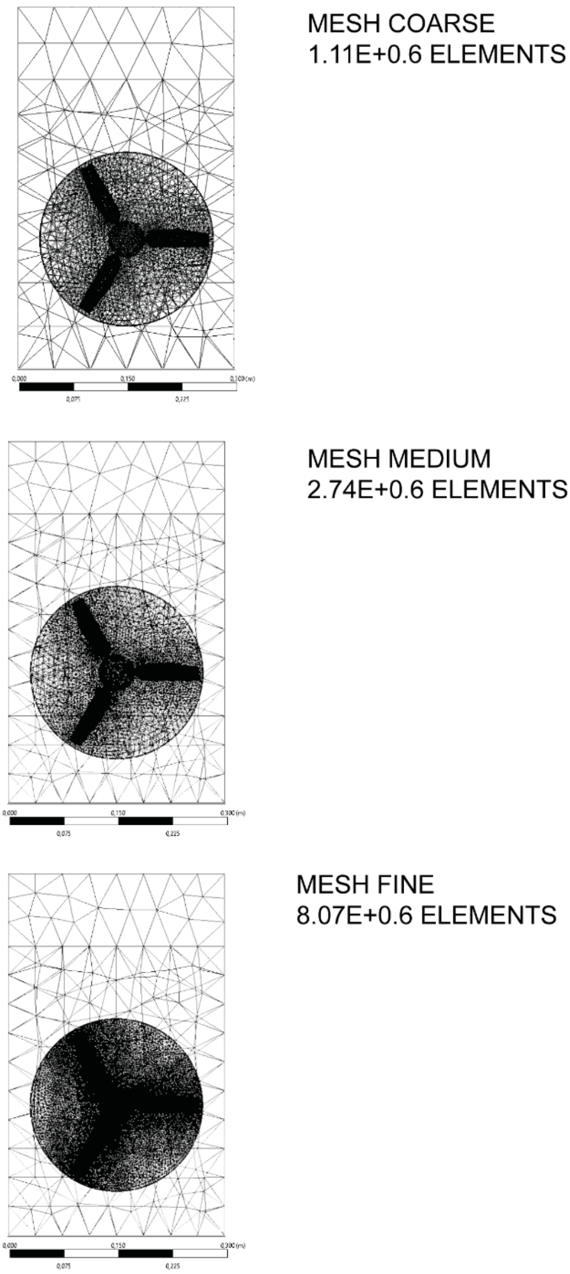

Figure 84 *Global Mesh Size sensitivity analysis front view*

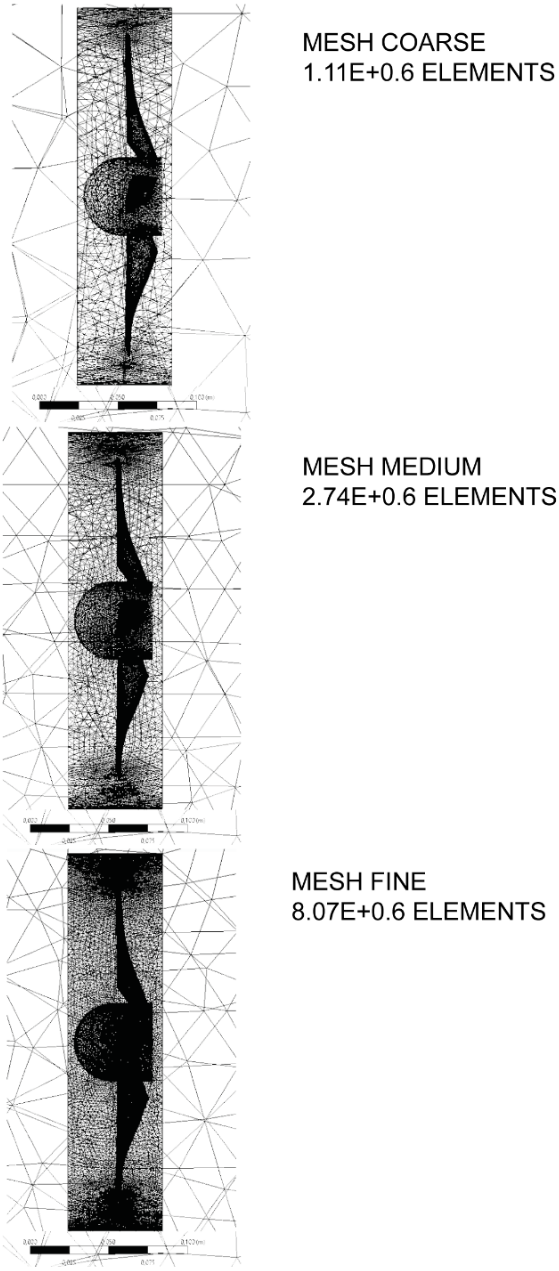

Figure 85 *Global Mesh Size sensitivity analysis side View*

However, as demonstrated by the authors [86] and in a transient simulation, if the size of the elements is not combined with a reduction of the time step, the simulation tends to become unstable also due to an increase in the Courant Number.

Therefore, the Courant Number expressed as:

$$Curant\ Number = V * \frac{\Delta t}{\Delta h} \tag{127}$$

Is the ratio between the temporal time step (Δt) and the time required by a fluid particle with V velocity to be convicted throughout a cell of dimension (Δh). It is defined as follows:

In the case of an explicit scheme for temporal discretization the CFL (Courant-Friedrichs-Lewy) criterion imposes a limit on the maximum allowed Courant Number value <1 [87] to ensure the stability of calculation; implicit methods, on the other hand, although to be unconditionally stable concerning the time step size [88].

Although theoretically valid, if the problem is studied with a linear stability analysis, when the time step is increased, non-linearity effects would become prominent and oscillatory solutions may occur. On these bases, the literature indicates that an operational Courant Number between 5 and 10 for viscous turbomachinery, solved with an implicit scheme, provides the best error-damping properties.

However, the time step size also defines the size of the rotation unity, which is crucial for a stable solution. So, for the specific case study, starting from one of the experimental velocity points in rpm and knowing the corresponding time necessary to fulfil a complete revolution by the inverse of angular velocity in [rps], and choosing the time required to move the turbine, one tiny fraction of a turn in the simulation, is possible to establish the ratio between degrees and time step values. For example, to a measured angular velocity of 162 rpm, corresponds a value of 2.70 [rps], this value in [rps], allows to obtain the time to fulfil a complete revolution equal to 0.37 s.

Therefore, the chosen time step size corresponds to the time in which in the numerical model the turbine makes 2.40 revolutions for unit time, precisely the model can simulate every 150° swept. Therefore, respecting the numerical stability criteria, the second-and third-time step has been selected. Namely, the Courant Number less than 1 computed for the coarsest mesh, was considered as a reference for the next timesteps. However, the time step also decreases due to the decrement of cell mesh characteristic length.

5.3. Boundary conditions and simulation properties of the HAHWT model

The Volume of Fluid (VOF) was applied in the present simulation to model the free-surface (air-water interface) and to extract the perfomance curve of the prototype. This model has been developed by [89], and it was selected for its capability of reproducing and capturing free-surface deformation.

For this model, the water volume fraction is defined as:

$$\alpha = \frac{V_w}{V} \tag{128}$$

where the V_w is the volume occupied by water in the cells and the V is the total volume of the misture. This value varies from 0 to 1. The physical prorierties of the multiphase mixture can be calculated as follows:

$$\rho = \alpha\rho_w + (1-\alpha)\rho_a \tag{129}$$

$$\mu = \alpha\mu_w + (1-\alpha)\mu_a \tag{130}$$

where ρ and μ are the mixture density and viscosity, respectively, the VOF governing equations are the mass, momentum and volume conservation equations. The phases share standard pressure and velocity fields allowing us to solve a single momentum equation.

$$\rho\frac{\delta\vec{u}}{\delta t} + \rho\nabla(\vec{u}\vec{u}) = -\nabla \mathrm{p} + \mu\nabla^2\vec{u} + \rho\vec{g} + \Gamma_a \tag{131}$$

where u and p are the velocity and the pressure field, g is the acceleration vector due to gravity, and Γ_a is the surface tension term. The latter was set equal to 0.072. Therefore, according to this approach, the interface tracking between two fluids, for the specific case of water and air, is accomplished by solving the volume fraction continuity equation for each phase, excluding the reference phase as in the following equation:

$$\frac{\partial}{\partial t}(\alpha\rho_w) + \nabla(\alpha\rho_w\bar{v}) = \sum_{w=1}^{k-1}\gamma_{w\to a} \tag{132}$$

Where a and w are the reference phase (water) and (air) and the secondary phase, k is the total number of phases that could be more than two, and γ is the mass flow rate per unit volume to each secondary phase to the reference one.

As suggested in the literature [90], [91], the most appropriate turbulent model for this aerodynamic/hydrodynamic problem is a *k-ω* model developed by Menter. Therefore, the Reynolds Averaged Navier Stokes Equations (RANS) are solved using the Shear Stress Transport (*k-ω* SST) turbulence model. This model offers improving prediction of adverse pressure gradients in the near wall region compared to the standard *k-ω* and *k-ε* models. Furthermore, the model is proportional to the turbulent shear stress and kinetic energy inside the layer wake region [92].

The velocity estimated experimentally upstream of the turbine was set as inlet boundary conditions. Whereas, a constant gauge pressure of 0 Pa was set at the outlet as in **Figure 86.**

Moreover, since for each height of the tested downstream control gate, a different average velocity inlet was measured, in accordance with the decrease of the upstream water head. Then, in greater detail, the velocity inlet value was changed in the numerical model for each tested cases. Similarly, the outlet boundary condition has been modified according to the level gap of the control gate. As a result, the upper surface was set as a symmetry boundary to model zero-shear slip walls, while the bottom was selected as a no-slip wall and called a channel bed boundary. As a result, the turbines blades are set as no-slip walls rotating with the surrounding rotational domain—finally, all other boundaries, including the control gate, have no-slip walls.

No-slip walls circular volume involving the turbine and corresponding to the rotational domain has a surface in contact with the stationary domain. This surface was set as one of the interface boundary conditions, along with the interface that concerns the contact surface between the two fluids considered, namely water and air.

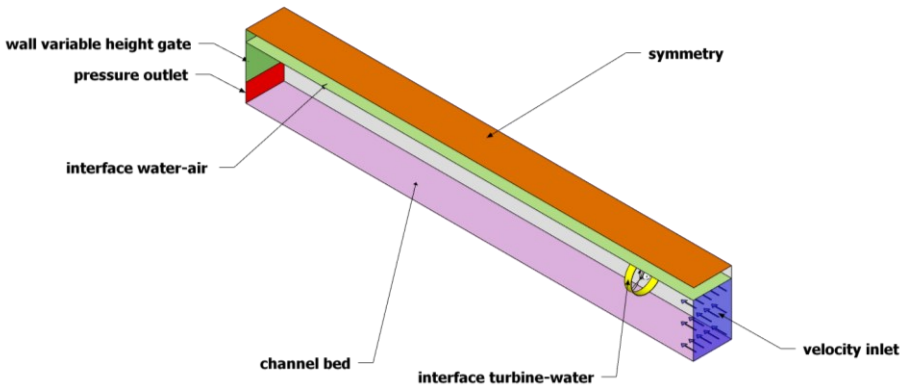

Figure 86 *Implemented Boundary Conditions and Interfaces*

The pressure-based solver was chosen with implicit formulation because it provides a faster converged steady-state solution than explicit formulation. Furthermore, First Order Implicit Transient Formulation was set because it returns excellent accuracy in shorter computational time.

The Semi Implicit Method for Pressure-Linked Equations (SIMPLE) algorithm was applied to complete the Pressure-Velocity field established by the RANS equations. This model provides an iterative procedure to achieve convergence, and it is based upon an approximation used to the velocity field to solve the momentum equation. Then, to solve the subsequent iteration, the pressure gradient term is computed as a function of the pressure distribution of the previous iteration. So an updated pressure distribution is defined, correcting the face's mass fluxes and the cell velocities. The convergence criteria for relative residuals' momentum continuity and turbulence parameters were set to 10^{-4}. The semi-Implicit-Method produced pressure correction for Pressure-Linked equations (SIMPLE) and Staggering Pressuring Option (PRESTO!) schemes, which were compared, and showed similar results.

The pressure Interpolation Scheme selected was body-force-weighted, coupled with VOF simulations. Second Order Upwind discretisation was implemented to solve Momentum, Turbulent Kinetic energy and Dissipation Rate. The Second Order Upwind can achieve more accurate results when the flow is aligned with mesh, especially if the mesh is tetrhtetrahedral and the flow is complex. The Spatial discretisation was based on the Least Square Cell Based gradient, and the Compressive method was selected to solve the Volume Fraction equation.

Chapter VI

Results and general discussion

In Chapter VI the Performance Curves (P-ω), (Cp-TSR) extracted experimentally are analyzed and discussed, consistently with the methodology has been described in Chapter IV (**section 4.2**). Then, to validate the numerical model implemented, a comparison between the point extracted numerically and those obtained experimentally are conducted. Together with another validation strategy which allows to compare the water depths measured experimentally and numerically. To this end, the accuracy of the implemented model and how it can be used for the future application are discussed.

6.1. Upstream velocity effect on performance characteristics

In **Figure 87**, we can see the performance curves extracted experimentally in terms of P-ω for the three increasing flow rates. It is worth noticing that each point of these curves is a mean of instantaneous value measured in same observation time frame, according to an increasing tension applied on the electrical brake, which is installed on the top of the prototype.

Moreover, each curve corresponds to one upstream velocity value from 0.43 m/s to 0.68 m/s in the three flowrates considered.

The performance curves are shifted up in the (P-ω) chart of **Figure 87** as soon as the velocity inlet and the flow rate grow. By way of example, in the case of minimum flowrate (Q_1) considered, the absolute percentage of velocity increment it is equal to 4.65%, going through $v_1 = 0.43$ m/s to $v_2 = 0.45$ m/s, then the velocity increase further, passing from $v_2 = 0.45$ m/s to $v_3 = 0.47$ m/s with an increment of 4.44%. Later, the Δv computed between $v_3 = 0.47$ m/s and $v_4 = 0.62$ m/s, is the maximum increment for all tested cases, equal to 32%. Finally, a slightly increment is tested passing into the so-called totally opened condition from v_4 = 0.62 m/s to v_5 = 0.64 m/s, with relative increment of 3.23%.

The **Table 11** shown in detail both increment and decrement in percentage of velocity and related Maximum Mechanical Power (MMP) measured.

Table 11 Velocity and Mechanical Power increment in percentage

Q_1 = 0.052 m³/s					
v velocity inlet [m/s]	**μ Power max [W]**				
0.43	0.50				
0.45	0.67	Δv_{12}	4.65%	ΔP_{12}	33.89%
0.47	0.84	Δv_{23}	4.44%	ΔP_{23}	24.58%
0.62	2.64	Δv_{34}	31.91%	ΔP_{34}	215.72%
0.64	2.33	Δv_{45}	3.23%	ΔP_{45}	-11.68%
Q_2 = 0.059 m³/s					
0.43	0.89				
0.47	0.92	Δv_{12}	9.30%	ΔP_{12}	3%
0.50	1.28	Δv_{23}	6.38%	ΔP_{23}	40%
0.63	3.88	Δv_{34}	26.00%	ΔP_{34}	202%
0.65	1.48	Δv_{45}	3.17%	ΔP_{45}	-62%
Q_3 = 0.065m³/s					
0.44	1.10				
0.50	1.36	Δv_{12}	13.64%	ΔP_{12}	24%
0.51	1.81	Δv_{23}	2.00%	ΔP_{23}	33%
0.66	5.25	Δv_{34}	29.41%	ΔP_{34}	191%
0.68	5.07	Δv_{45}	3.03%	ΔP_{45}	-3%

As can be seen from the shown **Table 11**, according to the increment in velocity, the Mechanical Power increase as well, up to reach an increment than is greater than 100% due to the abrupt increment in velocity. This passage is located between speed point three and speed point four, which corresponds to a percentage increment in speed of 32%, 26% and 29%, respectively for Q_1, Q_2 and Q_3. However, the experimental results show that a further minimum increment in velocity, on the contrary, corresponds to a decrease in Mechanical Power extracted, this is also explained in the chart presented in **Figure 87**, where the light blue curves is lowered than yellow ones.

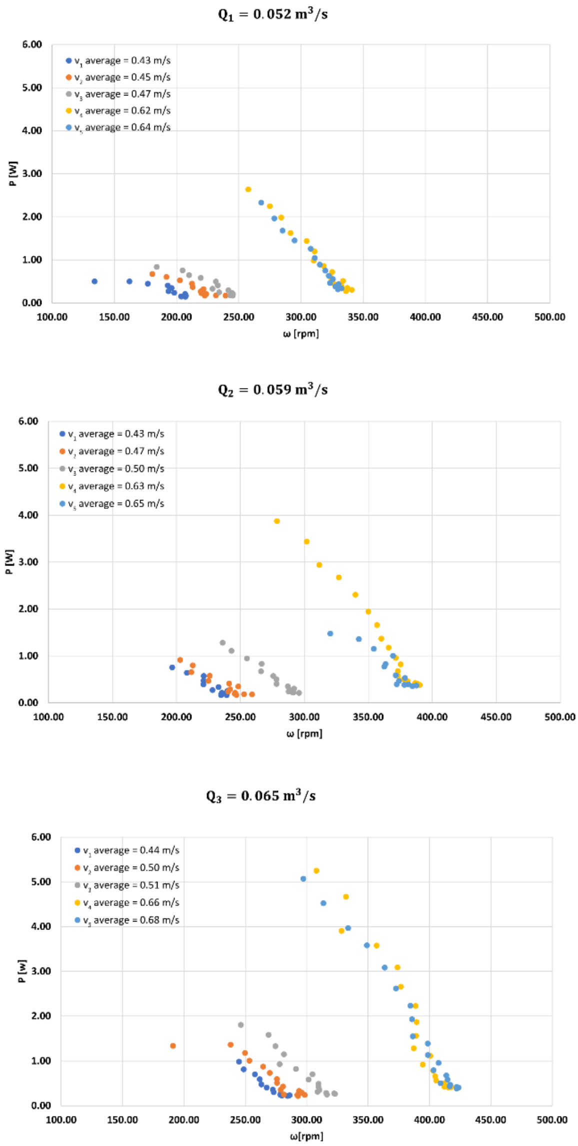

Figure 87 P-ω Performance curves in the three flowrates considered and five current conditions.

Suppose we select only the Maximum Power Points recorded for each considered flow rates and, plot them against the corresponding fluid inlet velocity range considered, as in **Figure 88**. In that case, we can notice that, regardless of the considered flowrate, the Mechanical Power decreases abruptly beyond a velocity value of about 0.62 m/s. More precisely, the velocity point corresponding to the MPP are 0.62, 0.63, 0.66, respectively, for the three flow rates.

This is due to the opening condition of the downstream control gate. Therefore, when the gate is nearly open (condition which coincides with maximum analyzed velocity), the water level on the upstream side is nearly at the same elevation as the turbine and, due to the surface drop on the downstream side (see **Figures 73, 74, 75** the case in which h_{gate} it is equal to 0.16 0.19 0.20 m from the base plane, respectively**)**, corresponds to the case in which the backside of the rotor is exposed to the air. Therefore, the interference between water and air decreases the Power Production.

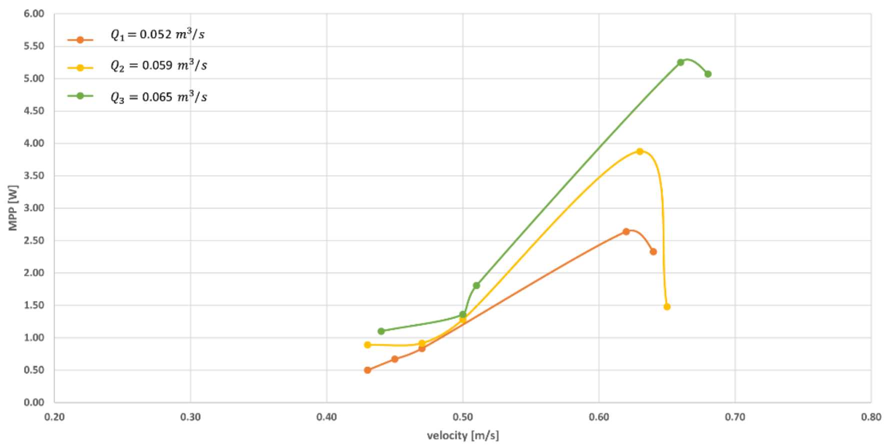

Figure 88 *Maximum Power Point (MPP) versus inlet velocity*

Nevertheless, very often the performance curves are expressed in terms of non-dimensional parameters like TSR on C_P as in **Figure 89**, to better compare the turbine performances in different flowrates and upstream velocity conditions. The Power Coefficient is computed as the Mechanical Power measured on the Maximum Theoretical Power Available, whereas the Tip Speed Ratio is computed as the Angular Velocity recorded, multiplied by the Turbine Radius, all divided to the average inlet velocity. It is evident that these two non-dimensional parameters are strictly dependent on the velocity field evaluation. This implies that the average velocity assessed for a reference cross section upstream of turbine, through the water depth measurement, also involves the reduction in velocity detected close to the walls. This implies a likely TSR and C_P overestimation.

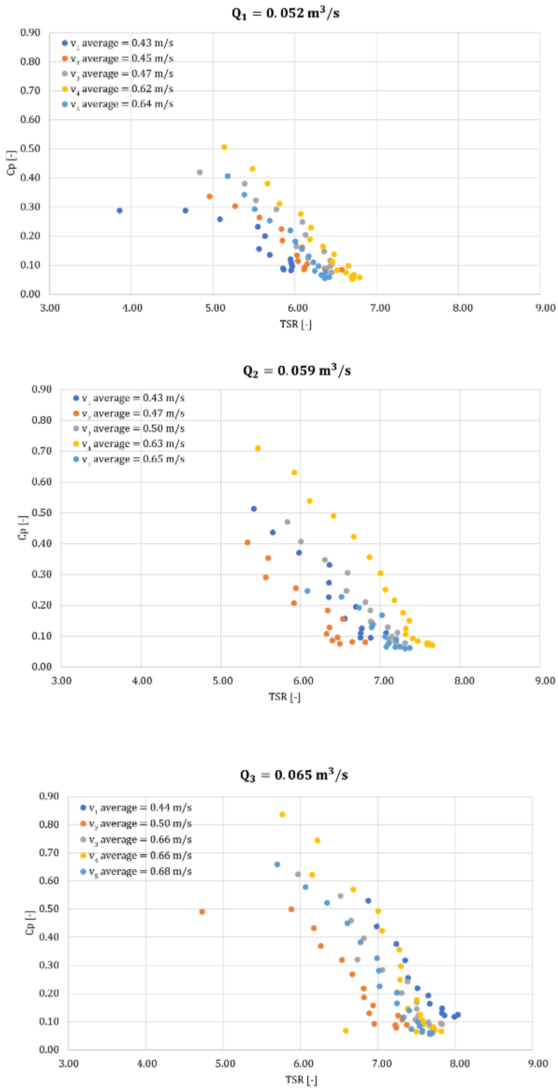

Figure 89 *Cp-TSR Performance curves in the three flowrates and five current conditions*

However, regardless of the overestimation of C_P and TSR, the range in which the prototype works goes from a TSR ranging from 4 to 8 and, from C_p of 0.30 to 0.84.

It is worth noting that the experimental performance curves are strongly different due to the Blockage Effect; in fact, if we consider an ideal turbine, these curves would be identical. This is because the Blockage gradually increases according to the downstream control gate rising. Moreover, the experimental results confirmed that the Betz Limit (C_{Pmax} = 0.59) is not applicable. For instance, at highest flow rate Q_3, the peak Power Coefficient at the minimum velocity is equal to 0.59, whereas at the maximum velocity exceed the Betz limit up to 41% reaching a value of 0.84, as in **Table 12** below.

Table 12 *Increment and decrement in percentage of Cp*

	Q_1 = 0.052 m³/s		
v velocity inlet [m/s]	**Cp [-]**		
0.43	0.29		
0.45	0.34	ΔC_{p12}	17%
0.47	0.42	ΔC_{p23}	25%
0.62	0.51	ΔC_{p34}	21%
0.64	0.41	ΔC_{p45}	-20%
	Q_2 = 0.059 m³/s		
0.43	0.44		
0.47	0.40	ΔC_{p12}	-7%
0.5	0.47	ΔC_{p23}	16%
0.63	0.71	ΔC_{p34}	51%
0.65	0.25	ΔC_{p45}	-65%
	Q_3 = 0.065 m³/s		
0.44	0.59		
0.50	0.50	ΔC_{p12}	-16%
0.51	0.62	ΔC_{p23}	25%
0.66	0.84	ΔC_{p34}	34%
0.68	0.74	ΔC_{p45}	-12%

On the other hand, if we combine the curves extracted, setting the same velocity value and, changing the flowrate considered as in **Figure 90** - from the minimum velocity, which corresponds to the fully filled channel with a control gate slightly closed, to the maximum, which corresponds to the fully opened condition, the effect of increasing flowrate also affects the Power extraction, causing a shift of the curves towards the increasing angular velocity axis.

This means that the prototype rotates more quickly according to both the flowrates and the velocity increase.

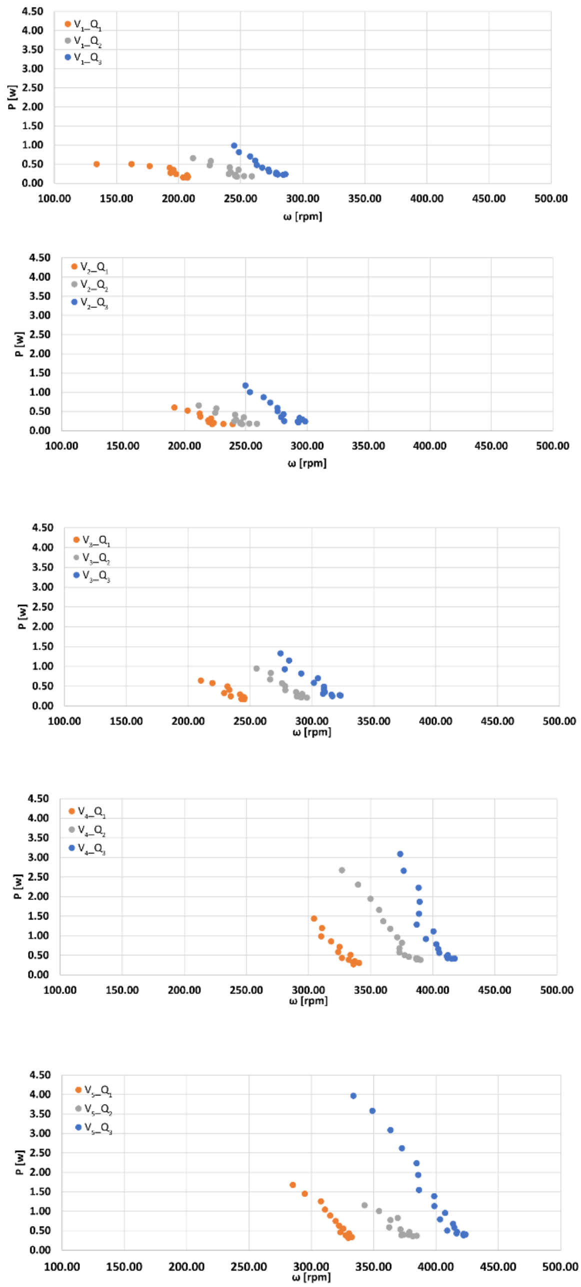

Figure 90 *Performance curves sorted for the same velocity.*

It is worth noting that the minimum velocity point also corresponds to the minimum Blockage applied, as summarized in **Table 13**.

Table 13 Blockage and Froude Number considered in the experiments.

v_{inlet} [m/s]	h_{up} [m]	Br [%]	Fr [-]
Q_1 = 0.052 m³/s			
0.43	0.40	36%	0.22
0.45	0.38	38%	0.23
0.47	0.37	39%	0.25
0.62	0.28	52%	0.37
0.64	0.27	54%	0.39
Q_2 = 0.059 m³/s			
0.43	0.45	32%	0.20
0.47	0.42	35%	0.23
0.5	0.39	37%	0.26
0.63	0.31	47%	0.36
0.65	0.3	49%	0.38
Q_3 = 0.065 m³/s			
0.44	0.49	30%	0.20
0.50	0.44	33%	0.24
0.51	0.43	34%	0.25
0.66	0.33	44%	0.37
0.68	0.32	46%	0.38

The Blockage Br in fact accelerates the flow around the rotor, producing more power than that is produced in unrestricted flow case. However, the same problem can be observed from another viewpoints.

The experimental water channel is horizontal. For this reason, the current is unstable, and evaluating the Froude Number allows us to identify the approach to critical depth. This dimensionless number is computed from the evaluation of upstream water depth, in what has been considered the reference section upstream. As can be understood, the **Table 13** the Froude number increases with Blockage, this because for a sub-critical flow, the water depth goes down as the energy is extracted, increasing the Blockage effect. In fact, the difference in static head around the turbine rotor makes the total available energy grater then the kinetic one. Moreover, as can be seen from the **Figure 91** the C_P suddenly decreases when the Froude number quickly increases, and this happen between speed point three and speed point four. Precisely, the Froude Number is incremented of respectively 52%, 41% and 48%, from velocity point three to velocity point four. Therefore, from the **Table 13**, we can see that Froude Number moves from 0.25 to 0.37 in Q_1, from 0.26 to 0.36 in Q_2 and from 0.25 to 0.37 in Q_3.

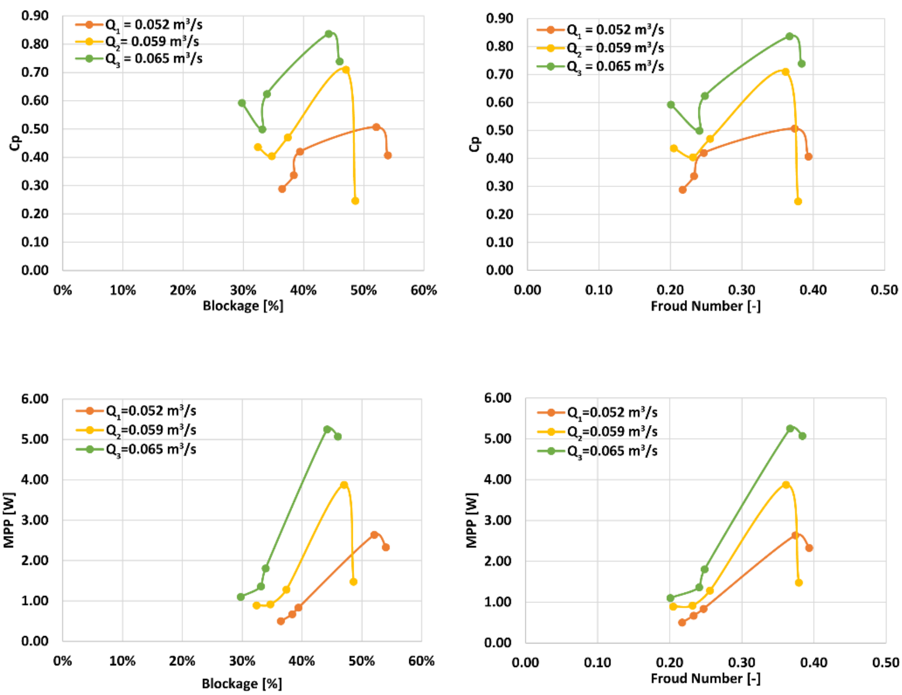

Figure 91 Cp vs Br and Froude Number; MPP vs Br and Froude Number

Essentially, beyond the Blockage value that straddles v_4 and v_5, so when the Blockage ranging from 39% to 52% in Q_1, from 37% to 47% in Q_2 and, from 34%

to 44%, respectively, the water level at the upstream side is nearly at the same rotor elevation.

However, due to the drop in water surface downstream of turbine, which is linked to the power extraction, the rotor backside is exposed to air, as shown in **Figures 73**, **74** and **75**.

Therefore, the decline in the power coefficient depends on two factors:

1. the turbine is not entirely covered with water, reducing the effective area,
2. the partial flow separation occurs as the air enters the suction side of the blade, as reported in [93] for partial submerged turbines.

The flow separation affects the Lift Force, producing negative torque values and causing the suddenly drop in power coefficient. **Figure 92** shows the C_P variation according to velocity and Blockage effect through a surface chart.

It is evident that the Blockage has a beneficial effect on power production until separation effects take over which, on the contrary, sharply decrease the performance of the analyzed prototype.

Finally, the Froude Number maximizes the power extraction, and from conducted calculations, it has been proved that all the points along the channel are subcritical.

In terms of absolute percentage, therefore they increment each other enough, approximating themselves to critical condition but never reached it.

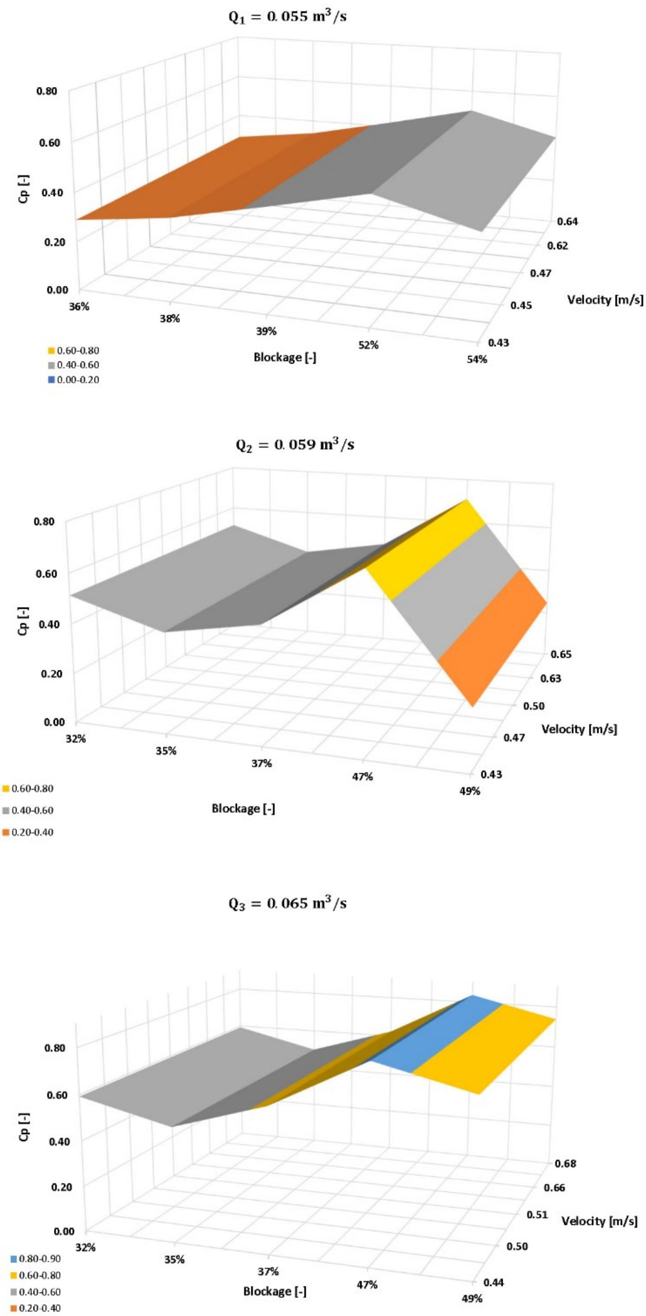

Figure 92 *Surface chart of Cp vs Blockage and Velocity*

6.2. Comparison between analytical model and experimental results

To better understand the present study, the experimental results are first compared with the calculation of LMADT explained in detail in the **Appendix 2**. In this analytical model, a simplified hypothesis is assumed which does not account for the turbine rotational speed.

Moreover, in the analytical model the calculation sequence considers the Maximum Power Coefficient function of:

- By-pass Coefficient β_4,
- Blockage Coefficient B_r,
- Turbine velocity $\alpha 4$ Coefficient,
- Wake flow velocity Coefficient α_{4w}.

This implies that in unconfined condition, the C_p max is equal to Betz limit, and the Blockage and By-pass coefficients would be constant. However, in the channel case, it has been demonstrated that the values are strongly affected by the operating conditions.

The axial induction factors *a* physically measures how the turbine presence can stop the flowing water to obtain the maximum available power output. The angular velocity able to reach the maximum power corresponds to the α value which is correlated with the Maximum Power analytically computed.

The optimum power is obtained by solving the quadratic polynomial equation through a MATLAB code:

$$\left(\frac{1}{2}F_r^2\right)\beta^4 + (2\alpha F_r^2)\beta^3 - (2 - 2B + F_r^2)\beta^2 - (4\alpha + 2\alpha F_r^2 - 4)\beta + \left(\frac{1}{2}F_r^2 + 4\alpha - 2B\alpha^2 - 2\right) = 0 \qquad (133)$$

where $Fr = v/\sqrt{gh}$ is the experimental upstream Froude Number.

The calculation has been solved for α values ranging from 0.11 to 0.99, in the three flowrates and the whole velocity points tested, deducted from the water level measurements.

The analytical results confirmed that the MPPs are reached when the α value is equal to 1/3 of the inlet current and gradually decreases according to the increment in α value.

Figure 93 shows the experimental and analytical comparison, thus, in the point where the analytical model does not give imaginary solutions. This happens precisely when in the experiments for each flowrate, the Froude Number increases of 52%, 41% and 48%, respectively from velocity point three to velocity point four. In these points in fact, it was observed experimentally that the water elevation at upstream side is nearly at the same rotor elevation. This means that the separation phenomenon is reducing the rotor performances through these points. The current begins to be instable exactly because it approximates the critical conditions. This is the reason why these experimental points have been delated from the comparison.

Therefore, this also implies that exists a strict relationship between submersion elevation and rotor performances.

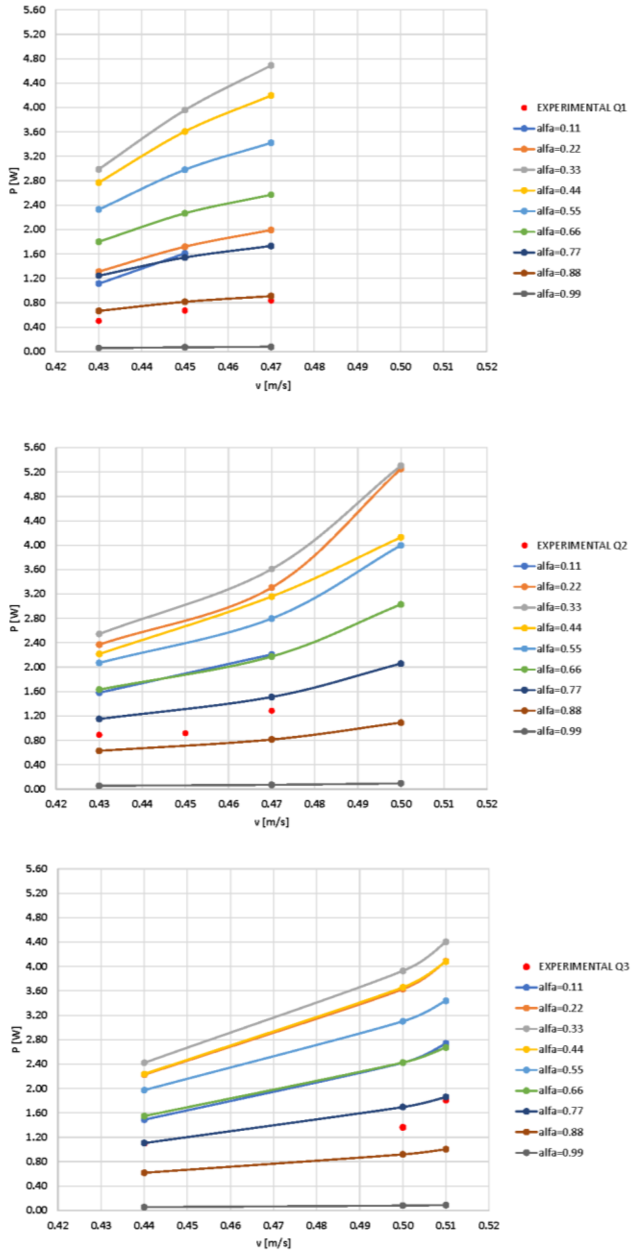

Figure 93 Experimental and analytical comparison in P-v chart

Experiential results position themselves at a lower α value than what is computed as the best α value from the analytical calculations.

However, we can see in **Figure 93** that the experimental points shifted up according to the flowrate increment as the analytical ones. Moreover, the curves interpolating these points tend to have an increasingly marked upward curvature as the flowrate increase. On the other hand, the analytical model confirms that the best α value is equal to 1/3.

Conversely, the experimental points are closer to α value of 0.77 and 0.88 than to $\alpha = 0.33$.

This because the analytical model does not consider friction losses from the channel walls and the precision and bias errors correlated to the experimental measurements. This may explain the discrepancy between analytical and experimental results.

At this regard, **Figures 94** demonstrates that the Peak Power Coefficient concerning the upstream inlet velocity increases with velocity.

Nevertheless, for the analytical results the peak Power Coefficient tends to Betz limit, for the lowest velocity values and so when the Blockage applied is minimum.

However, the higher velocity is considered, the higher difference between flowrates is detectable.

On the other hand, **Figure 95** shows that the Blockage Ratio variation increases at increasing the upstream velocity.

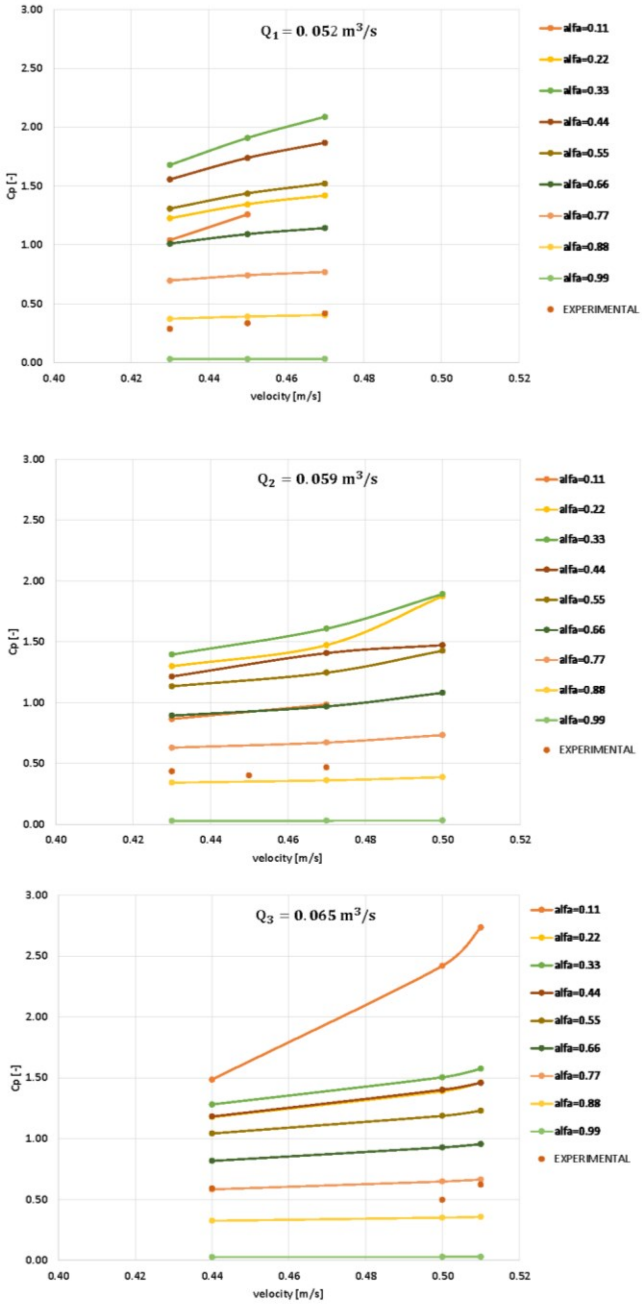

Figure 94 *Experimental and analytical results in Cp-v chart.*

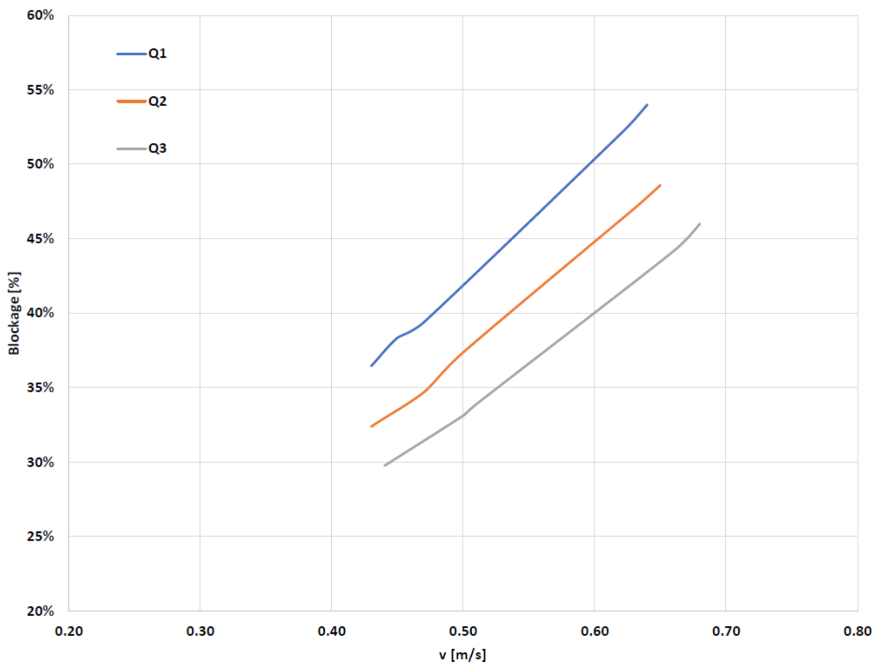

Figure 95 *Blockage variation with upstream inlet velocity at flowrate increasing.*

6.3. Numerical model validation

The numerical model has been validated with experimental results using two different approaches.

Firstly, the experimental performance curves in terms of TSR-C_P were compared with numerical ones, in specific operative conditions for each velocity and flow rate value considered in the experiments.

In greater details, due to the long computational time costs (steady state plus 10 s transient simulations spend 5 days of computation), the performance curves were compared rather than along each point, in 15 specific operative conditions, corresponding to the same voltage value of 5.5 V.

Therefore, 5 points for each flow rate, corresponding to five downstream control gate height and consequentially to all tested cases. As a result, the comparison from the slightly closed to nearly opened condition, getting close to the critical flow case, was conducted.

Nevertheless, referring to the same braking tension applied to the rotor means a specific measured angular velocity value is associated with it. This value increases according to the inlet current velocity, so passing from the lowest to the highest velocity tested point.

Therefore, the angular velocity measured is then applied to the interface boundary condition of the rotational domain. Moreover, the value associated to the inlet boundary condition is deducted from the water depth measurement in the reference section.

In other words, referring to the same electric voltage brake value, means conceptually that if the velocity increments, the numerical-experimental point of comparison is moved along the decreasing branch of the TSR-C_p performance curve.

However, 15 comparison points are not enough to validate the CFD Model, for this reason three cases were selected to trace a complete numerical curve, even though the high computational costs.

Specifically, three experimental cases were selected to trace the whole numerical curve in the Cp-TSR plane.

- The first selected case (C_1) is one in which the flowrate assumes its minimum value, i.e., $Q_{1,}$ =0.052 m^3/s and the channel is fully filled; therefore, the control-gate downstream is slightly closed and consequentially the velocity upstream, is the minimum value experimentally tested v_1=0.43 m/s.
- The second selected case (C_2) is one in which the flowrate assumes its intermediate value, i.e., Q_2=0.059 m^3/s and the control gate downstream assumes an intermediate height, so the velocity v_3 its equal to 0.50 m/s.
- The third selected case (C_3) is one in which the flowrate assumes its maximum tested value, i.e., Q_3=0.065 m3/s and the velocity is the maximum as well and it is equal to v_5=0.68 m/s.

From **Figure 96 to Figure 98** all the numerical points simulated for each experimentally tested velocity inlet and flowrate are plotted in the plane Cp-TSR. As we can see, the numerical model almost always overestimates the experimental points, except in $Q_1\_V_1$, $Q_2\_V_1$, $Q_3\_V_3$ and, $Q_3\_V_4$ cases where, conversely, returns a lower value than what experimentally measured.

Figure 99 depicts the relative error between experimental and numerical results, showing a maximum value always lower than 15%.

It is worth noting that to better understand the results numerically extracted, it would be useful to trace at last one or two complete performance curves, in different flow scenarios. Therefore, the inlet velocity current should be fixed in one of the tested flowrates, and varied the angular velocity applied to the interface between rotational domain and stationery one, it could be traced the entire performance curve along the power stage.

These are the cases that has more points and are signed on the plots as C_1 in Figure 96, C_2 in Figure 97, and C_3 in Figure 98, respectively. This is further evidence confirming that the CFD model slightly overestimates the C_p coefficient.

However, a reasonably good match has been found between experimental and numerical results for the whole range of tip speed ratios. The higher percentage of error is shown in the minimum velocity case for Q_1 and Q_2, and in the critical velocity point V_4 in the flowrate case of Q_2= 0.059 m^3/s. All the other points compared remain around a relative error of about 5%.

$Q_1 = 0.052\ m^3/s$

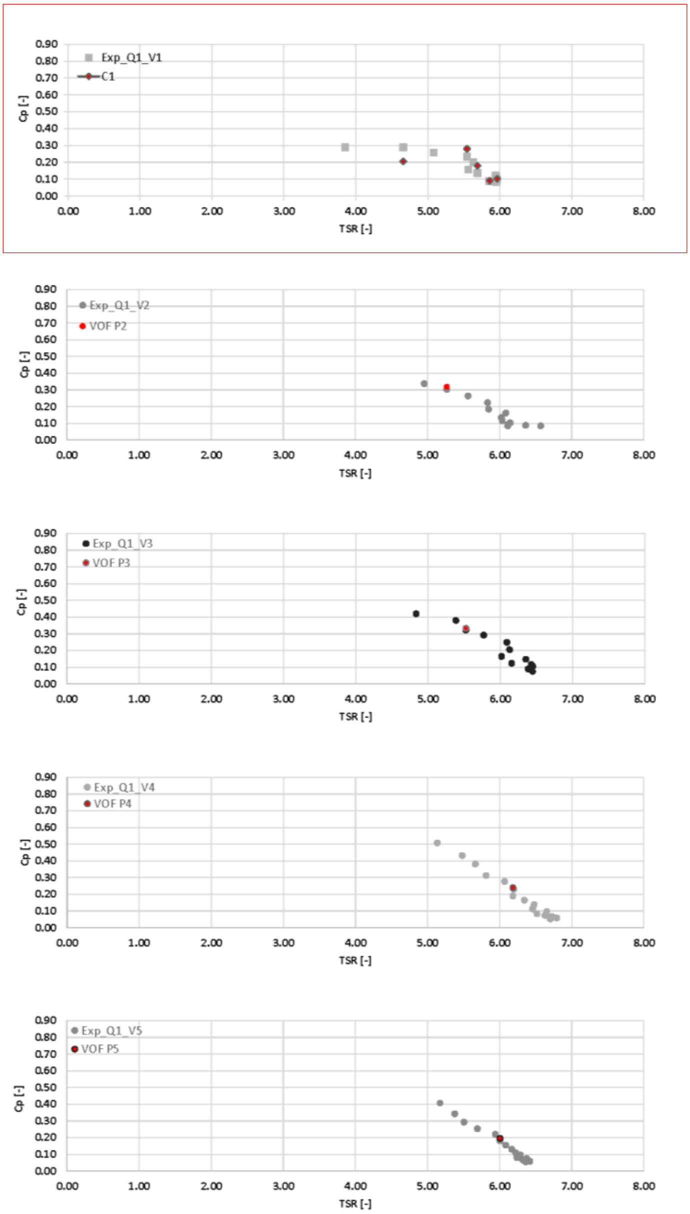

Figure 96 *Experimental and Numerical comparison in terms of TSR-C_P in Q_1 flowrate case*

$$\mathbf{Q_2 = 0.059\ m^3/s}$$

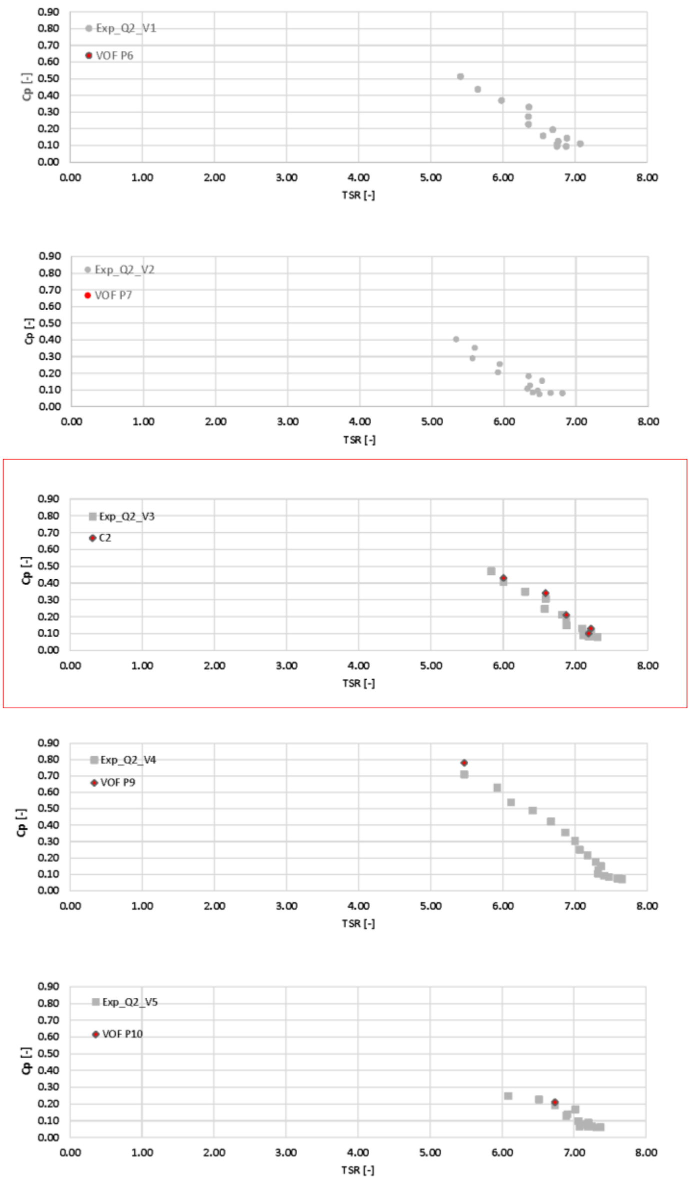

Figure 97 *Experimental and Numerical comparison in terms of TSR-C_P in Q_2 flowrate case*

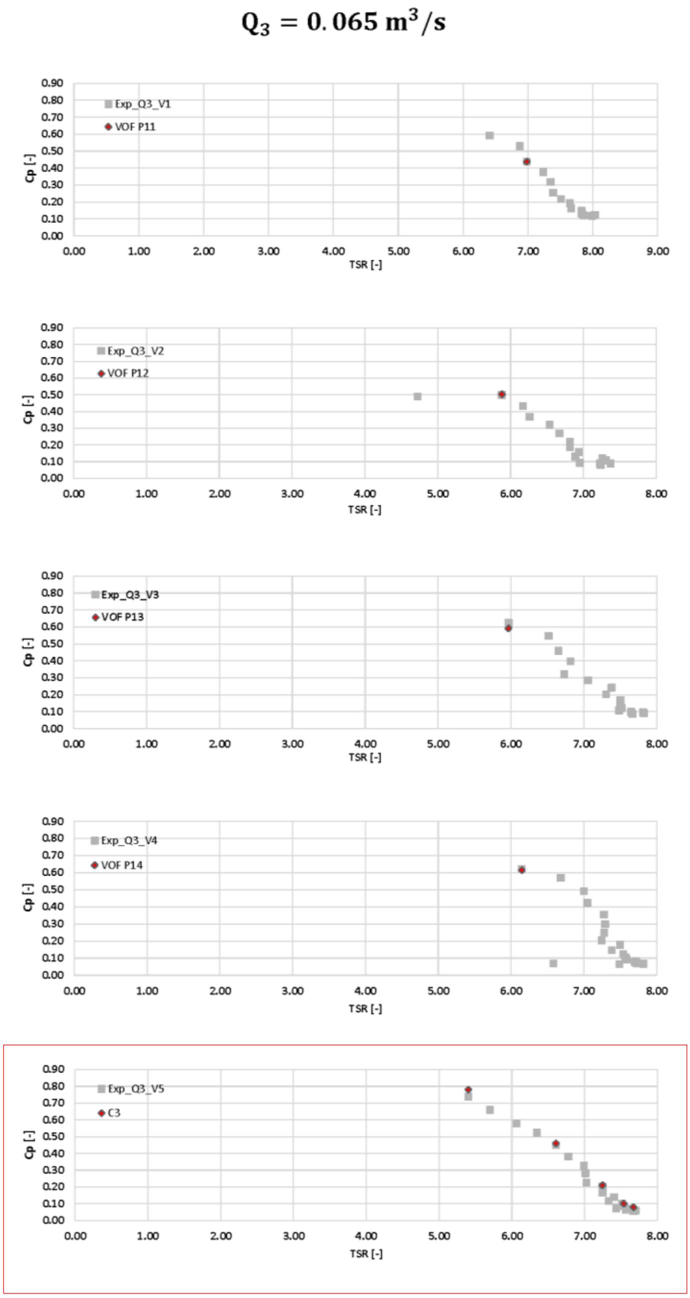

Figure 98 *Experimental and Numerical comparison in terms of TSR-C_P in Q_3 flowrate case*

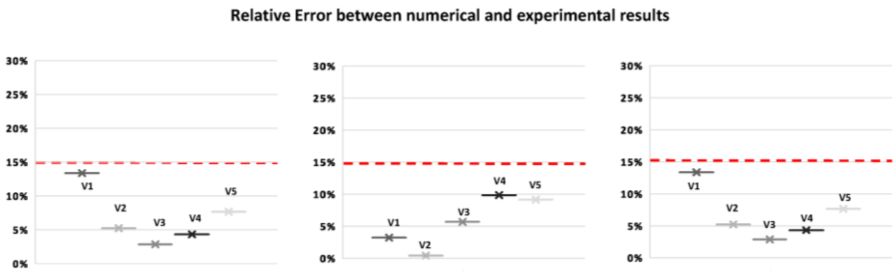

Figure 99 Relative error concerning the experimental results measured.

The second CFD Model validation strategy deals with the comparison of free surface variation measured in terms of water depth, to what the numerical model returns in terms of water volume fraction computed for each experimental known section, located upstream and downstream of the turbine, respectively.

The second validation strategy has been implemented to directly prove how the CFD model is also able to predict the free-surface variation.

To this end, the water depth numerically computed in the same section of measured water depth gives information on the model prediction capacity.

Nevertheless, we have selected the cases concerning the first three values of velocity for each flow rate.

Therefore, it is going to present the case from the fully filled condition and control gate slightly closed with the minimum velocity and so minimum Blockage, up to the intermediate flow field configuration, where the control gate is not nearly opened but the velocity flow field reaches an average value of 0.50 m/s, for the analyzed cases.

Figure 100 to **Figure 102** show the results of the comparison through a scaled scheme, in the 13 sections in which the water depth was measured covering a length of 1.3 m from the upstream to the downstream side of the turbine section. On the left side, a graduated line allows reading the corresponding value of the measured and computed water depth, respectively.

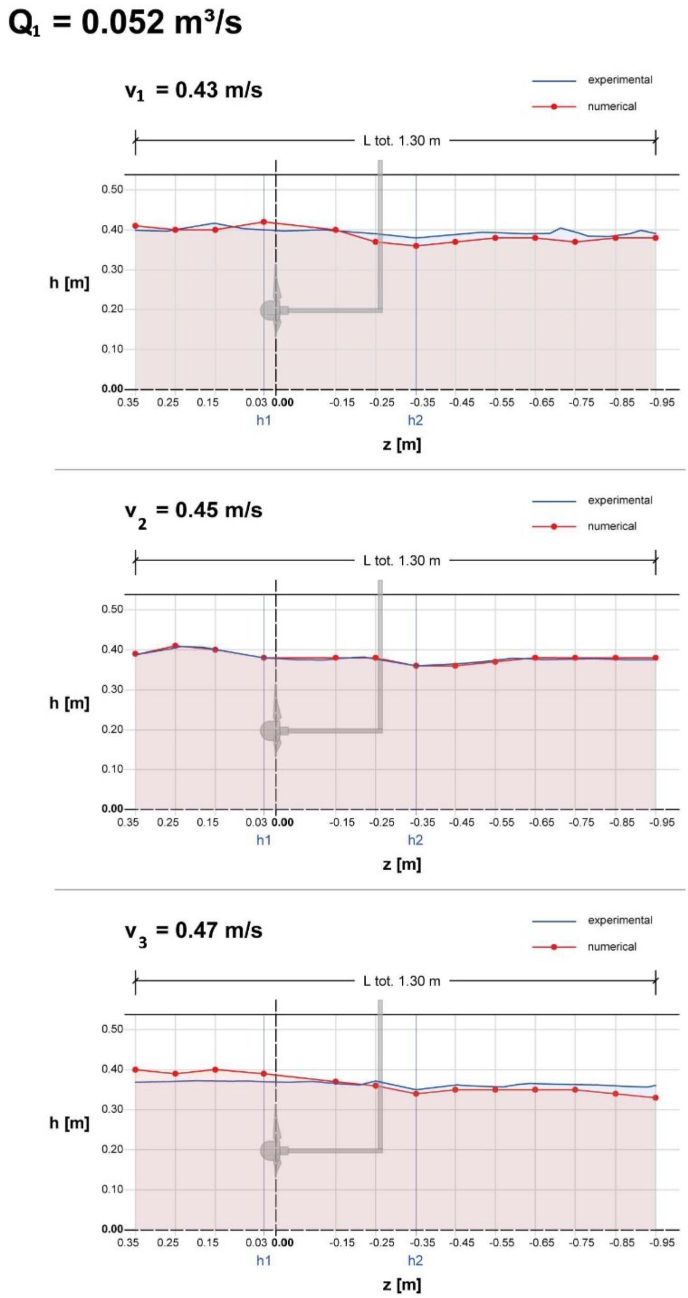

***Figure 100** Numerical Model validation through experimental and numerical comparison of water depth Q_1*

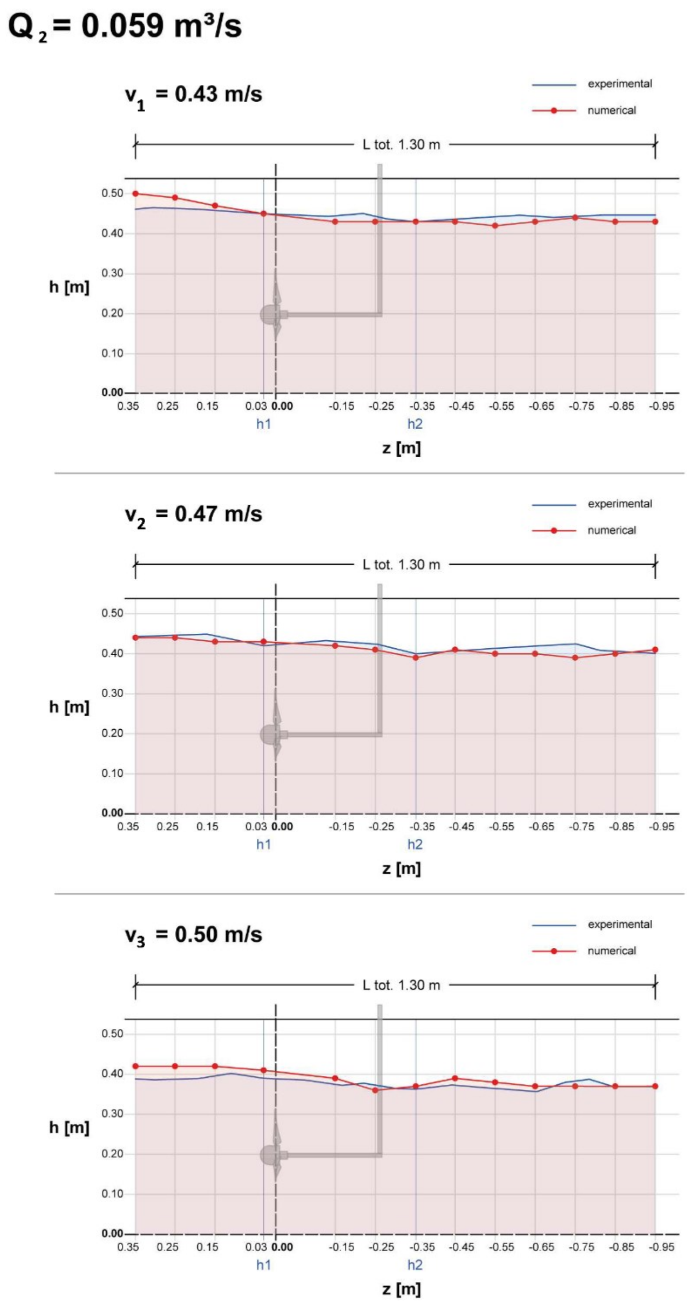

Figure 101 *Numerical Model validation through experimental and numerical comparison of water depth* Q_2

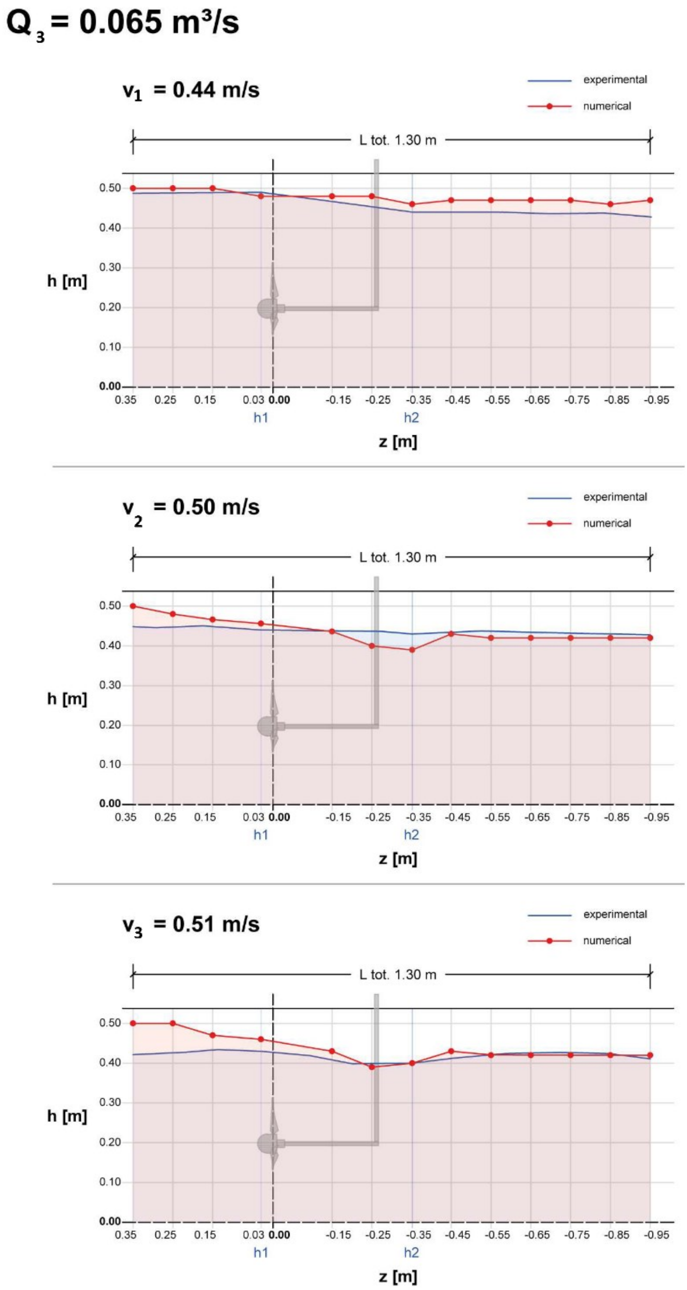

***Figure 102** Numerical Model Validation through experimental and numerical comparison of water depth Q_3*

As deductible from the **Figures 100-102**, a good match between numerical and experimental results is observable.

However, in all results considered, the CFD Model overestimates the water depth, especially in the upstream side of the turbine. This difference is even more evident where the flow rate and the velocity increase, even though, the model simulates quite well the water depth drops downstream of the turbine, marking the water drop which is as evident as the velocity and flow rate increase. Taking as an example the case Q_3_V_2 the model returns a lower water depth than what experimentally measured.

It was possible to create this schematic representation of the free water surface variation in the channel, due to the implementation of a VOF (Volume of Fluid) model, able to simulate not only the longitudinal variation, but also the interaction of channel wall boundaries and air domain. Through a transition area from water and air computed by the volume fraction associated to each cell.

The **Figures 103, 104** and **105** show the water volume fraction contour plotted on a cut plane parallel to the flow direction and so perpendicular to the inlet boundary.

Through these figures we try to highlight in a different way from the previous schemes, what the model foreseen, scaled and overlapped to the original photograph took during the experiments with the water volume fraction computed numerically.

On the contrary, it has been proved that when the Power Coefficient reaches the highest recorded values, the numerical model does not give good results; this perhaps is due to the current approximation to the critical flow conditions. **Figure 106** shows the discrepancy obtained in the v_4 case for the minimum, medium and maximum flow rate considered in the experiments, in terms of water depth.

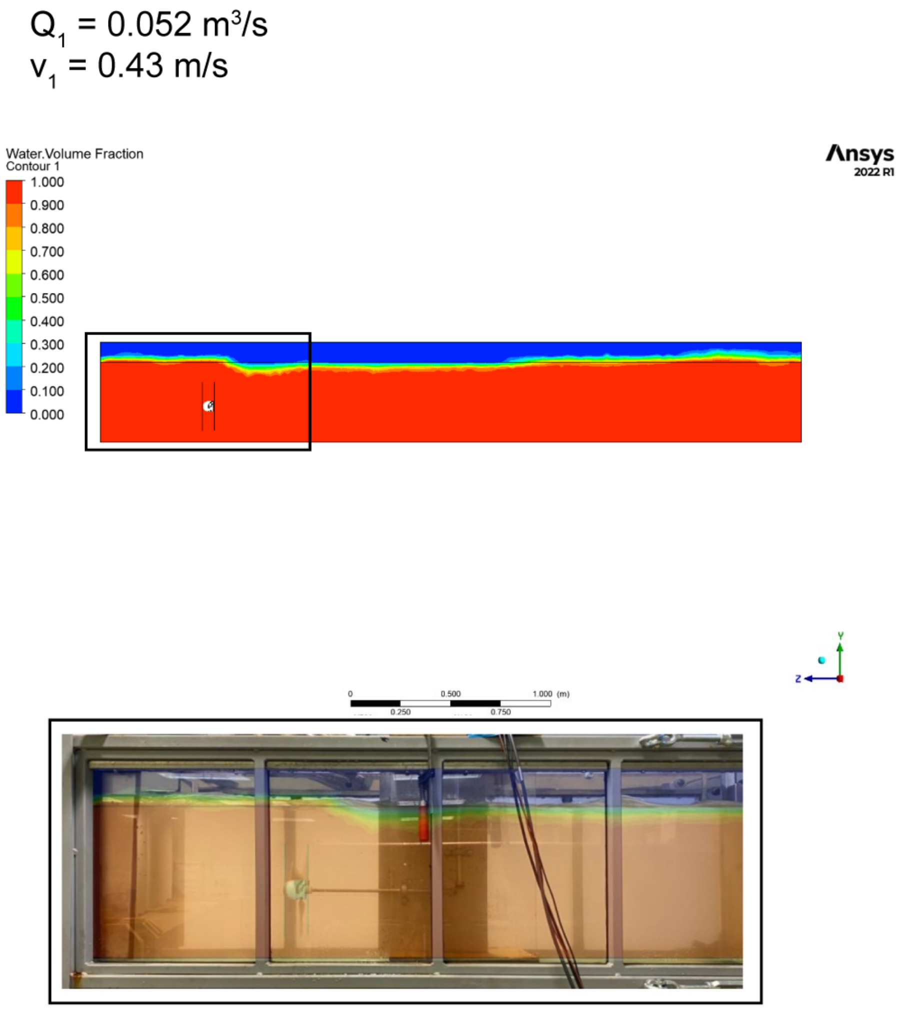

Figure 103 *Overlapping between water volume fraction contour computed from the CFD model and the photograph taken in the experiments in the Q1_v1 case.*

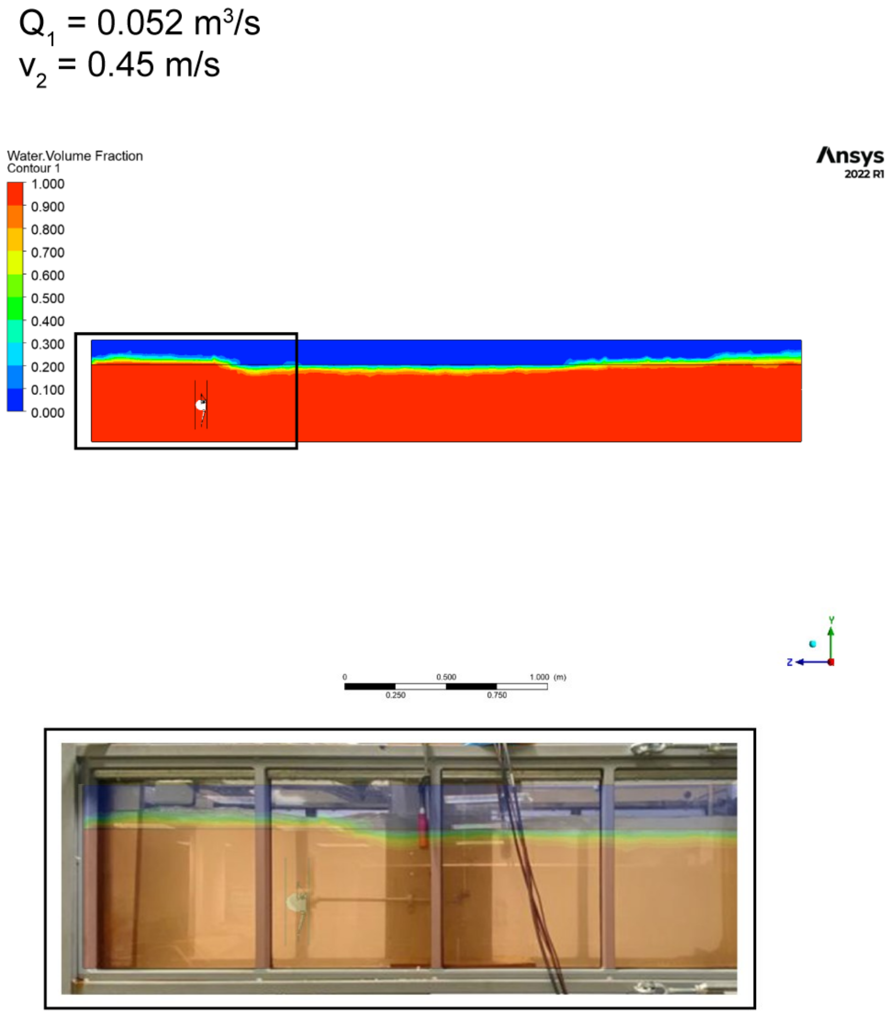

Figure 104 *Overlapping between water volume fraction contour computed from the CFD model and the photograph taken in the experiments in the Q1_v2 case.*

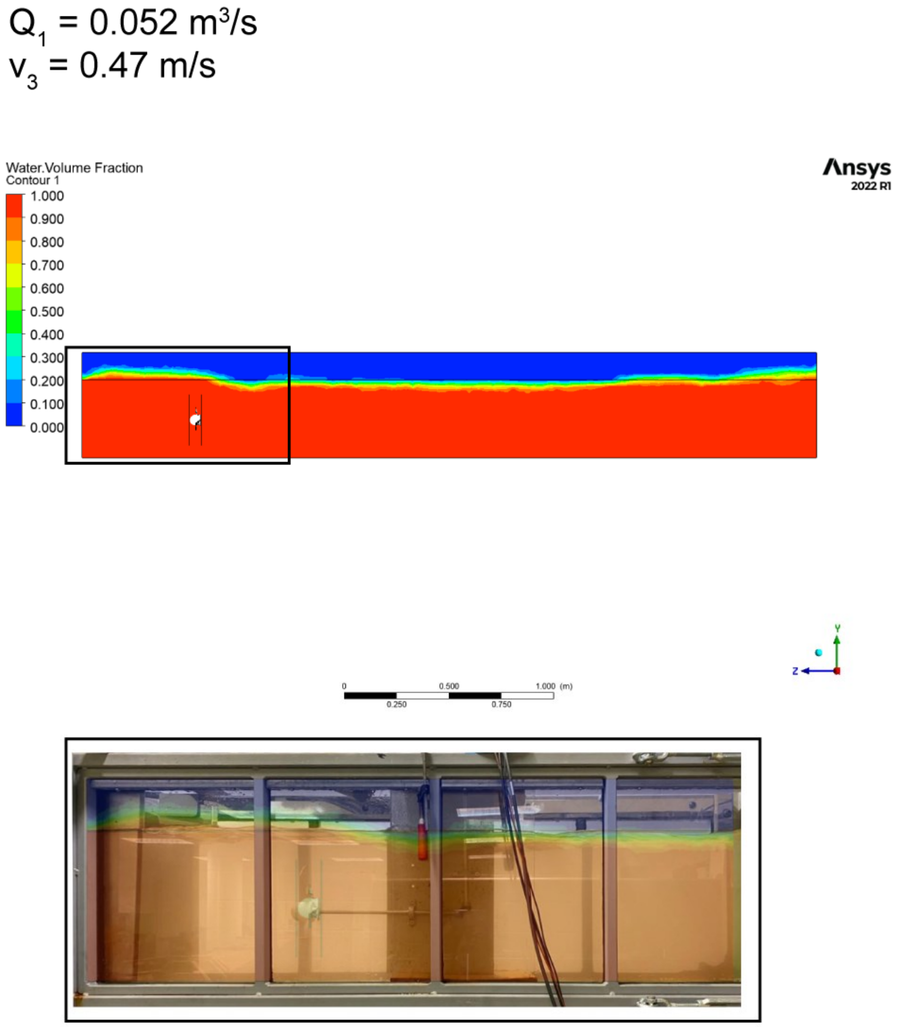

Figure 105 *Overlapping between water volume fraction contour computed from the CFD model and the photograph taken in the experiments in the Q1_v3 case.*

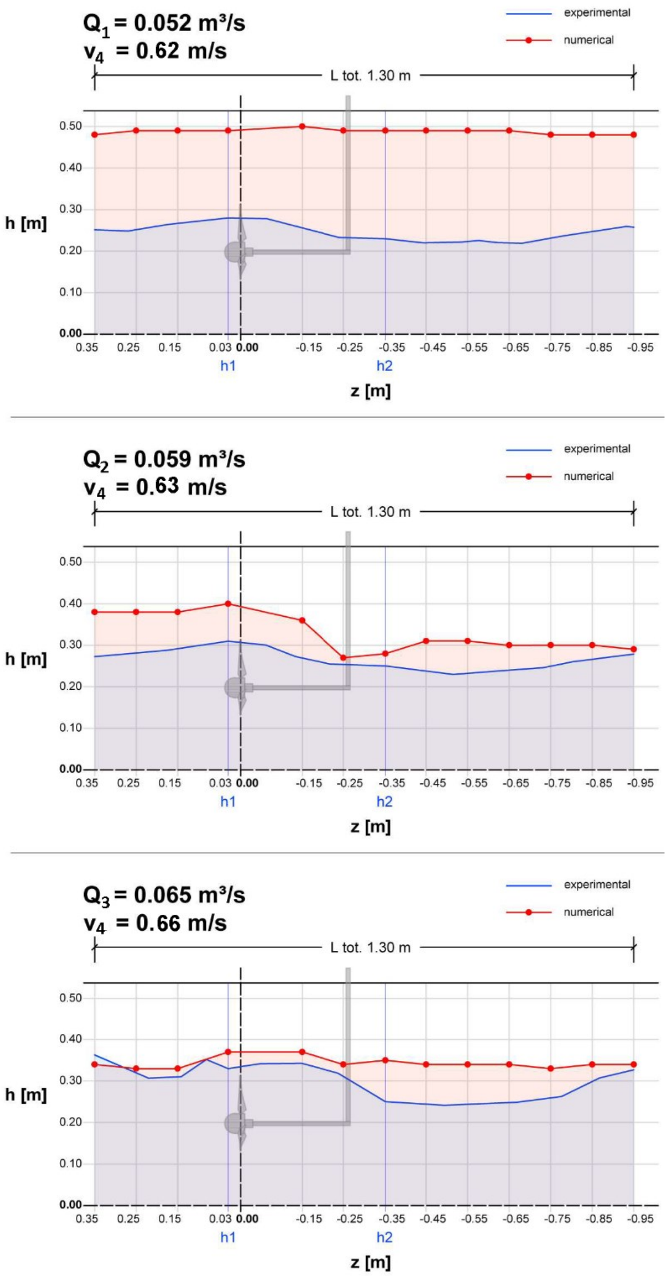

Figure 106 *Numerical discrepancy with respect to the experimental results in Q_1, Q_3 and Q_4 v_4 case*

In conclusion, we can assume that the numerical model calibrated with experimental results does not return a reliable matching in overall tested cases, highlighting the importance of experimental characterization of this kind of turbines.

On the other hand, the CFD Model allows us to understand and visualise the wake recovery length and, how the reduction in water height amplifies the produced wake downstream. This phenomenon is translated in a more evident height drop downstream of turbine, according to blockage increment. The streamwise velocity profile along the streamwise direction is plotted in **Figure 107,** in the highest flowrate Q_3 case and the maximum velocity flow condition v_5 considered in the numerical simulations.

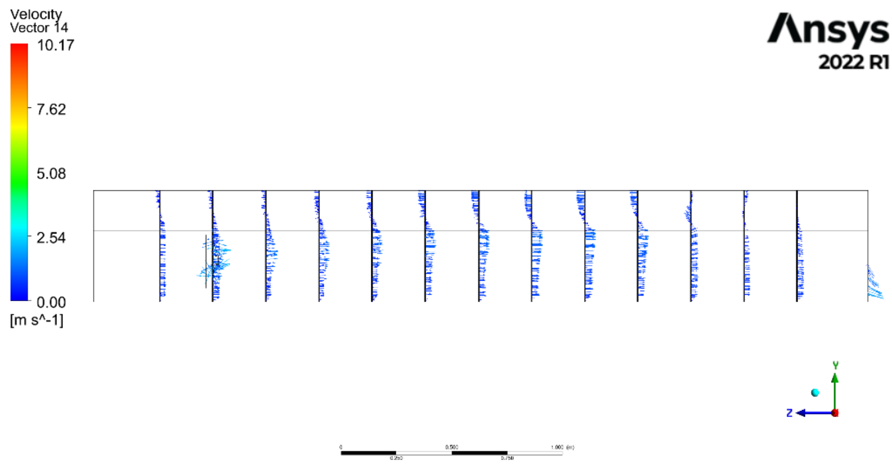

Figure 107 *Streamwise velocity profile along the streamwise direction from 1 D upstream to 11 D downstream*

We clearly appreciate an inversion of velocity profile, which is gradually reduced until arriving at the last section located at 11D downstream of turbine, thus exactly before the control gate section. This inversion is produced by the wake expansion downstream due to turbine rotations. Moreover, the atmospheric pressure downstream, in the part of channel exposed to the air, attracts the distorted streamlines. This combined effect produced the free-surface deformation marking evident the heigh drop downstream of the turbine. In **Figure 108** we can see the velocity profile in terms of v_w, so the component along the streamwise direction (-z) on water height Y [m]. These velocity profiles extracted from ANSYS FLUENT are computed projecting the velocity vectors on four lines perpendicular to the flow direction, located in the middle of the channel at 1D, 2D, 3D, and 10D downstream of turbine, respectively.

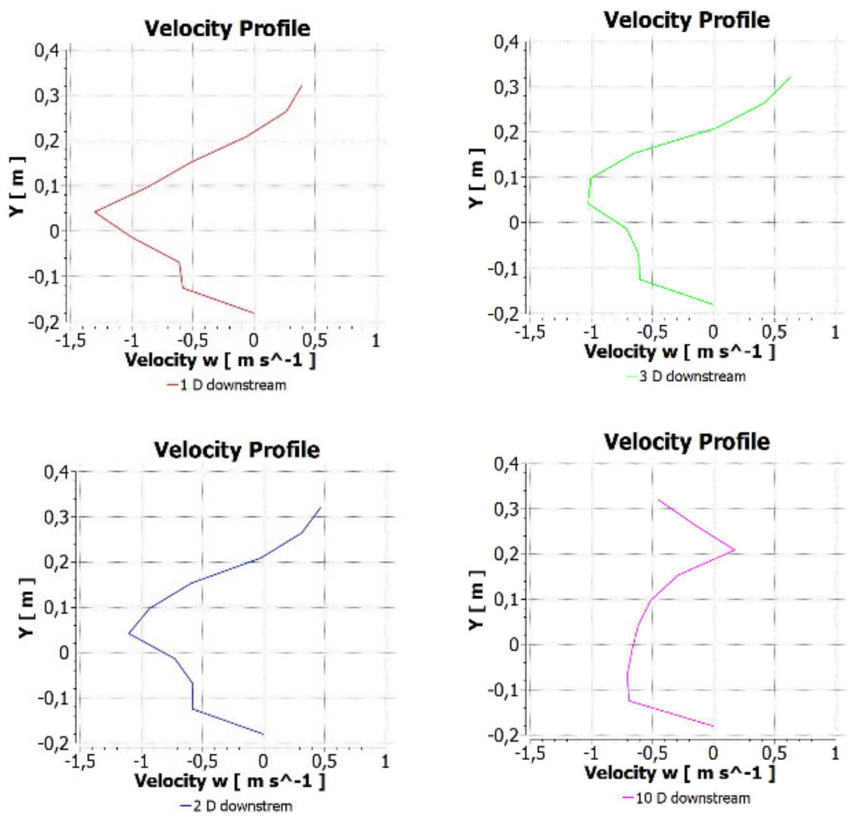

__Figure 108__ Velocity Profile along the streamwise velocity component in four selected cases downstream of the turbine

Figure 106 shows through the velocity profiles the wake's decrement produced downstream of turbine, which is responsible of the streamlines inversion that is as evident as the section is close to the turbine position.

Therefore, as a result 1D downstream of turbine it is observed the highest decrement in streamwise velocity component.

Another possibility to visualize the wake is through the velocity contours projected on different planes upstream and downstream of turbine, located at a mutual length of 1 D, as in **Figure 109**. It turns out one more time, that the negative velocity area related to the wake propagation varies according to the distance from the turbine section.

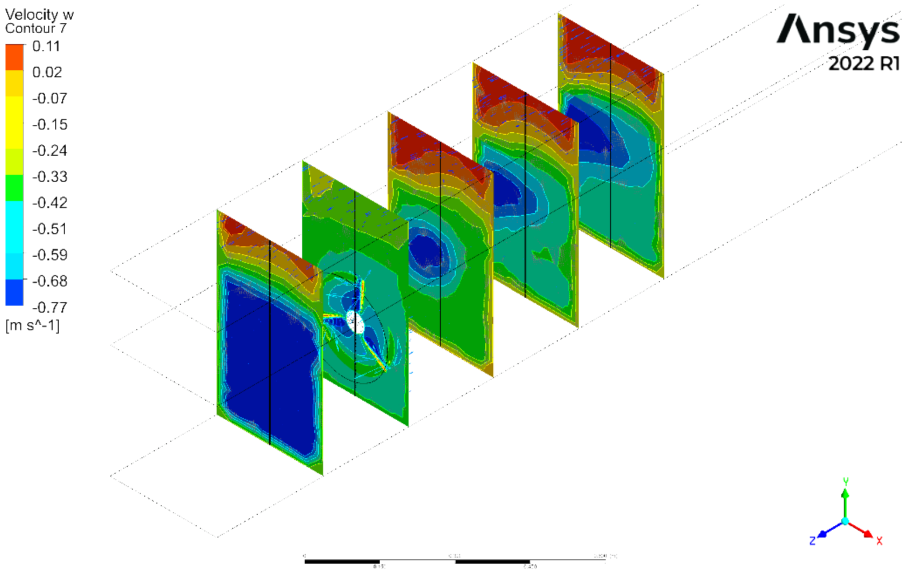

Figure 109 *Streamwise contour on five different planes upstream and downstream of turbine*

6.4. Scale considerations

To extend the present work based on the numerical and experimental characterization of a HAHWT to a real case study, it is necessary to understand how to think and consequently how to possibly scale the prototype. Sure enough, the turbine prototype developed in this work has a dimension conditioned by the size of the test rig. Therefore, the model is small compared to those used to generate electricity, which should be bigger than in the case of a real field test. Larger models would work better than smaller ones, among other things, because the ratio of mechanical losses to power output decreases at the turbine size increases. However, in the hydrokinetic turbines, the scale considerations are more complex than for wind turbines where the kinematic similarity is function of Strouhal number and the Power Coefficient is exclusively function of TSR [94]. This sub-chapter clarifies how to proceed when reasoning about scale considerations and what type of similarities it is may be considered between a prototype and an actual turbine.

In a low velocity scenario, the Reynolds Number has a crucial role. Because, for small Reynolds Number, the lift-based turbine performances are usually reduced due to the low performance of blade profile (as demonstrated in **Figure 36** of Chapter III). Therefore, larger turbines so with larger chord (as expressed in **Eq. (10)** of Chapter II), which is the characteristic parameter for turbine blade profile, has better efficiency characteristics for low velocities condition. This means that for the same Tip Speed Ratio, the Reynolds Number is proportional to the turbine size. On the other hand, also the Froude Number influence the kinematic similarity for the hydrokinetic turbines.

Typically, it is hard to maintain the same Froude Number value in case the turbine size changes. At this regard, in the tests performed for the specific case study, at different current velocity conditions, it corresponds to a different value of Froude Number, and this is the reason for the multiple C_P-TSR curves.

This also allows to analyze qualitatively the performance of larger turbines. Therefore, at the same upstream velocity, a larger turbine will have a smaller Froude Number and will produce a larger Blockage, as in Eq. (133). Moreover, as experimentally proved, larger Blockage generates higher Power Coefficient, so it can be confidently stated that a larger turbine at the same velocity will perform better than the studied model.

In general terms, the laws of similitude which provide basis for the interpretation of physical and numerical model results, can be summarized through three different approaches:

1 Geometrical similarity
2 Kinematic similarity
3 Dynamic similarity

1) Geometrical similarity means that flow field and boundary geometry of model (marked with subscript m) and prototype (subscript p) have the same shape. Therefore, the ratio between corresponding lengths in the model and prototype are the same, and can be expressed through the following three relationships:

For the Characteristic lengths we have:

$$d_r = \frac{d_p}{d_m} = \frac{l_p}{l_m} = l_r \tag{134}$$

For the Area:

$$\frac{A_p}{A_m} = \left(\frac{d_p}{d_m}\right)^2 = \left(\frac{l_p}{l_m}\right)^2 \tag{135}$$

For the Volume:

$$\frac{Vol_p}{Vol_m} = \left(\frac{d_p}{d_m}\right)^3 = \left(\frac{l_p}{l_m}\right)^3 \tag{136}$$

In case of turbine the characteristic length could be:

The chord length

The rotor radius

The blade length

2) Kinematic similarity means that as well as having the flow fields with the same shape, the ratios of corresponding velocities and accelerations must be the same through the flow. This implies that flows with geometrically similar streamlines are kinematically similar:

$$\frac{\overrightarrow{V_{1p}}}{\overrightarrow{V_{1m}}} = \frac{\overrightarrow{V_{2p}}}{\overrightarrow{V_{2m}}} \tag{137}$$

$$\frac{\overrightarrow{a_{1p}}}{\overrightarrow{a_{1m}}} = \frac{\overrightarrow{a_{2p}}}{\overrightarrow{a_{2m}}} \tag{138}$$

3) Dynamic similarity means that, to maintain the geometric and kinematic similarity between flow fields, the forces acting on corresponding fluid masses must be related by ratios like those for kinematic similarity.
4) Completely similarity requires simultaneously satisfaction of geometric, kinematic, and dynamic similarities.

The scalar magnitude of forces affecting a flow field can be:

Pressure forces $F_P = (\Delta P)A = \Delta p l^2$

Inertia forces $F_I = Ma = \rho l^3 \left(\frac{V^2}{l}\right) = \rho V^2 l^2$

Gravity forces $F_G = Mg = \rho l^3 g$

Viscous forces $F_V = \mu \left(\frac{dv}{dy}\right) A = \mu \left(\frac{V}{l}\right) l^2 = \mu V l$

Elasticity forces $F_E = EA = El^2$

Surface tension $F_T = \sigma l$

where l and V are the characteristic length and velocity for the system.

To obtain dynamic similarity between two flow fields when all these forces act, the corresponding force ratio must be the same in model and prototype.

However, in most engineering problems, some of the forces above may not act, and can be neglected, or may oppose other forces in such a way that the effect of both is reduced. Therefore, in a similitude problem to understand the fluid phenomena is necessary to determine how the problem can be simplified by the elimination of irrelevant, negligible, or compensating forces.

Commonly, for scale reasoning on turbines are two the main approaches adopted:

Reynolds similarity → viscous-dominant flow

For low-speed submerged body problem, there are no surface tension phenomena, negligible compressibility effects, and gravity does not affect the flow field.

The Dynamic similarity is obtained between model and prototype when the Reynolds numbers (ratio of inertia to viscous forces) are the same.

$$\left(\frac{Vl}{\nu}\right)_p = Re_p = Re_m = \left(\frac{Vl}{\nu}\right)_m \tag{139}$$

This means that the ratio of any corresponding forces will be the same.

Consider Drag force $D = c\rho V^2 l^2$

$$\left(\frac{D}{F_I}\right)_p = \left(\frac{D}{F_I}\right)_m \tag{140}$$

$$\left(\frac{D}{\rho V^2 l^2}\right)_p = \left(\frac{D}{\rho V^2 l^2}\right)_m \tag{141}$$

Froude similarity → open channel flow, free surface flow, gravity-dominant flow

For flow field about an object moving close to or on to the surface of a liquid, compressibility, surface tension frictional effects may be ignored.

$$Fr_p = \left(\frac{V}{\sqrt{gl}}\right)_p = Fr_m = \left(\frac{V}{\sqrt{gl}}\right)_m \tag{142}$$

$$\frac{V_m}{V_p} = \sqrt{\frac{g_m}{g_p}\frac{l_m}{l_p}} \tag{143}$$

If we maintain the Reynolds number unchanged, we adapt a Reynolds similarity approach, vice versa, if we keep unchanged the Froude number, we are used a Froude similarity.

6.5. Conclusion and future works

Horizontal Axis Hydrokinetic Water Turbine are auspicious option to herness low velocity currents. However, the real behaviour under realistic flow velocity is still a challenge issue.

The present dissertation gives an exhaustive overview on the methodology adapted to design the prototype, giving information about its behaviour inside a recirculation water channel, in a low velocity scenario. It has been analysed the influence of fundamental parameters which affect the turbine performance, such as:

- Flow rate
- Upstream velocity
- Froude Number
- Blockage Effect
- Free-surface effect

The presented work goes through the HAHWT design, experimental and numerical tested and, can be summarized as follows:

- Before designed the tested prototype, a preliminary 2D Computational Fluid Dynamics Model has been developed, with aim of study the influence of walls domain on the Power Output extraction. The reference analytical calculation proposed in Appendix 1, was used to compute the value of pressure drop that maximize the power extraction. A reasonably good match between analytical and numerical results was found.
- The Eppler 818 blade profile with a solidity of 0.10 at the 75% of blade span, and a reference TSR of 4 have been considered for the turbine model design which has a total diameter of 0.240 m.
- With increasing upstream velocity, it has been proved that the power extracted rises as well, with a consequently increment in rotational speed. On the other hand, it has been observed that there is a strict correlation between Blockage effect and flow current conditions. To this end, the maximum power point recorded, is drawn when the Froude Number approximates the highest evaluated value. Afterwards, due to the current approximation to not totally submerged condition, which causes the reduction in the submersion level and the approximation of water height to the turbine. This means that when the turbine is exposed to the air the performances decrease abruptly.

- It has been demonstrated that the performance curves of this prototype cannot be traced on the unstable part of the curve, thus at the left side concerning the recorded MPP. Therefore, on the growing branch of the performance curve, the rotational velocity tends to decrease concerning the MPP. This because the laboratory set-up is not equipped with angular velocity active control system.
- As expected, the upstream velocity plays a key role in the turbine performance, even if the turbine submerged level decreases above the turbine height and the overall performance decreases sharply.
- For a constant flowrate, on the other hand, the peak power shifted up according to the increasing in blockage, that for a sub-critical flow, increase with reduction in water level. The Blockage effect produces a flow compression able to accelerate the current between the turbine and the channel wall, in the so-called by-pass area. As a result, the maximum power point moving away from the unrestricted flow condition.
- The Linear Momentum Actuator Disk Theory gained for an open channel flow (Appendix 2), based on the experimental data, shows that the experimental axial induction factor *a*, results lower than that foreseen from the analytical calculation sequences. Since the analytical model likely underestimates the friction losses from the channel walls.
- It has been proved that Betz limit is not applicable to confined domain, like the channel in which the prototype has been tested.
- The turbine efficiency is low for small upstream velocity and reach its maximum value of approximately 80% above the 0.50 m/s.
- The Power Coefficient was numerically computed for 15 tested cases by applying the CFD Volume of Fluid (VOF) Model, returning results that showed a good agreement with the same points experimentally computed. Moreover, three complete numerical curves are traced, even though the high computational costs, in three flow rate cases C_1, C_2 and C_3 curves (see section 6.3), giving a good mech with experimental curves.
- The energy extraction is directly proportional to the heigh drop downstream of turbine and is as high as the water-surface level does

not exceed the rotor height. Otherwise, the power output is decremented. The shape of water surface affect also the wake recovery length.

From the results reached with this Ph.D. thesis work, the following improvements could be considered for the next research developments:

- Other hydrofoil profiles could be tested and compared to understand how the performance efficiency is linked to the chosen profile.
- An active blade patch control system can be tested on turbine prototype to experimentally trace the entire performance curve along the power stage.
- The CFD Model could be validated also with a further approach by entirely extracting the performance curves along the power stage, choosing operative conditions of interest.
- The prototype could be scaled and tested in another channels, with different hydraulic and flow field conditions, keeping in mind the similarity approach, introduced in the last paragraph 6.4.
- The influence of the channel slope and the turbine immersion could be also studied both experimentally and numerically.

6.6. Research Novelty and Contributions

The main novelty introduced by the present thesis work, is basically related to the optimization approach applied to design of the turbine blade, even though it has a limited size.

Moreover, the application of both experimental and numerical approaches gives to the research a solid scientific value, showing the importance of always correlating to an experimental study a numerical one, validated through the results obtained experimentally.

Among other things, it has been widely demonstrated in literature [95] [96] [97][98][99][100] that the hydrokinetic applications may be inserted in different scenarios including:

- Rivers

- Canals
- Costal sea-currents
- Irrigation systems
- Estuaries and outflows

Resulting a low-cost alternative, with a minimum space required, low infrastructures costs and no environmental impact.

A real example of German innovative start-up called Smart Hydro Power (*https://www.smart-hydro.de/*) is one of examples of portable horizontal axis turbine fabrications to supply the base load power in the most remote areas all around the World. This means that the present study has a real applicability if it will be associated with an electrical generator. It is moreover evident that, how the literature suggests, are several the technics to install the generator, with the aid of floating mooring or rigid mooring on which the generator could be fixed, with different position: out of water or protected by watertight chamber. The submerged generator, is the solution often preferred but has also some drawbacks, resulting in a more difficult design.

The possible placement of hydrokinetic turbines in the surrounding river basins therefore offer significant economic advantages to the local community. From design/implementation point of view, the primary advantages associated with hydrokinetic turbines are:

- No alteration of natural pathways of streams: unlike wind power, river flow is predictable and unidirectional in nature which eliminates the need of changing the flow direction or additional fast control mechanisms (i.e., yawing is required in wind turbines) and allows fixed turbine orientation for long term application.
- Higher level of energy due to the near surface placement: since the Power is directly proportional to the density of water, Area swept by the rotor and the cubic value of average velocity (see Eq. (2) pag.26). This implies that due to the typical velocity profile of a river or channel, the higher the rotor's proximity to the surface, the higher the energy harnessed.

- Reduced environmental hazards: in contrast to large hydropower systems, the impact of hydrokinetic turbines on the river course, ecosystem and wildlife is small due to the compact scalable design.
- Noise and aesthetics-Unlike wind turbine, underwater installation of hydrokinetic turbines causes no noise disturbance and has a negligible visual impact. The impact on river navigation, swimming and boating can be minimized by efficient design. At turbine installation locations, the placement of drawbridges or moveable bridge arrangements can also make unobstructed navigation pathways in rivers.
- In conclusion, this thesis work could be studied in an array scheme, as in **Figure 110,** to maximize the energy extraction not only related on a single turbine but installed in parallel along a feasible section of a channel or river. The total amount of energy is not so high related to a single turbine application but could be useful to provide energy in continues, so 24 hours per day and 365 days per year.

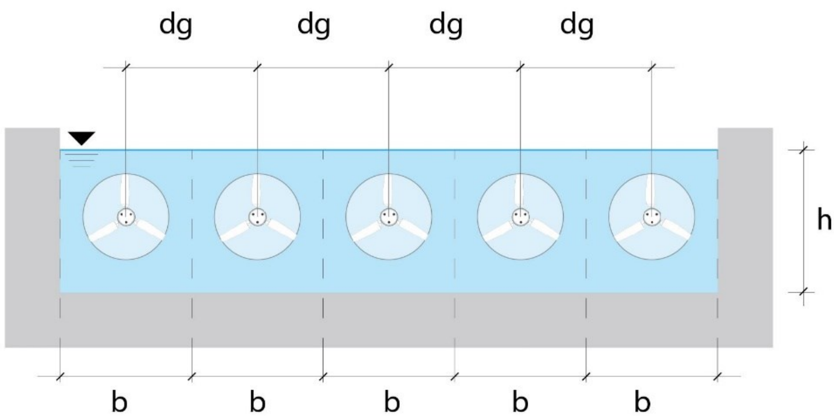

Figure 110 *Hypothesis of an array installation*

References

1. Abd El Aziz, Y. *Renewables 2022 Global Status Report Germany Factsheet*; **2022**; ISBN 9783948393045.
2. GSE Rapporto Statistico 2020 Energia. **2020**.
3. Scherer, L.; Pfister, S. Global water footprint assessment of hydropower. *Renew. Energy* **2016**, *99*, 711–720, doi:10.1016/j.renene.2016.07.021.
4. Toreti, A.; Bavera, D.; Acosta Navarro, J.; Cammalleri, C.; de Jager, A.; Di Ciollo, C.; Hrast Essenfelder, A.; Maetens, W.; Magni, D.; Masante, D.; et al. Drought in Europe – August 2022. *Publ. Off. Eur. Union, Luxemb. JRC130493* **2022**, 24, doi:10.2760/264241.
5. Ferreira, C.S.S.; Seifollahi-Aghmiuni, S.; Destouni, G.; Ghajarnia, N.; Kalantari, Z. Soil degradation in the European Mediterranean region: Processes, status and consequences. *Sci. Total Environ.* **2022**, *805*, 150106, doi:10.1016/j.scitotenv.2021.150106.
6. Wan, W.; Zhao, J.; Popat, E.; Herbert, C.; Döll, P. Analyzing the Impact of Streamflow Drought on Hydroelectricity Production: A Global-Scale Study. *Water Resour. Res.* **2021**, *57*, doi:10.1029/2020WR028087.
7. IEA Global electricity demand is growing faster than renewables, driving strong increase in generation from fossil fuels.
8. Elbatran, A.H.; Yaakob, O.B.; Ahmed, Y.M.; Shabara, H.M. Operation, performance and economic analysis of low head micro-hydropower turbines for rural and remote areas: A review. *Renew. Sustain. Energy Rev.* **2015**.
9. Santos, I.F.S. dos; Camacho, R.G.R.; Tiago Filho, G.L.; Botan, A.C.B.; Vinent, B.A. Energy potential and economic analysis of hydrokinetic turbines implementation in rivers: An approach using numerical predictions (CFD) and experimental data. *Renew. Energy* **2019**, doi:10.1016/j.renene.2019.05.018.
10. protezionecivile.tn.it Diga di Specchieri.
11. Hydro, A. HYDRO NEWS 06-2013 • ENGLISH. **2013**.
12. https://reneweconomy.com.au/tasmania-touts-its-battery-of-the-

nation-half-the-cost-of-snowy-2-0-55880/.

13. Johnstone, C.M.; Pratt, D.; Clarke, J.A.; Grant, A.D. A techno-economic analysis of tidal energy technology. *Renew. Energy* **2013**, *49*, 101–106, doi:10.1016/j.renene.2012.01.054.

14. Segura, E.; Morales, R.; Somolinos, J.A. Cost assessment methodology and economic viability of tidal energy projects. *Energies* **2017**, *10*, 1–27, doi:10.3390/en10111806.

15. Coiro, D.P.; Troise, G.; Bizzarrini, N.; Lazzerini, G.; Di Noia, L.P.; Iannuzzi, D.; Coppola, M. Design of GEMSTAR tidal current fixed pitch rotor controlled through a Permanent Magnet Generator (PMG) de-fluxing technique. *IET Renew. Power Gener.* **2020**, *14*, 2897–2907, doi:10.1049/iet-rpg.2020.0434.

16. Tian, W.; Mao, Z.; Ding, H. Design, test and numerical simulation of a low-speed horizontal axis hydrokinetic turbine. *Int. J. Nav. Archit. Ocean Eng.* **2018**, doi:10.1016/j.ijnaoe.2017.10.006.

17. Benavides-Morán, A.; Rodríguez-Jaime, L.; Laín, S. Numerical Investigation of the Performance, Hydrodynamics, and Free-Surface Effects in Unsteady Flow of a Horizontal Axis Hydrokinetic Turbine. *Processes* **2022**, doi:10.3390/pr10010069.

18. Round, G.F. *Incompressible Flow Turbomachines: Design, Selection, Applications, and Theory*; **2004**; ISBN 9780750676038.

19. Williamson, S.J.; Stark, B.H.; Booker, J.D. Experimental optimisation of a low-head pico hydro turgo turbine. In Proceedings of the IEEE International Conference on Sustainable Energy Technologies, ICSET; **2012**.

20. Williamson, S.J.; Stark, B.H.; Booker, J.D. Performance of a low-head pico-hydro Turgo turbine. *Appl. Energy* **2013**, doi:10.1016/j.apenergy.2012.06.029.

21. Cobb, B.R.; Sharp, K. V. Impulse (Turgo and Pelton) turbine performance characteristics and their impact on pico-hydro installations. *Renew. Energy* **2013**, doi:10.1016/j.renene.2012.08.010.

22. Ghosh, T.K.; Prelas, M.A. *Energy resources and systems*; 2009; ISBN 9789048123827.

23. Paish, O. Small hydro power: Technology and current status. *Renew.*

Sustain. Energy Rev. **2002**, doi:10.1016/S1364-0321(02)00006-0.

24. Stapenhorst, F.W.E. The Ossberger cross-flow turbine. **1980**.
25. Sammartano, V.; Filianoti, P.; Morreale, G.; Sinagra, M.; Tucciarelli, T. Banki-Michell micro-turbines for energy production in water distribution networks. In Proceedings of the Sustainable Hydraulics in the Era of Global Change - Proceedings of the 4th European Congress of the International Association of Hydroenvironment engineering and Research, IAHR 2016; **2016**.
26. Sinagra, M.; Sammartano, V.; Morreale, G.; Tucciarelli, T. A new device for pressure control and energy recovery in water distribution networks. *Water (Switzerland)* **2017**, doi:10.3390/w9050309.
27. Abbas, A.; Alam, M.; Kumar, R. Analytical analysis of combined effect of interior guide tube and draft tube on cross flow turbine performance. *Mater. Today Proc.* **2020**, *46*, 5372–5377, doi:10.1016/j.matpr.2020.08.796.
28. Sinagra, M.; Picone, C.; Aricò, C.; Pantano, A.; Tucciarelli, T.; Hannachi, M.; Driss, Z. Impeller optimization in crossflow hydraulic turbines. *Water (Switzerland)* **2021**, *13*, 1–19, doi:10.3390/w13030313.
29. Loots, I.; Van Dijk, M.; Barta, B.; Van Vuuren, S.J.; Bhagwan, J.N. A review of low head hydropower technologies and applications in a South African context. *Renew. Sustain. Energy Rev.* **2015**.
30. Dellinger, G. Etude expérimentale et optimisation des performances hydrauliques des vis, **2015**.
31. Carravetta, A.; Del Giudice, G.; Fecarotta, O.; Ramos, H.M. Energy Production in Water Distribution Networks: A PAT Design Strategy. *Water Resour. Manag.* **2012**, doi:10.1007/s11269-012-0114-1.
32. Pugliese, F.; De Paola, F.; Fontana, N.; Giugni, M.; Marini, G. Experimental characterization of two Pumps As Turbines for hydropower generation. *Renew. Energy* **2016**, doi:10.1016/j.renene.2016.06.051.
33. Lima, G.M.; Junior, E.L.; Brentan, B.M. Selection of Pumps as Turbines Substituting Pressure Reducing Valves. *Procedia Eng.* **2017**, doi:10.1016/j.proeng.2017.06.249.
34. Puertas-Frías, C.M.; Willson, C.S.; García-Salaberri, P.A. Design and economic analysis of a hydrokinetic turbine for household

applications. *Renew. Energy* **2022**, *199*, 587–598, doi:10.1016/j.renene.2022.08.155.

35. Khan, M.J.; Iqbal, M.T.; Quaicoe, J.E. A technology review and simulation based performance analysis of river current turbine systems. *Can. Conf. Electr. Comput. Eng.* **2006**, 2288–2293, doi:10.1109/CCECE.2006.277821.

36. Cardona-Mancilla, C.; Del Río, J.S.; Chica-Arrieta, E.; Hincapié-Zuluaga, D. Horizontal axis hydrokinetic turbines: A literature review [Turbinas hidrocinéticas de eje horizontal: Una revisión de la literatura]. *Tecnol. y Ciencias del Agua* **2018**.

37. Kinsey, T.; Dumas, G. Impact of channel blockage on the performance of axial and cross-flow hydrokinetic turbines. *Renew. Energy* **2017**, *103*, 239–254, doi:10.1016/j.renene.2016.11.021.

38. Lee, J.H.; Park, S.; Kim, D.H.; Rhee, S.H.; Kim, M.C. Computational methods for performance analysis of horizontal axis tidal stream turbines. *Appl. Energy* **2012**, *98*, 512–523, doi:10.1016/j.apenergy.2012.04.018.

39. Balduzzi, F.; Zini, M.; Molina, A.C.; Bartoli, G.; De Troyer, T.; Runacres, M.C.; Ferrara, G.; Bianchini, A. Understanding the aerodynamic behavior and energy conversion capability of small darrieus vertical axis wind turbines in turbulent flows. *Energies* **2020**, *13*, 1–15, doi:10.3390/en13112936.

40. Sinagra, M.; Sammartano, V.; Aricò, C.; Collura, A.; Tucciarelli, T. Cross-Flow turbine design for variable operating conditions. *Procedia Eng.* **2014**, *70*, 1539–1548, doi:10.1016/j.proeng.2014.02.170.

41. Ladokun, L.L.; Ajao, K.R.; Sule, B.F. Hydrokinetic energy conversion systems: Prospects and challenges in Nigerian hydrological setting. *Niger. J. Technol.* **2013**, *32*, 538–549.

42. Khan, M.J.; Bhuyan, G.; Iqbal, M.T.; Quaicoe, J.E. Hydrokinetic energy conversion systems and assessment of horizontal and vertical axis turbines for river and tidal applications: A technology status review. *Appl. Energy* **2009**.

43. Hansen, M.O.L. Aerodynamics of wind turbines, Earthscan. *James & James* **2008**, *8*, 14.

44. Babunski, D.; Lazarevikj, M.; Zaev, E.; Markov, Z. Direct Tool for Generation of the Geometry of a Francis Turbine Guide Vane System. *2020 9th Mediterr. Conf. Embed. Comput. MECO 2020* **2020**, 8–11, doi:10.1109/MECO49872.2020.9134214.

45. Doherty, T.O.; Doherty, D.M.O.; Hernández Madrigal, T.; Mason-Jones, A.; O'Doherty, T.; O'Doherty, D. The effect of solidity on a tidal turbine in low speed flow. *Proc. 12th Eur. Wave Tidal Energy Conf. Cork, Irel.* **2017**, {835\hyphen 1}--{835\hyphen 9}.

46. Consul, C. a; Willden, R.H.J.; Ferrer, E.; McCulloch, M.D. Influence of Solidity on the Performance of a Cross-Flow Turbine. *Proc. 8th Eur. Wave Tidal Energy Conf. Uppsala, Sweden* **2009**, 484–493.

47. Duquette, M.M.; Visser, K.D. Numerical implications of solidity and blade number on rotor performance of horizontal-axis wind turbines. *J. Sol. Energy Eng. Trans. ASME* **2003**, *125*, 425–432, doi:10.1115/1.1629751.

48. Rector, M.C.; Visser, K.D.; Humiston, C.J. Solidity, blade number, and pitch angle effects on a one kilowatt HAWT. *Collect. Tech. Pap. - 44th AIAA Aerosp. Sci. Meet.* **2006**, *10*, 7281–7290, doi:10.2514/6.2006-608.

49. Subhra Mukherji, S.; Kolekar, N.; Banerjee, A.; Mishra, R. Numerical investigation and evaluation of optimum hydrodynamic performance of a horizontal axis hydrokinetic turbine. *J. Renew. Sustain. Energy* **2011**, *3*, doi:10.1063/1.3662100.

50. Barbarić, M.; Guzović, Z. Investigation of the possibilities to improve hydrodynamic performances of micro-hydrokinetic turbines. *Energies* **2020**, doi:10.3390/en13174560.

51. Ma, N.; Lei, H.; Han, Z.; Zhou, D.; Bao, Y.; Zhang, K.; Zhou, L.; Chen, C. Airfoil optimization to improve power performance of a high-solidity vertical axis wind turbine at a moderate tip speed ratio. *Energy* **2018**, *150*, 236–252, doi:10.1016/j.energy.2018.02.115.

52. Aguilar, J.; Velásquez, L.; Romero, F.; Betancour, J.; Rubio-Clemente, A.; Chica, E. Numerical and experimental study of hydrofoil-flap arrangements for hydrokinetic turbine applications. *J. King Saud Univ. - Eng. Sci.* **2021**, doi:10.1016/j.jksues.2021.08.002.

53. Shen, W.Z.; Mikkelsen, R.; Sørensen, J.N.; Bak, C. Tip loss corrections for wind turbine computations. *Wind Energy* **2005**, *8*, 457–475,

doi:10.1002/we.153.

54. Hansen, M.O.L. *Aerodynamics of wind turbines: Third edition*; **2015**; ISBN 9781317671022.

55. Lim, H.W. Performance Analysis of Hydrokinetic Turbine Blade Section Using CFD. *Avestia Publ. Adv. Renew. Energy* **2019**, *2*.

56. Ranjbar, M.H.; Zanganeh, H.; Gharali, K.; Nasrazadani, S.A.; Kia, H.Z. Reaching the Betz Limit Experimentally and Numerically. *Energy Equip. Sys* **2019**.

57. Chen, T.Y.; Liou, L.R. Blockage corrections in wind tunnel tests of small horizontal-axis wind turbines. *Exp. Therm. Fluid Sci.* **2011**, *35*, 565–569, doi:10.1016/j.expthermflusci.2010.12.005.

58. Kolekar, N.; Banerjee, A. Performance characterization and placement of a marine hydrokinetic turbine in a tidal channel under boundary proximity and blockage effects. *Appl. Energy* **2015**, doi:10.1016/j.apenergy.2015.03.052.

59. Houlsby, G.T.T.; Draper, S.; Oldfield, M.L.G.L.G. Application of Linear Momentum Actuator Disc Theory to Open Channel Flow by. *Rep. no. OUEL* **2008**.

60. Rahimian, M.; Walker, J.; Penesis, I. Performance of a horizontal axis marine current turbine– A comprehensive evaluation using experimental, numerical, and theoretical approaches. *Energy* **2018**, *148*, 965–976, doi:10.1016/j.energy.2018.02.007.

61. Rachman, A.; Balaka, R.; Delly, J. A Mathematical Model for Predicting the Performance of a Horizontal Axis River Current Turbine with Consideration of Blade Parameters. *Proceeding Int. Conf. Exhib. Sustain. Energy Adv. Mater. (ICE SEAM 2011)* **2011**, 66–74.

62. Whelan, J.I.; Graham, J.M.R.; Peiró, J. A free-surface and blockage correction for tidal turbines. *J. Fluid Mech.* **2009**, *624*, 281–291, doi:10.1017/S0022112009005916.

63. Houlsby, G.T.; Vogel, C.R. The power available to tidal turbines in an open channel flow. *Proc. Inst. Civ. Eng. Energy* **2017**, doi:10.1680/jener.15.00035.

64. Benavides-Morán, A.; Rodríguez-Jaime, L.; Laín, S. Numerical Investigation of the Performance, Hydrodynamics, and Free-Surface

Effects in Unsteady Flow of a Horizontal Axis Hydrokinetic Turbine. *Processes* **2022**, *10*, doi:10.3390/pr10010069.

65. Zhang, T.; Lam, W.H.; Cui, Y.; Jiang, J.; Sun, C. Tip-Bed Velocity and Scour Depth of Horizontal-Axis. 1–24.

66. Yass, M.A.R.; Aziez, S.A.; Rasheed, R.M. Highest Power Coefficient of Horizontal Axis Wind Turbine (HAWT) Using Multiple Airfoil Section. **2020**, doi:10.13140/RG.2.2.14029.05609.

67. Batu, T.; Lemu, H.G. Comparative Study of the Effect of Chord Length Computation Methods in Design of Wind Turbine Blade Comparative Study of the Effect of Chord Length Computation Methods in Design of Wind Turbine Blade. **2020**, 0–10, doi:10.1007/978-981-15-2341-0.

68. Johnson, D.A.; Gu, M.; Gaunt, B. Wind Turbine Performance in Controlled Conditions : BEM Modeling and Comparison with Experimental Results. **2016**, *2016*, doi:10.1155/2016/5460823.

69. Glauert, H. Airplane Propellers. In *Aerodynamic Theory*; 1935.

70. de Vries, O. *Fluid Dynamic Aspects of Wind Energy Conversion.*; **1979**; ISBN 9283513266.

71. Nishi, Y.; Sato, G.; Shiohara, D.; Inagaki, T.; Kikuchi, N. Performance characteristics of axial flow hydraulic turbine with a collection device in free surface flow field. *Renew. Energy* **2017**, *112*, 53–62, doi:10.1016/j.renene.2017.04.047.

72. Riglin, J.; Chris Schleicher, W.; Liu, I.H.; Oztekin, A. Characterization of a micro-hydrokinetic turbine in close proximity to the free surface. *Ocean Eng.* **2015**, *110*, 270–280, doi:10.1016/j.oceaneng.2015.10.026.

73. Anyi, M.; Kirke, B. Hydrokinetic turbine blades: Design and local construction techniques for remote communities. *Energy Sustain. Dev.* **2011**, *15*, 223–230, doi:10.1016/j.esd.**2011**.06.003.

74. Bethune, J.D. *Engineering Design and Graphics with SolidWorks*; **2016**; Vol. 28; ISBN 9780134507699.

75. ANSYS FLUENT经典完整培训教材.pdf.

76. Celik, I.B.; Ghia, U.; Roache, P.J.; Freitas, C.J.; Coleman, H.; Raad, P.E. Procedure for estimation and reporting of uncertainty due to discretization in CFD applications. *J. Fluids Eng. Trans. ASME* **2008**, *130*,

0780011–0780014, doi:10.1115/1.2960953.

77. Pla - hd. 829.

78. Bahaj, A.S.; Molland, A.F.; Chaplin, J.R.; Batten, W.M.J. Power and thrust measurements of marine current turbines under various hydrodynamic flow conditions in a cavitation tunnel and a towing tank. *Renew. Energy* **2007**, doi:10.1016/j.renene.2006.01.012.

79. RTI User ' s Manual User ' s Manual ユーザーズマニュアル. **2010**, *2886*, 1–38.

80. Lazzerini, G.; Coiro, D.P.; Troise, G.; D'Amato, G. A comparison between experiments and numerical simulations on a scale model of a Horizontal-Axis current turbine. *Renew. Energy* **2022**, *190*, 919–934, doi:10.1016/j.renene.2022.03.162.

81. Lamont, E.A.; Vegas, L.A.S.; November, N. Pronulsion Conference. **1973**.

82. Moffat, R.J. Contributions to the theory of single-sample uncertainty analysis. *J. Fluids Eng. Trans. ASME* **1982**, *104*, 250–258, doi:10.1115/1.3241818.

83. Manual, U. IN-LINE TORQUE SENSORS.

84. Brakes, H.; Brakes, C.-C.; Brakes, M.; Clutches, H.; Brakes, L.B.; Brakes, P.M.; Brakes, C.P. w w w. m a g t r o l . c o m. **1953**.

85. Maître, T.; Amet, E.; Pellone, C. Modeling of the flow in a Darrieus water turbine: Wall grid refinement analysis and comparison with experiments. *Renew. Energy* **2013**, *51*, 497–512, doi:10.1016/j.renene.2012.09.030.

86. Balduzzi, F.; Bianchini, A.; Maleci, R.; Ferrara, G.; Ferrari, L. Critical issues in the CFD simulation of Darrieus wind turbines. *Renew. Energy* **2016**, *85*, 419–435, doi:10.1016/j.renene.2015.06.048.

87. Ferziger, J.H.; Perić, M.; Street, R.L. *Computational Methods for Fluid Dynamics, Fourth Edition*; **2019**; ISBN 9783319996936.

88. Lain, S.; Osorio, C. Simulation and evaluation of a straight-bladed darrieus-type cross flow marine turbine. *J. Sci. Ind. Res. (India).* **2010**, *69*, 906–912.

89. C. W Hirt and B.D. Nichols Volume of Fluid (VOF) Method for the

Dybamics of free Boundaries. *Iran. J. Sci. Technol. - Trans. Electr. Eng.* **2018**, *42*, 357–366, doi:10.1007/s40998-018-0069-1.

90. F.R. Menter *Zonal two equation k-w turbulence models for aerodynamic flows*; **1993**;

91. Menter, F.R. Two-equation eddy-viscosity turbulence models for engineering applications. *AIAA J.* **1994**, *32*, doi:10.2514/3.12149.

92. Wilcox, D.C. *Turbulence Modeling for CFD*; DCW Industries, Inc La Cafiada, C. 91011, Ed.; Third.; **2006**; ISBN 978-1-928729-08-2 (1-928729-08-8).

93. Birjandi, A.H.; Bibeau, E.L.; Chatoorgoon, V.; Kumar, A. Power measurement of hydrokinetic turbines with free-surface and blockage effect. *Ocean Eng.* **2013**, doi:10.1016/j.oceaneng.2013.05.023.

94. Li, B.; Zhou, D.L.; Wang, Y.; Shuai, Y.; Liu, Q.Z.; Cai, W.H. The design of a small lab-scale wind turbine model with high performance similarity to its utility-scale prototype. *Renew. Energy* **2020**, *149*, 435–444, doi:10.1016/j.renene.**2019**.12.060.

95. Ramadan, A.; Nawar, M.A.A.; Mohamed, M.H. Performance evaluation of a drag hydro kinetic turbine for rivers current energy extraction - A case study. *Ocean Eng.* **2020**, *195*, 106699, doi:10.1016/j.oceaneng.2019.106699.

96. Tan, K.W.; Kirke, B.; Anyi, M. Small-scale hydrokinetic turbines for remote community electrification. *Energy Sustain. Dev.* **2021**, *63*, 41–50, doi:10.1016/j.esd.2021.05.005.

97. Bekker, A.; van Dijk, M.; Niebuhr, C.M.; Hansen, C. Framework development for the evaluation of conduit hydropower within water distribution systems: A South African case study. *J. Clean. Prod.* **2021**, *283*, 125326, doi:10.1016/j.jclepro.2020.125326.

98. Aristizábal-Tique, V.H.; Villegas-Quiceno, A.P.; Arbeláez-Pérez, O.F.; Colmenares-Quintero, R.F.; Vélez-Hoyos, F.J. Development of riverine hydrokinetic energy systems in colombia and other world regions: A review of case studies. *DYNA* **2021**, *88*, 256–264, doi:10.15446/dyna.v88n217.93098.

99. Saini, G.; Kumar, A.; Saini, R.P. Assessment of hydrokinetic energy - A case study of eastern Yamuna canal. *Mater. Today Proc.* **2020**, *46*, 5223–

5227, doi:10.1016/j.matpr.2020.08.595.

100. Colmenares-Quintero, R.F.; Latorre-Noguera, L.F.; Rojas, N.; Kolmsee, K.; Stansfield, K.E.; Colmenares-Quintero, J.C. Computational framework for the selection of energy solutions in indigenous communities in Colombia: Kanalitojo case study. *Cogent Eng.* **2021**, *8*, doi:10.1080/23311916.2021.1926406.

Appendix 1

Linear Momentum Actuator Disk Theory (LMADT) in parallel-sided tube

Houlsby's analytical model equations

8. LINEAR MOMENTUM ACTUATOR DISC THEORY IN A PARALLEL-SIDED TUBE

8.1 Geometry of the flow

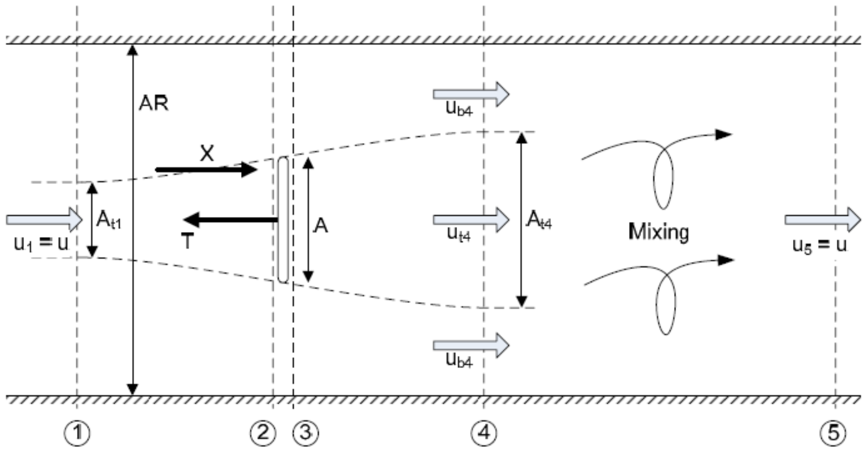

Figure 3: One dimensional linear momentum actuator disc theory in a finite medium bounded by a parallel-sided tube

8.2. CONTINUITY RELATIONS

Region		Station 1	Station 2	Station 3	Station 4	Station 5
Turbine	Area	$A_{1t} = A\alpha_2$	$A_{2t} = A_{3t} = A$		$A_{4t} = A\dfrac{\alpha_2}{\alpha_4}$	
	Velocity	$u_{1t} = u$	$u_{2t} = u_{3t} = u\alpha_2$		$u_{4t} = u\alpha_4$	
	Volumetric flow	$q_{1t} = q_t = uA\alpha_2$	$q_{2t} = q_{3t} = uA\alpha_2$		$q_{4t} = uA\alpha_2$	
	Pressure	$p_{1t} = p$	p_{2t}	p_{3t}	$p_{4t} = p_4$	
By-pass	Area	$A_{1b} = A(R - \alpha_2)$			$A_{4b} = A\left(R - \dfrac{\alpha_2}{\alpha_4}\right)$	
	Velocity	$u_{1b} = u$			$u_{4b} = u\dfrac{(R - \alpha_2)}{(R - \alpha_2/\alpha_4)}$	
	Volumetric flow	$q_{1b} = q_b = uA(R - \alpha_2)$			$q_{4b} = uA(R - \alpha_2)$	
	Pressure	$p_{1b} = p$			$p_{4b} = p_4$	
Total	Area	$A_1 = AR$			$A_4 = AR$	$A_5 = AR$
	Velocity	$u_1 = u$	Varies		Varies	$u_5 = u$
	Volumetric flow	$q_1 = q = uAR$			$q_4 = uAR$	$q_5 = uAR$
	Pressure	$p_1 = p$	Varies	Varies	p_4	$p_5 = p - \dfrac{T}{AR} = p - \Delta p$

Table 3

8.3. NOMENCLATURE

Symbol	Definition
u	Stream velocity (uniform)
ρ	Fluid density
g	Gravity
p	Pressure (gauge)
h	Stream height/hydrostatic head
α_2	Turbine flow velocity coefficient
α_4	Turbine wake flow velocity coefficient
β_4	Bypass flow velocity coefficient
A	Area of the turbine defined as an actuator disc
R	Area ratio
b	Width of flow (open channel)
B	§8: Blockage ratio ($1/R$) §9: Blockage ratio (A/bh)
T	Thrust from the actuator disc to the fluid
X	Reaction between the turbine flow and bypass flow
P	Power extracted by the turbine
P_W	Power dissipate in downstream mixing
C_P	Dimensionless power coefficient, normalised by upstream kinetic flux
C_{P*}	Dimensionless power coefficient, normalised by upstream kinetic flux and the pressure drop across the actuator disc
C_{PW}	Dimensionless power dissipation in downstream mixing, normalised by upstream kinetic flux
C_T	Dimensionless thrust coefficient, normalised by upstream kinetic pressure
C_{TL}	Dimensionless thrust coefficient, normalised by turbine kinetic pressure
η	Efficiency of a turbine in a finite flow
F_r	Froude number = $u/\sqrt{gh}$

Subscripts	Definition
t	Turbine flow
b	Bypass flow
1,2,3…	Station of the flow

8.4. COMMENTARY AND DERIVATION

We consider a finite flow, confined in a tube. The main parameters are defined in Table 1 and shown in Fig.1. The key difference is that the by-pass flow is no longer at constant velocity and one can deduce $u_{4b} = u = \frac{(R-\alpha_2)}{(R-\frac{\alpha_2}{\alpha_4})} = u\beta_4$. It follows the Bernoulli in the by-pass flow gives:

$$p_4 - p = \frac{1}{2}\rho u^2(1-\beta_4^2) = \frac{1}{2}\rho u^2 1 - \frac{(R-\alpha_2)^2}{(R-\alpha_2/\alpha_4)^2} \tag{13}$$

From the equation (1) (2) (3), obtained in an open-flow condition, applying the Bernoulli equation from section 1 to 2 and 3 t 4. And since the pressures are assumed to be equal in the two by-pass sections, so are the velocity. (See the entire paper)

Equation (1) and (3) are ungagged, but (2) becomes:

$$p_{3t} + \frac{1}{2}\rho u^2 a_2^2 = p_4 + \frac{1}{2}\rho u^2 a_4^2 \tag{14}$$

On combining (1); (3) ;(13) and (14) one obtains:

$$\frac{1}{2}\rho u^2(\beta_4^2 - \alpha_4^2) = \frac{1}{2}\rho u^2\left(\frac{(R-\alpha_2)^2}{(R-\alpha_2/\alpha_4)^2} - \alpha_4^2\right) = \frac{T}{A} \tag{15}$$

The momentum equation for the entire flow between stations 1 and 4 is written:

$$pAR - p_4AR - T = u^2\,A\rho\alpha_2(\alpha_4 - 1) + u^2\,A\rho(R-\alpha_2)\left(\frac{(R-\alpha_2)^2}{(R-\alpha_2/\alpha_4)} - 1\right) \tag{16}$$

Which can be simplified in:

$$p - p_4 = \frac{T}{RA} + \rho u^2 \frac{\alpha_2(1-\alpha_4)^2}{\alpha_4(R-\frac{\alpha_2}{\alpha_4})} \tag{17}$$

Combining (817) with (13) and (15) gives:

$$-\frac{1}{2}\rho u^2(1-\beta_4^2) = \frac{1}{2}\rho u^2\frac{(\beta_4^2-\alpha_4^2)}{R} + \rho u^2\frac{\alpha_2(1-\alpha_4)^2}{\alpha_4(R-\frac{\alpha_2}{\alpha_4})} \tag{18}$$

After some manipulations this leads to:

$$R\alpha_4^2(2\alpha_2 - 1 - \alpha_4) + \ \alpha_2(2\alpha_4^2 + \alpha_2 - 3\alpha_4\alpha_2) = 0 \tag{19}$$

Now we can consider two limits:

As R→∞; $\alpha_2 = \frac{1+\alpha_4}{2}$

As R→1 ; $-{\alpha_4}^2 - {\alpha_3}^2 + \alpha_2(2\alpha_4^2 + \alpha_2 - 3\alpha_4\alpha_2) = 0$; which consist with $\alpha_2 \to 1; \alpha_4 \to 1;$ and in fact leads to $\alpha_2 = \alpha_4$.

For general R, solve the quadratic:

$$(1-3\alpha_4)\alpha_2^2+2(R+1)\alpha_4^2\alpha_2-R\alpha_4^2(1+\alpha_4)=0$$

Th most convenient for of the solution is:

$$\alpha_2=\frac{R(1+\alpha_4)}{(R+1)+\sqrt{(R-1)^2+R(1-1/\alpha_4)^2}}=\frac{(1+\alpha_4)}{(1+B)+\sqrt{(1-B)^2+B(1-1/\alpha_4)^2}} \tag{20}$$

The power is then given by:

$$P=Tu_{2t}=Tu\alpha_2=\frac{1}{2}\rho Au^3\alpha_2\left(\frac{(R-\alpha_2)^2}{(R-\frac{\alpha_2}{\alpha_4})^2}-\alpha_4^2\right)=$$

$$=\frac{1}{2}\rho Au^3\alpha_2R\alpha_2\alpha_4^2(1-\alpha_4)\left(\frac{(R+\alpha_4)^2-2\alpha_2}{(R\alpha_4-\alpha_2)^2}\right)$$

$$=\frac{1}{2}\rho Au^3\alpha_2(1-\alpha_4)\left(\frac{(1+\alpha_4)-2B\alpha_2}{(1-B\alpha_2/\alpha_4)^2}\right)=\frac{1}{2}\rho Au^3C_p \tag{21}$$

It is found numerically that this is always maximized by $\alpha_4=\frac{1}{3}$ for which $\alpha_2=\frac{2R}{3(R+1)}$ and the power is:

$$P=\frac{1}{2}\rho Au^3\frac{16}{27}\left(\frac{R}{(R-1)}\right)^2=\frac{1}{2}\rho Au^3C_p \tag{22}$$

Note, however, that as R→1 the Power extracted becomes infinite. This is because of the drop of pressure in the tube. Since from simple statics:

$$\Delta P=\frac{T}{AR}=\frac{1}{2}\rho Au^2B(1-\alpha_4)\left(\frac{(1+\alpha_4)-2B\alpha_2}{(1-B\alpha_2/\alpha_4)^2}\right)$$

A mor rational measure of the performance might be $C_{p*}=\frac{P}{\frac{1}{2}\rho Au^3+uA\Delta P}=\frac{C_p}{1+BC_t}$, where:

$$C_T=\frac{T}{\frac{1}{2}\rho Au^2}=(1-\alpha_4)\left(\frac{(1+\alpha_4)-2B\alpha_2}{(1-B\alpha_2/\alpha_4)^2}\right)$$ Thus:

$$C_{P*}=\frac{\alpha_2(1-\alpha_4)\left(\frac{(1+\alpha_4)-2B\alpha_2}{(1-B\alpha_2/\alpha_4)^2}\right)}{1+B(1-\alpha_4)\left(\frac{(1+\alpha_4)-2B\alpha_2}{(1-B\alpha_2/\alpha_4)^2}\right)}=\frac{\alpha_2(1-\alpha_4)}{\left(\frac{(1-B\alpha_2/\alpha_4)^2}{(1+\alpha_4)-2B\alpha_2}\right)+B(1-\alpha_4)} \tag{23}$$

After substituting (20), this may be optimized as a function of α4 value for each value of B. Note that all the above solutions are entirely compatible with the original Betz solution R→∞.

At this stage we can also reconsider the force X acting between the turbine flow and the by-pass flow. Previously this force has been zero, but now with inclusion of the volume boundary we can expect that it is finite and positive. Considering momentum across the bypass flow we can write:

$$pA(R-\alpha_2)-p_4A\left(R-\frac{\alpha_2}{\alpha_4}\right)-X=u^2A\rho(R-\alpha_2)\left(\frac{(R-\alpha_2)}{(R-\frac{\alpha_2}{\alpha_4})}-1\right) \tag{24}$$

If we concern ourselves only with pressure above atmospheric, we can take p=0, also substituting for p_4 from (13), (24) can be rewritten as

$$-\frac{1}{2}\rho u^2A(1-\beta^2)\left(R-\frac{\alpha_2}{\alpha_4}\right)-X=u^2A\rho(R-\alpha_2)(\beta_4-1)$$

So that

$$X=\frac{1}{2}\rho u^2A\left(2(R-\alpha_2)(\beta_4-1)+(1-\beta^2)\left(R-\frac{\alpha_2}{\alpha_4}\right)\right)$$

$$=\frac{1}{2}\rho u^2A(1-\beta_4)\left(-2(R-\alpha_2)+(1+\beta^2)\left(R-\frac{\alpha_2}{\alpha_4}\right)\right)$$

$$=\frac{1}{2}\rho u^2A(1-\beta_4)\left(-2(R-\alpha_2)+(1+\beta^2)\left(R-\frac{\alpha_2}{\alpha_4}\right)\right)$$

$$=\frac{1}{2}\rho u^2A(1-\beta_4)\left(-2(R-\alpha_2)\left(R-\frac{\alpha_2}{\alpha_4}-\alpha_2\right)\right)$$

$$=\frac{1}{2}\rho u^2A(1-\beta_4)\left(\alpha_2-\frac{\alpha_2}{\alpha_4}\right)$$

Since $\alpha_2>\alpha_4$ and $\beta_4>1$ for all values of R, it is following that X must also be greater than 0 for all values of R

The power lost in the wake mixing process may also be determined. First, it is necessary to determine the change of pressure from stations 4 to 5:

$$(p_4-p_5)RA=\rho u^2A\left(R-\alpha_2\alpha_4-(R-\alpha_2)\frac{(R-\alpha_2)}{(R-\alpha_2/\alpha_4)}-\right) \tag{25}$$

$$p_4-p_5=-\rho u^2\frac{\alpha_2(1-\alpha_4)^2}{\alpha_4(R-\alpha_2/\alpha_4)} \tag{26}$$

$$P_W=\frac{1}{2}\rho u^3A\alpha_2{\alpha_4}^2+\frac{1}{2}\rho u^3A(R-\alpha_2){\beta_4}^2-\frac{1}{2}\rho u^3AR+ARu(p_4-p_5)$$

$$=\frac{1}{2}\rho u^3A\left(\alpha_2{\alpha_4}^2+\frac{(R-\alpha_2)^3}{(R-\frac{\alpha_2}{\alpha_4})^2}-R\right)-\rho u^3AR\frac{\alpha_2(1-\alpha_4)^2}{\alpha_4(R-\frac{\alpha_2}{\alpha_4})}$$

$$=\frac{1}{2}\rho u^3A\alpha_2R\left(\frac{R\left({\alpha_4}^2+\frac{2}{\alpha_4}-3\right)+\alpha_2(3-2\alpha_4-1/{\alpha_4}^2)-2(1/\alpha_4-2+\alpha_4)(R-\alpha_2/\alpha_4}{(R-\frac{\alpha_2}{\alpha_4})^2}\right)$$

$$= \frac{1}{2}\rho u^3 A\alpha_2(1-\alpha_4)^2 R\left(\frac{R+\alpha_2(1-2\alpha_4)/\alpha_4{}^2}{(R-\frac{\alpha_2}{\alpha_4})^2}\right)$$

$$= \frac{1}{2}\rho u^3 A\alpha_2(1-\alpha_4)^2\left(1+\frac{B\alpha_2(1-B\alpha_2)}{\alpha_4{}^2(1-B\frac{\alpha_2}{\alpha_4})^2}\right) \quad (27)$$

Note that as R→∞ this gives the same asymptotic solution as for the constant pressure case. We can also calculate:

$$\frac{P_W}{P} = (1-\alpha_4)\frac{1+B\alpha_2(1-2\alpha_4)/\alpha_4{}^2}{(1+\alpha_4)-2B\alpha_2} \quad (28)$$

8.5. CALCULATION SEQUENCE

1. Specify principal dimensioning parameters ρ,u, and A
2. (Optionally specify upstream pressure p, which acts as purely additive term to all pressures)
3. Specify blockage ratio 0≤B≤1 and dimensionless velocity factor 0≤ α_4 ≤1
   a) $\alpha_2 = \frac{(1+\alpha_4)}{(1+B)+\sqrt{(1-B)^2+B(1-1/\alpha_4)^2}}$
   b) $\beta_4 = \frac{(1-B\alpha_2)}{(1-B\alpha_2/\alpha_4)}$
   c) $C_T = (\beta_4{}^2 - \alpha_4{}^2)$
   d) $C_{TL} = \frac{C_T}{\alpha_2^2}$
   e) $C_P = \alpha_2 C_T$
   f) $C_p^* = \frac{C_p}{1+BC_T}$
   g) $C_{PW} = \alpha_2(1-\alpha_4)^2\left(1+\frac{B\alpha_2(1-B\alpha_2)}{\alpha_4^2(1-B\alpha_2/\alpha_4)^2}\right)$
   h) $\eta = \frac{C_P}{C_P+C_{PW}} = \frac{P}{P+P_W}$

8.6. DIMENSIONED QUANTITIES:

i) $T = \frac{1}{2}\rho u^2 A C_T$
j) $P = \frac{1}{2}\rho u^3 A C_P$
k) $P_W = \frac{1}{2}\rho u^3 A C_{PW}$
l) $Pressure\ drop\ across\ turbine\ \Delta_{PT} = \frac{T}{A}$
m) $Downstream\ pressure\ p_5 = p - \frac{BT}{A}$

Appendix 2

Linear Momentum Actuator Disk Theory (LMADT) in an open channel flow

Houlsby's analytical model equations

9. LINEAR MOMENTUM ACTUATOR DISC THEORY IN AN OPEN CHANNEL FLOW

9.1 Geometry of the flow

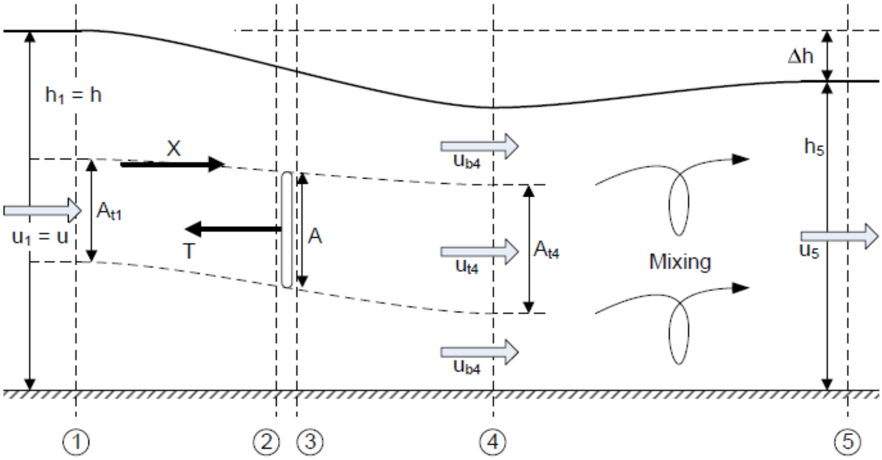

Figure 4: One dimensional linear momentum actuator disc theory in an open channel flow

9.2 Continuity relations

Region		Station 1	Station 2	Station 3	Station 4	Station 5
Turbine	Area	$A_{1t} = bhB\alpha_2$	$A_{2t} = A_{3t} = bhB$		$A_{4t} = bhB\dfrac{\alpha_2}{\alpha_4}$	
	Velocity	$u_{1t} = u$	$u_{2t} = u_{3t} = u\alpha_2$		$u_{4t} = u\alpha_4$	
	Volumetric flow	$q_{1t} = q_t = ubhB\alpha_2$	$q_{2t} = q_{3t} = ubhB\alpha_2$		$q_{4t} = ubhB\alpha_2$	
	Elevation head	$h_{1t} = h$	h_{2t}	h_{3t}	$h_{4t} = h_4$	
By-pass	Area	$A_{1b} = bh(1 - B\alpha_2)$			$A_{4b} = bh\dfrac{(1 - B\alpha_2)}{\beta_4}$	
	Velocity	$u_{1b} = u$			$u_{4b} = u\beta_4$	
	Volumetric flow	$q_{1b} = q_b = uhb(1 - B\alpha_2)$			$q_{4b} = uhb(1 - B\alpha_2)$	
	Elevation head	$h_{1b} = h$			$h_{4b} = h_4$	
Total	Depth	$h_1 = h$			h_4	$h_5 = h - \Delta h$
	Velocity	$u_1 = u$	Varies		Varies	$u_5 = \dfrac{uh}{(h - \Delta h)}$
	Volumetric flow	$q_1 = q = ubh$			$q_4 = ubh$	$q_5 = ubh$
	Pressure force	$p_1 = \dfrac{1}{2}\rho g h^2$	Varies	Varies	$p_4 = \dfrac{1}{2}\rho g h_4^2$	$p_5 = \dfrac{1}{2}\rho g(h - \Delta h)^2$

Table 4

9.3. COMMENTARY AND DERIVATION

The open channel flow calculation follows a similar pattern t before, except that in the Bernoulli calculation the total head is now employed. We assume that at stations 1, 4, and 5 the pressure can be treated as hydrostatic. In some senses the calculation is a hybrid between the calculation at constant pressure and the one in a fixed tube: the downstream dimensions of the flow are not fixed, but there are relationships between dimension and velocity and between dimension and pressure force.

We start by noting that in the by-pass flow:

$$h + \frac{u^2}{2g} = h_4 + \frac{u^2\beta_4^2}{2g} \tag{29}$$

As said before, Bernoulli in the turbine flow upstream and downstream of the turbines gives:

$$h + \frac{u^2}{2g} = h_{2t} + \frac{u^2\alpha_2^2}{2g} \tag{30}$$

$$h_{3t} + \frac{u^2\alpha_2^2}{2g} = h_4 + \frac{u^2\alpha_4^2}{2g} \tag{31}$$

And the equilibrium of the turbine gives:

$$\rho g(h_{2t} - h_{3t})Bbh = T \tag{32}$$

Combining Eqs. (29), (30), (31) and (32) gives:

$$h_{2t} - h_{3t} = \frac{T}{\rho gBbh} = \frac{u^2}{2g}(\beta_4^2 - \alpha_4^2) \tag{33}$$

$$T = \frac{\rho u^2 Bbh}{2}(\beta_4^2 - \alpha_4^2) \tag{34}$$

Now consider the momentum equation between stations 1 and 4, which gives:

$$\frac{1}{2}\rho gb(h^2 - h_4^2) - T = \rho u^2 bhB\alpha_2(\alpha_4 - 1) + \rho u^2 hb(1 - B\alpha_2)(\beta_4 - 1) \tag{35}$$

Eliminating T between (34) and (35) gives

$$\frac{1}{2}g(h^2 - h_4^2) - Bh\frac{u^2}{2}(\beta_4^2 - \alpha_4^2) = u^2bhB\alpha_2(\alpha_4 - 1) + u^2b(1 - B\alpha_2)(\beta_4 - 1) \tag{36}$$

And we can make use of the continuity relationship.

$$h_4 = Bh\frac{\alpha_2}{\alpha_4} + h\frac{(1-B\alpha_2)}{\beta_4} \tag{37}$$

Note also the following forms.

$$\beta_4 = (h - B\alpha_2)/(h_4 - B\alpha_2/\alpha_4 \tag{38}$$

$$\alpha_2 = \frac{\alpha_4}{Bh}\frac{(h(1-\beta_4)+\beta_4(h-h_4))}{\alpha_4-\beta_4} \tag{39}$$

To eliminate (in principle) h_4 and β_4 between (29), (36) and (37), leaving, as previously, a relationship between $\alpha_2$and α_4. First eliminate h_4 to give:

$$\left(1 - \left(\frac{B\alpha_2}{\alpha_4} + \frac{(1-B\alpha_2)}{\beta_4}\right)\right) = \frac{u^2}{2gh}(\beta_4 - 1) \tag{40}$$

And

$$\left(1 - \left(\frac{B\alpha_2}{\alpha_4} + \frac{(1-B\alpha_2)}{\beta_4}\right)^2\right) = \frac{u^2}{gh}\left(2B\alpha_2(\alpha_4 - 1) + 2(1 - B\alpha_2)(\beta_4 - 1) + B\left({\beta_4}^2 - {\alpha_4}^2\right)\right) = \frac{u^2}{gh}\left(2B\alpha_2(\alpha_4 - \beta_4) + 2(\beta_4 - 1) + B\left({\beta_4}^2 - {\alpha_4}^2\right)\right) \tag{41}$$

It is convenient later to write the results in terms of upstream Froud Number $Fr = u/\sqrt{gh}$.

Dividing (41) by (40) we obtain

$$\left(1 + \frac{B\alpha_2}{\alpha_4} + \frac{(1-B\alpha_2)}{\beta_4}\right) = \frac{2}{({\beta_4}^2-1)}\left(2B\alpha_2(\alpha_4 - \beta_4) + 2(\beta_4 - 1)(\beta_4 - 1) + B\left({\beta_4}^2 - {\alpha_4}^2\right)\right) \tag{42}$$

Which re-arranges to

$$B\alpha_2(\beta_4 - \alpha_4)\left(4 + \frac{({\beta_4}^2-1)}{\alpha_4\beta_4}\right) = 2B\left({\beta_4}^2 - {\alpha_4}^2\right) + \frac{(1-\beta_4)^3}{\beta_4} \tag{43}$$

Leading to the solution

$$\alpha_2 = \frac{(2(\beta_4+\alpha_4) - \frac{(\beta_4-1)^3}{B(\beta_4(\beta_4-\alpha_4)}}{4+\frac{({\beta_4}^2-1)}{\alpha_4\beta_4}} \tag{44}$$

Rewriting (40) as

$$B\alpha_2 \frac{(\beta_4-\alpha_4)}{\alpha_4\beta_4} = \frac{\beta_4-1}{\beta_4} - \frac{u^2}{2gh}({\beta_4}^2-1) \tag{45}$$

And dividing (44) and (45) to eliminate α_2 we obtain after some manipulations:

$$\left(4\alpha_4\beta_4 + \left({\beta_4}^2-1\right)\right)\left((\beta_4-1) - \frac{Fr^2}{2}\left({\beta_4}^2-1\right)\beta_4\right) = 2B\left({\beta_4}^2-{\alpha_4}^2\right)\beta_4 - (\beta_4 - 1)^3 \tag{46}$$

Which is quadratic in β_4

$$\frac{Fr^2}{2}{\beta_4}^4 + 2\alpha_4 Fr^2{\beta_4}^3 - (2-2B+Fr^2){\beta_4}^2 - (4\alpha_4 + 2\alpha_4 Fr^2 - 4)\beta_4 + \left(\frac{Fr^2}{2} + 4\alpha_4 - 2B{\alpha_4}^2 - 2\right) = 0 \tag{47}$$

As B→0 and $\beta_4 \to 1$ note the limit

$$\frac{B}{(\beta_4-1)} = \frac{2\alpha_4}{(1-{\alpha_4}^2)}\left(1-\frac{u^2}{gh}\right) \tag{48}$$

The downstream head can be calculated from overall momentum:

$$\frac{1}{2}\rho gb(h^2-(h-\Delta h)^2) - T = \rho bhu\left(\frac{uh}{h-\Delta h} - u\right) \tag{49}$$

$$\frac{1}{2}\left(2\frac{\Delta h}{h} - \left(\frac{\Delta h}{h}\right)^2\right) - \frac{T}{\rho bgh^2} = \frac{u^2}{gh}\left(\frac{\Delta h}{h-\Delta h}\right) \tag{50}$$

$$\frac{1}{2}\left(2\frac{\Delta h}{h} - \left(\frac{\Delta h}{h}\right)^2\right) - \frac{T}{\rho bgh^2} = Fr^2\left(\frac{\Delta h/h}{1-\Delta h/h}\right) \tag{51}$$

Where $C_T = \frac{T}{\frac{1}{2}\rho Bbhu^2}$ so that $\frac{T}{\rho Bgh^2} = \frac{C_T BFr^2}{2}$

This is a cubic in $\Delta h/h$:

$$\frac{1}{2}\left(\frac{\Delta h}{h}\right)^3 - \frac{3}{2}\left(\frac{\Delta h}{h}\right)^2 + \left(1 - Fr^2 + \frac{C_T BFr^2}{2}\right)\frac{\Delta h}{h} - \frac{C_T BFr^2}{2} = 0 \tag{52}$$

The power lost in the mixing is calculated as:

$$P_W = \frac{1}{2}\rho u^3 bhB\alpha_2{\alpha_4}^2 + \frac{1}{2}\rho u^3 bh(1-B\alpha_2){\beta_4}^2 - \frac{1}{2}\rho u^3 bh\left(\frac{\Delta h}{h-\Delta h}\right)^2 + hbu(h_4 - h_5)\rho g = \frac{1}{2}\rho u^3 bhB\alpha_2{\alpha_4}^2 + \frac{(1-B\alpha_2)}{B}{\beta_4}^2 - \frac{1}{B}\left(\frac{1}{1-\frac{\Delta h}{h}}\right)^2 + \frac{2(h_4-h_5)g}{u^2 B} \tag{53}$$

Alternatively, it can be useful simply to calculate the total power taken out of the flow:

$$P + P_W = \frac{1}{2}\rho u^3 bh - \frac{1}{2}\rho u^3 bh\left(\frac{h}{h-\Delta h}\right)^2 + hbu(h-h_5)\rho g = \frac{1}{2}\rho u^3 bh\left(1 - \left(\frac{1}{1-\frac{\Delta h}{h}}\right)^2 + \frac{\frac{2\Delta h}{h}}{Fr^2}\right) = \rho gubh\Delta h\left(1 - Fr^2\frac{1-\Delta h/2h}{(1-\Delta h/h)^2}\right) \quad (54)$$

Therefore, the efficiency of the turbine is simply:

$$\eta = \frac{P}{P+P_W} = \frac{P}{\rho gubh\Delta h}\left(1 - Fr^2\frac{1-\Delta h/2h}{(1-\Delta h/h)^2}\right)^{-1} \quad (55)$$

9.4. CALCULATION SEQUENCE

1.Specify principal dimensioning parameters ρ g and h

2. (Optionally specify width b, which acts as purely scaling term on power and force)

3. Specify upstream Froud number $Fr = u/\sqrt{gh}$, blockage ratio 0≤B≤1 and dimensionless velocity factor 0≤α_4 ≤1

4. Calculate dimensionless quantities:

a. Solve for β_4

$$\frac{Fr^2}{2}{\beta_4}^4 + 2\alpha_4 Fr^2{\beta_4}^3 - (2-2B+Fr^2){\beta_4}^2 - (4\alpha_4 + 2\alpha_4 Fr^2 - 4)\beta_4 + \left(\frac{Fr^2}{2} + 4\alpha_4 - 2B{\alpha_4}^2 - 2\right) = 0$$

Such that $\beta_4 > 1$ and 1> $\alpha_r > \alpha_4$

b. $\alpha_2 = \dfrac{(2(\beta_4+\alpha_4) - \frac{(\beta_4-1)^3}{B(\beta_4(\beta_4-\alpha_4)}}{4+\frac{({\beta_4}^2-1)}{\alpha_4\beta_4}}$

c. $C_T = (\beta_4^2 - \alpha_4^2)$

d. $C_{TL} = \dfrac{C_T}{\alpha_2^2}$

e. Solve for $\Delta h/h$ from:

$$\frac{1}{2}\left(\frac{\Delta h}{h}\right)^3 - \frac{3}{2}\left(\frac{\Delta h}{h}\right)^2 + \left(1 - Fr^2 + \frac{C_T B Fr^2}{2}\right)\frac{\Delta h}{h} - \frac{C_T B Fr^2}{2} = 0$$

f. $C_P = \alpha_2 C_T$

g. $C_P + C_{PW} = \frac{1}{B}\left(1 - \left(\frac{1}{1-\Delta h/h}\right)^2 + \frac{2\Delta h/h}{Fr^2}\right)$

h. $\eta = \frac{C_P}{C_P + C_{PW}} = \frac{P}{P+P_W}$

5. Calculate dimensioned quantities:

i. $T = \frac{1}{2}\rho u^2 BbhC_T$

j. $P = \frac{1}{2}\rho u^3 BbhC_P$

k. $P_W = \frac{1}{2}\rho u^3 BbhC_{PW}$

l. $\Delta h = h\frac{\Delta h}{h}$

m. $Pressure\ drop\ across\ turbine\ \Delta_{PT} = \frac{T}{Bbh}$

9.5. SOLUTION SPACE OF THE MODEL

The quadratic by equation (47) will yield real solutions for β_4 only for a subset of input variables Fr, B, α_4. To determine the range of this subset we can reconsider the equations derived in 9.3. Both equation (29) and equation (35) express quantities that will have a minimum value when plotted against h_4. These minimum values indicate that the flow within the bypass and the far wake, respectively, will be exactly critical. If h_4 is specified as less, then this critical point no real solutions will exist for a given upstream discharge rate. More specifically the turbine will block th flow and the hydraulic jump will result.To determinate the critical point considers equation (29). Mathematically the condition of critical flow can be expressed as

$$\frac{dE}{dh_4} = \frac{d}{dh_4}\left(\frac{\beta_4^2}{2g} + h_4\right) = \frac{hFr^2}{2}\frac{d}{dh_4}\beta_4^2 + 1 = 0 \tag{56}$$

Giving the condition

$$\frac{d(\beta_4^2)}{dh_4} = \frac{2}{hFr^2} \tag{57}$$

A similar exercise can be done for equations (35) to determine the minimum momentum. However, it can be shown numerically that in all cases the bypass condition given by (57) is reached at the point when solutions to the quadratic (47) become complex. The far wake will never reach critical conditions before the bypass flow. Therefore, the solution space of this open channel model is bounded by the requirement that the bypass flow remains sub-critical, r mathematically $\frac{d(\beta_4^2)}{dh_4} < \frac{2}{hFr^2}$

UNIONE EUROPEA
Fondo Europeo di Sviluppo Regionale

MINISTERO DELL'UNIVERSITA' E DELLA RICERCA

PON
Ricerca e Innovazione
2014 - 2020

UNIVERSITY OF NAPLES FEDERICO II
Department of Civil, Architectural, and Environmental Engineering
Ph.D. Course in Civil Systems Engineering

UNIVERSITY OF OVIEDO
Department of Energy
Hydraulic Engineering

DIGITAL VERSION